NASA Contractor Report 165854

(NASA-CR-165854) APPLICATION OF THE FINITE ELEMENT METHOD TO ROTARY WING AEROELASTICITY Final Report (California Univ.) 232 p HC A11/MF A01 CSCL 20K

N82-20561

Unclas
G3/39 09312

APPLICATION OF THE FINITE ELEMENT METHOD TO ROTARY WING AEROELASTICITY

F. K. Straub and P. P. Friedmann

THE UNIVERSITY OF CALIFORNIA
Los Angeles, California 90024

Grant NSG-1578
February 1982

National Aeronautics and
Space Administration

Langley Research Center
Hampton, Virginia 23665

FOREWORD

This research was conducted at the Mechanics and Structures Department, School of Engineering and Applied Science, University of California, Los Angeles under NASA Grant NSG - 1578 funded by the Structures Laboratory AVRADCOM Research and Technology Laboratories and NASA Langley Research Center, Hampton, VA.

The research was monitored by Dr. C.E. Hammond and Dr. Warren Young from the Structures Laboratory. The authors wish to express their appreciation to the grant monitors for their useful comments and suggestions.

The principal investigator for the grant was Professor Peretz P. Friedmann. This document constitutes the first author's Ph.D dissertation.

SUMMARY

A finite element method for the spatial discretization of the dynamic equations of equilibrium governing rotary-wing aeroelastic problems is presented. The equations of motion are nonself-adjoint, nonlinear, and in partial differential form. For this class of problems, variational principles are not available. Thus, formulation of the finite element equations is based on weighted Galerkin residuals. This Galerkin finite element method reduces algebraic manipulative labor significantly, when compared to the application of the global Galerkin method to similar problems. However, more computer time is spent on the numerical calculations.

To illustrate the application of the Galerkin finite element method, the coupled flap-lag aeroelastic stability boundaries of hingeless helicopter rotor blades in hover are calculated. The finite element method is used to remove the spatial dependence from the equations. The ensuing set of nonlinear, ordinary differential equations is linearized about an appropriate nonlinear static equilibrium position. The number of nodal degrees of freedom in the discretized system is reduced significantly through a normal mode transformation. The nonlinear static equations, determining the equilibrium position, are solved iteratively using the Newton-Raphson method. The linearized dynamic equations are reduced to the standard eigenvalue problem from which the aeroelastic stability boundaries are obtained.

The convergence properties of the Galerkin finite element method are studied numerically by refining the discretization process. Results indicate that four or five elements suffice to capture the dynamics of the blade with the same accuracy as the global Galerkin method. However, for a reliable analysis, two modes for each elastic degree of freedom are required, since the second lag mode determines system stability for certain values of elastic coupling.

Next, the method is applied to the more practical coupled flap-lag-torsion aeroelastic stability and response problem of hingeless helicopter rotor blades in trimmed forward flight. Emphasis is placed on consistent discretization of the torsional degree of freedom.

No previous finite element solutions for the stability and response of nonlinear, nonconservative systems with periodic coefficients are available. Therefore, the general formulation is specialized to the coupled flap-lag problem in forward flight which is used to establish the computational feasiblity of the Galerkin finite element method in the forward flight regime.

The nonlinear, periodic coefficient, finite element equations are linearized about a nonlinear time dependent equilibrium position, namely, the steady-state response of the system. This response is obtained iteratively using quasilinearization. Aeroelastic stability is determined from the linearized perturbation equations using Floquet theory.

TABLE OF CONTENTS

Page

Page

LIST OF SYMBOLS

a = two-dimensional lift curve slope

a_n^e = element nodal parameters, Eq. (2.6)

$\underset{\sim}{a}^e$ = element nodal displacement vector, Eqs. (3.12) and (4.19)

$\underset{\sim}{a}$ = system nodal displacement vector

$[A], [A^K]$ = coefficient matrix of dynamic equations in first-order state variable form, Eqs. (3.23), (4.28), and (4.35b)

$[A_1], [A_2], [A_1^e], [A_2^e], [\bar{A}_2^e], [A_3^e]$ = aerodynamic operators and stiffness matrices, Appendix D and F

b_m = modal parameters, Eq. (2.2)

$\{b_m\}$ = vector of modal parameters, Eqs. (3.7) and (4.16)

$\bar{b} = \frac{b}{R}$ = airfoil semichord

$\{b^K\}$ = forcing vector in the linearized dynamic equations in first-order state variable form, Eq. (4.28)

$[B], [B^e]$ = bending stiffness operators and matrices, Appendix D

$[B_1^e], [B_2^e]$ = element stiffness matrices, Appendix F

$[B_c^1]$ = boundary condition term, due to root torsional stiffness, Appendix F

$B_{22}, B_{23}, B_{33}, B_4$ = nondimensional bending rigidities, Appendix B

$B_{m22}, B_{m23}, B_{m33}, B_{m4}, B_{m0}$ = nondimensional mass moments of inertia, Appendix B

C_{d0} = blade profile drag coefficient

C_{DP} = helicopter parasite drag coefficient, $\dfrac{2D_P}{\rho_A \pi R^2 V^2}$

C_{Mf} = fuselage pitching moment coefficient, $\dfrac{M_f}{\rho_A \pi \Omega^2 R^5}$

C_T = rotor thrust coefficient, $\dfrac{T}{\rho_A \pi R^2 \Omega^2 R^2}$

C_W = helicopter weight coefficient, $\dfrac{W}{\rho_A \pi R^2 \Omega^2 R^2}$

$\{c\}$ = forcing vector in final static equations, Eq. (3.18), Appendix D

$[C^K]$, $[C]$ = damping matrix in linearized dynamic equations, Eqs. (4.25d) and (4.36b)

$[C_1^e], [C_2^e], [C_{21}^e]$ = element matrices, velocity dependent inertia loads, Appendix F

$[C_{Ax}]$, $[C_{Ax}^e]$, $[C_{Ax}^{ei}]$ = operators and matrices due to axial shortening effect, Appendix D and F

$[C_{T2}]$ = tension operator, Appendix D

$D_x^i = \dfrac{\partial^i}{\partial x_0^i}$ = differential operator

D_P = parasite drag of helicopter, opposite to flight direction, Fig. 7 a,b

$[d]$ = damping matrix in dynamic equations, Eqs. (3.19) and (4.22), Appendix D and G

$[D_1],[D_2],[D_3],$ $[D_1^e],[D_2^e],[D_3^e],$ $[D_{22}^e],[D_{23}^e]$	=	aerodynamic damping operators and matrices, Appendix D and F
$[D_S^e]$	=	structural damping element matrix, Appendix F
$\bar{e}_1 = \frac{e_1}{\ell}$	=	blade root offset from axis of rotation, Fig. 3
$\hat{e}_x,\hat{e}_y,\hat{e}_z$	=	unit vector triad in x_0, y_0, and z_0 directions, respectively, before deformation, Fig. 3a
$\hat{e}'_x,\hat{e}'_y,\hat{e}'_z$	=	unit vector triad $\hat{e}_x$, $\hat{e}_y$, and $\hat{e}_z$, respectively, after deformation, Fig. 3b
E	=	number of finite elements (also, Young's modulus of elasticity)
fR	=	distance between hub center and helicopter center of gravity, along the fuselage axis, Fig. 7a,b
f_S R	=	distance between hub center and wind tunnel model support point, along the fuselage axis, Fig. 7b
$\underset{\sim}{f}^e$	=	element torsion displacements, Eq. (4.19), Fig. 5
f_m	=	generalized coordinate, m^{th} torsion mode
{f}	=	forcing vector in dynamic equations, Eq. (4.22), Appendix G
F_1,F_2,F_3,F_4,F_5	=	coefficients in the aerodynamic loads, Eqs. (4.14d - h)
F	=	known function, Eq. (2.1)
{F} , $\{F^e\}$	=	constant forcing terms, Eqs. (3.6) and (3.14), Appendix D

$\{F_I^e\}$, $\{F_A^e\}$ = inertia and aerodynamic loads, respectively, independent of displacements, Eq. (4.20), Appendix F

$\{F^K\}$ = operator, Eqs. (4.25a,b)

g^e, g_n^e = element flap displacements, Eqs. (3.12) and (4.19), Figs. 3b and 5

g_m = generalized coordinate, m^{th} flap mode

g_{SL}, g_{SF}, g_{ST} = structural damping coefficients in lag, flap, and torsion, respectively, $\bar{g}_{SL} = g_{SL}/m_0 \Omega$, $\bar{g}_{SF} = g_{SF}/m_0 \Omega$, and $\bar{g}_{ST} = g_{ST}/m_0 \Omega \ell$

GJ = blade torsional rigidity, $\bar{GJ} = GJ/(m_0 \Omega^2 \ell^4)$

$\underset{\sim}{G}$, $\underset{\sim}{G}^K$ = operators, Eqs. (4.22) and (4.25a)

[G], $[G^e]$ = gyroscopic operator and matrix, Appendix D

hR = distance between hub center and helicopter center of gravity, along the shaft axis, Figs. 7

h_S R = distance between hub center and wind tunnel model support point, along the shaft axis, Fig. 7b

$\underset{\sim}{h}^e$, h_n^e = element lag displacements, Eqs. (3.12) and (4.19), Figs. 3b and 5

h_m = generalized coordinate, m^{th} lag mode

H = rotor horizontal force, Figs. 7

H_S = horizontal force at support point in wind tunnel model, Fig. 7b

I_2, I_3 = principal moments of inertia for lagwise and flapwise bending, Appendix B, $\bar{EI}_2 = EI_2/(m_0 \Omega^2 \ell^4)$,

$\bar{EI}_3 = EI_3/(m_0 \Omega^2 \ell^4)$

I_b = blade mass moment of inertia in flap, Appendix B

I_{m2}, I_{m3} = cross-sectional mass moments of inertia, Appendix B, $\bar{I}_{m2} = I_{m2}/(m_0 \ell^2)$, $\bar{I}_{m3} = I_{m3}/(m_0 \ell^2)$

$[I]$ = unit matrix

$[I_1]$, $[I_1^e]$, $[I_2^e]$ = operator and element matrices, acceleration dependent inertia loads, Appendix D and F

$\underset{\sim}{i}$, $\underset{\sim}{j}$, $\underset{\sim}{k}$ = unit vector triad for x,y,z system, Figs. 3

k_1, k_2, k_3 = inflow functions, Eq. (4.3)

K = index, identifying the quasilinearization steps

K_ϕ = root torsional spring stiffness, $\bar{K}_\phi = K_\phi/(m_0 \Omega^2 \ell^3)$

$[k]$ = stiffness matrix in dynamic equations, Eqs. (3.19) and (4.22), Appendix D and G

$[K_1]$, $[K_1^e]$, $[K_2^e]$ = operator and element matrices, displacement dependent inertia loads, Appendix D and F

ℓ = length of elastic portion of blade, Fig. 3a

ℓ_e = length of finite element, nondimensionalized with respect to ℓ, Fig. 5

$\bar{m} = \frac{m}{m_0}$ = mass per unit length of the blade

m_0 = reference value for mass per unit length of blade

M = total number of modes used in analysis

M_L, M_F, M_T = number of lag, flap, torsion modes, respectively, used in analysis

M_f = pitching moment of fuselage, Figs. 7

M_{pa} = average pitching moment due to one blade, Figs. 7

M_x, M_1, M_2, M_3 = elastic moments, Eqs. (4.10), nondimensional

$[m]$ = mass matrix, Eqs. (3.19) and (4.22), Appendix D and G

$[M^K], [M]$ = mass matrix in linearized dynamic equations, Eqs. (4.25e) and (4.36c)

n_b = number of blades in rotor

N = number of element shape functions for each elastic degree of freedom

N_h = number of harmonics used in the Fourier analysis of the periodic response

N_{psi} = number of steps per revolution when computing the transition matrices and initial conditions

N_{rki} = number of steps per revolution used in the Runge-Kutta integration

N_{rev} = index, identifying consecutive rotor revolutions

$\underline{P}$ = distributed external force vector per unit length of blade, nondimensional, subscripts I, A, and D represent inertia, aerodynamic and structural damping contributions, respectively, Eqs. (4.11)-(4.15)

P = differential operator, Eq. (2.1)

q = unknown function, Eq. (2.1)

$\{q\}$ = vector of unknown lag, flap, and torsion displacements

q^g, $\{q^g\}$ = global approximation to q and $\{q\}$, respectively, Eqs. (2.2), (3.7) and (4.16)

q^e, $\{q^e\}$ = element, (local) approximation to q and $\{q\}$, respectively, Eqs. (2.6), (3.12) and (4.19)

$\{q\}$ = vector of generalized modal coordinates, Eqs. (3.16) and (4.21)

$\{\bar{q}\}$ = vector defining converged nonlinear steady-state response of modal coordinates

$\underline{q}$ = distributed external moment vector per unit length of blade, nondimensional, Fqs. (4.11) - (4.15)

Q, $\bar{Q}$ = differential operators, Eqs. (2.1) and (2.5)

R_c = blade elastic coupling parameter

R = blade radius, Fig. 3a

$\bar{r}_e = r_e/\ell$ = $\bar{x}_0$ coordinate of inboard node of element e, Fig. 5

$[S_B]$ = bending stiffness operator, Appendix D

$[S_{T1}]$ = centrifugal tension operator, Appendix D

$[s_L]$ = matrix of linear terms in the static equilibrium equations, Eq. (3.18), Appendix D

$[s_{NL}]$ = matrix of nonlinear terms in the static equilibrium position equations, Eq. (3.18), Appendix D

$[S^K]$, $[S]$ = stiffness matrix in linearized dynamic equations, Eqs. (4.25c) and (4.36a)

t = time

$\bar{T}$ = tensile force in blade, nondimensionalized by $(m_0 \Omega^2 \ell^2)$, Appendix B

T = rotor thrust, Figs. 7

T_S = support point resultant force in thrust direction, Fig. 7b

$[T_1], [T_2], [T_1^e], [T_2^e], [T_2^{ei}]$ = tension operators and matrices defined in Appendix D and F

$\bar{u} = \frac{u}{\ell}$ = axial displacement of blade, inextensional, Appendix B

$\bar{v} = \frac{v}{\ell}$ = elastic lag displacement, Fig. 3b

$\bar{v}^g, \bar{v}^e$ = global and local approximation to $\bar{v}$

V = helicopter forward speed, Figs. 7

$\bar{w} = \frac{w}{\ell}$ = elastic flap displacement, Fig. 3b

$\bar{w}^g, \bar{w}^e$ = global and local approximation to $\bar{w}$

x,y,z = rotating coordinate system, Figs. 3, $\bar{x} = x/R$

$\hat{X},\hat{Y},\hat{Z}$ = inertial reference frame

$\bar{x}_0 = x_0/\ell$ = spanwise coordinate for elastic portion of the blade, Figs. 3

$\bar{x}_e = x_e/\ell$ = element coordinate, Fig. 5

$\bar{x}_A = x_A/b$ = blade cross section offset between aerodynamic and elastic centers, Fig. 4; positive for A.C. before E.C.

$\bar{x}_I = x_I/\ell$ = blade cross section offset between center of gravity and elastic center, Fig. 4

x_{IS}, x_{IC} = components of $\ddot{\bar{x}}_I$, Appendix B

x_{II} = blade cross section offset between tension center and elastic center, Fig. 4

x_L = hub loss factor

x_U = tip loss factor

$\{y\}$ = first-order state variable vector of generalized modal coordinates, Eqs. (3.22) and (4.23a)

$\{\bar{y}\}$ = converged nonlinear steady-state response portion of $\{y\}$

Greek Symbols

α_R = rotor angle of attack, Figs. 7

β_1 = first fundamental frequency constant for bending

β_p = blade preconing, inclination of the feathering axis with respect to the hub plane, Figs. 3

γ = Lock number, Appendix B

γ_F = flight path angle, Figs. 7

Γ = coefficient, Appendix B

$\underset{\sim}{\gamma}$, $\{\gamma_n\}$ = vector of element lag interpolation polynomials, Appendix C

ε, $\underset{\sim}{\varepsilon}$ = residuals

ε_D = symbolic order of magnitude quantity, equal to elastic blade slopes in bending

$\bar{\varepsilon}$ = small prescribed number used in convergence tests, Figs. 5 and 8

ζ_n^e = element shape function, defined in global domain, Eq. (2.7)

ζ_k = real part of λ_k

$\zeta_{iL}, \zeta_{iF}, \zeta_{iT}$ = real part of eigenvalue associated with predominant i^{th} lag, flap, or torsion mode

η, ζ = principal coordinates of a blade cross section (η is the axis of symmetry), Fig. 4

$\underset{\sim}{\eta} = \{\eta_n\}$ = vector of element flap interpolation polynomials, Appendix C

θ = collective pitch setting in hover

θ_c = critical value of θ at which linearized system is neutrally stable

θ_B = blade pretwist, built-in about elastic axis

θ_G = total geometric pitch angle, Eq. (4.2), Fig. 4

θ_r = pitch angle, Eq. (4.1)

$\theta_0, \theta_{1s}, \theta_{1c}$ = collective and cyclic pitch components, Eq. (4.1)

λ = inflow ratio

$\lambda_0, \lambda_s, \lambda_c$ = components of λ, Eq. (4.3)

λ_k = k^{th} eigenvalue of Eq. (3.23), k^{th} characteristic exponent of Eqs. (4.29) and (4.35b)

Λ_k = k^{th} characteristic multiplier of Eqs. (4.29) and (4.35b)

$[\Lambda]$ = modal transformation matrix, Eqs. (3.16) and (4.21)

μ = advance ratio, $(V \cos \alpha_R)/(\Omega R)$

ρ = mass density of blade material

ρ_A = mass density of air

σ = solidity ratio, Appendix B

ϕ = elastic torsion deformation

ϕ^g, ϕ^e = global and local approximation to ϕ

$\underset{\sim}{\phi}$, $\{\phi_n\}$ = vector of element torsion interpolation polynomials, Appendix C

Φ_m = global shape function, Eq. (2.2)

$[\Phi_m]$ = matrix of global shape functions, Eqs. (3.7), (4.16)

$[\Phi^K]$, $[\Phi]$ = transition matrix, Eqs. (4.32) and (4.37)

Ψ = azimuthal angle, measured from straight aft position, dimensionless time ($\Psi = \Omega t$)

Ψ_n^e = element shape functions, Eq. (2.6)

$[\Psi]$ = matrix of element shape functions, Eqs. (3.12) and (4.19)

ω_k = imaginary part of λ_k

$\bar{\omega}_{L1NR}, \bar{\omega}_{F1NR}, \bar{\omega}_{T1NR}$ = first nonrotating uncoupled lag, flap, and torsion frequency, respectively, Appendix B

$\bar{\omega}_{L1}, \bar{\omega}_{F1}, \bar{\omega}_{T1}$ = first rotating uncoupled lag, flap, and torsion frequencies, respectively, nondimensionalized with respect to Ω

Ω = constant rotor speed of rotation, Figs. 3

Special Symbols

$(\dot{\ }) = \frac{1}{\Omega}\frac{\partial}{\partial t} = \frac{\partial}{\partial \psi}$

$(\ )_{,x} = \frac{\partial}{\partial x_0}$

$(\ )^0$ = static equilibrium position portion of a quantity

$\Delta(\ )$ = perturbation portion of a quantity

$(\underset{\sim}{\ })$ = vector quantity

$[\ ]^S$ = assembled system matrix

LIST OF FIGURES

LIST OF TABLES

SECTION 1

INTRODUCTION AND REVIEW OF PERTINENT LITERATURE

1.1 Introduction

Rotary-wing aircraft are widely used today in both civilian and military versions. However, performance characteristics must be improved to meet requirements on improved speed, range, payload, maneuverability, maintenance and comfort. Of the many components governing the performance of rotary-wing aircraft, the rotor is of outstanding importance. Consequently, one of the most active research areas in aeroelasticity today is rotary-wing aeroelasticity.

The coupled flap (bending out-of-plane of rotation), lag (bending in-plane of rotation), and torsional aeroelastic behavior of an isolated rotor blade is the basic building block from which a more complete system analysis can be developed. A clear understanding of the single blade behavior, governed by the complex interaction of structural, inertia, and aerodynamic forces, is therefore imperative. Both, stability and response, must be well understood. Terminology and configuration parameters associated with hingeless rotor blades which have become an increasingly attractive concept are given in Figs. 1.2.

Several studies have derived equations capable of simulating the motion of this configuration with varying degrees of sophistication. A comprehensive review of recent developments in this area is given by

Friedmann [1]. The most significant conclusion from previous research is the fact that the rotary-wing aeroelastic stability problem is inherently nonlinear. As a consequence, the correct treatment of this aeroelastic stability problem requires the derivation of the dynamic equations of equilibrium in a careful and consistent manner such that moderate deflections, based upon the assumption of small strains and finite slopes, are properly incorporated in the mathematical model [1], [2]. When the equations of motion are formulated in this manner, nonlinear terms can appear in the structural, inertia and aerodynamic operators associated with this aeroelastic problem and the final equations of motion will have a partial differential nonlinear form [1], [2].

In rotary-wing aeroelasticity the nonlinear equations of motion in partial differential form are usually solved by applying Galerkin's method to eliminate the spatial dependence of the problem [1] - [3]. This procedure yields a set of coupled nonlinear ordinary differential equations for the dynamics of the blade. It is common practice, [1] - [3], to obtain actual aeroelastic stability boundaries by linearizing the equations of motion about an appropriate equilibrium position and extracting stability information from the eigendata associated with the linearized system.

Typical studies, [1] - [3], dealing with practical blade configurations in hover, or in forward flight, are representative of the algebraic complexity encountered when applying Galerkin's method to rotary-wing aeroelastic problems. From the inspection of these and

similar studies it is clear that methods of solution based upon the modal Galerkin method lead to extremely cumbersome algebraic manipulations, which have to be carried out manually or by alternative means such as algebraic manipulative systems. In some cases, the amount of algebraic manipulations associated with the global Galerkin method is so excessive as to prohibit treatment of complicated blade configurations in a realistic manner. Therefore, in this study the spatial dependence will be eliminated using a Galerkin type finite element method. This essentially local Galerkin method enables one to discretize the partial differential equations of motion directly. Consequently, a significant reduction in the algebraic manipulative labor required for the solution of the problem is accomplished.

During the past fifteen years, the finite element method has undergone explosive growth and, at the present, it has evolved from a structural analysis tool to a general mathematical method for solving partial differential equations, which is competitive with finite differences, for general applications, and superior to finite differences in structural dynamics applications [4] - [8]. For conservative self-adjoint, linear problems, the finite element model for the system can be conveniently generated by applying appropriate variational principles. Existence of these variational principles will also, in most cases, guarantee the convergence of the method. For nonself-adjoint, nonconservative problems, such as the flutter or aeroelastic problem, variational principles are not available. Thus, generation of the finite element model for aeroelastic, nonconservative systems is more

complicated and convergence of the method is not guaranteed [9].

The rotary-wing aeroelastic problem is nonself-adjoint, nonconservative and nonlinear, thus, formulation of a finite element method for this problem is by no means straightforward. However, finite element discretization of these equations of motion will essentially eliminate the cumbersome algebraic manipulations associated with the global Galerkin method.

The purpose of the present study is to develop a local Galerkin method of weighted residuals [5] - [8], [10], [11], which is used to discretize the spatial dependence of the equations resulting in a finite element formulation of the rotary-wing aeroelastic problem. This method is applied directly to the equations of motion in partial differential form and leads to a finite element formulation of the rotary-wing aeroelastic problem, avoiding the excessive algebraic manipulations required by the application of Galerkin's method when using global modes (i.e., conventional method).

To illustrate the method and establish its convergence properties, the method is applied to some typical rotating blade free vibration problems and to the coupled flap-lag aeroelastic stability calculation of a hingeless helicopter rotor blade in hover. Comparison of the solutions obtained, by using the finite element method, with previously published results is used to establish the convergence properties of the method. It is concluded that this formulation has the potential of becoming a powerful and practical tool for solving rotary-wing aeroelastic stability or response problems.

Next, the Galerkin finite element method is extended to discretize the coupled flap-lag-torsion aeroelastic stability and response problem of hingeless helicopter rotor blades in forward flight. In this case, the equations of motion contain periodic time-varying coefficients. For simple blade configurations, finite element solutions for the flap-lag case are compared with previously published results. In addition, more complicated blade configurations can be treated efficiently. Here, the full potential of the new method becomes evident, as it enables one to model the blade more realistically to a degree which has not been achieved previously.

1.2 Review of Discretization Procedures Used in Rotary-Wing Dynamics and Aeroelasticity

The rotary-wing aeroelastic problem is governed by partial differential equations. The first step in solving these equations is to discretize the spatial dependence of the dependent variables such that a set of ordinary differential equations is obtained. Analysis of these equations will yield the dynamic system behavior.

Typically, Galerkin's method of weighted residuals is used for the discretization procedure [1] - [3]. Thus, each elastic degree of freedom is represented as a finite sum of mode shapes. These modes are taken as the coupled [3] or uncoupled [2] free vibration modes of a rotating blade. They are generated from the uncoupled free vibration mode shapes of a nonrotating blade, for which exact expressions are available. Most studies, in particular those considering the

forward flight case, use only one mode for each elastic degree of freedom. When more than one mode is used, the complexity of the problem leads to extremely cumbersome algebraic manipulations which, in some cases, are so excessive as to prohibit realistic treatment of complicated blade configurations.

Thus, it becomes compulsory to look for alternative discretization procedures. Two such methods, the integrating matrix method and the finite element method, will be introduced in this section. There are, of course, other methods. However, these two have been applied more widely to rotating beam problems and seem to have greater promise with respect to treatment of aeroelastic problems.

The integrating matrix method (IMM) provides a means to eliminate the spatial dependence in rotating beam vibration problems. Vakhitov developed the method and used it to solve for static deflections of beams [12] and for coupled bending-torsion vibrations of a rotating blade [13]. However, only few numerical results were presented. Hunter [14] extended the numerical scope of the method and investigated coupled bending-bending vibrations of a rotating propeller blade. Subsequently, several researchers applied the IMM to a variety of rotating beam vibration problems. White [15] formulated the coupled bending-torsion problem. Murthy [16] investigated flapwise bending and coupled flap-torsion vibrations. White and Malatino [18] solved the flap-lag and the nonlinear torsion problem for the same propeller blade as considered by Hunter [14]. Finally, Kvaternik, White, and Kaza [19] used the IMM to solve nonlinear flap-lag and axial vibration

problems. They also indicated the possibility of applying the IMM in aeroelastic stability analyses of helicopter rotor blades. In what follows, a brief description of the IMM, its basic properties and numerical performance when applied to rotating beam problems, is given.

The IMM is based on direct numerical integration. The integrating matrix may be viewed as a matrix operator which by premultiplying a vector, containing as elements the values of a function at discrete stations along the blade, transforms it into another vector having the integrals of the function (from one end of the blade to each station) as elements. To account for the boundary condition, a constant vector has to be added. In order to apply the IMM towards the solution of a differential equation, it is necessary to write the differential equation, or an integrated form of it, at a number of stations along the blade. The resulting set of equations has to be cast in matrix form. The integrating matrix can then be used to express the equations in terms of one set of unknowns, either the displacements or the fundamental derivatives (second-order for bending, first-order for torsion) at each station. Thus, discretization is achieved and the vibration problem is now posed in the form of a matrix eigenvalue problem.

Derivation of the integrating matrix is based on piecewise polynomial interpolation. If, for convenience, equally spaced collocation points are chosen, Newton's forward-difference interpolation formula can be used to express the polynomial coefficients in terms of the

function values at the appropriate collocation points. Integration of the polynomial expressions yields the elements of the integrating matrix.

The IMM always leads to nonsymmetric system matrices, even when considering a self-adjoint problem. Furthermore, the matrices are not banded. The eigenvectors are not orthogonal with respect to the system matrices. Further, the IMM does not yield upper bound solutions. Last, the dynamic matrix is degenerate, leading to zero eigenvalues which correspond to infinite frequencies.

The inputs for the matrix equations are simply the values of the cross-sectional properties at the discrete stations. Nonuniform properties are therefore easily incorporated. Boundary conditions are readily applied when considering the clamped-free case. For other cases, modification of the method is necessary [12] and some of its appealing simplicity is lost.

The IMM has been applied to a number of static, vibration, and buckling problems of beams. Results were compared with exact and other approximate solutions, employing the finite difference, transfer matrix, and Rayleigh-Ritz methods, and with experimental results. Extensive convergence studies were performed by Hunter [14] for bending free vibrations of a cantilever beam. Overall, accuracy increases with the number of stations and the degree of the interpolating polynomials. In general, higher degree polynomial representation gives higher accuracy when using a fixed number of stations. However, the number of stations employed should always be considerably larger

(about twice as much) as the degree of the interpolating polynomials, especially when higher frequencies are desired. A convergence study for more complex systems, which for instance display dynamic instability, was not performed. Results for nonlinear problems are indicative of trends only.

The IMM has been established as a very useful tool to solve free vibration problems of rotating beams. The method is very accurate and converges well. This is not surprising as it is solely based on numerical integration. The IMM has the potential of being applied to rotary-wing aeroelastic problems. However, more information on its performance, when solving nonlinear and nonconservative problems, needs to be obtained. One particular disadvantage of the method is, that it does not yield orthogonal mode shapes. Thus, it becomes questionable whether modes from the IMM could be used to reduce the number of degrees of freedom, which is essential for calculating aeroelastic stability boundaries.

The finite element method (FEM) has been used extensively and with great success for the solution of beam vibration problems. In particular, it has been applied in the analysis of rotating blades. Solutions for the flapwise free vibrations of a pinned-free rotating beam using a Galerkin-type finite element method were presented by Nagaraj and Shantakumar [20]. Their treatment was based on a bending element with four degrees of freedom per node, satisfying all boundary conditions. Comparison with results obtained by using the global Galerkin method showed good agreement. A conventional finite element

model for the natural vibrations of tapered and pretwisted cantilevered rotor blades was formulated in Reference [21]. The equations were developed for coupled flap-lag-torsion motion. A simple finite element, having ten degrees of freedom, was employed. However, numerical results were restricted to flapwise bending of a rotating tapered beam and a nonrotating pretwisted beam. The results displayed satisfactory convergence trends and agreed well with previous sclutions.

Application of the FEM to nonlinear problems is, by now, standard. Many solution algorithms are available, and their numerical performance is well documented. In addition, the FEM has been used for the analysis of a large variety of nonconservative systems. Here, the Galerkin finite element method has found its most prominent area of application.

The FEM, in contrast to the IMM, can always be formulated such that it yields symmetric matrices for self-adjoint problems. This, together with the banded nature of the matrices represents an advantage for certain solution algorithms. Another advantage of the FEM is the handling of boundary conditions of any type without any modifications. On the other hand, formulation of nonlinear terms and, in particular, integral terms, as they appear in rotor blade equations, is quite straightforward when using the IMM. Finally, the FEM leads to orthogonal eigenvectors. Such eigenvectors have been successfully employed in coordinate transformations to reduce the number of degrees of freedom used to model a dynamic system. Such a reduction is of great importance, since the aeroelastic problem at hand requires a

large number of eigenproblem solutions. This last point and the large amount of information available on application of the FEM to nonlinear and nonconservative systems, represent the main advantages of the FEM over the IMM. It also should be noted that the IMM is purely a numerical integration procedure, while the FEM retains a relation to the physical properties of the system under consideration.

A thorough examination of the relevant FEM literature will follow in the next section. From this, it becomes clear that the Galerkin finite element method is extremely well suited for dealing with rotary-wing aeroelasticity. A further advantage in using a Galerkin-type finite element approach consists of the considerable amount of research done by applied mathematicians and engineers to establish the numerical properties of this method. This vigorous, ongoing research activity provides the aeroelastician with more information on the numerical aspects, and particularly, convergence properties of the method than is available on the integrating matrix method.

1.3 Review of Pertinent Literature on Finite Elements

From previous remarks, it is clear that two aspects of the finite element method are of particular concern here. Namely, application to problems which do not allow a variational formulation and nonlinear problems. Accordingly, the following literature review will emphasize these special features.

The finite element method (FEM) originated in the area of

structural analysis. Its formulation was based on elementary concepts such as the principle of virtual work or Castigliano's theorem. Recognizing that the FEM can be viewed as an application of the principle of stationary potential energy soon led to its use in other areas. In general, all problems for which a variational principle existed could be solved. This variational formulation also, in most cases, guarantees the convergence of the method with mesh refinement. However, there is a large number of problems for which no variational principle exists.

Olson [22] solved the nonself-adjoint panel flutter problem. He used the principle of virtual work to derive consistent aerodynamic load matrices. The eigenvalues did converge when the number of elements was increased. However, this convergence was not monotonic. Barsoum [23] used the extended Hamilton's principle to solve the dynamic stability of thin-walled beams subjected to nonconservative loading. The nonself-adjoint character of the system was reflected in the nonsymmetric load matrix. The same problem was treated by Kikuchi [9]. It is interesting to note that convergence of the results was best when the system was conservative, but became worse as the degree of nonconservativeness became dominant.

A much more general approach was first developed by Szabo and Lee [24]. They combined the method of weighted residuals, using Galerkin's weighting criteria, with the FEM to calculate stiffness matrices for problems in plane elasticity. This procedure requires only knowledge of the differential equations and boundary conditions in a given

domain and boundary. No variational concepts are involved. In Reference [24] the weighted residual of the governing differential equations was evaluated over the element (local domain). Integration by parts led to a formulation which yields the same element matrices as the conventional FEM. This also introduced element boundary terms, which would vanish in the element assembly process if (and only if) both the approximate displacement and stress fields were continuous. This is, in general, not the case. Therefore, inter-element boundary contributions were neglected while, for external boundaries, the actual boundary conditions were substituted.

Zienkiewicz and Parekh [25] applied the Galerkin weighted residual finite element method (GFEM) to transient field problems. In contrast to Reference [24], the residual was formulated for the system (global domain). Green's theorem was used to remove higher order continuity conditions between elements. Formally, no inter-element boundary terms appeared because the integration was carried out over the global domain.

A more rigorous treatment of the GFEM was presented by Hutton and Anderson [11]. They used approximating functions over the global domain which were nonzero only within the local domain. This made it possible to apply convergence results from the global Galerkin method. Further, it was clearly stated which of the boundary conditions have to be satisfied and what the inter-element continuity requirements are. Both issues are closely related to the integration by parts. It was also shown that inter-element boundary residuals need to be

introduced when deriving the equations on the element level. Finally, it was established that all those problems that can be solved using a variational approach are a subclass of those amenable to the GFEM. If a variational principle is available, both methods lead to the same results. Last, deriving the equations on the basis of virtual work is equivalent to using Galerkin's method as long as the geometric boundary conditions are homogeneous.

Aral, Mayer and Smith [26] discussed the relation between Galerkin's approach and true-, quasi-, and restricted variational principles. If available, they all lead to the same results. The approximating equations, using the GFEM, were derived on the element level. Consequently, inter-element boundary residuals were introduced to cancel identical terms arising from integration by parts over each element.

Use of the GFEM without performing integration by parts was illustrated in References [27] - [29]. Prasad and Murty [27] solved flexural beam vibration problems. They used seventh-order interpolating polynomials as shape functions to satisfy continuity requirements on the higher derivatives. Comparison with the conventional FEM (cubic interpolating polynomials) proved the GFEM, in this form, to be very accurate. In Reference [28] the stability of nonconservative systems was analyzed. Results were more accurate than those of Kikuchi [9]. This improved accuracy has to be attributed to the stipulation of higher-order continuity, see Barsoum [23]. A disadvantage of this particular implementation of the GFEM becomes apparent when

considering problems with mixed boundary conditions. Then it is necessary to perform a congruent coordinate transformation such that these boundary conditions can be satisfied [28], [29]. Furthermore, matrices which would be symmetric when applying integration by parts now become unsymmetric.

A comparative study of several finite element models applied to vibrations of beams was presented in Reference [30]. The basic features of the conventional-, hybrid-, least-square-, collocation-, and GFEM were discussed. The possibility of using the GFEM in nonlinear analyses was pointed out. Further material on several approximation procedures, used in conjunction with the FEM, can be found in Reference [8].

Application of the FEM to nonlinear structural problems has received considerable attention and a large number of publications on this subject are available. A comprehensive review of solution procedures applied in static analyses of structures, displaying both geometric and/or material nonlinearities, was presented by Tillerson, Stricklin and Haisler [31]. Selection of a solution procedure was shown to be governed by interaction of several factors, such as type of analysis, ease of implementation, storage space, problem size, desired accuracy, degree of nonlinearity, computational economy, and user experience. Another review by Gallagher [32] dealt with geometrically nonlinear problems. Construction of finite element equations and solution algorithms were created. It was shown that tensor notation [33], rather than matrix notation, permits a greater simplicity

and efficiency in formulating the equations. It was also pointed out that some advantage might be gained by using inconsistent formulations, in which simplified interpolation polynomials are used for computation of the nonlinear terms. Such an approach was used by Bergan and Clough [34]. A more detailed investigation of inconsistent formulations can be found in Reference [35]. Finally, Gallagher [32] suggested use of condensation techniques to reduce the number of degrees of freedom, prior to performing the nonlinear analysis computations. This could lead to significant savings in computational expense. The normal mode concept was applied for this purpose by Kavanagh [36].

The FEM has also been used successfully in problems of nonlinear structural dynamics. However, applications were mainly restricted to the transient response under impulsive loadings, such as impact, seismic, or blast loads, wherein the time history was found by numerical integration [37] - [39].

The first attempt to solve large amplitude natural vibrations of beams and plates was made by Mei [40], [41]. He calculated the nonlinear terms from the linear mode shape, multiplied by an amplitude factor, and then extracted the eigendata from the linearized system. Comparison with other analytical solutions and experimental data showed the FEM to match the experiments more closely. Convergence is monotonic with increasing mesh refinement. Mei, later on, included an iterative solution technique, where the nonlinear terms were calculated from the vibration mode shape of the previous iteration cycle [42], [43]. The iteration led to lower frequencies. The number of

iteration steps to achieve a certain accuracy was larger for higher values of the prescribed amplitude, i.e., it increased with the degree of nonlinearity. Convergence was not monotonic during the iteration. The same problems were solved in References [44] and [45] using the same iterative procedure. However, the nonlinear terms were modeled in a different manner, without making some of the simplifying assumptions used by Mei. Comparison of the period for the fundamental mode of a simply supported square plate showed results of Reference [45] to be more accurate than those of Reference [41]. This illustrates the importance of modeling the nonlinear terms adequately.

Of particular interest is Mei's finite element approach to nonlinear panel flutter [46] which represents a typical nonself-adjoint nonlinear aeroelastic problem. Development of the aerodynamic matrices was based on Olson's work [22]. Modeling of the nonlinear terms, the iterative solution procedure and equivalent linearization technique were taken from References [41] and [42]. For large deflections, the nonlinear effects, mainly due to membrane stresses, restrain the panel motion to bounded limit cycle oscillations with increasing amplitude as the dynamic pressure increases. In general, three to six iteration cycles were sufficient for convergence. Convergence with respect to the number of elements used was not studied for the nonlinear case. The FEM described the panel behavior correctly. However, a numerical comparison with previous nonlinear panel flutter solutions was not given. Thus, the accuracy of the nonlinear finite element solution cannot be assessed.

Finally, it is worthwhile to mention that the GFEM is very well suited for application to nonlinear problems. Oden [47] characterized it as "... perhaps the most powerful technique for generating acceptable finite element models of nonlinear equations." Rao and Raju [48] applied it to the post buckling analysis of uniform cantilever columns. Agreement of results with those found by using elliptic integrals was very good, even for a small number of elements. The GFEM was also used in nonlinear reactor dynamics [49] and nonlinear boundary layer flows [50]. This illustrates, again, the versatility of the GFEM.

1.4 Objectives of the Present Study

The objectives of the present study are summarized below:

1. Development of a local method of weighted residuals, using Galerkin's weighting criteria. This results in a finite element formulation which can be used to discretize nonself-adjoint and nonlinear partial differential equations encountered in rotary-wing aeroelasticity.

2. Application of this Galerkin finite element method (GFEM) to coupled flap-lag aeroelastic stability calculations of hingeless helicopter rotor blades in hover. The GFEM is used to transform the nonself-adjoint, nonlinear partial differential equations of motion into a set of ordinary nonlinear differential equations. The equations are then linearized about an appropriate nonlinear static equilibrium position. The

number of unknowns modeling the discretized system is reduced significantly through modal analysis. The nonlinear static equations are solved iteratively, using the Newton-Raphson method. The linearized dynamic equations yield a standard eigenvalue problem from which the aeroelastic stability boundaries are obtained. The convergence properties of the GFEM are studied numerically by refining the discretization procedure. Results will also be compared with previous analyses where the global Galerkin method was employed. It should be stressed here that the major interest is the spacewise discretization of a typical rotary-wing aeroelastic problem via the GFEM.

3. The Galerkin finite element method is used to discretize the coupled flap-lag-torsion aeroelastic stability and response problem of hingeless helicopter blades in trimmed forward flight. Emphasis is placed on consistent discretization of the torsional degree of freedom. The blade is assumed to have built-in twist, cross-sectional offsets between the aeroelastic center, center of gravity, and elastic center, and nonuniform mass and stiffness properties. Root-torsional spring stiffness and nonuniform cyclic inflow are also included in the model. When solving the discretized dynamic equations, a major complication arises due to the forward flight condition which introduces periodic time-varying coefficients in the equations of motion, as well as

a large number of additional aerodynamic loading terms.

Due to the complexity of this problem it was decided, at this stage, to specialize the general formulation to the coupled flap-lag problem in trimmed forward flight. This problem, which is computationally less expensive, is used to establish the computational feasibility of the Galerkin finite element method for the aeroelastic problem in forward flight. In this portion of the present study, the discretized, nonlinear ordinary differential equations of motion are linearized about a nonlinear time-dependent equilibrium position, namely, the steady-state response of the system. Aeroelastic stability boundaries are obtained from the linearized system.

For a number of sample problems, involving hingeless rotor blades, the finite element solutions are compared with previously published results obtained by using the global Galerkin method. The convergence properties of the Galerkin finite element method are studied numerically by varying the number of elements and mode shapes, i.e., by refining the discretization procedure. The sensitivity of the aeroelastic steady-state response and stability to variations in the parameters governing this problem is also considered.

SECTION 2

GALERKIN FINITE ELEMENT METHOD

From the preceding literature review it is evident that the Galerkin finite element method (GFEM) has been used successfully in treating a large number of nonself-adjoint and nonlinear problems. In the next section a brief description of the method will be given. Emphasis is placed on its application to nonself-adjoint systems. The GFEM, being applied directly to the governing differential equations, makes discretization of nonlinear terms straightforward. The ensuing nonlinear equations can then be solved with any of the algorithms used in the conventional finite element method. This aspect is treated in Sections 3.3 and 4.3.1.

2.1 Global Galerkin Method

The local Galerkin method, resulting in a finite element discretization, can best be clarified by illustrating its application to a simple system. More details can be found in References [8] and [11].

Consider the following differential equation

$$Q(q) + P(q) = F \tag{2.1}$$

which is defined in a domain D, where Q is a symmetric positive definite differential operator of order $2r$ and P is a general

operator of order r or less, representing the nonself-adjoint portion of the equation. Both are operating on an unknown function q to yield a given function F. Furthermore, the function q has to satisfy certain boundary conditions on the boundary S of the domain D. For simplicity, q is chosen as a scalar function; however, the subsequent development is equally applicable to vector functions.

Next, an approximate global solution having the form,

$$q^g = \sum_{m=1}^{M} \phi_m b_m \tag{2.2}$$

is assumed. The ϕ_m are linearly independent shape functions and the b_m are the undetermined parameters for this problem. When using the extended Galerkin method, the ϕ_m have to have continuous derivatives up to order $(r-1)$, i.e., C_{r-1} continuity. Further, they need to satisfy only the geometric boundary conditions, i.e., those containing derivatives of order not higher than $(r-1)$. This approximate solution is then substituted into the differential equation and the boundary conditions. The error is minimized by requiring orthogonality with respect to a set of weighting functions. Thus, an integral statement, equivalent to the differential equation and the boundary conditions, is obtained.

In the extended Galerkin method the original shape functions ϕ_m are chosen as weighting functions. It is then required that the sum of the weighted residuals of both the differential equation and the

natural boundary conditions, i.e., those containing derivatives of order r and higher, be zero [10]. Thus,

$$\int_D \Phi_m \varepsilon \, dD + \int_S \Phi_m \varepsilon_B \, dS = 0 , \qquad m = 1,2,\ldots,M , \tag{2.3}$$

where

$$\varepsilon = Q(q^g) + P(q^g) - F \tag{2.4}$$

and ε_B is the residual associated with the natural boundary conditions.

In many cases it is possible to apply integration by parts to Eq. (2.3). This reduces the order of differentiation in the symmetric operator Q, thus lowering requirements on the shape functions Φ_m from C_{2r-1} to C_{r-1} continuity. Furthermore, this algebraic step also yields terms which cancel some of the boundary residual contributions. As a matter of fact, formulation of the weighted boundary residual and its combination with the differential equation residual are made in such a way that, when integrating the last one by parts, identical terms of the boundary residual are canceled [10]. In the case where the natural boundary conditions are homogeneous, all boundary residual terms cancel out and Eq. (2.3) becomes

$$\int_D \{\bar{Q}(\Phi_m, q^g) + \Phi_m P(q^g) - \Phi_m F\} dD = 0 , \tag{2.5}$$

where $\bar{Q}$ denotes the operator Q after integration by parts.

Application of the extended Galerkin method to beam bending can be found in Reference [51].

2.2 Finite Element Approach

When formulating a finite element version of Galerkin's method the domain D is subdivided into E subdomains d, which are called elements. In each element an approximate solution of the form

$$q^e = \sum_{n=1}^{N} \psi_n^e a_n^e \tag{2.6}$$

is assumed, where a_n^e are the nodal parameters and ψ_n^e are linearly independent shape functions defined only in the subdomain associated with the element d. This local approximation can be extended over the whole domain D by defining

$$\zeta_n^e = \begin{cases} \psi_n^e & \text{inside d} \\ 0 & \text{outside d} \end{cases} . \tag{2.7}$$

Using Eq. (2.7), the global approximation can be expressed as

$$q^g = \sum_{e=1}^{E} \sum_{n=1}^{N} \zeta_n^e a_n^e . \tag{2.8}$$

After imposing compatibility conditions on the nodal parameters of adjacent elements (this is done during the process of assembly), equations (2.2) and (2.8) are equivalent.

Equation (2.5) can be rewritten using Eq. (2.8) as

$$\sum_{i=1}^{E} \sum_{n=1}^{N} \int_D \left\{ [\bar{Q}(\zeta_j^e, \zeta_n^i) + \zeta_j^e P(\zeta_n^i)] a_n^i - \zeta_j^e F \right\} = 0 , \qquad (2.9)$$

$$j = 1,2,\ldots,N, \quad e = 1,\ldots,E,$$

where $\bar{Q}$ is obtained from Q by means of the previously mentioned integration by parts. In addition, it is implicitly assumed that no inter-element discontinuities occur. Thus, the functions ζ_n^e and its derivatives of order less than r must be continuous such that derivatives from order r up to $(2r-1)$ are finite on element interfaces. Equation (2.9) represents all weighted residuals for one element and for the total assemblage of elements (i.e., $N*E$ weighted residuals), it represents an intermediate step and in reality only Eq. (2.10) below is used.

As a consequence of the linear independence of the ζ_n^e functions, Equation (2.9) can also be rewritten on the element level.

$$\sum_{n=1}^{N} \int_d \left\{ [\bar{Q}(\psi_j^e, \psi_n^e) + \psi_j^e P(\psi_n^e)] a_n^e - \psi_j^e F \right\} = 0 , \qquad (2.10)$$

$$j = 1,2,\ldots,N, \quad e = 1,2,\ldots,E .$$

Equation (2.10) thus represents a set of N equations for each element, from which the element matrices can be calculated.

Because of the unique choice of weighting functions in Galerkin's method and because of the integration by parts, $\bar{Q}$ yields symmetric matrices. Further, when P is equal to zero, Eq. (2.10) is the exact same expression as found when employing the variational formulation of the finite element method. Operator P leads to unsymmetric matrices. However, the banded nature of the system matrices is still preserved.

Assembly of the system matrices and enforcement of the geometric boundary conditions is handled as in the conventional finite element method.

Finally, it should be pointed out that when Equation (2.3) is solved directly, the approximate solution has to have C_{2r-1} continuity and must satisfy all boundary conditions. The generation of such finite elements is of course more difficult, in particular for nonlinear terms, than generation of elements for the solution of Equation (2.5). In addition, all matrices will be nonsymmetric. On the other hand, due to the higher-order continuity, one might expect more rapid convergence. Thus, it becomes obvious that integration by parts plays an important role.

2.3 Convergence Properties

The Galerkin finite element method is equivalent to the

conventional finite element method when considering self-adjoint problems. It is well known that elements which are conforming and are able to approximate constant strain will ensure convergence for this class of problems. Some elements even display monotonic convergence, thus allowing use of efficient extrapolation procedures and give an upper bound on the potential energy.

Based on Mikhlin's work [52], [53], Hutton and Anderson [11] and Kikuchi [9] established convergence criteria for the Galerkin finite element method when applied to a wider class of problems than those amenable to the variational FEM. However, numerical results show that convergence is, in general, not monotonic [22] and becomes less rapid when the nonself-adjoint character of the system under consideration becomes more pronounced [9].

Convergence studies for the Galerkin finite element method, when applied to nonlinear systems, are of numerical nature only [48]. Noor and Whiteman [54] derived an error bound for a certain class of nonlinear problems, solvable by the GFEM. There are a number of studies on convergence, accuracy, and stability of the FEM in nonlinear problems. They are, however, either too general to be useful for practical applications or restricted to certain special classes of problems. On the other hand, a large number of nonlinear problems have been solved using the FEM with great success.

The comments made in this section are basically to be understood as an indication of the ongoing research effort. The rotary-wing aeroelastic problem -- because of its complexity -- will hardly be

accessable to any convergence proof. Thus, for the time being, convergence can only be established numerically [55], i.e., by refining the discretization process.

SECTION 3

APPLICATION OF THE METHOD TO THE FLAP-LAG AEROELASTIC PROBLEM IN HOVER

3.1 Brief Description of the Coupled Flap-Lag Equations of Motion

The coupled flap-lag equations of motion used in this study serve mainly as an illustrative example for the application of a Galerkin-type finite element method to rotary-wing aeroelasticity. The flap-lag equations for hover are obtained from the general equations which have been presented in Reference [2], by an appropriate elimination of the terms associated with forward flight and the torsional degree of freedom.

The geometry of the problem is shown in Figures 3 and 4. A few important assumptions made in the derivation of these equations are briefly stated below:

1. The blade is assumed to have moderate deflections, which implies small strains and finite rotations or slopes. These elastic rotations are assumed to be of order ε_D ($\varepsilon_D \simeq 0.20$) so that terms of $O(\varepsilon_D)^2$ are negligible compared to terms of order one, $O(1)$. The blade can bend in two mutually perpendicular directions. Initially the blade is straight;

during deformation the Euler-Bernoulli assumption is used. The structural operators resulting from these assumptions have been presented in Reference [56].

2. The blade has only precone β_p; it is cantilevered to the hub and there is no built-in twist. Aerodynamic, tension, mass, and elastic centers coincide, i.e., all cross-sectional offsets are zero. Inertia and stiffness properties are assumed to be uniform.

3. There is no coupling between blade and fuselage dynamics, i.e., pitch, roll, and yaw motions shown in Figure 1 are not coupled with the dynamics of the blade.

4. Two-dimensional quasisteady aerodynamic loads are used; apparent mass, stall, and compressibility are neglected.

5. An ordering scheme identical to the one in Reference [2] is used and quantities having the magnitude of the squares of the blade slopes are neglected when compared to one, i.e.,

$$O(1) + O(\varepsilon_D^2) \simeq O(1) \quad .$$

This ordering scheme is given in Section 4.1. Note, that in Section 3, $\bar{e}_1 = O(\varepsilon_D)$ is assumed.

Using these assumptions, the coupled flap-lag equations of motion for hover can be written as follows.

Axial equilibrium:

$$\bar{T}_{,x} + (\bar{x}_0 + \bar{e}_1) + 2\dot{\bar{v}} = 0 \qquad (3.1)$$

Flap equilibrium:

$$- B_{23}\,\bar{v}_{,xxxx} - B_{33}\,\bar{w}_{,xxxx} + (\bar{w}_{,x}\,\bar{T})_{,x} - \beta_p(\bar{x}_0 + \bar{e}_1) - 2\beta_p\,\dot{\bar{v}}$$

$$- \ddot{\bar{w}} + \Gamma\{\theta\bar{x}_0(\bar{x}_0 + 2\bar{e}_1) - (\bar{x}_0 + \bar{e}_1)\,\frac{R}{\ell}\,\lambda - \bar{x}_0\,\beta_p\bar{v} + (2\theta\bar{x}_0 - \frac{R}{\ell}\,\lambda)\dot{\bar{v}}$$

$$- (\bar{x}_0 + \bar{e}_1)\dot{\bar{w}} - \bar{x}_0\,\bar{v}\,\bar{w}_{,x} + \bar{x}_0^2\,\bar{v}_{,x}\,\bar{w}_{,x} - \dot{\bar{v}}\dot{\bar{w}}\} = 0 \qquad (3.2)$$

Lag equilibrium:

$$- B_{22}\,\bar{v}_{,xxxx} - B_{23}\,\bar{w}_{,xxxx} + (\bar{v}_{,x}\,\bar{T})_{,x} + \frac{\partial}{\partial\Psi}\int_0^{\bar{x}_0} (\bar{v}_{,x}^2 + \bar{w}_{,x}^2)d\bar{x}_0$$

$$+ \bar{v} - \ddot{\bar{v}} + 2\beta_p\,\dot{\bar{w}} + \Gamma\{-\theta(\bar{x}_0 + \bar{e}_1)\,\frac{R}{\ell}\,\lambda + (\frac{R}{\ell}\,\lambda)^2 - \frac{C_{d0}}{a}\,\bar{x}_0(\bar{x}_0 + 2\bar{e}_1)$$

$$+ (2\,\frac{R}{\ell}\,\lambda\,\beta_p - \theta\,\bar{x}_0\,\beta_p)\bar{v} - (\theta\,\frac{R}{\ell}\,\lambda + 2\,\frac{C_{d0}}{a}\,\bar{x}_0)\dot{\bar{v}}$$

$$+ [2\,\frac{R}{\ell}\,\lambda - \theta(\bar{x}_0 + \bar{e}_1)]\dot{\bar{w}} + (2\,\frac{R}{\ell}\,\lambda - \theta\bar{x}_0)\bar{v}\,\bar{w}_{,x}$$

$$- \frac{R}{\ell}\,\lambda\,\bar{x}_0\,\bar{v}_{,x}\,\bar{w}_{,x} + 2\beta_p\,\bar{v}\,\dot{\bar{w}} - \theta\,\dot{\bar{v}}\,\dot{\bar{w}} + \dot{\bar{w}}^2$$

$$+ 2\bar{v}\,\bar{w}_{,x}\,\dot{\bar{w}} - \bar{x}_0\,\bar{v}_{,x}\,\bar{w}_{,x}\,\dot{\bar{w}}\} = 0 \qquad (3.3)$$

The boundary conditions are given by [56]

at $\bar{x}_0 = 0$;

$$\bar{v} = \bar{w} = \bar{v}_{,x} = \bar{w}_{,x} = 0 \quad , \qquad (3.4)$$

at $\bar{x}_0 = 1$;

$$B_{22}\,\bar{v}_{,xxx} + B_{23}\,\bar{w}_{,xxx} = 0 \qquad (3.5a)$$

$$B_{23}\,\bar{v}_{,xxx} + B_{33}\,\bar{w}_{,xxx} = 0 \tag{3.5b}$$

$$B_{22}\,\bar{v}_{,xx} + B_{23}\,\bar{w}_{,xx} = 0 \tag{3.5c}$$

$$B_{23}\,\bar{v}_{,xx} + B_{33}\,\bar{w}_{,xx} = 0 \tag{3.5d}$$

and $$\bar{T} = 0. \tag{3.5e}$$

3.2 Implementation of the Galerkin Finite Element Method

The Galerkin finite element method, as developed in Section 2, is now applied to Equations (3.2) and (3.3). To facilitate manipulation of these equations they are rewritten in matrix operator form.

$$\begin{aligned}[L_1]\{\ddot{q}\} - [C_{Ax}(\underset{\sim}{q}, \bar{x}_0)]\{\dot{q}\} + ([G] + [D_1(\bar{x}_0)] \\ + [D_2(\underset{\sim}{q}, \dot{\underset{\sim}{q}})] + [D_3(\underset{\sim}{q}, x_0)])\{\dot{q}\} - [C_{T2}(\underset{\sim}{q}, \bar{x}_0)]\{\dot{q}\} \\ + ([S_B] - [S_{T1}(\bar{x}_0)] - [K_1] + [A_1(\bar{x}_0)] \\ + [A_2(\underset{\sim}{q}, \bar{x}_0)]\{q\} = \{F(x_0)\}\end{aligned} \tag{3.6}$$

where $\{q\} = \begin{Bmatrix} \bar{v} \\ \bar{w} \end{Bmatrix}$. Other quantities are defined in Appendix D. It should be noted that the tension $\bar{T}$ was eliminated using the axial equation.

According to Eq. (2.2), an approximate global solution is given by

$$\{q^g\} = \begin{bmatrix} \Phi_1 \cdots \Phi_{ML} & \underset{\sim}{0} \\ \underset{\sim}{0} & \Phi_{ML+1} \cdots \Phi_{ML+MF} \end{bmatrix} \{b_m\} = [\Phi_m]\{b_m\} \,. \quad (3.7)$$

Upon substitution into the differential equations and boundary conditions, it yields the residuals $\{\varepsilon\}$ and $\{\varepsilon_B\}$. The weighted Galerkin residuals become

$$\int_0^1 \underset{M\times 2}{[\Phi_m]^T} \underset{2\times 1}{\{\underset{\sim}{\varepsilon}_Q + \underset{\sim}{\varepsilon}_p - \underset{\sim}{F}\}} d\bar{x}_0 + [\Phi_m]^T \underset{\sim}{\varepsilon}_B\Big|_1 = 0 \,, \quad (3.8)$$

where

$$\underset{\sim}{\varepsilon}_Q = [S_B]\{q^g\} - [S_{T1}]\{q^g\} - [C_{T2}]\{\dot{q}^g\} + [I_1]\{\ddot{q}^g\} - [K_1]\{q^g\}$$

$$= [B]\, D_x^4\{q^g\} - D_x([T_1]\{q^g\} + [T_2]\{\dot{q}^g\}) + [I_1]\{\ddot{q}^g\} - [K_1]\{q^g\} \quad (3.9a)$$

$$\underset{\sim}{\varepsilon}_p = ([C_{Ax}] + [G] + [D_1] + [D_2] + [D_3])\{\dot{q}^g\} + ([A_1] + [A_2])\{q^g\} \quad (3.9b)$$

$$[\Phi_m]^T \underset{\sim}{\varepsilon}_B\Big|_1 = \langle -[\Phi_m]^T [B]\, D_x^3\{q^g\} + D_x[\Phi_m]^T [B]\, D_x^2\{q^g\}$$

$$+ [\Phi_m]^T([T_1]\{q^g\} + [T_2]\{\dot{q}^g\})\rangle\Big|_{\bar{x}_0 = 1} \quad (3.9c)$$

and $D_x^i = \partial^i/\partial\bar{x}_0^i$.

Integrating the $\underset{\sim}{\varepsilon}_Q$ term by parts, Eq. (3.8) becomes

$$\int_0^1 \left\{ \underset{\sim}{\bar{\varepsilon}}_Q + [\Phi_m]^T (\underset{\sim}{\varepsilon}_p - \underset{\sim}{F}) \right\} d\tilde{x}_0 = \underset{\sim}{0} \quad , \qquad (3.10)$$

$M \times 1$

where

$$\underset{\sim}{\bar{\varepsilon}}_Q = D_x^2[\Phi_m]^T [B]\, D_x^2\{q^g\} + D_x[\Phi_m]^T [T_1]\{q^g\}$$

$$+ D_x[\Phi_m]^T [T_2]\{\dot{q}^g\} + [I_1]\{\ddot{q}^g\} - [K_1]\{q^g\} \, . \qquad (3.11)$$

Inside the element the displacements are given by

$$\{q^e\} = \begin{Bmatrix} \bar{v}^e \\ \bar{w}^e \end{Bmatrix} = \sum_{n=1}^{N} \begin{bmatrix} \gamma_n & 0 \\ 0 & \eta_n \end{bmatrix} \begin{Bmatrix} h_n^e \\ g_n^e \end{Bmatrix}$$

$$= \begin{bmatrix} \underset{\sim}{\chi}^T & \underset{\sim}{0} \\ \underset{\sim}{0} & \underset{\sim}{\eta}^T \end{bmatrix} \begin{Bmatrix} \underset{\sim}{h}^e \\ \underset{\sim}{g}^e \end{Bmatrix} = [\Psi(\bar{x}_e)]\{a^e(\psi)\} \, . \qquad (3.12)$$

In the present analysis, ordinary beam-type bending [5] - [7] representation was chosen for modeling the flap-lag motion; the geometry of the element is illustrated in Figure 3b, where $\underset{\sim}{g}^e$ and $\underset{\sim}{h}^e$ represent symbolically the four nodal degrees of freedom associated with flapwise and lagwise bending, respectively. Thus, $N = 4$, $\gamma_n = \eta_n$ are cubic Hermite interpolation polynomials, Appendix C, and h_n^e and g_n^e represent nodal displacements and slopes for lag

(h_n^e) and flap (g_n^e), respectively. For convenience, the superscript e is omitted from the shape function matrix $[\Psi]$.

As has been indicated previously, stability boundaries in rotary-wing aeroelasticity can be obtained by linearizing the equations of motion about an appropriate equilibrium position. For the case of coupled flap-lag in hover, the equilibrium position is taken as the static nonlinear equilibrium position and the dynamic equations of motion are perturbed about this equilibrium position, i.e.,

$$\{a^e(\psi)\} = \{a^{eO}\} + \{\Delta\, a^e(\psi)\} \quad . \tag{3.13}$$

Equation (3.12) is now extended over the global domain, in the sense of Eq. (2.7) and substituted, together with Eq. (3.13), into Eq. (3.10). This yields the nonlinear static equilibrium position

$$([B^e] + [T_1^e] - [K_1^e] + [A_1^e] + [A_2^e])\{a^{eO}\} = \{F^e\} \tag{3.14}$$

where it should be noted that $[A_2^e]$ also depends on $\{a^{eO}\}$ and thus Eq. (3.14) is nonlinear.

Similarly, the linearized dynamic equilibrium equations are given by

$$[I_1^e]\{\Delta\ddot{a}^e\} + ([G^e] + [D_1^e] + [D_2^e] + [D_3^e])\{\Delta\dot{a}^e\} + [T_2^e]\{\Delta\dot{a}^e\}$$

$$+ \sum_{i=e+1}^{E} [T_2^{ei}]\{\Delta\dot{a}^i\} - [C_{Ax}^e]\{\Delta\dot{a}^e\}$$

$$- \sum_{i=1}^{e-1} [C_{Ax}^{ei}]\{\Delta\dot{a}^i\} + ([B^e] + [T_1^e] - [K_1^e]$$

$$+ [A_1^e] + [\bar{A}_2^e])\{\Delta a^e\} = \{0\}, \qquad e = 1,2,\ldots,E \; . \qquad (3.15)$$

Equations (3.14) and (3.15) are equations written at the element level, thus $[B^e], [I_1^e], \ldots,$ etc., represent element matrices which are defined in Appendix D. For the cubic shape functions which have been selected, six-point Gaussian quadrature yields the exact element matrices. Evaluation of the constant term $\{F^e\}$ and the linear terms $[B^e]$, $[T_1^e]$, $[K_1^e]$ and $[A_1^e]$ in the static equilibrium equations, Eq. (3.14), is straightforward. The quadratic term $[A_2^e]$ depends on the static equilibrium position itself. Since the nonlinear equilibrium position equation will be solved by iteration, $[A_2^e]$ could be evaluated using the value of $\{a^{eO}\}$ from the previous iterative step. Here, a different approach is taken. Rather than calculating $[A_2^e]$, the nonlinear system matrix, Eq. (3.18), is calculated directly; see Appendix E. All the terms in the dynamic equation, Eq. (3.15), are linear. However, the matrices $[D_2^e]$, $[D_3^e]$, $[T_2^e]$, $[T_2^{ei}]$, $[C_{Ax}^e]$, $[C_{Ax}^{ei}]$ and $[\bar{A}_2^e]$ depend on the static equilibrium position, which is

a known quantity after the static problem has been solved. Thus, after numerically integrating the triple (quadruple, for $[D_3^e]$) products of the shape functions, again using six-point Gaussian quadrature, the known values of $\{a^{eO}\}$ are used to evaluate those element matrices.

The assembly of the element matrices into the complete system matrices is the same as in the conventional finite element method. It should be noted, however, that bandedness of the velocity proportional matrix is destroyed due to terms of type

$$\sum_{i=e+1}^{E} [T_2^{ei}]\{\Delta\dot{a}^i\} \quad \text{and} \quad \sum_{i=1}^{e-1} [C_{Ax}^{ei}]\{\Delta\dot{a}^i\}$$

which are a consequence of the inner integrals over the global domain in the operators $[C_{T2}]$ and $[C_{Ax}]$.

Here, it should be mentioned that the nonlinear terms were modeled completely consistent with the linear terms. No simplifying assumptions were involved. This, of course, implies added computer time and storage.

Equations (3.14) and (3.15) can now formally be written on the system level. Thus, the partial differential equations, Eqs. (3.2) and (3.3), are reduced to a system of ordinary differential equations by using the Galerkin finite element method.

3.3 Method of Solution

Before actually solving the finite element equations, the considerable number of unknowns representing the nodal degrees of freedom will be reduced by applying modal analysis. The basic assumption is that the nodal displacement vector can be expressed in terms of a small number of mode shapes which approximate the free vibration mode shapes of the system. Thus,

$$\left.\begin{aligned} \{a^0\} &= [\Lambda]\{q^0\} \\ \{\Delta a\} &= [\Lambda]\{\Delta q\} \end{aligned}\right\}, \tag{3.16}$$

where $[\Lambda]$ is the modal transformation matrix containing as columns the first M approximate free vibration mode shapes of a rotating blade. In the present study, unless otherwise noted, the M_F lowest uncoupled flap modes and the M_L lowest uncoupled lag modes are used, i.e., $M = M_L + M_F$. These mode shapes are also determined by using the finite element approach as applied to the rotating beam free vibration problem. Since the free vibration equations are self-adjoint, the Galerkin finite element method for this case is identical to a conventional finite element method. Furthermore, $\{q^0\}$ and $\{\Delta q\}$ are the reduced vectors of generalized coordinates. For the static equilibrium position

$$\{q^0\} = \{h_1^0, h_2^0, \ldots, h_{M_L}^0, g_1^0, g_2^0, \ldots, g_{M_F}^0\}^T , \tag{3.17}$$

and similarly, $\{\Delta q\}$ is the reduced perturbation vector of the generalized coordinates. The $h_1^0, h_2^0, \ldots,$ etc., can be interpreted as amplitudes of the corresponding mode shapes. They constitute the new unknowns of the problem. As a general rule, use of M assumed modes will yield $M/2$ actual mode shapes and frequencies with good accuracy.

Clearly, modal analysis provides an effective reduction in the size of the eigenvalue problem required for the solution of the dynamic system equations. This is a considerable advantage since determination of stability boundaries requires repeated solutions of the eigenvalue problem. Furthermore, due to this approach, the bandedness of the finite element system matrices becomes irrelevant since the reduced system matrices are fully populated anyway. Also, the geometric boundary conditions can be enforced implicitly through the free vibration mode shapes. Finally, it is important to realize that modal analysis facilitates the solution of the nonlinear static equilibrium equations. Thus, the reduced number of unknowns allows one to calculate the derivatives of the nonlinear terms conveniently and a relatively efficient solution algorithm, based on the Newton-Raphson technique can be used; see Appendix E.

The final equations, after modal reduction, for static equilibrium are

$$[s_L]\{q^0\} + [s_{NL}(q^0)]\{q^0\} = \{c\} \tag{3.18}$$

and for dynamic equilibrium

$$[m]\{\Delta\ddot{q}\} + [d]\{\Delta\dot{q}\} + [k]\{\Delta q\} = \underset{\sim}{0} \tag{3.19}$$

where, for example

$$[m] = [\Lambda]^T [I_1]^S [\Lambda] \quad . \tag{3.20}$$

All matrices are defined in Appendix A.

Solution of the aeroelastic problem, Eqs. (3.18) and (3.19), is accomplished in two stages. First, the nonlinear equations for the static equilibrium position, Eq. (3.18), are solved using a Newton-Raphson scheme, described in Appendix E. This method has proven itself as one of the best solution techniques available in geometrically nonlinear analyses [31]. It is extremely accurate and possesses second-order convergence. Furthermore, the completely numerical formulation of the FEM, together with the small number of modal coordinates, reduces the cost of forming and inverting the Jacobian matrix, Eq. (E.3) in the appendix. This cost usually would have to be accounted for as one of the major drawbacks of the Newton-Raphson method. Another drawback is its sensitivity to the choice of the initial solution vector.

In the present case, the nonlinear solution from the previous value of pitch setting, Θ, is taken as the initial guess. For the first value of Θ the linear solution is chosen as the initial

guess. The iteration is considered to have converged when the absolute change of each generalized coordinate during an iteration cycle is less than 10^{-4}. If the method fails to converge, the system usually can be considered as being statically unstable [57]. Such a situation was not encountered for the flap-lag problem in hover.

Next, the dynamic equations, Eq. (3.19), are formed and converted into first-order state variable form,

$$\begin{Bmatrix} \Delta\ddot{\underset{\sim}{q}} \\ \hline \Delta\dot{\underset{\sim}{q}} \end{Bmatrix} = \left[\begin{array}{c|c} -[m]^{-1}[d] & -[m]^{-1}[k] \\ \hline [I] & [0] \end{array}\right] \begin{Bmatrix} \Delta\dot{\underset{\sim}{q}} \\ \hline \Delta\underset{\sim}{q} \end{Bmatrix} \quad . \tag{3.21}$$

Assuming solutions of the form

$$\begin{Bmatrix} \Delta\dot{\underset{\sim}{q}} \\ \Delta\underset{\sim}{q} \end{Bmatrix} = \{y\}\, e^{\lambda\psi} \tag{3.22}$$

results in a standard eigenvalue problem

$$[A]\{y\} = \lambda\{y\} \tag{3.23}$$

where $[A]$ is a constant nonsymmetric matrix. Equation (3.23) is easily solved using one of the available eigenvalue solvers. The eigenvalues appear in complex conjugate pairs

$$\lambda_k = \zeta_k \pm i\omega_k \quad . \tag{3.24}$$

Thus, the perturbed motion about the static equilibrium position is stable when all $\zeta_k < 0$. The stability boundary is obtained by systematically varying the pitch setting θ until one of the ζ_k is zero. More details can be found in Section 5.1.

SECTION 4

APPLICATION OF THE METHOD TO THE FLAP-LAG-TORSION AEROELASTIC PROBLEM IN FORWARD FLIGHT

In this section the Galerkin finite element method (GFEM) is applied to a more practical problem, namely, the coupled flap-lag-torsion aeroelastic stability and response calculation of hingeless rotor blades in forward flight. The torsional degree of freedom generates an additional equation of motion, associated with this added degree of freedom. The torsional degree of freedom also yields a number of nonlinear bending-torsion coupling terms in the structural operator. Since the torsional equation of motion is of second order with respect to the spatial variable, as compared to fourth order for bending, special care has to be exercised when discretizing the equations via the Galerkin finite element method. When solving the discretized dynamic equations, a major complication arises due to the forward flight condition which introduces periodic time varying coefficients in the equations of motion. Due to this flight condition a large number of additional aerodynamic loading terms appear in the equations of motion.

4.1 Brief Description of the Equations of Motion

The equations of motion for the flap-lag-torsion problem in

forward flight are coupled nonlinear, nonconservative, partial differential equations with periodic coefficients. The structural operator is taken from Reference [56]. The inertia and aerodynamic loads are taken from Reference [2].

The geometry of the problem is described in Figures 3 and 4. In addition to the assumptions made in Section 3.1 for the hover problem, the following assumptions are made:

1. The blade has an angle of built-in twist $\theta_B(\bar{x}_O)$, occurring about the undeformed elastic axis. Recall that the undeformed elastic axis is assumed to be straight and coincident with the feathering axis.
2. The blade cross-sectional aerodynamic center, center of gravity, and elastic center are distinct points. The tension center coincides with the elastic center, i.e., $x_{II} = 0$.
3. The elastic torsional deformations of the blade occur about the deformed elastic axis. Root torsional deformation, due to pitch link or control system flexibility, is assumed to occur about the feathering axis.
4. Cross-sectional stiffness and inertia properties, offsets, and airfoil chord vary along the blade.
5. Structural or mechanical damping of viscous type is included.

6. Aerodynamic effects associated with forward flight introduce cyclic pitch variations, thus, the pitch angle is given by

$$\theta_r(\psi) = \theta_0 + \theta_{1s} \sin \psi + \theta_{1c} \cos \psi , \qquad (4.1)$$

and the total geometric pitch angle is

$$\theta_G(\bar{x}_0 , \psi) = \theta_B(\bar{x}_0) + \theta_r(\psi) \quad . \qquad (4.2)$$

7. The inflow is represented by the following general functional form

$$\lambda(\bar{x} , \psi) = \lambda_0 \, k_1(\bar{x}) + \lambda_s \, k_2(\bar{x}) \sin \psi + \lambda_c \, k_3(\bar{x}) \cos \psi . \qquad (4.3)$$

8. The effect of reversed flow is included in an exact manner.

It should be pointed out that the influence of axial forces on the torsional rigidity of the rotor blade and the effect of cross-sectional warping due to torsion is neglected in Reference [56]. Furthermore, the effects of stall and compressibility are not included in the aerodynamic loads of Reference [2]. Although the above effects may be important for certain rotor blades and certain flight conditions, no attempt is made to include them in the present study, since its primary objective is the application of the Galerkin finite

element method.

In applying the ordering scheme, according to Assumption 5 in Section 3.1, the following orders of magnitude are assigned to the various parameters in this study:

$$\frac{v}{\ell} = \frac{w}{\ell} = \phi = O(\varepsilon_D) \quad ,$$

$$\frac{\ell}{R} \quad , \quad \frac{x_0}{\ell} \quad , \quad \frac{e_1}{\ell} \quad , \quad \frac{x_A}{b} = O(1) \quad ,$$

$$\mu \quad , \quad \sin\Psi \quad , \quad \cos\Psi \quad , \quad \frac{\partial}{\partial \bar{x}_0} \quad , \quad \frac{\partial}{\partial \Psi} = O(1) \quad ,$$

$$\theta_0 \quad , \quad \theta_{1s} \quad , \quad \theta_{1c} = O(\varepsilon_D^{1/2}) \quad ,$$

$$\frac{b}{R} \quad , \quad \beta_p \quad , \quad \lambda_0 \quad , \quad \lambda_s \quad , \quad \lambda_c = O(\varepsilon_D) \quad ,$$

$$\frac{u}{\ell} \quad , \quad \frac{x_I}{i} \quad , \quad \frac{I_{m2}}{m_0 \ell^2} \quad , \quad \frac{I_{m3}}{m_0 \ell^2} \quad , \quad \frac{C_{10}}{a} = O(\varepsilon_D^2) \quad .$$

Using these assumptions, the coupled equations of motion for forward flight are presented below. Note that the equations are written in the reference frame $\hat{e}$, which represents the undeformed blade.

Axial equilibrium:

$$\bar{T}_{,x} + p_{xI} = 0 \quad . \tag{4.4}$$

Lag equilibrium:

$$-\left(M_{3,x} + \bar{G}\bar{J}_{\phi,x}\,\bar{w}_{,xx} - \bar{v}_{,x}\,\bar{T}\right)_{,x} - q_{3I,x} + p_{yI} + p_{yA} + p_{yD} = 0 \quad . \tag{4.5}$$

Flap equilibrium:

$$\left(M_{2,x} - \bar{G}\bar{J}_{\phi,x}\,\bar{v}_{,xx} + \bar{w}_{,x}\,\bar{T}\right)_{,x} + q_{2I,x} + p_{zI} + p_{zA} + p_{zD} = 0 \quad . \tag{4.6}$$

Torsion equilibrium:

$$M_{x,x} + M_{l}\quad q_{lI} + q_{xA} + q_{xD} = 0 \quad . \tag{4.7}$$

The corresponding boundary conditions are:

at $\bar{x}_0 = 0$:

$$\bar{v} = \bar{w} = \bar{v}_{,x} = \bar{w}_{,x} = 0 \quad , \tag{4.8a}$$

$$M_x - \bar{K}_{\phi} = 0 \quad , \tag{4.8b}$$

at $\bar{x}_0 = 1$:

$$-M_{3,x} - \bar{G}\bar{J}_{\phi,x}\,\bar{w}_{,xx} + \bar{v}_{,x}\,\bar{T} - q_{3I,x} = 0 \quad , \tag{4.9a}$$

$$M_{2,x} + \bar{G}\bar{J}\phi_{,x}\,\bar{v}_{,xx} + \bar{w}_{,x}\,\bar{T} + q_{2I,x} = 0 \quad , \qquad (4.9b)$$

$$M_3 = -M_2 = M_x = 0 \quad , \qquad (4.9c)$$

$$\bar{T} = 0 \quad . \qquad (4.9d)$$

The boundary conditions at the free end, $\bar{x}_0 = 1$, are natural boundary conditions, expressing the fact that the shears, moments, and tension at the blade tip are zero. At the blade root, $\bar{x}_0 = 0$, the boundary conditions for bending involve only geometric quantities, i.e., the bending displacements and slopes. The mixed boundary condition for torsion, Equation (4.8b), is a result of the root torsional spring.

Equations (4.4) - (4.9) are written in a general form which is most suitable when using the Galerkin finite element method to discretize the spatial dependence. All quantities appearing in these equations are defined below.

The elastic moments are given by:

$$M_3 = (\bar{E}\bar{I}_2 \cos^2 R_c\,\Theta_G + \bar{E}\bar{I}_3 \sin^2 R_c\,\Theta_G)\bar{v}_{,xx} + (\bar{E}\bar{I}_2 - \bar{E}\bar{I}_3)$$
$$\cdot\ [(\tfrac{1}{2}\bar{w}_{,xx} - \phi\bar{v}_{,xx}) \sin 2R_c\,\Theta_G + \phi\bar{w}_{,xx} \cos 2R_c\,\Theta_G] \quad , \qquad (4.10a)$$

$$M_2 = -(\bar{E}\bar{I}_2 - \bar{E}\bar{I}_3)[(\tfrac{1}{2}\bar{v}_{,xx} + \phi\bar{w}_{,xx}) \sin 2R_c\,\Theta_G + \phi\bar{v}_{,xx} \cos 2R_c\,\Theta_G]$$
$$- (\bar{E}\bar{I}_2 \sin^2 R_c\,\Theta_G + \bar{E}\bar{I}_3 \cos^2 R_c\,\Theta_G)\bar{w}_{,xx} \quad , \qquad (4.10b)$$

$$M_1 = (\bar{E}\bar{I}_2 - \bar{E}\bar{I}_3)$$

$$\cdot \left[\frac{1}{2} (\bar{v}^2_{,xx} - \bar{w}^2_{,xx}) \sin 2R_c \Theta_G - \bar{v}_{,xx} \bar{w}_{,xx} \cos 2R_c \Theta_G \right] , \quad (4.10c)$$

$$M_x = \bar{G}\bar{J}(\phi_{,x} + \bar{v}_{,xx} \bar{w}_{,x}) \quad . \quad (4.10d)$$

The distributed force and moment vectors, per unit length of the undeformed elastic axis, are expressed as:

$$\underset{\sim}{p} = p_x \hat{e}_x + p_y \hat{e}_y + p_z \hat{e}_z \quad , \quad (4.11a)$$

$$\underset{\sim}{q} = q_x \hat{e}_x + q_y \hat{e}_y + q_z \hat{e}_z \quad . \quad (4.11b)$$

In general, these loads contain inertia, aerodynamic, and structural damping contributions, denoted by the subscripts I, A and D, respectively. In writing the equations of motion, (4.4) - (4.7), the final form of the loads, Reference [2], has been used. Note, however, that due to a more consistent application of the ordering scheme, the torsional inertia load, Equation (4.13c), differs in some higher-order terms.

Inertia loads:

$$p_{xI} = \bar{m}(\bar{e}_1 + \bar{x}_O + 2\dot{\bar{v}}) \quad , \quad (4.12a)$$

$$p_{yI} = \bar{m}(\bar{v} - \ddot{\bar{v}} + 2\beta_p \dot{\bar{w}} - 2\dot{\bar{u}} + \bar{x}_I \cos \Theta_G + \bar{x}_I \ddot{\Theta}_G \sin \Theta_G) \quad , \quad (4.12b)$$

$$p_{zI} = \bar{m}(-\beta_p(\bar{e}_1 + \bar{x}_0) - \ddot{\bar{w}} - 2\beta_p \dot{\bar{v}} - \bar{x}_I \ddot{\theta}_G \cos\theta_G) \quad . \qquad (4.12c)$$

$$q_{3I} = -\bar{m}\,\bar{x}_I \cos\theta_G(\bar{e}_1 + \bar{x}_0) + \dot{\theta}_G(\bar{I}_{m2} - \bar{I}_{m3}) \sin 2\theta_G$$

$$\simeq q_{zI} \qquad ,(4.13a)$$

$$q_{2I} = \bar{m}\,\bar{x}_I \sin\theta_G(\bar{e}_1 + \bar{x}_0) - 2\dot{\theta}_G(\bar{I}_{m2} \sin^2\theta_G + \bar{I}_{m3} \cos^2\theta_G)$$

$$\simeq q_{yI} \qquad ,(4.13b)$$

$$q_{1I} = \bar{m}\,\bar{x}_I[\sin\theta_G(\ddot{\bar{v}} - \bar{v} + \bar{v}_{,x}(\bar{e}_1 + \bar{x}_0))$$

$$+ \cos\theta_G(-(\beta_p + \bar{w}_{,x})(\bar{e}_1 + \bar{x}_0) - \ddot{\bar{w}} - 2\beta_p \dot{\bar{v}}$$

$$+ \phi(\ddot{\bar{v}} - \bar{v}) + \dot{\phi}\bar{v}_{,x}(\bar{e}_1 + \bar{x}_0) - 2\bar{w}_{,x} \dot{\bar{v}})] - (\bar{I}_{m2} + \bar{I}_{m3})$$

$$\cdot (\ddot{\theta}_G + \ddot{\phi} + \bar{w}_{,x} \ddot{\bar{v}}_{,x}) - (\bar{I}_{m2} - \bar{I}_{m3})$$

$$\cdot [\cos 2\theta_G(\dot{\phi} - \beta_p \bar{v}_{,x} + 2\phi \dot{\bar{v}}_{,x}) + \sin 2\theta_G(\tfrac{1}{2} + \dot{\bar{v}}_{,x})]$$

$$- (\bar{I}_{m2} \sin^2\theta_G + \bar{I}_{m3} \cos^2\theta_G)\, 2\dot{\bar{w}}_{,x}(1 + \dot{\bar{v}}_{,x})$$

$$\simeq \bar{v}_{,x}\, q_{yI} + \bar{w}_{,x}\, q_{zI} + q_{xI} \qquad ,(4.13c)$$

Aerodynamic loads:

$$P_{yA} = -\Gamma[(\theta_G F_1 - F_2 + \dot{\theta}_G F_4)F_2 + \frac{C_{dO}}{a} F_1^2 + \beta_p(\theta_G F_1 - 2F_2)\bar{v}$$

$$+ (\theta_G F_2 + 2\frac{C_{dO}}{a} F_1)F_3 \bar{v}_{,x} + (\theta_G F_1 - 2F_2 + \dot{\theta}_G F_4)F_3 \bar{w}_{,x}$$

$$+ F_1F_2\phi + (\theta_G F_1 - 2F_2 - 2\beta_p F_3)\bar{v}\,\bar{w}_{,x} + (\theta_G F_3^2 + F_1F_2)\bar{v}_{,x}\,\bar{w}_{,x} -$$

$$- F_3^2 \bar{w}_{,x} \bar{w}_{,x} + (\beta_p F_1 \bar{v} + F_2 F_3 \bar{v}_{,x} + F_1 F_3 \bar{w}_{,x})\phi$$

$$+ (-2\bar{v} + F_1 \bar{v}_{,x})F_3 \bar{w}_{,x} \bar{w}_{,x} + (F_1 \bar{v} + F_3^2 \bar{v}_{,x})\bar{w}_{,x} \phi$$

$$+ (\Theta_G F_2 + 2 \frac{C_{dO}}{a} F_1)\dot{\bar{v}} + (\Theta_G F_1 - 2F_2 + \dot{\Theta}_G F_4)\dot{\bar{w}} + F_2 F_4 \dot{\phi}$$

$$+ (\Theta_G F_3 \bar{w}_{,x} + F_2 \phi)\dot{\bar{v}} + (\Theta_G F_3 \bar{v}_{,x} - 2\beta_p \bar{v} - 2F_3 \bar{w}_{,x} + F_1 \phi)\dot{\bar{w}}$$

$$+ F_3 F_4 \bar{w}_{,x} \dot{\phi} + F_3 \phi \bar{w}_{,x} \dot{\bar{v}} + (-2\bar{v} \bar{w}_{,x} + F_1 \bar{v}_{,x} \bar{w}_{,x} + F_3 \phi \bar{v}_{,x})\dot{\bar{w}}$$

$$+ \Theta_G \dot{\bar{w}} \dot{\bar{v}} - \dot{\bar{w}} \dot{\bar{w}} + F_4 \dot{\bar{w}} \dot{\phi} + \phi \dot{\bar{w}} \dot{\bar{v}}] \quad , \tag{4.14a}$$

$$p_{zA} = -\Gamma[(-\Theta_G F_1 + F_2 - \dot{\Theta}_G F_4)F_1 + \beta_p F_1 \bar{v} + (F_2 - 2\Theta_G F_1)F_3 \bar{v}_{,x}$$

$$+ F_1 F_3 \bar{w}_{,x} - F_1^2 \phi + F_1 \bar{v} \bar{w}_{,x} + (F_3^2 - F_1^2)\bar{v}_{,x} \bar{w}_{,x}$$

$$- 2F_1 F_3 \bar{v}_{,x} \phi + (F_2 - 2\Theta_G F_1)\dot{\bar{v}} + F_1 \dot{\bar{w}} - F_1 F_4 \dot{\phi}$$

$$+ (F_3 \bar{w}_{,x} - 2F_1 \phi)\dot{\bar{v}} + F_3 \bar{v}_{,x} \dot{\bar{w}} + \dot{\bar{v}} \dot{\bar{w}}] \quad , \tag{4.14b}$$

$$q_{xA} = -\Gamma \bar{b}^2 \frac{R^2}{\ell^2} (0.5 - \bar{x}_A)(1 - \bar{x}_A)(\dot{\Theta}_G + \dot{\phi})F_1$$

$$- \Gamma \bar{b} \frac{R}{\ell} \bar{x}_A[(F_2 - \Theta_G F_1)F_1 + \beta_p F_1 \bar{v} + (F_2 - 2\Theta_G F_1)F_3 \bar{v}_{,x}$$

$$+ F_1 F_3 \bar{w}_{,x} - F_1^2 \phi + F_1 \bar{v} \bar{w}_{,x} + (F_3^2 - F_1^2)\bar{v}_{,x} \bar{w}_{,x}$$

$$- 2F_1 F_3 \bar{v}_{,x} \phi + (F_2 - 2\Theta_G F_1)\dot{\bar{v}} + F_1 \dot{\bar{w}}$$

$$F_3 \bar{w}_{,x} \dot{\bar{v}} - 2F_1 \phi \dot{\bar{v}} + F_3 \bar{v}_{,x} \dot{\bar{w}} + \dot{\bar{v}} \dot{\bar{w}}] \quad , \tag{4.14c}$$

where

$$F_1 = \bar{e}_1 + \bar{x}_0 + \mu \frac{R}{\ell} \sin \Psi \quad , \tag{4.14d}$$

$$F_2 = \lambda \frac{R}{\ell} + \mu \frac{R}{\ell} \beta_p \cos \Psi \quad , \tag{4.14e}$$

$$F_3 = \mu \frac{R}{\ell} \cos \Psi \quad , \tag{4.14f}$$

$$F_4 = \bar{b} \frac{R}{\ell} (1.5 - \bar{x}_A) \quad , \tag{4.14g}$$

$$F_5 = \bar{b}^2 \frac{R^2}{\ell^2} (0.5 - \bar{x}_A)(1 - \bar{x}_A) \quad . \tag{4.14h}$$

Damping loads:

$$p_{yD} = - \bar{g}_{SL} \dot{\bar{v}} \quad , \tag{4.15a}$$

$$p_{zD} = - \bar{g}_{SF} \dot{\bar{w}} \quad , \tag{4.15b}$$

$$q_{xD} = - \bar{g}_{ST} \dot{\phi} \quad . \tag{4.15c}$$

The coupled flap-lag-torsion problem is thus defined by Equations (4.5) - (4.7), together with the elastic moments, Equations (4.10), and the loads, Equations (4.12) - (4.15). Note, that the tension $\bar{T}$ will be eliminated using the axial equation and corresponding boundary condition, Equations (4.4) and (4.9d). The axial displacement, $\bar{u}$, will be replaced using the assumption that the blade is inextensional in the axial direction, an assumption which is commonly made in rotary-wing aeroelasticity.

4.2 Discretization of the Equations of Motion Using the Galerkin Finite Element Method

The first step in solving the equations of motion, presented in the previous section, is the discretization of the spatial dependence. This is accomplished through application of the Galerkin finite element method. Subsequently, modal analysis is used to reduce the number of discrete unknowns describing the problem.

The procedure followed here is similar to that described in Section 3.2, for the hover problem. Therefore, only the major steps will be outlined. However, special emphasis is placed on the appropriate modeling of the torsional degree of freedom.

The approximate global solution given by Equation (3.7) is extended to include the torsional deformation:

$$\{q^g\} = \begin{Bmatrix} v^g \\ w^g \\ \phi^g \end{Bmatrix} = \underset{3\times M}{[\Phi_m]} \underset{M\times 1}{\{b_m\}} \quad . \tag{4.16}$$

This solution is now substituted into the flap-lag-torsion equations of motion, Equations (4.5) - (4.7), and the corresponding boundary conditions. Recall, that in the extended Galerkin method the shape functions Φ_m need to satisfy only the geometric boundary conditions. Therefore, both the natural boundary conditions at the blade tip, Equations (4.9a - c), and the mixed boundary condition, due to the root-

torsional spring, Equation (4.8b), contribute to the boundary residual.

The weighted Galerkin residual, obtained through appropriate combination of the weighted differential equation and boundary condition residuals is given below.

$$\int_0^1 [\Phi_m]^T \left\langle \left\{ \begin{array}{l} -(M_{3,x} + \bar{G}\bar{J}\phi_{,x}\,\bar{w}_{,xx} - \bar{v}_{,x}\,\bar{T})_{,x} - q_{3I,x} \\ (M_{2,x} + \bar{G}\bar{J}\phi_{,x}\,\bar{v}_{,xx} + \bar{w}_{,x}\,\bar{T})_{,x} + q_{2I,x} \\ M_{x,x} \end{array} \right\}^g \right.$$

$$\left. + \left\{ \begin{array}{l} p_{yI} + p_{yA} + p_{yD} \\ p_{zI} + p_{zA} + p_{zD} \\ M_1 + q_{1I} + q_{xA} + q_{xD} \end{array} \right\}^g \right\rangle d\bar{x}_0$$

$$+ [\Phi_{m(1)}]^T \left\{ \begin{array}{l} (M_{3,x} + \bar{G}\bar{J}\phi_{,x}\,\bar{w}_{,xx} - \bar{v}_{,x}\,\bar{T} + q_{3I}) - M_3 \\ -(M_{2,x} + \bar{G}\bar{J}\phi_{,x}\,\bar{v}_{,xx} + \bar{w}_{,x}\,\bar{T} + q_{2I}) + M_2 \\ -M_x \end{array} \right\}^g_{\bar{x}_0 = 1}$$

$$+ [\Phi_{m(0)}]^T \left\{ \begin{array}{c} 0 \\ 0 \\ M_x - \bar{K}_\phi\,\phi \end{array} \right\}^g_{\bar{x}_0 = 0} = \underset{\sim}{0} \; . \qquad (4.17)$$

Integrating by parts and cancelling the boundary terms, the final expression, corresponding to Equation (3.10), is obtained as:

$$\int_0^1 \Bigg\langle [\Phi_m]^T_{,xx} \begin{Bmatrix} M_3 \\ -M_2 \\ 0 \end{Bmatrix}^g + [\Phi_m]^T_{,x} \begin{Bmatrix} -\bar{G}\bar{J}\bar{\phi}_{,x}\,\bar{w}_{,xx} + \bar{v}_{,x}\,\bar{T} - q_{3I} \\ \bar{G}\bar{J}\bar{\phi}_{,x}\,\bar{v}_{,xx} + \bar{w}_{,x}\,\bar{T} + q_{2I} \\ M_x \end{Bmatrix}^g - [\Phi_m]^T \begin{Bmatrix} p_{yI} + p_{yA} + p_{yD} \\ p_{zI} + p_{zA} + p_{zD} \\ M_1 + q_{1I} + q_{xA} + q_{xD} \end{Bmatrix}^g \Bigg\rangle d\bar{x}_0$$

$$+ [\Phi_{m(0)}]^T \begin{Bmatrix} 0 \\ 0 \\ \bar{K}_{\phi}\,\phi \end{Bmatrix}^g_{\bar{x}_0 = 0} = \underset{\sim}{0} \; . \qquad (4.18)$$

In the interior of the element the displacements are given by:

$$\{q^e\} = \begin{Bmatrix} \bar{v}^e \\ \bar{w}^e \\ \phi^e \end{Bmatrix} = \begin{bmatrix} \underset{\sim}{\gamma}^T & \underset{\sim}{0} & \underset{\sim}{0} \\ \underset{\sim}{0} & \underset{\sim}{\eta}^T & \underset{\sim}{0} \\ \underset{\sim}{0} & \underset{\sim}{0} & \underset{\sim}{\phi}^T \end{bmatrix} \begin{Bmatrix} \underset{\sim}{h}^e \\ \underset{\sim}{g}^e \\ \underset{\sim}{f}^e \end{Bmatrix}$$

$$= [\Psi(\bar{x}_e)]\{a^e(\Psi)\} \quad . \tag{4.19}$$

For bending, the same cubic Hermite interpolation polynomials as in the hover case are used, see Appendix C. The nodal parameters are the lag and flap displacements and slopes at the element boundaries, see Figure 3b . This element satisfies the requirement of C_1 continuity of the global solution, since it provides interelement continuity for bending displacements and slopes. Bending strains vary linearly within the element which goes beyond the minimum requirement of constant strain within the element.

The torsion equation of motion is of second order with respect to the spatial variable. Thus, a linear interpolation will achieve the required C_0 continuity and constant strain. However, in the coupled bending-torsion analysis, it is desirable to use a torsion element which provides the same accuracy as the bending element. This allows discretization of the torsional variable with the same number of elements as needed for the adequate modeling of bending.

In the present analysis, an improved torsion element, providing linear variation of torsional strain, is obtained by using the torsion deformation at the element mid-point as additional nodal parameter, see

Figure 5. Thus, $N = 3$, and the ϕ_n are quadratic interpolation polynomials [58], given in Appendix C.

In general, refined finite elements can be obtained using any number of internal nodes. An alternative approach is the use of higher order derivatives (second for bending and first for torsion, or higher) as nodal parameters. These higher-order elements, however, experience difficulties in modeling concentrated loads. Furthermore, the boundary conditions involving the higher-order derivatives must be satisfied. Therefore, such elements were not considered. Results for free vibrations of beams, using elements with internal nodes or higher-order continuity can be found in References [59] and [60].

In conclusion, it can be stated that the elements selected in the present study are the most basic (or simple) elements which yield a consistent formulation for coupled bending and torsion. This takes on an additional significance in light of the large number of nonlinear terms which have to be modeled. The exact form of the element interpolation polynomials $\underset{\sim}{\gamma}$, $\underset{\sim}{\eta}$, and $\underset{\sim}{\phi}$ is given in Appendix C.

The element displacements, Equation (4.19), are now extended over the global domain in the sense of Equation (2.7) and then substituted into the integrated Galerkin residual, given by Equation (4.18). This yields the nonlinear, periodic element equations.

$$([I_1^e] + [I_2^e(\underset{\sim}{a}^e)])\{\ddot{a}^e\}$$

$$+ \Big([C_1^e] + [D_S^e] + [D_1^e] + [C_2^e(\underset{\sim}{a}^e)] + [T_2^e(\underset{\sim}{a}^e)] -$$

$$- [C^e_{Ax}(\underset{\sim}{a}^e)] + [D^e_2(\underset{\sim}{a}^e)] + [D^e_3(\underset{\sim}{a}^e)] + [C^e_{21}(\dot{\underset{\sim}{a}}^e)] + [D^e_{22}(\dot{\underset{\sim}{a}}^e)]$$

$$+ [D^e_{32}(\underset{\sim}{a}^e, \dot{\underset{\sim}{a}}^e)] \Big) \{\dot{a}^e\}$$

$$+ \left(\sum_{i=e+1}^{E} [T^{ei}_2(\underset{\sim}{a}^e)] - \sum_{i=1}^{e-1} [C^{ei}_{Ax}(\underset{\sim}{a}^i)] \right) \{\dot{a}^i\}$$

$$+ \Big([B^e_1] + [T^e_1] + [K^e_1] + [A^e_1] + [B^e_2(\underset{\sim}{a}^e)] + [K^e_2(\underset{\sim}{a}^e)]$$

$$+ [A^e_2(\underset{\sim}{a}^e)] + [A^e_3(\underset{\sim}{a}^e)] \Big) \{a^e\} + \{F^e_I\} + \{F^e_A\} + [B^1_c]\{a^1\} \delta_{el}$$

$$= \underset{\sim}{0} \quad \text{for} \quad e = 1,2,\ldots,E \ . \tag{4.20}$$

All element matrices in Equation (4.20), indicated by the superscript e, are defined in Appendix F. The structural operator is associated with the matrices $[B^e_1]$ and $[B^e_2]$. The axial tension results in the contributions represented by $[T^e_1]$, $[T^e_2]$ and $[T^{ei}_2]$. The inertia loads are included in $[I^e_1]$, $[I^e_2]$, $[C^e_1]$, $[C^e_2]$, $[K^e_1]$, $[K^e_2]$, $\{F^e_I\}$, $[C^e_{Ax}]$ and $[C^{ei}_{Ax}]$, where the last two matrices are due to the axial shortening effect. The aerodynamic loads are contained in the $[D^e_1]$, $[D^e_2]$, $[D^e_{22}]$, $[D^e_3]$, $[D^e_{32}]$, $[A^e_1]$, $[A^e_2]$, $[A^e_3]$ and $\{F^e_A\}$ matrices. The structural damping effect is represented by $[D^e_S]$. Finally, the $[B^1_c]$ matrix accounts for the root torsional condition, where the Kronecker delta, δ_{el}, indicates that this term is only present in the first element, i.e., the element at the root of the blade.

The functional dependence of the element matrices on the nodal displacements is as indicated in Equation (4.20). Note, that the matrices in Equation (4.20) have both single and double numerical subscripts. The first subscript is an identifier of nonlinear terms. A first subscript having a value of 2 or 3 is indicative of quadratic or cubic terms, respectively. A second subscript is attached to all velocity-dependent element matrices. All element matrices are evaluated using six-point Gaussian quadrature. The nonuniform element properties are included in the numerical integration.

Next, the element matrices are assembled into the complete system matrices. The nodal parameters within the nonlinear element matrices are replaced by their modal representation,

$$\{a\} = [\Lambda]\{q\} \quad , \tag{4.21}$$

using M_L lag, M_F flap, and M_T torsion free vibration mode shapes of the rotating blade. Subsequently, the modal reduction process is completed by pre- and post-multiplying the system matrices with the modal transformation matrix, $[\Lambda]$, and its transpose. For more details regarding the treatment of nonlinear terms, see Appendix E.

The final equations of motion, in terms of the reduced set of M modal degrees of freedom, can be written symbolically as:

$$\underset{\sim}{G} = [m(\underset{\sim}{q})]\{\ddot{q}\} + [d(\underset{\sim}{q}, \dot{\underset{\sim}{q}})]\{\dot{q}\} + [k(\underset{\sim}{q})]\{q\} + \{f\} = \underset{\sim}{0} \quad . \tag{4.22}$$

All matrices in Equation (4.22) are defined in Appendix G. Note, that the inertia, damping, and stiffness terms have both linear and nonlinear contributions. Also recall, that for forward flight, most matrices have periodic coefficients, i.e.,

$$\underset{\sim}{G}(q, \dot{q}, \ddot{q}, \Psi) = \underset{\sim}{G}(q, \dot{q}, \ddot{q}, \Psi + 2\pi) \quad ,$$

with the common period being 2π, which corresponds to one blade revolution.

For convenient numerical treatment, Equation (4.22) is re-written in first-order state variable form.

$$\{\dot{y}\} = \begin{Bmatrix} -[m(\underset{\sim}{q})]^{-1} \left([d(\underset{\sim}{q}, \dot{\underset{\sim}{q}})]\{\dot{q}\} + [k(\underset{\sim}{q})]\{q\} + \{f\}\right) \\ \{\dot{q}\} \end{Bmatrix} , \quad (4.23)$$

and

$$\{y\} = \begin{Bmatrix} \dot{\underset{\sim}{q}} \\ \underset{\sim}{q} \end{Bmatrix} . \quad (4.23a)$$

It should be understood that

$$\{\dot{y}\} = \{\dot{y}(\underset{\sim}{y}, \Psi)\}$$

is a periodic function depending nonlinearly on $\{y\}$.

4.3 Method of Solution

As indicated before, Equations (4.22), governing the aeroelastic behavior of an isolated blade, are a set of coupled, nonlinear ordinary differential equations with periodic coefficients. It has been shown in previous research, References [1] and [61], that in forward flight the aeroelastic stability and response problem of an isolated blade is strongly coupled with the overall equilibrium of the helicopter. The overall equilibrium of the helicopter in forward flight is normally obtained by enforcing the overall force and moment equilibrium of the complete helicopter. Such an analysis is called trim analysis. The results of this trim analysis are used as input to the aeroelastic analysis of the blade. Details of the trim procedures and the mutual interaction between the trim analysis and the aeroelastic analysis are presented in Section 4.3.3.

A solution to Equation (4.22) will provide both stability and response information. A response solution of Equation (4.23), subject to known initial conditions, can be obtained by numerical integration. However, this approach can become expensive in terms of computer time, since the transient response might be significant for a large number of rotor revolutions. Furthermore, numerical integration has proved itself to be a somewhat unreliable tool when dealing with periodic systems, unless it is complemented by explicit stability information. Therefore, in this study, the desired information about

the aeroelastic stability of the blade is obtained from the eigendata extracted from a linearized system. The linearized equations are obtained by linearizing the nonlinear equations, Equation (4.23), about a suitable equilibrium position. An equilibrium position is considered to be suitable if perturbations about it are sufficiently small, such that terms containing nonlinear products of the perturbation quantities can be neglected. For the case of forward flight, the primary source of excitation is periodic. Thus, the approximate nonlinear steady-state response of the blade is used as an equilibrium position about which the equations are linearized. Subsequently, the stability analysis of the linearized perturbation equations is explicitly considered.

4.3.1 Nonlinear Steady-State Response of Periodic Systems

Previous analyses, see References [2] and [61], have used a simple harmonic balance technique to calculate the time dependent equilibrium position. This approach is algebraically very tedious. Furthermore, since terms above the first harmonic were not retained, the accuracy of the resulting equilibrium position is somewhat questionable. Another shortcoming of the harmonic balance method is its failure to provide sufficient information on the stability of the response solution.

In the present study, the equilibrium position is obtained by applying an algorithm which has been developed in Reference [62] for

the steady-state response calculation of linear systems. In order to apply this method to the aeroelastic problem in forward flight, quasilinearization [63], [64] is used to transform the nonlinear equations (4.23) into a sequence of linear equations. The steady-state response for the linearized system at each iteration step is then obtained using the method of Reference [62]. In the limit, the sequence of linear problems converges to the solution of the original nonlinear problem. Additional and general information on quasilinearization can be found in Reference [64].

The method employed in this study has two key ingredients, namely, quasilinearization and the linear periodic response solution. These ingredients are described in detail below.

Quasilinearization, as formulated in Reference [63], employs the first-order equations, i.e., Equation (4.23). However, when the Galerkin finite element method is used for spatial discretization it is more convenient to start with the second-order system, Equation (4.22). These equations are expanded in a Taylor series about a previous solution, keeping only linear terms. The linearized second-order system is then transformed into first-order form.

During the K^{th} iteration step, the previous solution is denoted by $\{q^{K-1}(\psi)\}$. This solution has to satisfy the boundary conditions exactly, i.e., it must be periodic,

$$\{q^{K-1}(\psi)\} = \{q^{K-1}(\psi + 2\pi)\} \quad ,$$

and its derivatives with respect to Ψ must be known up to the highest order appearing in the derivatives of $\underset{\sim}{G}$ (see Equations (4.25) below). Furthermore, it is assumed that the derivatives of $\underset{\sim}{G}$ exist and that they are also periodic in Ψ. Thus,

$$\delta\underset{\sim}{G} = \left[\underset{\sim}{G} + \frac{\partial \underset{\sim}{G}}{\partial \underset{\sim}{q}} \delta\underset{\sim}{q} + \frac{\partial \underset{\sim}{G}}{\partial \dot{\underset{\sim}{q}}} \delta\dot{\underset{\sim}{q}} + \frac{\partial \underset{\sim}{G}}{\partial \ddot{\underset{\sim}{q}}} \delta\ddot{\underset{\sim}{q}} + \cdots \right]_{\underset{\sim}{q}^{K-1}}$$

$$= \underset{\sim}{0} \quad . \tag{4.24}$$

To write Equation (4.24) in a more compact fashion the following quantities are defined; for additional details, see Appendix G.

$$\underset{\sim}{G}^K = \underset{\sim}{G}(\underset{\sim}{q}^{K-1}, \dot{\underset{\sim}{q}}^{K-1}, \ddot{\underset{\sim}{q}}^{K-1})$$

$$= [m(\underset{\sim}{q}^{K-1})]\{\ddot{q}^{K-1}\} + \{F^K\} \quad , \tag{4.25a}$$

$$\{F^K\} = [d(\underset{\sim}{q}^{K-1}, \dot{\underset{\sim}{q}}^{K-1})]\{\dot{q}^{K-1}\}$$

$$+ [k(\underset{\sim}{q}^{K-1})]\{\underset{\sim}{q}^{K-1}\} + \{f\} \quad , \tag{4.25b}$$

$$[S^K] = \frac{\partial \underset{\sim}{G}}{\partial \underset{\sim}{q}} (\underset{\sim}{q}^{K-1}, \dot{\underset{\sim}{q}}^{K-1}, \ddot{\underset{\sim}{q}}^{K-1}) \quad , \tag{4.25c}$$

$$[C^K] = \frac{\partial \underset{\sim}{G}}{\partial \dot{\underset{\sim}{q}}} (\underset{\sim}{q}^{K-1}, \dot{\underset{\sim}{q}}^{K-1}) \quad , \tag{4.25d}$$

$$[M^K] = \frac{\partial \underset{\sim}{G}}{\partial \ddot{\underset{\sim}{q}}} (\underset{\sim}{q}^{K-1}) = [m(\underset{\sim}{q}^{K-1})] \quad . \tag{4.25e}$$

The variation, δq, which is the difference between the current and the previous solution, i.e.,

$$\delta q = \{q^K\} - \{q^{K-1}\} \quad , \tag{4.26}$$

is now substituted, together with Equations (4.25), into Equation (4.24), which is rewritten as:

$$[M^K]\{\ddot{q}^K\} + [C^K]\{\dot{q}^K\} + [S^K]\{q^K\} - [C^K]\{\dot{q}^{K-1}\} - [S^K]\{q^{K-1}\} + \{F^K\} = \underset{\sim}{0} \quad . \tag{4.27}$$

Equation (4.27) represents the linearized second-order system during the K^{th} quasilinearization step. Using

$$\{y^K\} = \begin{Bmatrix} \dot{q}^K \\ q^K \end{Bmatrix} \quad \text{and} \quad \{y^{K-1}\} = \begin{Bmatrix} \dot{q}^{K-1} \\ q^{K-1} \end{Bmatrix} ,$$

Equation (4.27) is transformed into first-order from:

$$\{\dot{y}^K\} = [A^K(y^{K-1}, \dot{y}^{K-1}, t)]\{y^K\} + \{b^K(y^{K-1}, t)\} \quad , \tag{4.28}$$

where

$$[A^K] = \begin{bmatrix} -[M^K]^{-1}[C^K] & -[M^K]^{-1}[S^K] \\ [I] & [0] \end{bmatrix} , \tag{4.28a}$$

The variation, δq, which is the difference between the current and the previous solution, i.e.,

$$\delta q = \{q^K\} - \{q^{K-1}\} \quad , \tag{4.26}$$

is now substituted, together with Equations (4.25), into Equation (4.24), which is rewritten as:

$$[M^K]\{\ddot{q}^K\} + [C^K]\{\dot{q}^K\} + [S^K]\{q^K\} - [C^K]\{\dot{q}^{K-1}\} - [S^K]\{q^{K-1}\} + \{F^K\} = \underset{\sim}{0} \quad . \tag{4.27}$$

Equation (4.27) represents the linearized second-order system during the K^{th} quasilinearization step. Using

$$\{y^K\} = \begin{Bmatrix} \dot{q}^K \\ q^K \end{Bmatrix} \quad \text{and} \quad \{y^{K-1}\} = \begin{Bmatrix} \dot{q}^{K-1} \\ q^{K-1} \end{Bmatrix} ,$$

Equation (4.27) is transformed into first-order from:

$$\{\dot{y}^K\} = [A^K(y^{K-1}, \dot{y}^{K-1}, t)]\{y^K\} + \{b^K(y^{K-1}, t)\} \quad , \tag{4.28}$$

where

$$[A^K] = \begin{bmatrix} -[M^K]^{-1}[C^K] & -[M^K]^{-1}[S^K] \\ [I] & [0] \end{bmatrix} , \tag{4.28a}$$

$$\{b^K\} = \begin{Bmatrix} -[M^K]^{-1}\left(-[C^K]\{\dot{q}^{K-1}\} - [S^K]\{q^{K-1}\} + \{F^K\}\right) \\ \\ \{0\} \end{Bmatrix} . \quad (4.28b)$$

Both $[A^K]$ and $\{b^K\}$ are periodic in ψ (with period 2π) and dependent on the previous solution, y^{K-1}.

The solution of Equation (4.28), i.e., the periodic response $\{y^K(\psi)\}$, is then used as the previous solution for the next iteration step. This process is continued until convergence is achieved, at which step $\{y^K(\psi)\}$ represents the periodic steady-state response of the nonlinear system, which is denoted as $\{\bar{y}(\psi)\}$. This solution is used as the equilibrium position for the stability calculation.

For periodic systems of the type encountered in rotary-wing aeroelasticity, quasilinearization is particularly attractive because the numerical treatment required for the linear analysis of such systems is available. Quasilinearization is a generalized Newton-Raphson method. It possesses second-order convergence [64]. Selection of the initial solution is crucial to the success of the method. Additional information on quasilinearization and its properties, as applied to rotary-wing problems, can be found in Reference [63].

In the present study, two options for initiating the quasilinearization process were implemented. Stability information in forward flight is usually plotted as a function of the advance ratio μ. Therefore, at a given value of μ, either the linear response

of the system (with all nonlinear terms deleted) was used as the initial solution, or the nonlinear response for a previous lower value of μ was used as the initial solution.

The linear, periodic response solution of Equation (4.28) is calculated using the algorithm developed in Reference [62] for linear systems. Recall that Equation (4.28) is the K^{th} linear approximation to the original nonlinear problem, Equation (4.23); therefore, the method of [62] is applicable. The solution procedure is outlined below, using the notation associated with the K^{th} quasilinearization step.

Urabe [65] has shown that if the multipliers, Λ_k, $k = 1,2,\ldots,2M$, of the homogeneous part of Equation (4.28),

$$\{\dot{y}^K\} = [A^K(\psi)]\{y^K\} \tag{4.29}$$

are all different from one, then Equation (4.28) has one and only one periodic solution, of period 2π, given by

$$\{y^K(\psi)\} = [\Phi^K(\psi)]\left\{ \int_0^{\psi} [\Phi^K(s)]^{-1} \{b^K(s)\}ds + \{y^K(0)\} \right\} , \tag{4.30}$$

with the initial condition

$$\{y^K(0)\} = ([I] - [\Phi^K(2\pi)])^{-1}[\Phi^K(2\pi)] \int_0^{2\pi} [\Phi^K(s)]\{b^K(s)\}ds, \tag{4.31}$$

where $[\Phi^K(\psi)]$ is the fundamental matrix of Equation (4.29), defined by

$$[\dot{\Phi}^K(\psi)] = [A^K(\psi)][\Phi^K(\psi)] \quad \text{and} \quad [\Phi^K(0)] = [I] \quad . \qquad (4.32)$$

It is important to note that $\{y^K(0)\}$ exists only if $([I] - [\Phi^K(2\pi)])$ is nonsingular. This is the case when the magnitudes of all the characteristic multipliers of Equation (4.29) are different from one, i.e., $|\Lambda_k| \neq 1$. If all $|\Lambda_k| < 1$, then the homogenous system, Equation (4.29), is asymptotically stable, according to Floquet theory [66], and $\{y^K(\psi)\}$ from Equation (4.30) is the desired steady-state solution. This response is then used as the previous solution in the next iteration step. If any one $|\Lambda_k| > 1$, then the homogeneous system is asymptotically unstable. In this case, although Equation (4.30) is still mathematically valid, the periodic solution is physically meaningless.

To find the periodic solution, first the initial conditions, Equation (4.31), are calculated. The transition matrix at the end of one period is evaluated using Hsu's approximate, semianalytical method (see Reference [67]). The periodic matrix $[A^K(\psi)]$ is approximated by a series of step functions. For each step, the matrix exponential is approximated by a finite number of terms of its defining series. The integral in Equation (4.31) is evaluated by taking a constant value of the integrand in each step and performing an ordinary summation. Thus, both $[\Phi^K(2\pi)]$ and $\{y^K(0)\}$ are evaluated simultaneously

during a single pass over one period.

Provided that the system linearized about $\{y^{K-1}(\Psi)\}$ is stable, the linearized system, Equation (4.28), is integrated using $\{y^{K}(0)\}$, i.e., Equation (4.31), as the initial condition. A fourth-order Runge-Kutta integration scheme with Gill coefficients and constant stepsize is used. This implies that Equation (4.30) is not used at all in the computations.

Instead of storing the response $\{y^{K}(\Psi)\}$ over one period (for use in the next quasilinearization step), a Fourier analysis with a finite number of terms is performed. The periodicity of the response is checked by integrating over several periods (i.e., blade revolutions) until the Fourier coefficients obtained in two subsequent periods agree within a desired accuracy.

The flow chart presented in Figure 6 summarizes the steady-state response calculation of periodic, nonlinear systems, as formulated in this section. The index K used in Figure 6 denotes the quasilinearization iteration index which is set to zero or one, depending on whether a linear or nonlinear initial solution is used. The integer NCONV indicates convergence of the response solution $\{y^{K}(\Psi)\}$, as compared to the solution from the previous quasilinearization step. At the beginning, NCONV is set to zero. When the response has converged it is set to one (see Step 10 in Figure 6). The quantity ε is a small prescribed number used in the convergence test and in the periodicity check. The integer K_{max} is the maximum allowed number of quasilinearization iteration steps. Note that

Figure 6 also includes the stability determination of the final linearized system, which is described in the next section.

4.3.2 Stability of the Linearized Periodic System

Stability is determined by deriving linearized perturbation equations about the equilibrium position, $\{\bar{y}(\Psi)\}$. Computation of this time-dependent, nonlinear equilibrium position has been described in the previous section; thus, at the present stage, the vector $\{\bar{y}(\Psi)\}$ is assumed to be known. Again, when using the finite element method, it is more convenient to deal initially with the second-order system. Therefore, let

$$\{q\} = \{\bar{q}\} + \{\Delta q\} \quad . \tag{4.33}$$

The equations of motion, Equation (4.22), are now expanded in a Taylor series about $\{\bar{q}\}$. Since, by definition, the perturbations $\{\Delta q\}$ are small, only linear terms are retained. Thus,

$$\delta \underset{\sim}{G} = \left[\underset{\sim}{G} + \frac{\partial \underset{\sim}{G}}{\partial \underset{\sim}{q}} \Delta \underset{\sim}{q} + \frac{\partial \underset{\sim}{G}}{\partial \dot{\underset{\sim}{q}}} \Delta \dot{\underset{\sim}{q}} + \frac{\partial \underset{\sim}{G}}{\partial \ddot{\underset{\sim}{q}}} \Delta \ddot{\underset{\sim}{q}} \right]_{\bar{\underset{\sim}{q}}} = \underset{\sim}{0} \quad . \tag{4.34}$$

Recognizing that $\underset{\sim}{G}(\bar{\underset{\sim}{q}}, \dot{\bar{\underset{\sim}{q}}}, \ddot{\bar{\underset{\sim}{q}}}, \Psi) = 0$, since $\bar{\underset{\sim}{q}}$ is the solution of Equation (4.22), Equation (4.34) is rewritten in first-order form as:

$$\{\Delta\dot{y}\} = \begin{Bmatrix} \Delta\ddot{q} \\ \Delta\dot{q} \end{Bmatrix}$$

$$= \left[\begin{array}{c|c} -[M]^{-1}[C] & -[M]^{-1}[S] \\ \hline [I] & [O] \end{array}\right] \{\Delta y\} , \qquad (4.35a)$$

or

$$\{\Delta\dot{y}\} = [A(\bar{y}, \dot{\bar{y}}, \psi)]\{\Delta y\}, \qquad (4.35b)$$

where

$$[S] = \frac{\partial G}{\partial \ddot{q}}(\bar{q}, \dot{\bar{q}}, \ddot{\bar{q}}) , \qquad (4.36a)$$

$$[C] = \frac{\partial G}{\partial \dot{q}}(\bar{q}, \dot{\bar{q}}) , \qquad (4.36b)$$

$$[M] = \frac{\partial G}{\partial \ddot{q}}(\bar{q}) . \qquad (4.36c)$$

The stability of the above homogeneous, linear, periodic system is determined according to Floquet theory [66]. The transition matrix of Equation (4.35b) is defined by

$$[\dot{\Phi}(\psi)] = [A(\psi)][\Phi(\psi)] \quad \text{and} \quad [\Phi(0)] = [I] . \qquad (4.37)$$

The characteristic multipliers are denoted by

$$\Lambda_k = \Lambda_{kR} + i \cdot \Lambda_{kI} , \qquad k = 1,2,\ldots,2M , \tag{4.38}$$

where M is the total number of modes used in the analysis. Knowing the Λ_k, the characteristic exponents

$$\lambda_k = \zeta_k + i\,\omega_k \tag{4.39}$$

are determined from

$$\zeta_k = \frac{1}{2(2\pi)} \ln (\Lambda_{kR}^2 + \Lambda_{kI}^2) , \tag{4.40a}$$

$$\omega_k = \frac{1}{2\pi} \tan^{-1}\left(\frac{\Lambda_{kI}}{\Lambda_{kR}} \right) . \tag{4.40b}$$

The linearized aeroelastic system is asymptotically stable if all $|\Lambda_k| < 1$, i.e., $\zeta_k < 0$. If any one $|\Lambda_k| > 1$, i.e., $\zeta_k > 0$, the system is asymptotically unstable. Stability boundaries, representing neutral stability, are obtained when $|\Lambda_k| = 1$ or $\zeta_k = 0$.

Comparing Equations (4.30) with Equations (4.25c - e), it is evident that the periodic matrix $[A(\bar{\underline{y}}, \dot{\bar{\underline{y}}}, \psi)]$ in the linearized stability equations, Equation (4.35b), is identical to $[A^K]$ in the response equations, Equation (4.28), when $\underline{y}^{K-1}$ is replaced by $\bar{\underline{y}}$. This means that after a converged response solution $\bar{\underline{y}}$ is obtained,

calculation of the transition matrix and the characteristic exponents, i.e., Steps 4 and 5 in Figure 6, is repeated one more time in order to determine the stability of the linearized system governed by Equation (4.35b). The transition matrix at the end of one period is evaluated using the semianalytical numerical scheme presented in Reference [67].

4.3.3 Trim Procedures

It has been shown in References [1] and [61] that, due to the inherently nonlinear nature of rotary-wing aeroelasticity, the correct treatment of the forward flight aeroelastic problem requires a coupled treatment of the dynamics of the blade and the overall equilibrium of the entire helicopter. In practice, overall equilibrium of a helicopter in forward flight is accomplished by pilot manipulation of the controls, such that the control variables yield a trimmed flight condition. The mathematical procedure used to simulate the equilibrium of a helicopter in forward flight is commonly denoted by the term trim analysis.

A simplified trim analysis, suitable for aeroelastic applications, has been developed in Reference [61]. The present study is based upon somewhat improved trim procedures, which are presented in Reference [63]. These trim procedures are suitable primarily for helicopters employing hingeless rotors. For the sake of completeness, the main features and assumptions of the trim procedures, described in detail in Reference [63], are summarized below.

1. Blade elastic flap dynamics, based upon a single mode representation are included.

2. Blade precone, β_p, offset x_A, and linear built-in twist are accounted for.

3. Variable inflow, given by Equation (4.3), and reversed flow effects are included.

4. The helicopter is assumed to be in straight, steady flight at constant speed, i.e., $\dot{\mu} = 0$.

5. Rotor shaft dynamics, $\dot{\Omega} \neq 0$, and tail rotor effects are not considered.

6. Stall and compressibility effects are neglected.

7. The linear steady-state flap response is evaluated using the method described in Section 4.3.1.

Two different trim procedures are considered.

Propulsive Trim (see Figure 7), simulates actual forward flight conditions. The advance ratio μ and the weight coefficient C_W (approximately equal to the thrust coefficient C_T) are specified and horizontal and vertical force equilibrium, as well as roll and pitch moment equilibrium, are satisfied. The computed trim outputs are the rotor angle of attack, α_R, the thrust coefficient C_T, the pitch components θ_0, θ_{1s}, θ_{1c}, the inflow λ, and the steady-state flap response.

Moment Trim (see Figure 7), simulates conditions under which a rotor would be tested in a wind tunnel. Pitching and rolling moments are maintained at zero. Force equilibrium is satisfied implicitly, since the rotor is mounted on a supporting structure. When using this trim procedure, μ, Θ_0, and α_R are specified and C_T, Θ_{1s}, Θ_{1c}, λ, and the flap response are computed.

The control settings, Θ_0, Θ_{1s}, Θ_{1c}, and the inflow λ obtained from the trim analysis are then used as input in the aeroelastic (single blade) analysis.

The iterative process, combining trim and aeroelastic analysis (see also, Figure 8), can now be described as follows: For a specific blade and a given flight condition (Steps 1 and 3 in Figure 8),

a) a trim analysis is performed to compute the trim values Θ_0, Θ_{1s}, Θ_{1c} and λ. (During the first trim analysis - Step 4 in Figure 8 - a simplified elastic flap response is calculated within trim.)

b) Using the trim values from a), the aeroelastic analysis is performed to calculate the stability and steady-state response of the rotor blade (Step 5 in Figure 8).

c) The flap response from a) is compared with the more accurate flap response obtained in b). If they agree within a desired accuracy, the results obtained in b) are the solution of the aeroelastic problem and the computations are terminated.

d) If the convergence test in c) is not met, the flap response from b) is imposed on the trim analysis. Subsequently, the trim values are recomputed (Step 7 in Figure 8). These new, improved trim values are then used to reevaluate the steady-state flap response from the aeroelastic analysis. This process is continued, iteratively, until the convergence test indicated in c) is passed.

SECTION 5

RESULTS AND DISCUSSION

The numerical results presented in this section are intended to illustrate the application of the Galerkin finite element method to rotary-wing aeroelasticity. It should be noted that the main emphasis is on the application of the method to hingeless rotored helicopters. However, the method is equally applicable to other types of rotors, such as teetering or articulated rotors. Furthermore, the method is eminently suitable for analysis of modern bearingless flexbeam-type rotors which have a complicated redundant structure. In the following section, three separate groups of results will be presented: First, results for some rotating beam-type free vibration problems will be given in terms of free vibration frequencies and mode shapes. Next, the coupled flap-lag aeroelastic stability boundaries in hover will be evaluated. In this case, the critical collective pitch angle at which instability occurs will be presented as a function of the inplane frequency. Finally, results illustrating the aeroelastic stability and response of the coupled flap-lag dynamics of a hingeless rotor blade in forward flight are presented. For this case the governing parameter is the advance ratio and the results will illustrate the variations of system damping and response as a function of advance ratio.

5.1 Some Computational Details

Due to the different nature of the hover and the forward flight cases, two separate computer programs were written. This approach permitted a more efficient treatment of each problem.

In the hover case all matrices are time invariant. Thus, for a uniform blade the basic parameters of the problem, i.e., the lag and flap stiffness, the collective pitch angle and the inflow, could be extracted from the element matrices. Hence, these quantities appear explicitly as scalar factors in the finite element equations. Therefore, after selecting the appropriate number of elements, the element matrices need to be calculated and assembled into the system matrices only once. Next, for a particular value of lag and flap stiffness, the uncoupled free vibration modes are calculated and the modal reduction is carried out. The reduced linear and nonlinear system matrices are stored. For a particular value of pitch setting the reduced system matrices are multiplied by the basic parameters and added up to give the final equations, Equations (3.18) and (3.19). The iterative Newton-Raphson solution to the nonlinear static equilibrium equations, Equation (3.18), is considered to have converged when the absolute change of each generalized coordinate is less than 10^{-4}.

The search for the stability boundary is started from zero pitch setting. The pitch setting is then increased in equal steps until the system becomes unstable. To obtain a more accurate estimate of θ_c, bisection is used in the interval in which the system has

become unstable. Subsequently, the pitch setting is incremented further to determine whether the system remains unstable. This search algorithm routine is a modified version of that used in Reference [57].

In forward flight most matrices contain periodic coefficients. Thus, calculation of the element matrices, assembly of the system matrices, and modal reduction has to be repeated at each value of the dimensionless time Ψ. Efficient programming and use of efficient methods to compute stability and response is, therefore, crucial for the effective treatment of this problem.

The efficient numerical computation of transition matrices is very important. Transition matrices are evaluated using the semi-analytical scheme presented in Reference [67]. To find the transition matrix at the end of one revolution (i.e., common period) and to compute the integral in the initial conditions, the interval 0 to 2π is divided into N_{psi} equal sectors. In each sector the required matrix exponential is approximated by the first five terms of its defining series expansion.

The periodic response of the K^{th} linearized system is computed with a fourth-order Runge-Kutta scheme with Gill coefficients. The first-order system is integrated over several revolutions using a step size of $2\pi/N_{rki}$. During each revolution, N_{rev}, where $N_{rev} = 1$ denotes the interval 0 to 2π, the response is Fourier analyzed, keeping N_h harmonics, i.e., $(1 + 2N_h)$ terms, for each generalized coordinate. An absolute change of less than 10^{-3} for each Fourier

coefficient indicates the periodicity and the convergence of the nonlinear response; see Steps 8 and 9 in Figure 8. The Runge-Kutta integration and Fourier analysis routines are improved versions of those used in Reference [62].

The trim results computed in this study are generated using the trim program from Reference [63]. In order to perform the trim and aeroelastic analyses iteratively, the trim program had to be linked to the finite element aeroelastic analysis program.

The eigenvalues of the dynamic system in hover, Equation (3.23), and the transition matrices at the end of one period (forward flight case) are obtained by utilizing the IMSL Mathematical Subroutine Library provided by IBM. First, the matrix is preconditioned by reducing its norm through exact diagonal similarity transformations. The matrix is then reduced to upper Hessenberg form by orthogonal similarity transformations. Finally, all eigenvalues are computed by using the QR method with origin shifts at each iteration.

All element matrices are evaluated using six-point Gaussian quadrature.

Results based on the global Galerkin method are computed using a modified version of Power's computer code, Reference [57]. Five nonrotating modes for each flap, lag, and torsion are used to obtain the uncoupled free vibration frequencies and mode shapes of the rotating blade.

5.2 Free Vibration Results

In order to validate the finite element method, uncoupled free vibrations of a cantilevered beam were considered first.

The convergence properties of the selected finite elements can best be evaluated by computing the free vibration bending and torsion frequencies of a nonrotating uniform beam. Figure 9 shows the relative accuracy of the finite element solutions, as compared to the exact solutions, when the number of elements is increased. The first bending and torsion frequencies, curves labeled 1B and 1T respectively, are obtained with excellent accuracy even when only two elements are used. The second and third bending and torsion frequencies (curves labeled 2B, 2T and 3B, 3T) are obtained with less than one percent error when three and five elements are used, respectively. Furthermore, it is apparent that the cubic interpolation bending element and the quadratic interpolation torsion element provide approximately the same accuracy. For comparison, the results for the first torsional frequency, when using the linear interpolation torsion element, are also shown. The performance of this element is considerably inferior when compared to the refined torsion element based upon quadratic interpolation. All elements exhibit uniform convergence. This was anticipated, since the finite element model for this conservative problem can be derived from a variational principle.

Results for the first bending frequency of a nonrotating, nonuniform beam are shown in Figure 10. The beam has linear width and

depth taper, the width and depth values at the free end being 80 percent of the respective root values. The ensuing quadratic mass and cubic bending stiffness distributions are approximated by using the functional values at ten equidistant points and assuming linear variation in between. Based on this approximation, the mass and stiffness properties within the elements are modeled in three different ways. First, the mass and stiffness within the element are assumed to be constant, using the average of the respective nodal values. Second, mass and stiffness are assumed to vary linearly within the element. Third, the beam properties are integrated together with the element shape functions, using six-point Gaussian quadrature. All frequencies are referenced to a six-element solution, where the exact functional form of the beam properties is included in the element integrals. Figure 10 shows that numerical integration of beam properties yields accuracy comparable to the case of a uniform beam (see curve 1B in Figure 9). Modeling the beam properties as linear within the element gives acceptable results. However, it is computationally more tedious. Lastly, using the constant model would require a significantly larger number of elements, solely for the purpose of modeling the nonuniform mass and stiffness properties.

In the present study, numerical integration of the nonuniform beam properties is chosen. It gives the best results and is computationally most easily implemented, since the element matrices are evaluated using numerical integration.

The free vibration problem of a uniform, rotating beam, having

in- and out-of-plane bending and torsion degrees of freedom, is considered next. The fundamental uncoupled lag, flap, and torsion frequencies are calculated using two methods:

1. A global Galerkin method in which five nonrotating modes of a uniform beam are used to obtain the fundamental, uncoupled, flap, lag, and torsion frequencies of a rotating beam, and
2. The Galerkin finite element method of weighted residuals.

Comparison between the two sets of results, showing the uncoupled rotating flap and lag frequencies, $\bar{\omega}_{F1}$ and $\bar{\omega}_{L1}$, and the torsion frequency, $\bar{\omega}_{T1}$ as a function of the nonrotating frequencies is shown in Figures 11 and 12, respectively. The results for the fundamental frequencies are identical when three or six elements are used, indicating that good accuracy can be obtained with a relatively small number of elements.

A comparison of the first- and second-flap mode shape, obtained using both methods is presented in Figure 13 for the nonrotating case and two different speeds of rotation. For this case, eight elements were used because it was more convenient to plot the results when slightly more elements were used. From a numerical convergence point of view, a smaller number of elements would have been adequate.

From these results it is clear that excellent agreement between the global Galerkin and the Galerkin finite element method is obtained for both frequencies and mode shapes.

The free vibration results presented in this section show that the selected cubic interpolation bending and quadratic interpolation torsion elements are very accurate, even when only a small number of elements is used. It is reasonable to expect that these elements will also perform very well in the aeroelastic analysis, since the aerodynamic loads do not depend on the strains. Modeling of strains, i.e., the higher-order derivatives of the elastic degrees of freedom, usually governs the accuracy and convergence of the finite element solution.

The actual number of elements used in the aeroelastic analysis will be governed by the number of modes retained in the modal reduction process.

5.3 Results for the Case of Hover

In this section the Galerkin finite element method is applied to a typical rotary-wing aeroelastic problem. The coupled flap-lag aeroelastic problem in hover [1], [68] is a convenient and simple example which can be used to illustrate the Galerkin finite element method. The finite element equations for this problem have been derived in Section 3.1.

In calculating numerical results, certain simplifying assumptions were made, since the objective of this section is primarily to illustrate the application of the Galerkin-type finite element method to rotary-wing aeroelasticity.

These simplifying assumptions are listed below:

1. The inflow was assumed to be constant over the blade and equal to the inflow at 0.75 span, i.e.,

$$\lambda = (a\sigma/16)[(1 + 24\theta/a\sigma)^{1/2} - 1] \quad . \tag{5.1}$$

2. Hub and tip losses were not included.

3. Structural damping was assumed to be zero.

Pertinent values of the data used in the calculations are presented in Table 5.1 below.

TABLE 5.1
CONFIGURATION PARAMETERS FOR FLAP-LAG IN HOVER

$a = 2\pi$;	$C_{d0} = 0.01$;	$\gamma = 5.0$;
$\bar{b} = 0.0313$;	$\bar{e}_1 = 0.0$;	$\beta_p = 0.0$;
$\sigma = 0.10$ (0.05);	$\bar{\omega}_{F1} = 1.15$ (1.0689);	
$\bar{\omega}_{L1}$, R_c, E, M, $\Rightarrow$ variable		

The numerical accuracy of the method can be best seen by comparing a global Galerkin solution, based on one uncoupled rotating elastic mode for each degree of freedom, with a local Galerkin finite element solution in which the blade is represented by three finite elements and where, for consistency with the global method, one uncoupled elastic rotating mode is used for each degree of freedom to reduce the number of nodal degrees of

freedom. The comparison between the two methods is presented in Table 1. For two separate collective pitch angles Θ, all pertinent values associated with these cases were evaluated. The agreement between the two methods is excellent when considering that only three elements are used to represent the blade. Similar comparisons were made for a variety of other cases, the results are not presented here since they would have been repetitive of the behavior illustrated by Table 1. The cases presented in Table 1 were stable configurations because the elastic coupling parameter R_c was taken as $R_c = 1.0$.

Convergence properties of the Galerkin finite element method, when applied to the aeroelastic problem, are considered next. It is important to note that convergence of Galerkin-type methods in aeroelasticity can be established only by numerical experimentation [55]. In rotary-wing aeroelastic problems this is further complicated due to their nonlinear nature. Convergence of the method can be investigated, alternatively, by varying the number of elements while retaining a fixed number of modes in the modal reduction process, or by changing the number of modes and maintaining a fixed number of elements. Convergence with respect to the nonlinear iterative solution technique is not investigated here. It should be noted, however, that convergence is very rapid. At most, three iteration cycles are required.

Figure 14 illustrates the convergence of stability boundaries for three different values of the elastic coupling parameter when the number of elements is allowed to vary from three to six, while the number of modes used in the modal reduction process is maintained at

one mode for each elastic degree of freedom. In all cases shown in the figure, the unstable regions tend to decrease as the number of elements is increased. The results for $E = 5$ and $E = 6$ are almost identical, indicating that four or five elements are sufficient to capture the bending dynamics of the blade.

Figure 15 shows the convergence characteristics when the number of elements is maintained at four, $E = 4$, while the number of modes used in the modal analysis is allowed to vary. The curves represent points at which the real part of those eigenvalues associated with predominant lag modes, i.e., ζ_{1L} and ζ_{2L}, is zero. The real part of the eigenvalues associated with predominant flap modes, i.e., ζ_{1F} and ζ_{2F}, is always negative. The coupled modes of the aeroelastic system, Eq. (3.23), can be identified as predominantly lag or flap modes by correlating the imaginary parts of the eigenvalues λ_k with the frequencies of the uncoupled rotating beam vibrations. System stability boundaries are obtained by piecewise combination of "1^{st} Lag" and "2^{nd} Lag" curves such that, overall, the lowest value of θ_c is maintained. For $R_c = 0.0$ and $R_c = 0.4$, system stability is determined by the behavior of the predominant first lag mode. The predominant second lag mode is always stable, i.e., $\zeta_{2L} < 0$. For $R_c = 0.0$ it is interesting to note that convergence trends differ, depending on whether the blade is soft inplane or stiff inplane. In the intermediate range of elastic coupling parameters, $0.5 \leq R_c \leq 0.8$, the possibility of a flap-lag type instability dominated by the second lag mode can occur. For $R_c = 0.6$ the system is unstable

due to the second lag mode when $\bar{\omega}_{L1} < 1.6$. Above $\bar{\omega}_{L1} = 1.6$, the first lag mode causes the system to become unstable. For $R_c = 0.8$ the second lag mode solely determines system stability. The first lag mode also becomes unstable, however, at higher values of θ. Finally, although not shown in the figure, it should be noted that the system is stable for R_c above 0.9 for the complete range of $\bar{\omega}_{L1}$ investigated. In conclusion, it can be said that the difference between taking two or four modes (i.e., $M = 2$ vs. $M = 4$) is relatively small with respect to the behavior of the first lag mode. This holds for values of $\bar{\omega}_{L1}$ up to 2.5, which is rarely exceeded in practical hingeless helicopter blade configurations. However, it is absolutely essential to use four modes, since the second lag mode governs system stability for intermediate values of elastic coupling.

In Figure 16 the number of elements is kept constant at six, $E = 6$, and the number of modes is changed. The behavior of the two- and four-mode model follows basically the same trends as those observed when four elements are used (see Fig. 15). When using six modes, as compared to four modes (i.e., $M = 6$ vs. $M = 4$), the same results are obtained, except for the instability associated with the third predominant lag mode. However, this instability occurs at very high pitch settings and is therefore not relevant for system stability. These results indicate that it is sufficient to use a total of four modes, two modes each for the elastic flap and lag degrees of freedom. As a cross-check, the four-element, four-mode solution for $R_c = 0.6$ is also shown in Fig. 16. The results are essentially the

same as in the six-element, four-mode solution. A difference occurs at $\bar{\omega}_{L1} \approx 0.8$ and $\bar{\omega}_{L1} \approx 1.6$; however, it is very small, indicating that four or five elements are sufficiently accurate even when four modes are used.

Figures 17 and 18 illustrate the influence of the elastic coupling parameter R_c on the real parts of the eigenvalues, which are a measure of modal damping and determine system stability. The pitch setting θ is kept constant and two different values of lag frequency $\bar{\omega}_{L1}$ are considered. The predominant flap modes are very stable and damping associated with them remains almost constant when the elastic coupling is changed. Damping of the predominant lag modes changes considerably with elastic coupling. Damping of the first mode is further strongly influenced by the value of $\bar{\omega}_{L1}$. It is also evident that the instability of the second lag mode is relatively weak and usually it can be eliminated by including a small amount of structural damping in the analysis.

A comparison of stability results when using uncoupled versus coupled mode shapes in the modal analysis is depicted in Figure 19. Use of coupled mode shapes should lead to more accurate results; however, it has the disadvantage that the coupled free vibration problem has to be recomputed for each increment of pitch setting. A total of four modes is used in each case. The four lowest frequency coupled modes include the two lowest lag and flap modes (predominant) when $\bar{\omega}_{L1} < 1.4$ and, for $\bar{\omega}_{L1} > 1.4$, the lowest lag and the three lowest flap modes (predominant). This means that the actual modal

representation changes with the inplane frequency $\bar{\omega}_{L1}$ when simply using the lowest frequency coupled modes. Thus, the analysis is not able to capture the behavior of the second predominant lag mode. Figure 19 shows that accuracy is not improved when using coupled modes. On the other hand, computing time increased roughly four-fold for this example. Therefore, use of coupled modes is not recommended. It should be noted that when six coupled modes were used the predominant second lag mode was present for all values of $\bar{\omega}_{L1}$ and its behavior was modeled correctly. However, computing cost increased in a prohibitive manner without any noticeable gain in accuracy when compared to the results using uncoupled modes.

In order to be able to compare the GFEM with the global Galerkin method, Powers' computer code [57] was modified by excluding torsion and introducing the elastic coupling parameter. The GFEM program was set up such that it can represent the governing dynamic equations of motion from Reference [57] without torsion. Then both methods were applied to the same problem. Figures 20 and 21 show that excellent agreement is obtained when using four or six uncoupled rotating modes. These are modeled by four or six elements in the GFEM and ten uncoupled nonrotating modes (five for flap and five for lag) in the global Galerkin method. Again, it is concluded that four elements and four modes will be sufficient to model simple flap-lag blade dynamics in hover.

Figure 22 illustrates the effect of using different sets of nonlinear equations of motion. In Reference [3] the global Galerkin

method based on four coupled rotating modes (one predominant lag, three predominant flap) is used. In the GFEM, four elements and four uncoupled rotating modes ($M_L = M_F = 2$) are used. Both, equations from Reference [57] (without torsion) and the present equations of motion are employed. Instability of the second lag mode at $R_c = 0.6$ is not shown. The trends established by the three solutions are, overall, the same. There are, however, marked differences in the actual numerical values, in particular, at $R_c = 0.0$. This must be attributed to the fact that the equations are slightly different. Furthermore, it should be noted that the flap-lag aeroelastic problem in hover, in the absence of elastic coupling terms, is very sensitive to small, higher-order terms; thus, small differences in these terms can lead to noticeable differences in the results. This also indicates that unless the equations are derived in an identical manner, differences can be observed for the same problem. These differences are, however, exaggerated by the fact that R_c was taken to be zero.

Figure 22 concludes the results presented for the flap-lag in hover problem. The numerical experience gained by applying the Galerkin finite element method to this basic rotary-wing aeroelastic problem provides valuable guidelines when dealing with the more practical flap-lag in forward flight problem, for which results are presented in the next section.

The computing times required to generate the stability boundaries in this section were only slightly larger than those required when using the global Galerkin method. This might seem to be somewhat

surprising; however, it has to be attributed to the fact that the finite element program was efficiently structured to avoid unnecessary recomputation of element matrices, assembly of system matrices, and modal reduction. The exact comparison of computing times for each method depends, of course, on the number of elements employed in the finite element model.

5.4 Results for Flap-Lag Blade Dynamics in Forward Flight

Numerical results presented in this section deal with the coupled flap-lag aeroelastic problem in forward flight. The finite element equations for the complete flap-lag-torsion problem in forward flight have been given in Section 4.2. No previous finite element solutions for the stability and response of nonlinear, nonconservative systems with periodic coefficients are available. In view of the novel features of the present research, where a finite element solution to such systems is given for the first time, it was deemed appropriate to avoid, initially, the added complexity of dealing with the torsional degree of freedom. However, it should be mentioned that the torsional equation of motion and the additional terms associated with the torsional degree of freedom in the lag and flap equations, do not introduce any conceptually new effects. They do, on the other hand, increase the size of the problem, imposing additional requirements on computer storage and computer time.

The coupled flap-lag finite element equations in forward flight

were obtained by simply disregarding all torsional submatrices (third row and column in the partitioned element matrices, see Equation (F.1)) and deleting all torsion terms in the nonlinear bending submatrices. This simplified system was carefully checked and found to be consistent with the ordering scheme. The method of solution presented in Section 4.3 was formulated in a general manner and is directly applicable to the flap-lag problem, as well as to the coupled flap-lag-torsion problem.

In calculating numerical results two types of inflow were included in the analysis.

1. Uniform inflow, where λ is given by Equation (5.2) and the cyclic inflow components, λ_s and λ_c, are set to zero; thus,

$$\lambda_0 = \mu \tan \alpha_R + \frac{C_T}{2\sqrt{\mu^2 + \lambda_0^2}} \quad . \qquad (5.2)$$

2. Nonuniform cyclic inflow, where λ_0 is given by Equation (5.2) and the total inflow is:

$$\lambda = \mu \tan \alpha_R + \frac{C_T}{2\sqrt{\mu^2 + \lambda_0^2}} (1 + 1.2\bar{x} \cos \psi) \quad . \qquad (5.3)$$

For calculating the inflow at $\mu = 0.0$ in the moment trim procedure, Equation (5.1) was used.

The numerical results obtained for the flap-lag problem in forward flight are presented in two groups.

First, results from the application of the Galerkin finite element method (GFEM) are compared with previous solutions, where the global Galerkin method (GGM) was used. This group also contains results illustrating the numerical properties of the solution procedure for the discretized dynamic equations, described in Section 4.3. Based on the experience gained with the hover problem, described in Section 5.2, three elements and, for consistency with the GGM results, a total of two modes were used. The elastic coupling parameter was set to $R_c = 1.0$. The data for this group of results is presented in Table 5.2.

TABLE 5.2

CONFIGURATION PARAMETERS FOR FLAP-LAG IN FORWARD FLIGHT
(Figures 23-30)

$\bar{\omega}_{L1} = 1.417$;	$\bar{\omega}_{F1} = 1.087$;	
$E = 3$;	$M = 2$;	$R_c = 1.0$;
$\bar{b} = 0.0313$;	$\gamma = 5.0$;	$\sigma = 0.05$;
N_{psi}, N_{rki}, N_h	$\Rightarrow$ variable.	

In all these cases, propulsive trim with a weight coefficient of $C_W = 0.01$ and uniform inflow was used. The actual trim values,

taken from the results of Reference [2], are listed in Table 2.

The second group of results deals with the convergence properties of the Galerkin finite element method and with the influence of several configuration parameters on system stability and response. The data values used for this group of results are presented in Table 5.3. For the soft inplane blade, these properties are close to those of the Boelkow BO-105 hingeless rotor.

TABLE 5.3

CONFIGURATION PARAMETERS FOR FLAP-LAG IN FORWARD FLIGHT
(Figures 31-39)

$\bar{\omega}_{Ll} = 0.732$ (1.417)		$\bar{\omega}_{Fl} = 1.125$;
$\bar{b} = 0.0275$;	$n_b = 4$;	$\gamma = 5.5$;
$\sigma = 0.07$;	$N_{psi} = N_{rki} = 60$;	$N_h = 10$;
E, M, R_c	$\Rightarrow$ variable.	

The trim values were calculated using the trim procedures from Reference [63]. In all cases, the fuselage pitching moment and the various trim offsets were set to zero. Propulsive trim values for a typical value of weight coefficient, $C_W = 0.005$, are shown in Table 3.

Parameters which remained unchanged for all forward flight results are: $\rho_A = 1.23$ kg/m^3 (0.00238 slugs/ft^3); $a = 2\pi$, C_{dO} =

$C_{DP} = 0.01$; $x_L = 0.0$; $x_U = 1.0$; $\bar{e}_1 = \beta_p = \bar{x}_A = \gamma_F = 0.0$; and $\eta_{SL} = \eta_{SF} = 0.0$. Furthermore, blade pretwist was set to zero, $\theta_B = 0.0$, and the blade properties were assumed to be uniform over the span. Other pertinent quantities are specified on the plots.

Stability results, showing the comparison between the Galerkin finite element method with the global Galerkin method, are given in Figures 23. The GGM results were taken from Reference [2], Figure 9, and Reference [61], Figure 9. In Reference [2] the same equations of motion as in the present study were employed. Three different values of torsional stiffness were considered. For the comparison, the results for the highest torsional stiffness, $\bar{\omega}_{T1} = 15.033$, were used. Reference [61] dealt with the flap-lag problem in forward flight. However, the equations of motion did not include some of the higher-order terms retained in the present study. In all three cases, stability results were obtained by linearizing the equations of motion about an approximate linear time-dependent equilibrium position. To simulate the harmonic balance method, as it was used in References [2] and [61], only the first harmonic, ($N_h = 1$) was used in generating the GFEM results. For two advance ratios, $\mu = 0.2$ and $\mu = 0.4$, ten harmonics were also used. To find the periodic response, the numerical integration was carried out over three blade revolutions and the Fourier coefficients, computed during the third revolution ($N_{rev} = 3$) were used. The number of azimuthal steps (per revolution) for both stability (N_{psi}) and response (N_{rki}) was taken as 120, which is identical to the

stepsize used in Reference [2].

The real part of the characteristic exponent for the predominant lag degree of freedom, ζ_{1L}, versus the advance ratio, μ, is plotted in Figure 23a. The value of ζ_{1L} is a measure of the overall damping associated with the first lag mode. The GFEM results exhibit the same trend as results from Reference [2]. The difference in ζ_{1L} is roughly the same for all advance ratios. This difference must be attributed to the absence of the torsional degree of freedom in the GFEM results. This conclusion is further confirmed by the fact that the GFEM results agree very well with those from Reference [61], up to an advance ratio of $\mu = 0.2$. When μ is increased above that, the additional higher-order nonlinear terms in the presently employed equations of motion become more important, so that eventually, at $\mu = 0.4$, the GFEM result is closer to the result from Reference [2].

Stability results for the flap degree of freedom, Figure 23b, generally show the same behavior as discussed above for lag. It should be pointed out that results for the characteristic exponents from References [2] and [61] exhibit the splitting, typical of periodic systems, for ζ_{1F} from $\mu = 0.2$ on upward, while the GFEM yields split values only at an advance ratio of $\mu = 0.4$. At lower values of μ the characteristic exponents appear in complex conjugate pairs. This difference between the two methods arises, probably due to the new procedure employed for solving the dynamic equations in the present study.

Agreement between the Galerkin finite element method and the

global Galerkin method results, presented in Figures 23, should be judged in light of the previously discussed differences in the blade model and in the procedure used to obtain the linear time-dependent equilibrium position. Overall, qualitative agreement between the two methods is quite good. Stability results at $\mu = 0.4$, using four finite elements, brought the GFEM results in even better agreement with results from Reference [2]. For the configuration in Figure 23, the blade motion was stable for all advance ratios considered.

When comparing GFEM results based on one harmonic ($N_h = 1$) with those using ten harmonics ($N_h = 10$), it is obvious that at $\mu = 0.2$ results for ζ_{1L} (Figure 23a) and ζ_{1F} (Figure 23b) are almost identical. At $\mu = 0.4$ there is a minor difference for the real part of the lag characteristic exponent. The flap degree of freedom, on the other hand, exhibits a rather remarkable change in ζ_{1F} when using ten instead of just one harmonic. This last result indicates that it is important to use more than one harmonic when considering advance ratios above $\mu = 0.2$.

Figures 24a and 24b illustrate the effect of the number of harmonics used in the Fourier analysis on the first approximation ($K = 1$) to the nonlinear steady-state lag and flap response. The blade tip displacements (generalized normalized coordinates) for $\mu = 0.4$, corresponding to the stability results in Figures 23, are plotted during the third blade revolution. Again, the contribution of the higher harmonics is more significant in flap than in lag. This,

as a matter of fact, explains the remarkable change in flap damping, as seen in Figure 23b.

Table 4 contains the Fourier coefficients of the response as plotted in Figures 24. From the relative magnitude of these coefficients it is apparent that, while it is essential to retain more than the first harmonics, it probably would be sufficient to use the first four harmonics. This conclusion was also found to be valid for other configurations.

Since the CPU time required for the Fourier analysis was very small, ten harmonics ($N_a = 10$) were used in all subsequent calculations.

Figures 25a and 25b address the question of how many blade revolutions, i.e., periods, should be integrated in order to obtain a periodic response. These plots show that the response is almost the same during the first ($N_{rev} = 1$) and the second ($N_{rev} = 2$) blade revolution. The difference between the response from the second and third blade revolution cannot be distinguished on the plots.

If the maximum absolute change of any Fourier coefficient, as compared to its value from the previous revolution, is taken as a measure of convergence, both the second and the third revolution yield Fourier coefficients which have converged within an accuracy of 10^{-3}. Thus, an error control parameter based on such an accuracy (10^{-3}) seems to be adequate. Also recall that in the derivation of the equations of motion the displacements were assumed to be of order

$\varepsilon_D \approx 0.2$ and terms of $O(\varepsilon_D^2)$ were neglected, as compared to terms of $O(1)$. Therefore, this error control quantity is also logically consistent with the ordering scheme. Furthermore, it should be noted that the initial conditions used for the numerical integration theoretically insure a periodic response. The effect of approximations and numerical errors in the actual calculation of the initial conditions will most likely be corrected with the integration over the second or third blade revolution. Any further integration will merely lead to an accumulation of errors in the integration routine.

Stability results (not shown), based on linearization about the steady-state response from the second and third revolution, did not change in any significant manner. This further confirms that an accuracy of 10^{-3} for the absolute change of the Fourier coefficients is sufficient.

Table 5 shows the first-order state variable vector at the first three full blade revolutions, for the response plotted in Figures 25. The elements of this vector are the lag and flap blade tip speeds and displacements in the rotating system. At the azimuthal angle $\Psi = 0$, this vector is identical to the initial conditions. From $\Psi = 2\pi$ on, only small changes occur. A monotonic convergence trend from one complete revolution to the next cannot be observed. However, by using the error control parameter associated with the harmonic components, as discussed previously in this section, the periodicity can be accurately determined.

Convergence of the results indicative of stability, Figures

26, and of response, Figures 27, with the number of quasilinearization steps was studied next. As expected, results for stability and response change markedly when going from the linear stability and response solution, $K = 0$, to the first nonlinear solution, $K = 1$. Stability results based on the first nonlinear equilibrium position, i.e., curves labeled $K = 2$ in Figures 26, show a further change only at the higher end of the advance ratio range, i.e., at $\mu = 0.4$. This result, again, emphasizes the importance of retaining higher order nonlinear terms when advance ratios above $\mu = 0.2$ are considered. Therefore, stability information should be obtained by linearization about a nonlinear time-dependent equilibrium position. For the configuration considered in Figures 26 (data from Table 5.2), the nonlinear terms decrease the stability margin of the lag degree of freedom for all values of μ. For the flap degree of freedom, stability is decreased only at $\mu = 0.4$; at lower values of μ the nonlinear terms are stabilizing. It is interesting to note that flap stability results are most sensitive to the number of quasilinearization steps used in the analysis, i.e., nonlinearities are more significant for flap. As a matter of fact, at $\mu = 0.4$ the question arises if, indeed, the lower of the two values of the characteristic exponent for flap has converged with the second iteration step; see Figure 26b.

Response results in Figures 27 show that nonlinear terms (K = 1) increase the amplitudes of both the lag and flap response, as compared to the linear solution (K = 0). When performing an additional iteration step, i.e., going from K = 1 to K = 2, the response remains practically unchanged. The corresponding response curves cannot be distinguished within the accuracy of Figures 27. Inspecting the Fourier coefficients at K = 2 for convergence, as compared with the previous iteration step K = 1, it was seen that the maximum absolute change of any Fourier coefficient at $\mu = 0.4$ is less than 10^{-3}.

The above question of convergence of the characteristic exponents with the number of quasilinearization steps was pursued further by allowing a third quasilinearization step (K = 3), for stability only, i.e., by linearizing the system about the nonlinear response from the second iteration step (K = 2). Figure 28 shows the relative change of the characteristic exponents versus the number of quasilinearization steps for the most critical cases presented in Figures 26. At $\mu = 0.4$ the exact solution was assumed to have been obtained with the third iteration (K = 3), while at $\mu = 0.2$, the second iterative solution (K = 2) was used as reference. The results in Figure 28 indicate that at $\mu = 0.4$ two iteration steps are needed, while at the lower value of advance ratio, $\mu = 0.2$, one iteration step is sufficient to obtain converged values for the characteristic exponents. Thus, it can be concluded that at higher advance ratios, use of a nonlinear equilibrium position is necessary

to obtain accurate stability information.

From the results presented in Figures 26 through 28, the following procedure was established to obtain converged nonlinear response and stability results. First, the quasilinearization iterations are carried on until the maximum absolute change of any Fourier coefficient of the response is less than 10^{-3}. Second, the system is linearized about this converged nonlinear steady-state response to yield the final explicit stability information, i.e., the real part of the characteristic exponents. It should be pointed out that convergence of the characteristic exponents with the number of iteration steps can also be monitored, since this information is available at each quasilinearization step. However, computationally, it would be very difficult to implement a convergence test based on the characteristic exponents, because their identification is complicated by the fact that the imaginary parts are not uniquely known and that they do not always appear in complex conjugate pairs. The identification would be particularly difficult in the case where more than one mode per elastic degree of freedom is considered.

The effect of the number of azimuthal stations in calculating stability and the initial conditions, N_{psi}, and the number of steps per blade revolution in the Runge-Kutta integration, N_{rki}, is illustrated in Figures 29 and 30. Note that all results presented for forward flight are obtained using the same step size for the stability and response calculation, i.e., $N_{psi} = N_{rki}$.

The relative change of the real part of the characteristic exponents at $\mu = 0.4$ versus the number of azimuthal steps, is shown in Figure 29. The solution with $N_{psi} = 120$ was assumed to be correct. Note that the flap degree of freedom does not have complex conjugate characteristic exponents, i.e., two distinct real parts are associated with it. Overall, results based on fourty steps are in excellent agreement. Even twenty steps, $N_{psi} = 20$, give acceptable results. These conclusions, however, should be viewed as dependent upon the particular configuration considered and the number of modes used to reduce the nodal degrees of freedom. When ten steps were used, the numerical procedure broke down. Note also, that for the particular configuration considered here (data from Table 5.2), the flap results converge slower than the lag results. The reason for this apparently being that higher harmonics are more significant for the flap response than for the lag response; see Figures 24. The higher harmonic response contributions obviously require a smaller stepsize for a certain, desired accuracy.

Figures 30a and 30b compare the lag and flap response, respectively, for 20 and 120 steps (per revolution). Agreement between the response curves for the different number of azimuthal steps is quite good, although the absolute values of the Fourier coefficients differs by more than 10^{-3}. When using 40 steps, the response could not be distinguished from the curves based on 120 steps, within the accuracy of the plot (result not shown). For this case ($N_{psi} = 40$), the absolute difference for the Fourier coefficients of the response

from the two different step sizes was less than 10^{-3}, indicating that forty steps would be sufficient.

Figure 30b concludes the results intended to illustrate the effects of the various parameters, associated with the solution procedure, on the blade dynamics in forward flight. These parametric studies were necessary since previous numerical experience was limited and restricted to the case where the linear steady-state response was used as the equilibrium position. No solutions to nonlinear aeroelastic periodic systems using quasilinearization were available.

From the numerical experience gained in this study, the following conclusions were drawn. It is important to retain more than the first harmonic in the Fourier analysis of the response. In subsequent calculations, ten harmonics, $N_h = 10$, were used. The nonlinear response was considered to be periodic and to have converged when the maximum absolute change of each Fourier coefficient was less than 10^{-3}. According to this criterion, periodicity was achieved with the second or third blade revolution and the quasilinearization procedure converged with the first $(K = 1)$ or second $(K = 2)$ nonlinear response, depending on the value of the advance ratio. Forty azimuthal steps were sufficient to obtain accurate response and stability solutions. In all subsequent calculations, sixty steps, $N_{psi} = N_{rki} = 60$, were used. This should be adequate even when more elements and mode shapes are used in the analysis.

The configuration for which these results were calculated

(data in Tables 5.2 and 2) correspond to a relatively high loading case ($C_W = 0.01$). The choice of parameters made above should thus be considered conservative when cases with a more moderate blade loading are sought. Therefore, the parametric study above was not repeated for the other blade configurations and discretization models considered in this study.

The convergence properties of the Galerkin finite element method are considered next. This is accomplished by changing the number of elements or the number of mode shapes in the modal reduction process. All the results are based on the configuration parameters given in Table 5.3.

The relative change in the real part of the characteristic exponent versus the number of elements is shown in Figure 31 for the soft in-plane blade, $\bar{\omega}_{L1} = 0.732$, and elastic coupling $R_c = 0.6$. The number of modes was kept constant at two. As reference, the five-element solution was used. It is apparent that excellent convergence is achieved, in particular, when considering that the results in Figure 31 are for a high advance ratio, $\mu = 0.4$. Interestingly, the accuracy for the flap degree of freedom is much higher than that for lag. This must be attributed to the lower stability margin for lag; see Figures 32. Overall, the three-element solution can be considered sufficiently accurate. It should be kept in mind, however, that the configuration in Figure 31 is stable. For a more critical case, more elements might be required to model the system accurately. Finally, it is interesting to compare Figure 31 with the accuracy for the

first bending frequency of a nonrotating beam in Figure 9. As expected, the solution of the aeroelastic problem does require a larger number of elements than the free vibration problem.

Figures 32 show system stability when changing the number of modes from two to four, while keeping the number of elements constant at $E = 4$. The aeroelastic damping for the fundamental modes, ζ_{1L} and ζ_{1F}, remains unchanged when using four modes as compared to two modes. The damping, i.e., real part of the characteristic exponents, for both predominant flap modes is practically constant for all advance ratios. The absolute value of ζ_{2F} is somewhat lower than that for the first flap mode, ζ_{1F}, however, both modes are strongly damped. The first lag mode has its lowest damping values at moderate advance ratios, $\mu = 0.1 - 0.2$. When the advance ratio is increased, the results indicate that the forward flight aerodynamics have a stabilizing effect. Overall, the smallest stability margin occurs at hover, $\mu = 0.0$, for the second predominant lag mode. However, with increasing advance ratios, more aeroelastic damping is fed into the second lag mode. For advance ratios, $\mu > 0.2$, the real parts of the characteristic exponents for both lag modes, ζ_{1L} and ζ_{2L}, are roughly the same.

The lag and flap blade tip response was plotted in Figures 33 and 34. The configuration considered is the same as that for which stability results were presented in Figures 31 and 32.

Figures 33 show the response for three different advance ratios,

obtained by using four elements and two modes. The time dependence of the response in forward flight ($\mu = 0.2, 0.4$) as compared to the static response in hover ($\mu = 0.0$) is clearly illustrated. The time dependent contribution to the lag displacements is basically a one per rev motion, while the major contribution to the flap displacements is a two per rev motion, i.e., it stems from the second harmonic. This is the same behavior as encountered for the stiff in-plane blade in Figures 24. Another interesting aspect of the response curves in Figures 33 is that the displacements at the advance ratio $\mu = 0.2$ are lower than those for hover. From the trim data in Table 3 it is obvious that there is a direct relation between the value of collective pitch setting θ_0 and the magnitude of the response. The largest displacements occur at the advance ratio $\mu = 0.4$ which has the largest value of θ_0.

The effect of the number of modes retained in the modal reduction process on the blade response at $\mu = 0.4$ is illustrated in Figures 34. The response of the second lag mode, h_2, is very small. Only in the reversed flow region can it be distinguished from zero. The second flap mode response, g_2, is more important. The behavior of the response associated with the first lag and flap mode, respectively, varies accordingly. For lag, the response of the first mode does not change significantly when going from two to four modes in the analysis. For flap, on the other hand, there is a sizeable change. When the response of the first and second flap mode (from the four-mode analysis, $M = 4$) are added together, its

maximum value is roughly 8 percent larger than that of the response based on the two-mode analysis (M = 2).

The effect of the number of modes used in the analysis was further investigated by considering stability of a stiff in-plane blade, $\bar{\omega}_{L1} = 1.417$, with elastic coupling $R_c = 0.8$. Results for the real part of the characteristic exponents are obtained by using two and four modes. In both cases, the blade is represented by four elements. The stability curves in Figures 35 exhibit the same general behavior as encountered for the soft in-plane blade (Figures 32). There are, however, two important differences. The second lag mode is unstable at $\mu = 0.0$, i.e., ζ_{2L} is positive. Thereafter, the forward flight aerodynamics introduce a considerable amount of damping, so that at $\mu = 0.1$ the second lag mode is more stable than the first lag mode by a factor of five. A further increase in the advance ratio, changes the value of ζ_{1L} such that it approaches the value of ζ_{2L}, and at $\mu = 0.4$ they are practically the same. The other interesting point is that at $\mu = 0.4$ only the four-mode solution exhibits splitting of the characteristic exponents (real part) associated with the first flap mode. The two-mode solution does not capture this effect.

Results presented in Figures 34 and 35 indicate that for both response and stability it is important to retain four modes in the analysis. Recall, that in the hover case the second predominant lag mode itself was the cause for system instability at certain values of the lag frequency $\bar{\omega}_{L1}$; see Figure 15. In the forward flight case

such an instability was not observed; however, the presence of the second lag and flap mode did change the response and, in certain cases, the stability behavior associated with the predominant first flap mode. Although this change did not result in a critical condition, it certainly will have an effect on blade bending moments and vibration levels. This, in turn, effects the fatigue life of the blades and the vibration levels in the fuselage.

The effect of the elastic coupling parameter R_c on the stability of the first and second predominant lag mode is shown in Figures 36 and 37, respectively, for the soft in-plane blade. The stability margin of the first lag mode (Figure 36) increases proportionally with the value of R_c throughout the entire range of advance ratios. The least stable configuration is obtained for zero elastic coupling, at low advance ratios ($\mu = 0.1 - 0.2$). The behavior of the second lag mode, (Figure 37), is quite different. The variation of damping versus the advance ratio depends strongly on the value of R_c. Lastly, it should be mentioned that the predominant flap modes are very stable and the damping associated with them remained almost constant when the elastic coupling was changed. The same observation was made for the hover case; see Figures 17 and 18.

A comparison of stability results for two values of the weight coefficient is presented in Figures 38. The damping associated with the second lag and flap mode is practically unaffected by the value of C_W. For the first flap mode the higher value of C_W reduces damping

increasingly with the advance ratio. Also note that at $\mu = 0.4$ the blade subjected to higher loads ($C_W = 0.01$) exhibits splitting of the real parts of the characteristic exponents for ζ_{1F}. Damping values for the first lag mode show a reversed trend. The lower value of $C_W = 0.005$ decreases ζ_{1L} considerably, in particular, at high advance ratios. Additional results (not presented here) for a still lower value of the weight coefficient, $C_W = 0.0025$, showed that the small stability margin of the predominant first lag mode at $\mu = 0.1$ was reduced even further. This is consistent with the physical behavior of the flap-lag instability in hover, since lower values of C_W at low advance ratios result in reduction of the aerodynamic damping available in the lag degree of freedom.

The results presented so far were based on the uniform inflow model, given by Equation (5.2). Figure 39 illustrates that the influence of the nonuniform inflow, Equation (5.3), on the stability results is minor. A small difference for the lag stability results can be observed only at $\mu = 0.1$. The flap stability results (not shown) were unaffected at all. These results suggest that either the configuration considered in Figure 39 is not sensitive to the inflow model, or the inflow representation must be more sophisticated than Equation (5.3) in order to have any effect on system stability.

Finally, it should be pointed out that all forward flight results presented in this study were obtained by using the linear equilibirum position as an initial guess in the quasilinearization procedure. For a test case, system response and stability were

computed, incrementing μ in four equal steps from $\mu = 0.0$ to $\mu = 0.4$. The linear response at the current value of μ, as well as the converged nonlinear response from the previous lower value of μ, were used as the initial guess for the nonlinear response solution. Both, the nonlinear response and the stability values of the linearized system, converged to the same solution for all values of μ, regardless of which type of initial guess was employed. Since using the linear initial guess was computationally cheaper, this option was chosen. It also has the additional advantage that results can be computed for any arbitrary value of advance ratio, without having to sweep the entire range of μ's, starting from zero up to the desired value of the advance ratio.

The results presented in this section for the flap-lag problem in forward flight indicate that this is basically a stable configuration. Figure 35a illustrates that the second lag mode instability encountered in the hover problem (Section 5.2) does not persist in the forward flight region. From results in Reference [2] it becomes clear that inclusion of the torisonal degree of freedom introduces instability, usually associated with the lag motion. However, only for torsionally soft blades does this instability manifest itself in the range of advance ratios considered in the present study.

The computational times required for the flap-lag problem in forward flight are quite significant. They depend on a number of parameters, such as the number of elements and modes, number of

azimuthal steps, number of quasilinearization iterations, and number of revolutions integrated. Furthermore, the configuration parameters also play a role, in as much as they determine the degree of nonlinearity of the system. To find the converged, nonlinear periodic response and linearized stability for one value of advance ratio, approximately 30 CPU seconds were needed in the three-element two-mode case. When using four elements, 40 CPU seconds were required. In the case of four elements and four modes, this value increased to approximately 100 CPU seconds. The computation of the element matrices of aerodynamic origin, which must be performed for each value of azimuth angle, takes up roughly 50 percent of these CPU times. A direct comparison with computing times necessary for the global Galerkin method was not possible since those results were generated using the harmonic balance method to compute the equilibrium position. All forward flight results were generated on an IBM 3033 computer.

Lastly, it should be mentioned that the iterative trim - aeroelastic analysis, as discussed in Section 4.3.3 and indicated by Steps 7 and 8 in Figure 8, was not used to generate results in the present study. It would have increased the computing times considerably, without contributing to the basic objective of this study which is primarily aimed at the application of the finite element method to rotary-wing aeroelasticity.

SECTION 6

CONCLUSIONS

This study presents the formulation of a Galerkin-type finite element method for nonselfadjoint, nonlinear aeroelastic rotary-wing problems. From the numerical results presented for the aeroelastic stability and response of hingeless helicopter rotor blades, the following conclusions can be drawn:

1. The Galerkin finite element method is a practical tool for formulating and solving rotary-wing aeroelastic problems. Since spatial discretization is applied directly to the partial differential equations, algebraic manipulative labor is reduced significantly when compared to the application of the global Galerkin method to similar problems. However, more computer time is spent in calculations.

2. Four or five elements are sufficient to capture the bending dynamics of the blade with the same accuracy as the global Galerkin method.

3. Normal mode transformation, combined with the Galerkin finite element formulation, reduces the number of nodal degrees of freedom significantly and enables one to deal efficiently with complex problems.

4. For the flap-lag problem in hover it is essential to use

two modes for each elastic degree of freedom, since the second lag mode determines system stability for certain values of elastic coupling.

5. The flap-lag problem in forward flight is basically stable. The lowest stability margins are associated with the lag degree of freedom at moderate advance ratios and low rotor loading. Inclusion of two modes for each elastic degree of freedom is necessary to determine blade response accurately.

6. Nonlinear effects are important for both stability and response, in particular, at high advance ratios.

7. Higher harmonic contributions to the periodic blade motion are significant, especially for flap stability and response.

At this point it should be mentioned that a portion of the research presented in this dissertation has already been published [69] and was presented at the Fourth European Rotorcraft and Powered Lift Aircraft Forum.

Based on the experience gained from the flap-lag problem, the Galerkin finite element formulation for the coupled flap-lag-torsion problem, presented in Section 4, can be implemented directly. It is expected that four or five elements are also adequate to model the coupled bending-torsional dynamics of the blade.

Finally, it should be noted that the Galerkin finite element method, as formulated in this study, provides a natural tool for dealing with the complex structural configurations encountered in modern bearingless flexbeam-type main rotors and tail rotors.

REFERENCES

1. Friedmann, P., "Recent Developments in Rotary-Wing Aeroelasticity," Journal of Aircraft, Vol. 14, No. 11, November 1977, pp. 1027-1041.

2. Shamie, J. and Friedmann, P., "Effect of Moderate Deflections on the Aeroelastic Stability of a Rotor Blade in Forward Flight," Forum Proceedings of the Third European Rotorcraft and Powered Lift Aircraft Forum, Paper No. 24, 1977.

3. Hodges, D.H. and Ormiston, R.A., "Stability of Elastic Bending and Torsion of Uniform Cantilever Rotor Blades in Hover with Variable Structural Coupling," NASA TND-8192, April 1976.

4. Strang, G. and Fix, G., An Analysis of the Finite Element Method, Prentice Hall, 1973.

5. Gallagher, R.H., Finite Element Analysis, Prentice Hall, 1975.

6. Huebner, K.H., The Finite Element Method for Engineers, John Wiley, 1975.

7. Segerlind, L.J., Applied Finite Element Analysis, John Wiley, 1976.

8. Zienkiewicz, O.C., The Finite Element Method, McGraw-Hill, 3-rd ed., 1977.

9. Kikuchi, F., "A Finite Element Method for Non-Self-Adjoint Problems," International Journal of Numerical Methods in Engineering, Vol. 6, 1973, pp. 39-54.

10. Finlayson, B.A. and Scriven, L.E., "The Method of Weighted Residuals - A Review," Applied Mechanics Reviews, Vol. 19, No. 9, September 1966, pp. 735-748.

11. Hutton, S.G. and Anderson, D.L., "Finite Element Method: A Galerkin Approach," Journal of Engineering Mechanics Division of ASCE, October 1971, pp. 1503-1520.

12. Vakhitov, M.B., "Integrating Matrices as a Means of Numerical Solution of Differential Equations in Structural Mechanics," Soviet Aeronautics, Vol. 9, 1966, pp. 27-33, Farady Press, Inc.

13. Vakhitov, M.B., "Calculation of Free, Joint Bent-Twist Oscillations of Revolving Helicopter Blade," News of Institutions of Higher Learning, Aeronautical Engineering, No. 4, 1966, pp. 47-69, Collection of Articles (U.S. Air Force Systems Command), AD-629441.

14. Hunter, W.F., "The Integrating Matrix Method for Determining the Natural Vibration Characteristics of Propeller Blades," NASA TN D-6064, December 1970.

15. White, W.F., "Effect of Compressibility on Three-Dimensional Helicopter Rotor Blade Flutter," Ph.D. Dissertation, Georgia Institute of Technology, School of Aerospace Engineering, March 1973.

16. Murthy, V.R., "Dynamic Characteristics of Rotor Blades: Integrating Matrix Method," AIAA Journal, Vol. 15, No. 4, 1977, pp. 595-597.

17. White, W.F., "Comment on 'Dynamic Characteristics of Rotor Blades: Integrating Matrix Method'," AIAA Journal, Vol. 15, No. 5, 1978, pp. 541-542.

18. White, W.F. and Malatino, R.E., "A Numerical Method for Determining the Natural Vibration Characteristics of Rotating Non-Uniform Cantilever Blades," NASA TM X-72751, October 1975.

19. Kvaternik, R.G., White, W.F., and Kaza, K.R.V., "Nonlinear Flap-Lag-Axial Equations of a Rotating Beam with Arbitrary Precone Angle," AIAA Paper 78-491, Proceedings of AIAA/ASME 19th Structures, Structural Dynamics and Materials Conference, Bethesda, Maryland, April 1978, pp. 214-227.

20. Nagaraj, V.T. and Shanthakumar, P., "Rotor Blade Vibrations by the Galerkin Finite Element Method," Journal of Sound and Vibration, Vol. 43, No. 3, 1975, pp. 575-577.

21. Murty, A.V.K. and Murthy, S.S., "Finite Element Analysis of Rotors," Mechanism and Machine Theory, Vol. 12, 1977, pp. 311-322.

22. Olson, M.D., "Finite Elements Applied to Panel Flutter," AIAA Journal, Vol. 5, No. 12, 1967, pp. 2267-2270.

23. Barsoum, R.S., "Finite Element Method Applied to the Problem of Stability of a Non-Conservative System," Int. J. Num. Meth. Engineering, Vol. 3, 1971, pp. 63-87.

24. Szabo, B.A. and Lee, G.C., "Derivation of Stiffness Matrices for Problems in Plane Elasticity by Galerkin's Method," Int. J. Num. Meth. Engineering, Vol. 1, 1969, pp. 301-310.

25. Zienkiewicz, O.C. and Parekh, C.J., "Transient Field Problems: Two-Dimensional and Three-Dimensional Analysis by Isoparametric Finite Elements," Int. J. Num. Meth. Engineering, Vol. 2, 1970, pp. 61-71.

26. Aral, M.M., Mayes, P.G. and Smith, Jr., C.V., "Finite Element Galerkin Method Solution to Selected Elliptic and Parabolic Differential Equations," Proceedings of the Third Air Force Conference on Matrix Methods in Structural Mechanics, WPAFB, Ohio, October 1971, pp. 215-243.

27. Prasad, K.S.R.K. and Murty, A.V.K., "Galerkin Finite Element Method for Vibration Problems," AIAA Journal, Vol. 11, No. 4, 1973, pp. 544-546.

28. Rao, G.V. and Rao, R.V.N., "Galerkin Finite Element Solution for the Stability of Cantilever Columns Subjected to Tangential Loads," AIAA Journal, Vol. 13, No. 5, 1975, pp. 690-691.

29. Rao, G.V. and Raju, K.K., "A Galerkin Finite Element Analysis of a Uniform Beam Carrying a Concentrated Mass and Rotary Inertia with a Spring Hinge," Journal of Sound and Vibration, Vol. 37 (4), 1974, pp. 567-569.

30. Murty, A.V.K., Rao, A.K. and Rao, G.V., "Finite Element Modelling of Natural Vibration Problems," in Theory and Practice in Finite Element Structural Analysis, ed. by Y. Yamada and R.H. Gallagher, University of Tokyo Press, 1973, pp. 323-338.

31. Tillerson, J.R., Stricklin, J.A. and Haisler, W.E., "Numerical Methods for the Solution of Nonlinear Problems in Structural Analysis," in Numerical Solution of Nonlinear Structural Problems, ed. by R.F. Hartung, ASME, 1973, pp. 67-102.

32. Gallagher, R.H., "Finite Element Analysis of Geometrically Nonlinear Problems," in Theory and Practice in Finite Element Structural Analysis, ed. by Y. Yamada and R.H. Gallagher, University of Tokyo Press, 1973, pp. 109-123.

33. Vos, R.G. and Vann, W.P., "A Finite Element Tensor Approach to Plate Buckling and Postbuckling," Int. J. Num. Meth. Engineering, Vol. 5, 1973, pp. 351-365.

34. Bergan, P.G. and Clough, R.W., "Large Deflection Analysis of Plates and Shallow Shells Using the Finite Element Method," Int. J. Num. Meth. Engineering, Vol. 5, 1973, pp. 543-556.

35. Oden, J.T., Akay, H.U. and Johnson, C.P., "Effect of Higher Order Terms in Certain Nonlinear Finite Element Models," AIAA Journal, Vol. 11, No. 11, 1973, pp. 1589-1590.

36. Kavanagh, K.T., "Orthogonal Mode Technique for Nonlinear Analysis: A New Approach to Static Analysis and to Computer Aided Design," Proceedings of Specialty Conference on the Finite Element Method in Civil Engineering, McGill University, 1972.

37. Wu, R.W.H. and Witmer, E.A., "Finite-Element Analysis of Large Transient Elastic-Plastic Deformations of Simple Structures, With Application to the Engine Rotor Fragment Containment/ Deflection Problem," NASA CR-120886, January 1972.

38. Hartzman, M. and Hutchinson, J.R., "Nonlinear Dynamics of Solids by the Finite Element Method," Computers and Structures, Vol. 2, 1972, pp. 47-77.

39. Mondkar, D.P. and Powell, G.H., "Finite Element Analysis of Non-Linear Static and Dynamic Response," Int. J. Num. Meth. Engineering, Vol. 11, 1977, pp. 499-520.

40. Mei, C., "Nonlinear Vibration of Beams by Matrix Displacement Method," AIAA Journal, Vol. 10, No. 3, 1972, pp. 355-357.

41. Mei, C., "Finite Element Displacement Method for Large Amplitude Free Flexural Vibrations of Beams and Plates," Computers and Structures, Vol. 3, 1973, pp. 163-174.

42. Mei, C., "Finite Element Analysis of Nonlinear Vibration of Beam Columns," AIAA Journal, Vol. 11, No. 1, 1973, pp. 115-117.

43. Mei, C. and Rogers, Jr., J.L., "Nastran Nonlinear Vibration Analysis of Beam and Frame Structures," NASA TM X-3278, September 1975, pp. 259-284.

44. Rao, G.V., Raju, K.K. and Raju, I.S., "Finite Element Formulation for the Large Amplitude Free Vibrations of Beams and Orthotropic Circular Plates," Computers and Structures, Vol. 6, 1976, pp. 169-172.

45. Rao, G.V., Raju, K.K. and Raju, I.S., "A Finite Element Formulation for Large Amplitude Flexural Vibrations of Thin Rectangular Plates," Computers and Structures, Vol. 6, 1976, pp. 163-167.

46. Mei, C., "A Finite-Element Approach for Nonlinear Panel Flutter," AIAA Journal, Vol. 15, No. 8, 1977, pp. 1107-1110.

47. Oden, J.T., Finite Elements of Nonlinear Continua, McGraw Hill, 1972, pp. 117-125, 279-283.

48. Rao, G.V. and Raju, P.C., "Post Buckling of Uniform Cantilever Columns - Galerkin Finite Element Solution," Engineering Fracture Mechanics, Vol. 9, 1977, pp. 1-4.

49. Nguyen, D.H. and Salinas, D., "Finite Element Solutions of Space - Time Nonlinear Reactor Dynamics," Nuclear Science and Engineering, Vol. 60, 1976, pp. 120-130.

50. Bismarck-Nasr, M.N., "A Finite Difference - Galerkin Finite Element Solution of Compressible Laminar Boundary-Layer Flows," Int. J. Num. Meth. Engineering, Vol. 12, 1978. pp. 711-719.

51. Fung, Y.C., Foundations of Solid Mechanics, Prentice Hall, 1965, pp. 338-339.

52. Mikhlin, S.G., Variational Methods in Mathematical Physics, Pergammon Press, Oxford, 1964.

53. Mikhlin, S.G., The Problem of the Minimum of a Quadratic Functional, Holden-Day, San Francisco, 1965.

54. Noor, M.A. and Whiteman, J.R., "Error Bounds for Finite Element Solutions of Mildly Nonlinear Boundary Value Problems," Numer. Math., Vol. 26, 1976, pp. 107-116.

55. Kornecki, A., "On Application of Galerkin's Method to Non-Self-Adjoint Problems," Technion-Israel Institute of Technology, Department of Agricultural Engineering, Report No. 101, August 1970.

56. Rosen, A. and Friedmann, P., "Nonlinear Equations of Equilibrium for Elastic Helicopter or Wind Turbine Blades Undergoing Moderate Deformation," University of California, Los Angeles, School of Engineering and Applied Science Report, UCLA-ENG-7718, January 1977, (Revised June 1977), also NASA CR-159478, December 1978.

57. Powers, R.W., "A Study of Several Approximation Concepts in Rotary-Wing Aeroelasticity," M.S. Thesis, Mechanics and Structures Department, University of California, Los Angeles, 1976.

58. Bathe, K.-J. and Wilson, E.L., Numerical Methods in Finite Element Analysis, Prentice Hall, 1976, pp. 127-130.

59. Carnegie, W., Thomas, J. and Dokumaci, E., "An Improved Method of Matrix Displacement Analysis in Vibration Problems," The Aeronautical Quarterly, Nov. 1969, pp. 321-332.

60. Thomas, J. and Dokumaci, E., "Improved Finite Elements for Vibration Analysis of Tapered Beams," The Aeronautical Quarterly, Vol. 24, 1973, pp. 39-46.

61. Friedmann, P. and Shamie, J., "Aeroelastic Stability of Trimmed Helicopter Blades in Forward Flight," Vertica, Vol. 1, 1977, pp. 189-211.

62. Kottapalli, S.B.R., Friedmann, P.P., and Rosen, A., "Aeroelastic Stability and Response of Horizontal Axis Wind Turbine Blades," AIAA Journal, Vol. 17, No. 12, Dec. 1979, pp. 1381-1389.

63. Friedmann, P.P. and Kottapalli, S.B.R., "Rotor Blade Aeroelastic Stability and Response in Forward Flight," AIAA Paper 80-0698, to be presented at the 21-st AIAA/ASME/ASCE/AHS Structures, Structural Dynamics and Materials Conference, May 12-14, 1980, Seattle, Washington. (A more detailed version to appear as UCLA School of Engineering and Applied Science Report.)

64. Roberts, S.M. and Shipman, J.S., Two Point Boundary Value Problems: Shooting Methods, American Elsevier, New York, 1972, pp. 87-109.

65. Urabe, M. "Galerkin's Procedure for Nonlinear Periodic Systems," Archive for Rational Mechanics and Analysis, Vol. 20, 1965, pp. 120-152.

66. Meirovitch, L., Methods of Analytical Dynamics, McGraw-Hill, New York, 1970, pp. 264-270.

67. Friedmann, P., Hammond, C.E., and Woo, T., "Efficient Numerical Treatment of Periodic Systems with Application to Stability Problems," Int. J. Num. Meth. Engineering, Vol. 11, 1977, pp. 1117-1136.

68. Ormiston, R.A. and Hodges, D.H., "Linear Flap-Lag Dynamics of Hingeless Helicopter Rotor Blades in Hover," Journal of the American Helicopter Society, Vol. 17, No. 2, April 1972, pp. 2-14.

69. Friedmann, P. and Straub, F., "Application of the Finite Element Method to Rotary-Wing Aeroelasticity," Proceedings of the Fourth European Rotorcraft and Powered Lift Aircraft Forum, Paper No. 24,

Stresa, Italy, September 1978; also published in Journal of the American Helicopter Society, Vol. 25, No. 1, January 1980, pp. 36-44.

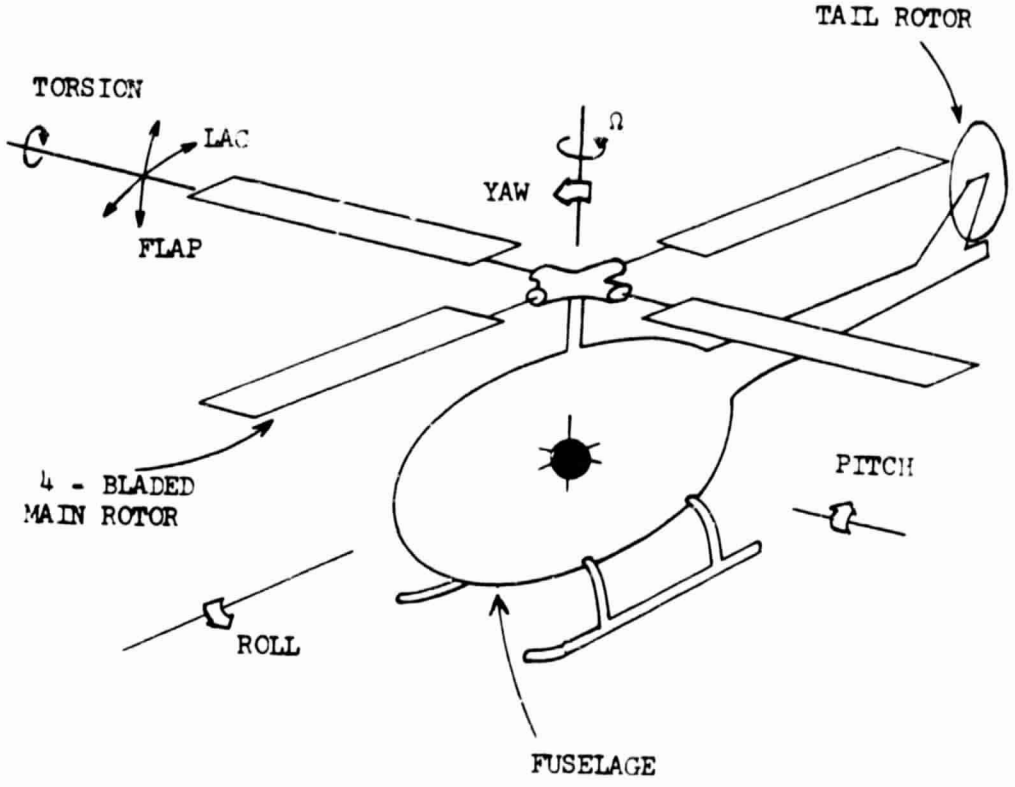

FIGURE 1: Rotor/Fuselage Model

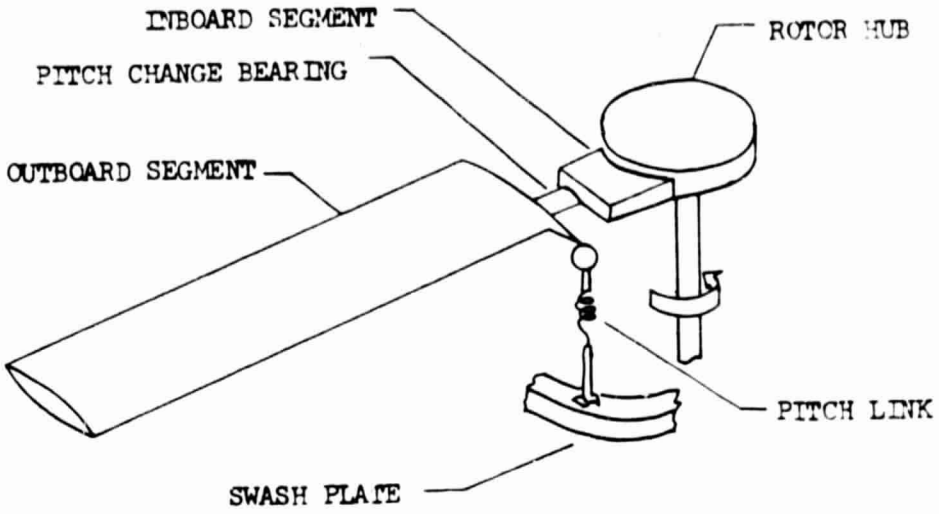

(a)

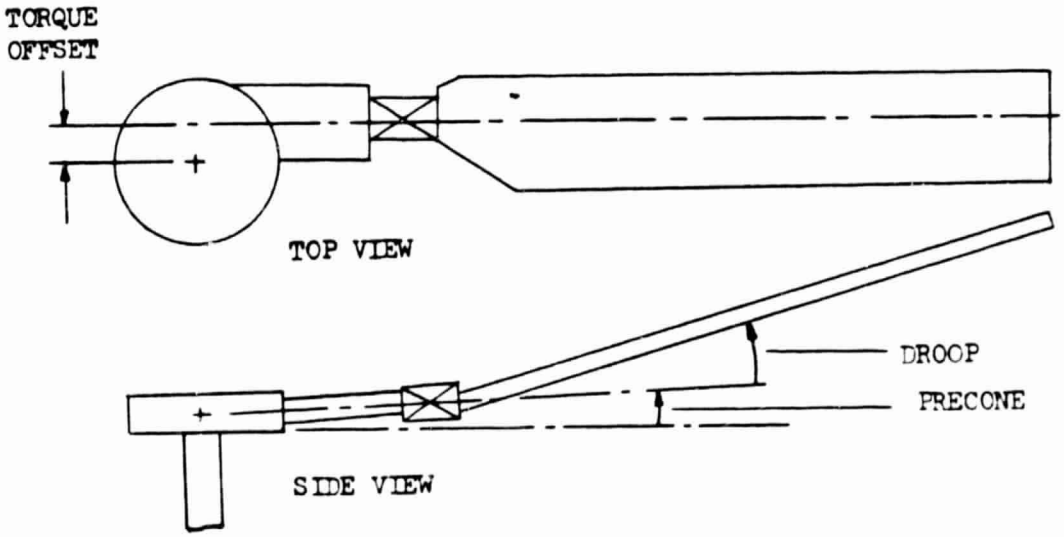

(b)

FIGURE 2: Elements and Configuration Parameters of a Hingeless Blade

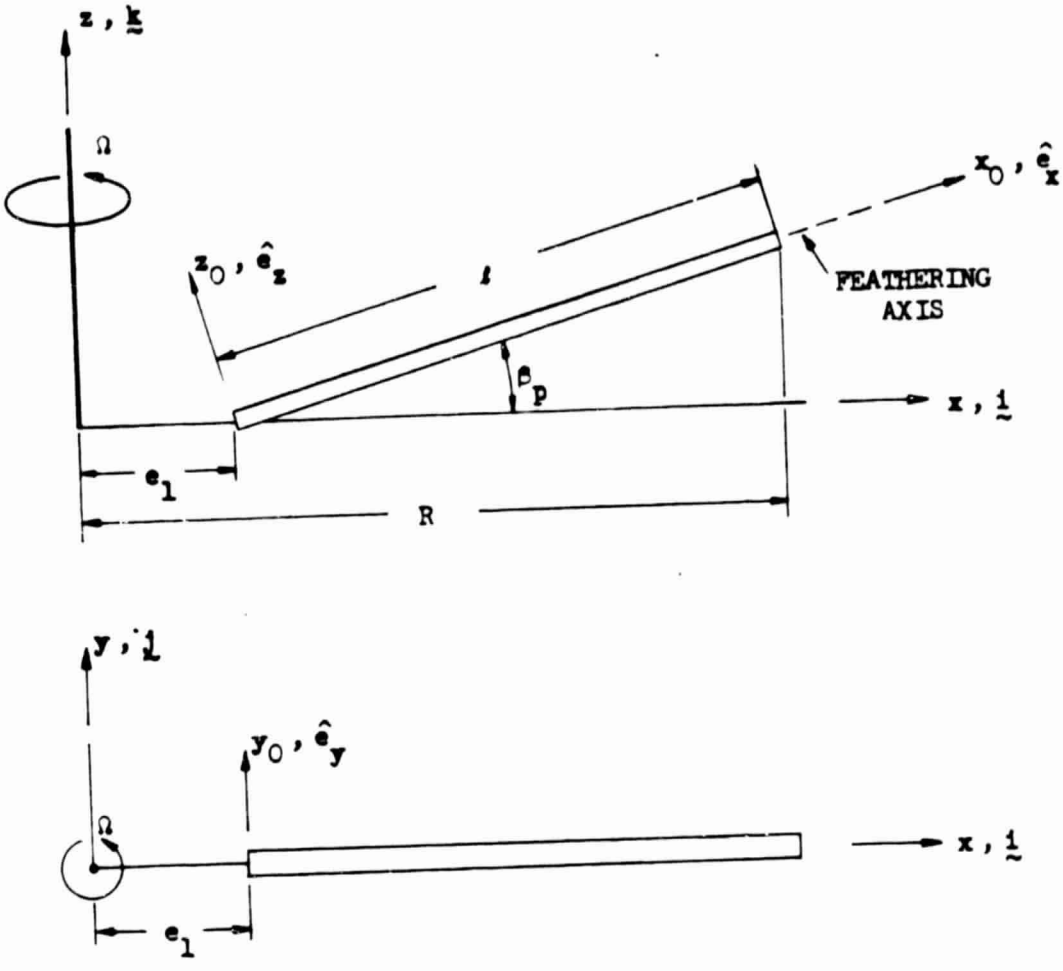

FIGURE 3a: Typical Description of the Undeformed Blade in the Rotating System x , y , z ($\underset{\sim}{i}$, $\underset{\sim}{j}$, $\underset{\sim}{k}$)

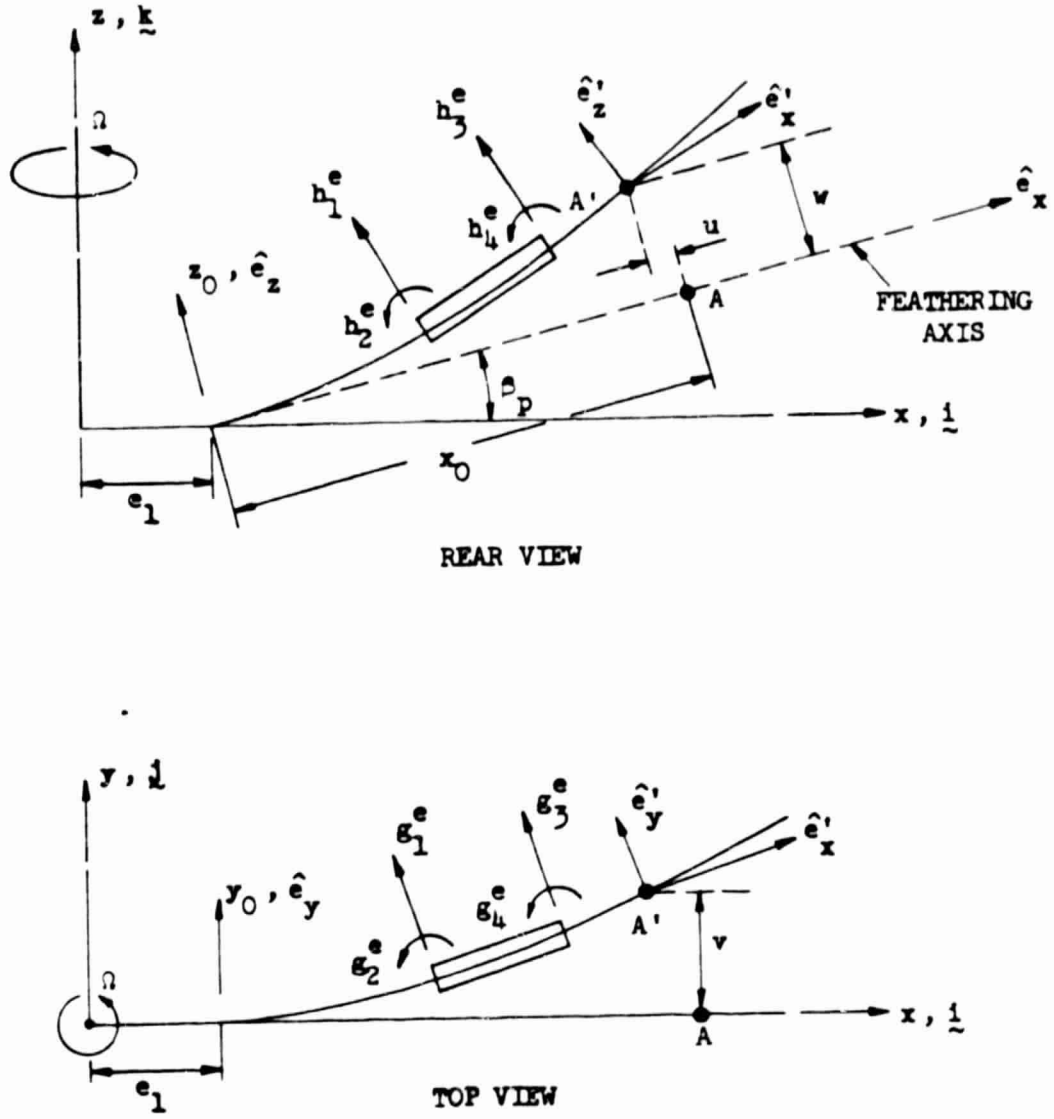

FIGURE 3b: Geometry of the Elastic Axis of the Deformed Blade and Schematic Description of the Finite Element Model for Flap and Lag

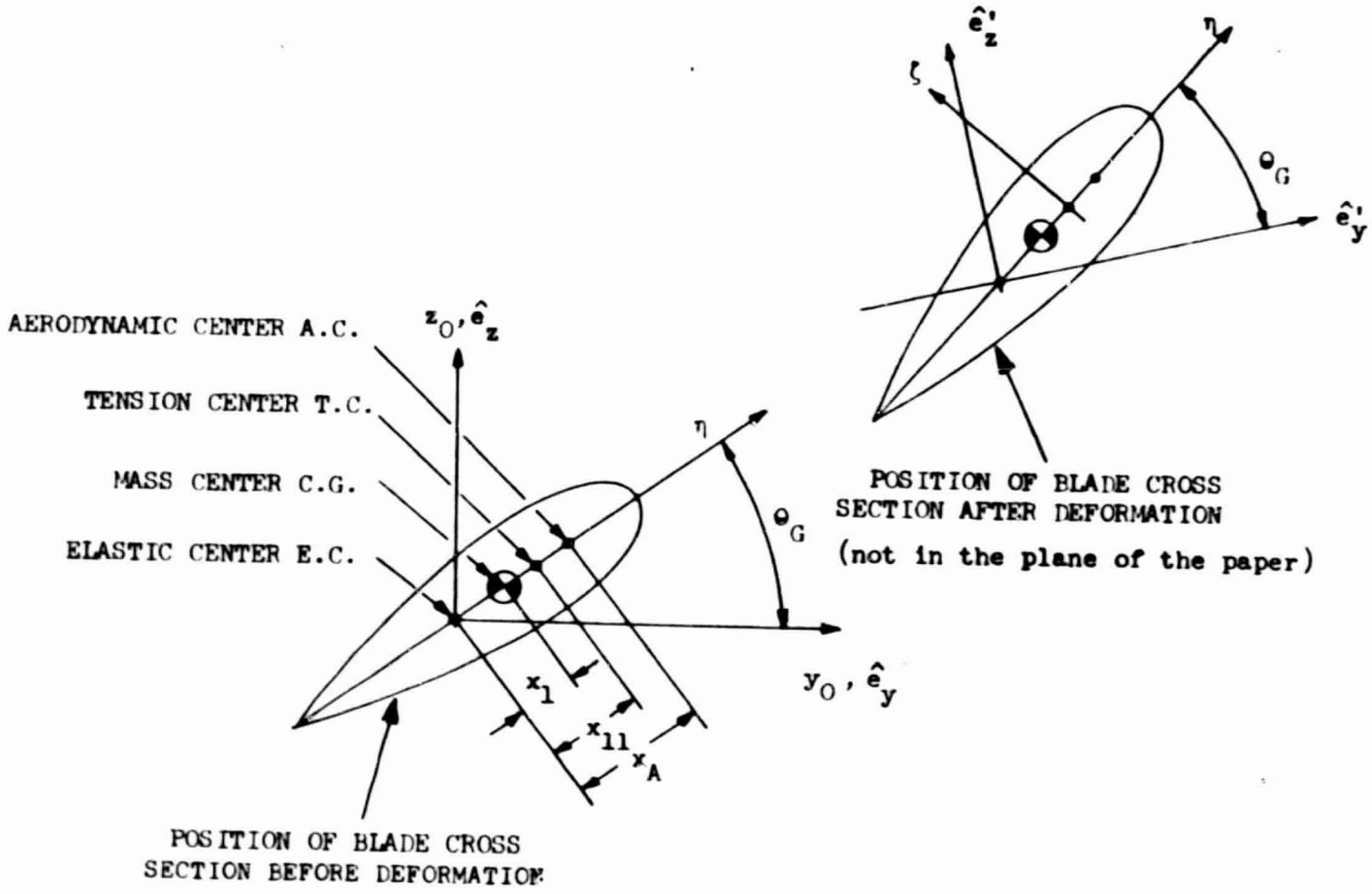

FIGURE 4: Blade Cross Section Positions Before and After Deformation

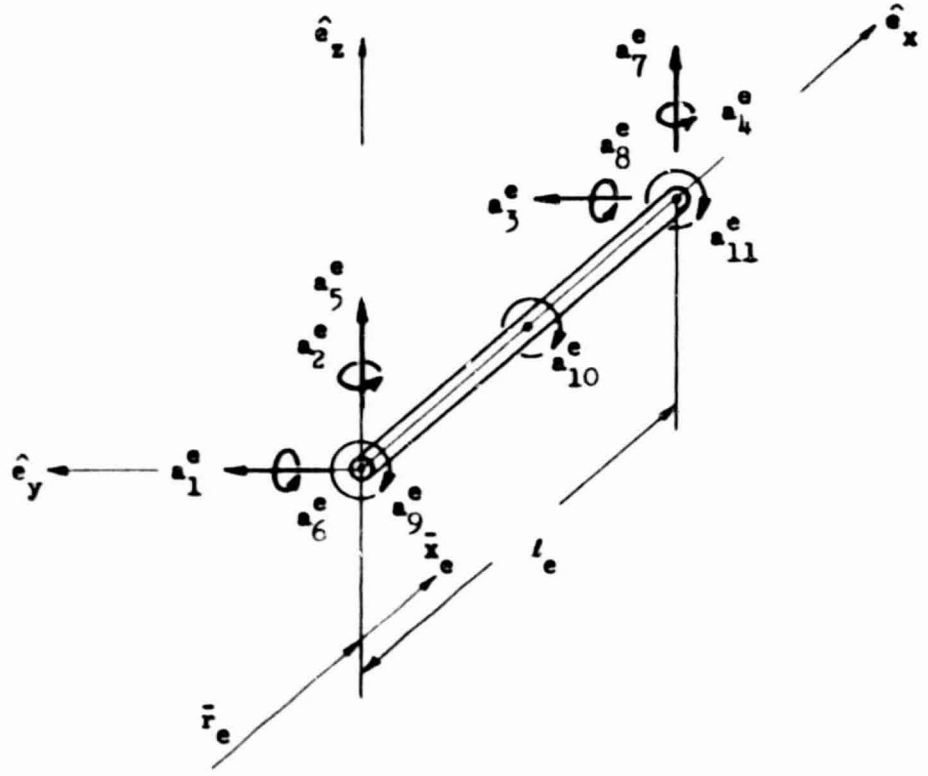

$$\underset{\sim}{h}^e = \begin{Bmatrix} a^e_1 \\ a^e_2 \\ a^e_3 \\ a^e_4 \end{Bmatrix}$$

$$\underset{\sim}{g}^e = \begin{Bmatrix} a^e_5 \\ a^e_6 \\ a^e_7 \\ a^e_8 \end{Bmatrix}$$

$$\underset{\sim}{f}^e = \begin{Bmatrix} a^e_9 \\ a^e_{10} \\ a^e_{11} \end{Bmatrix}$$

FIGURE 5: Coupled Lag-Flap-Torsion Element in the Undeformed Coordinate System

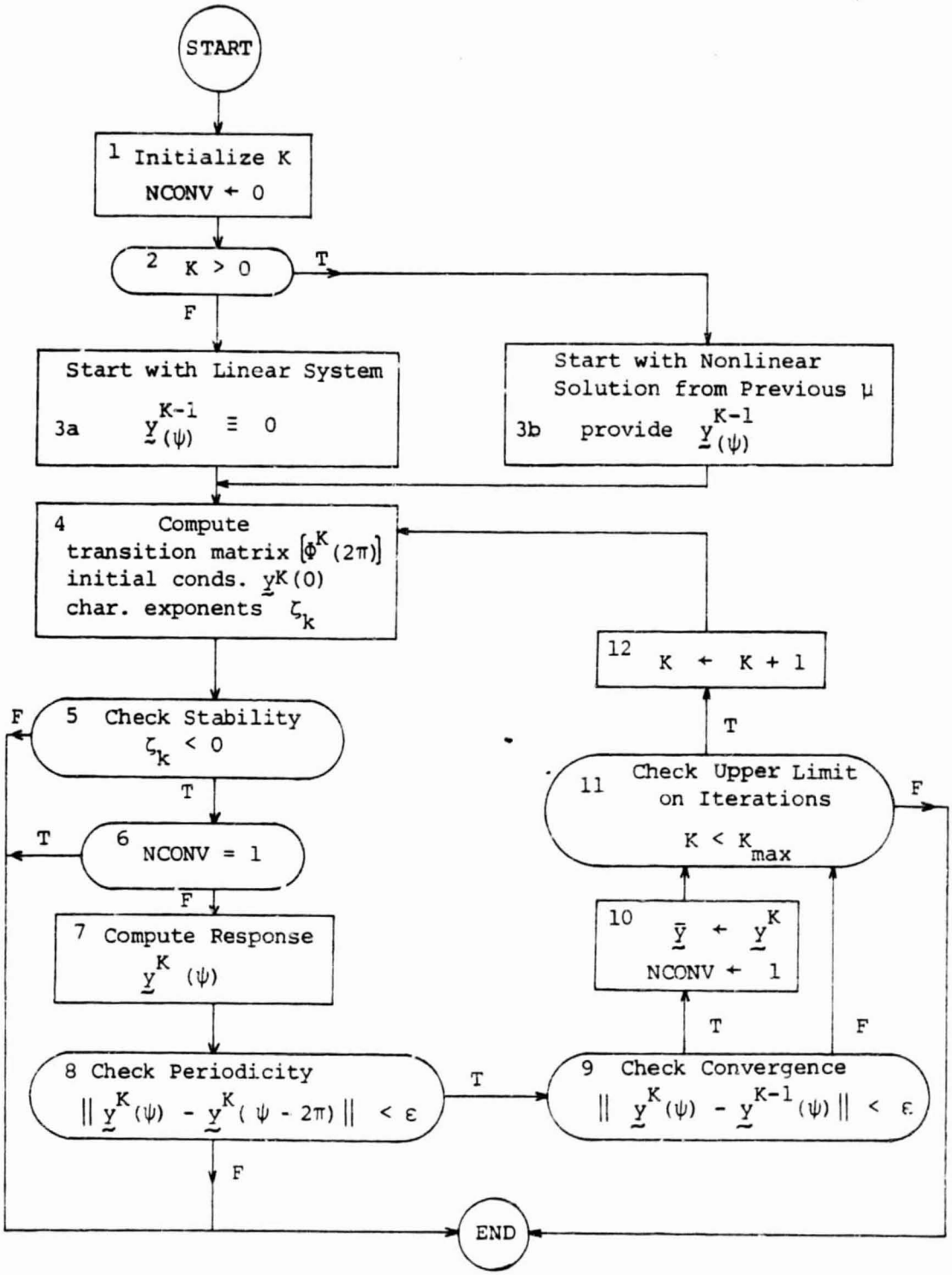

FIGURE 6: Flow Chart Illustrating the Stability and Response Calculations of the Nonlinear, Periodic Aeroelastic System

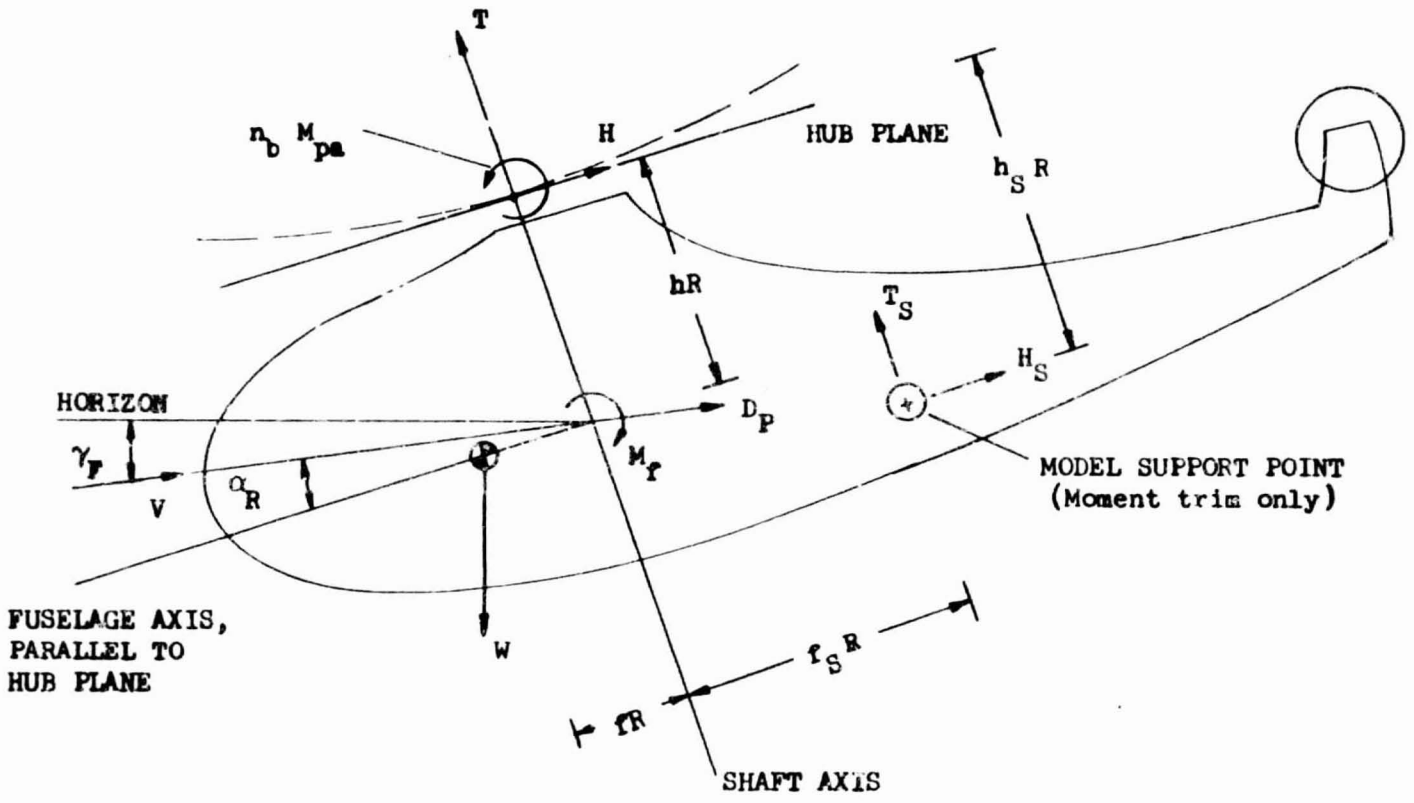

FIGURE 7: Configuration for Trim Procedures

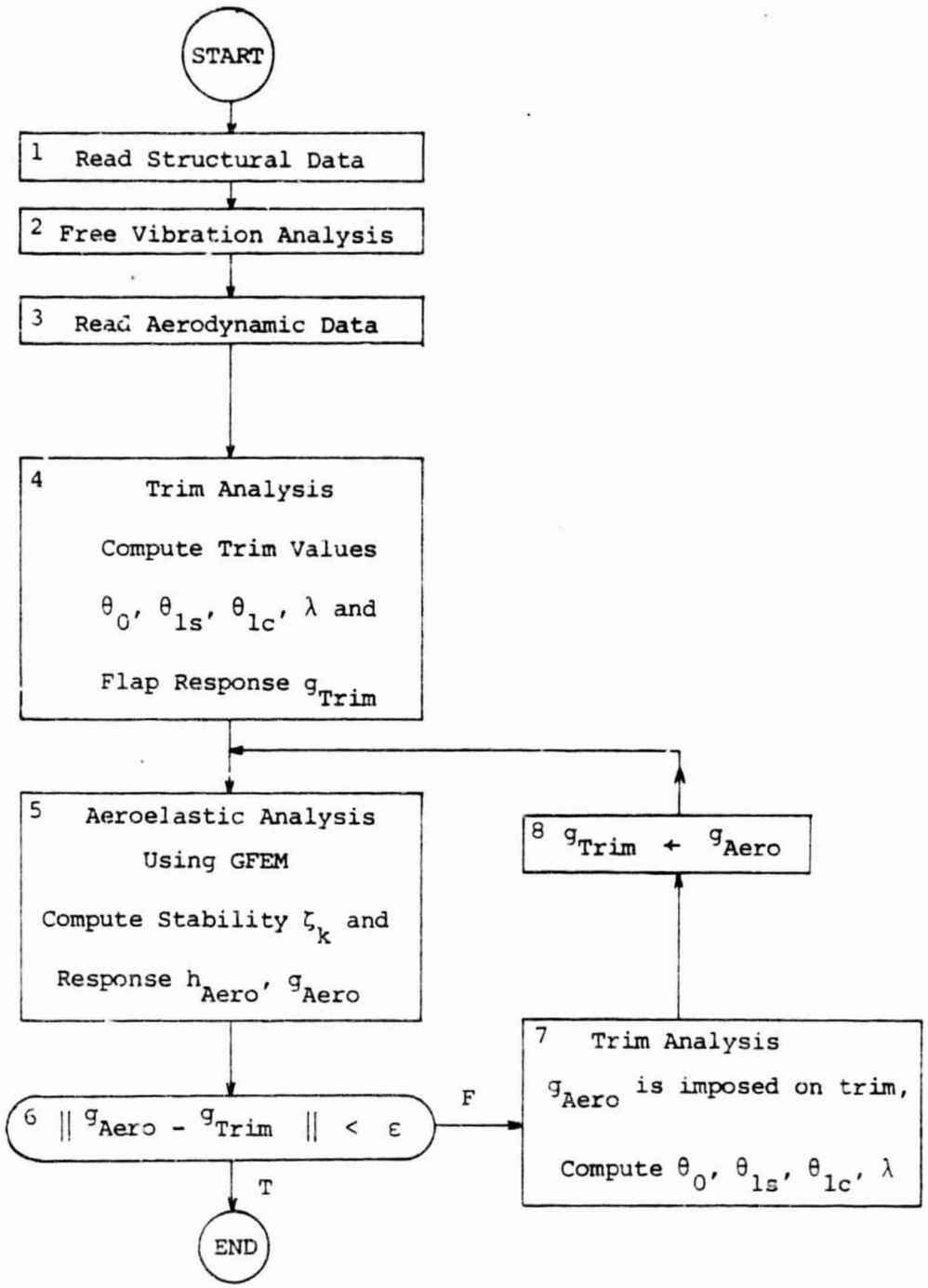

FIGURE 8: Aeroelastic Analysis in Forward Flight with Trim Iterations

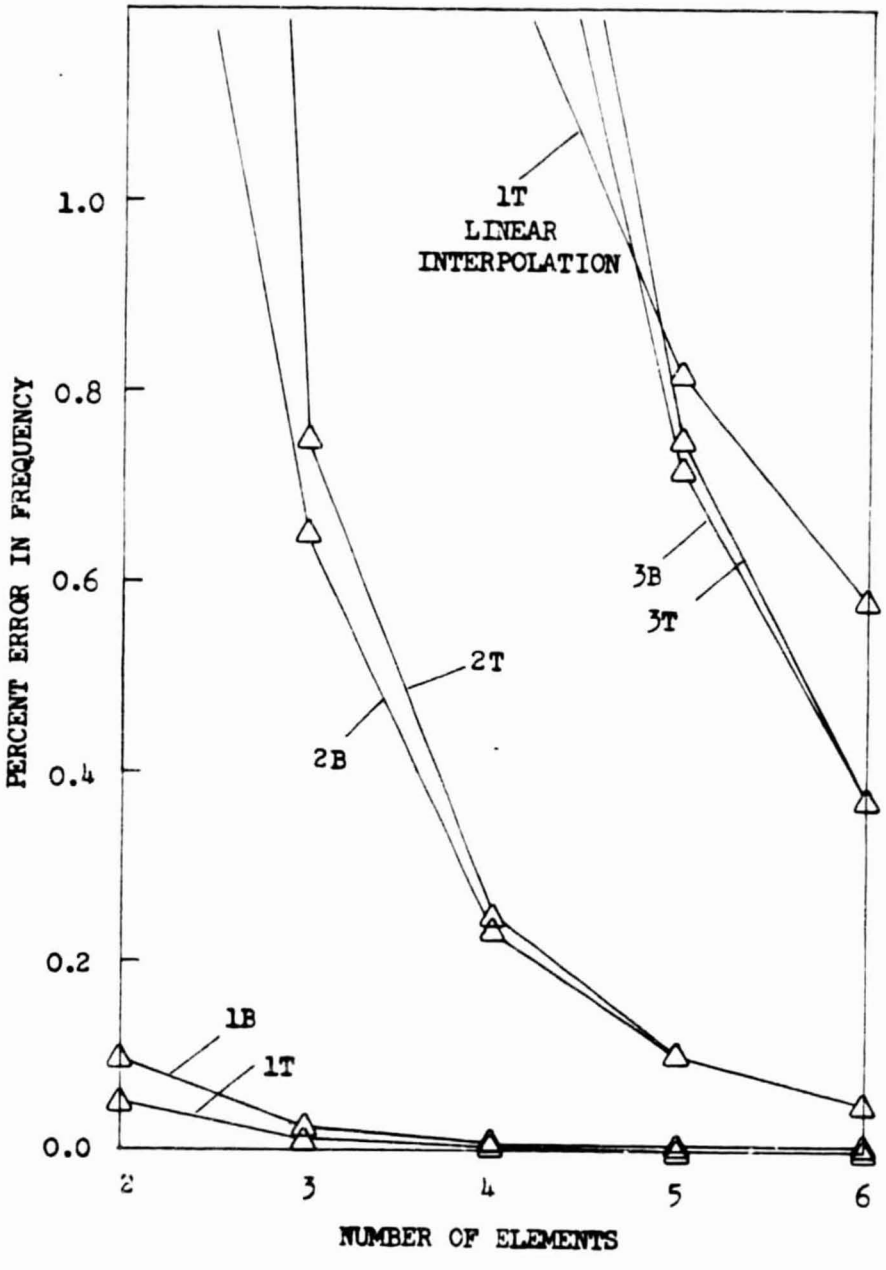

FIGURE 9: Accuracy of the First, Second and Third Bending and Torsion Frequency Versus Number of Elements for a Nonrotating Uniform Beam

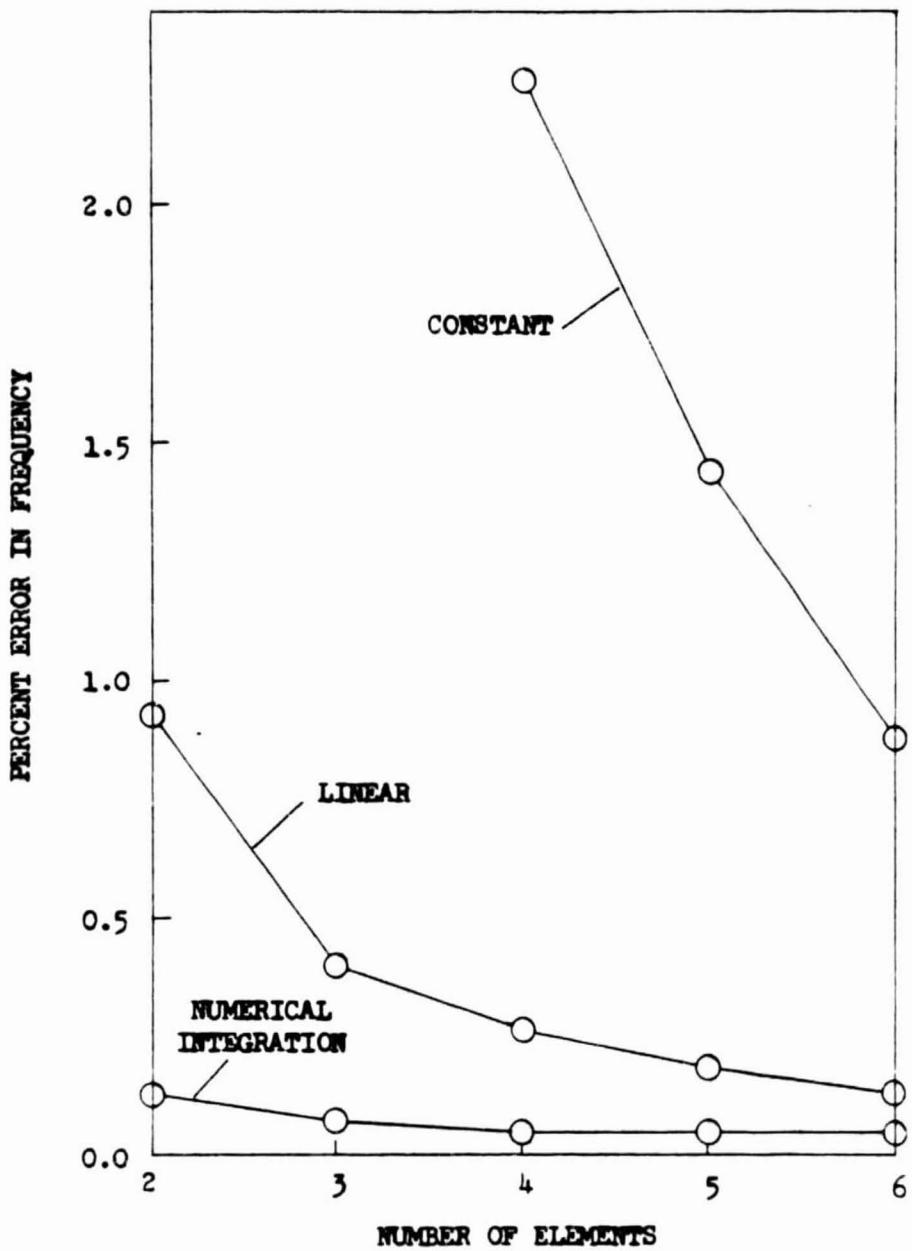

FIGURE 10: Finite Element Modeling of a Tapered, Nonrotating Beam (Mass and Stiffness Within the Element are Modeled as Constant, Linear and Using Numerical Integration). Results are for the Lowest Bending Frequency.

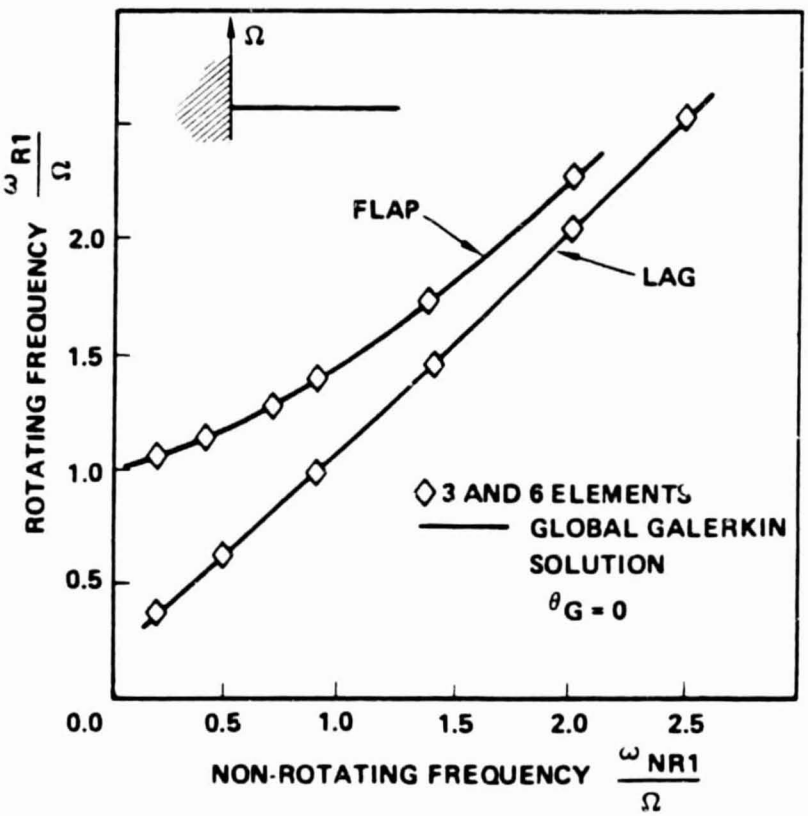

FIGURE 11: Comparison of the Methods in Calculating Fundamental Flap and Lag Frequencies of a Rotating Blade

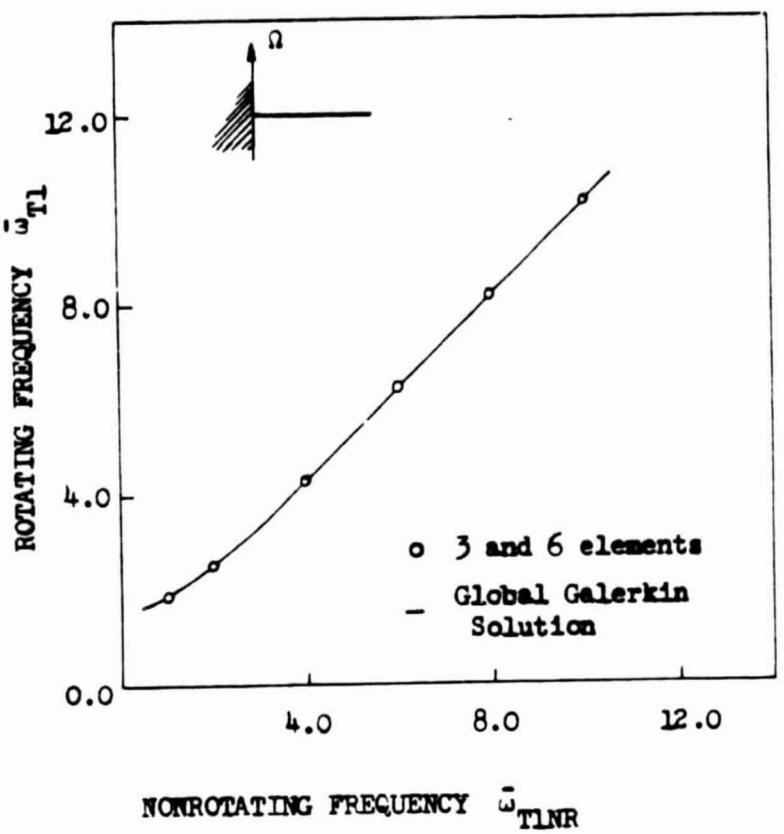

FIGURE 12: Comparison of the Methods in Calculating Fundamental Torsion Frequencies of a Rotating Blade

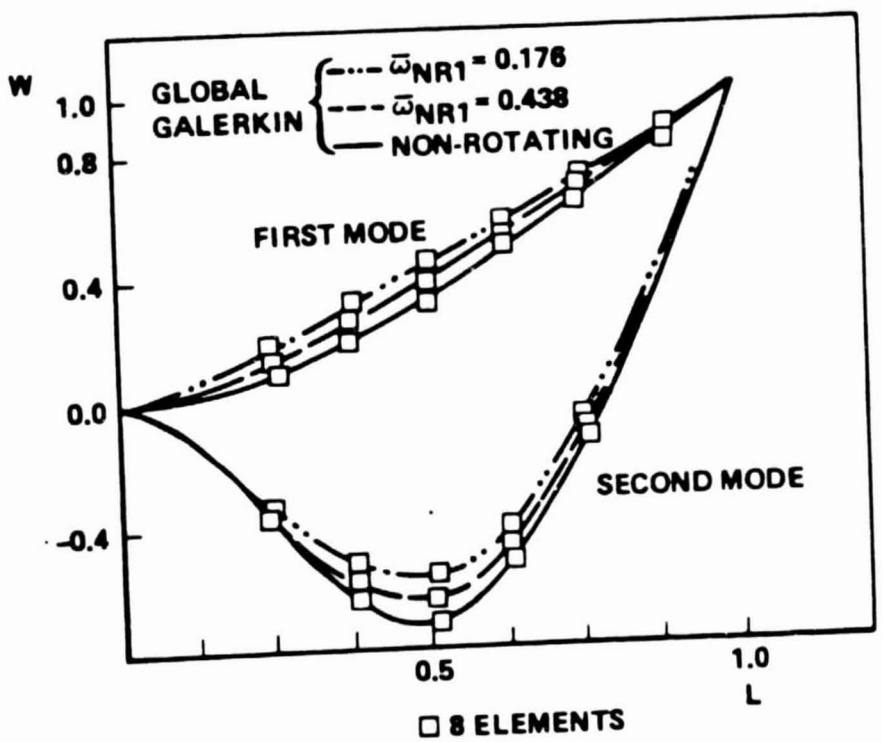

FIGURE 13: Comparison of the Methods in Calculating First and Second Flapwise Mode Shapes of a Rotating Beam

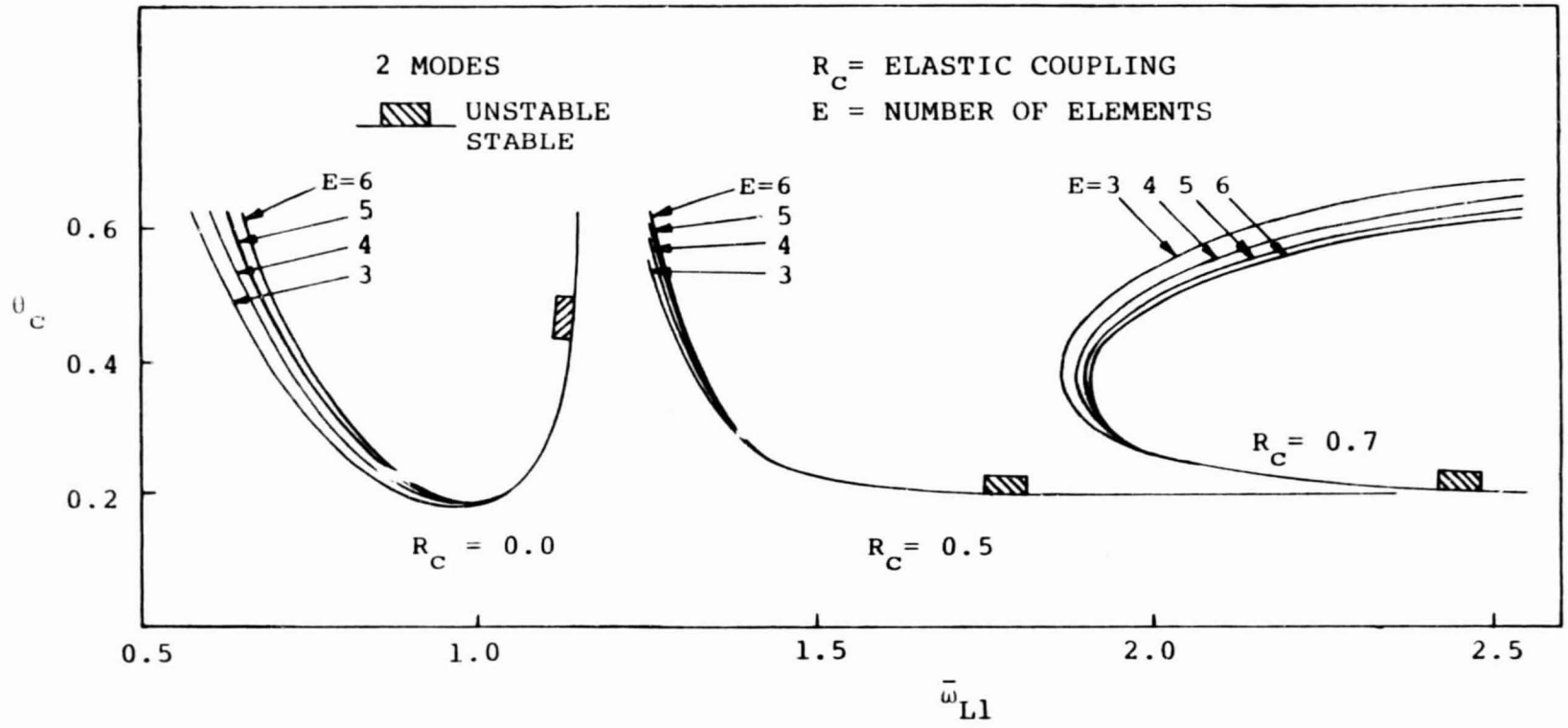

FIGURE 14: Convergence of the Flap-Lag Stability Boundaries When the Number of Elements is Changed*

(σ = 0.05; γ = 5.0; $\bar{\omega}_{F1}$= 1.0689)

* θ_c is critical pitch setting at which linearized system becomes unstable

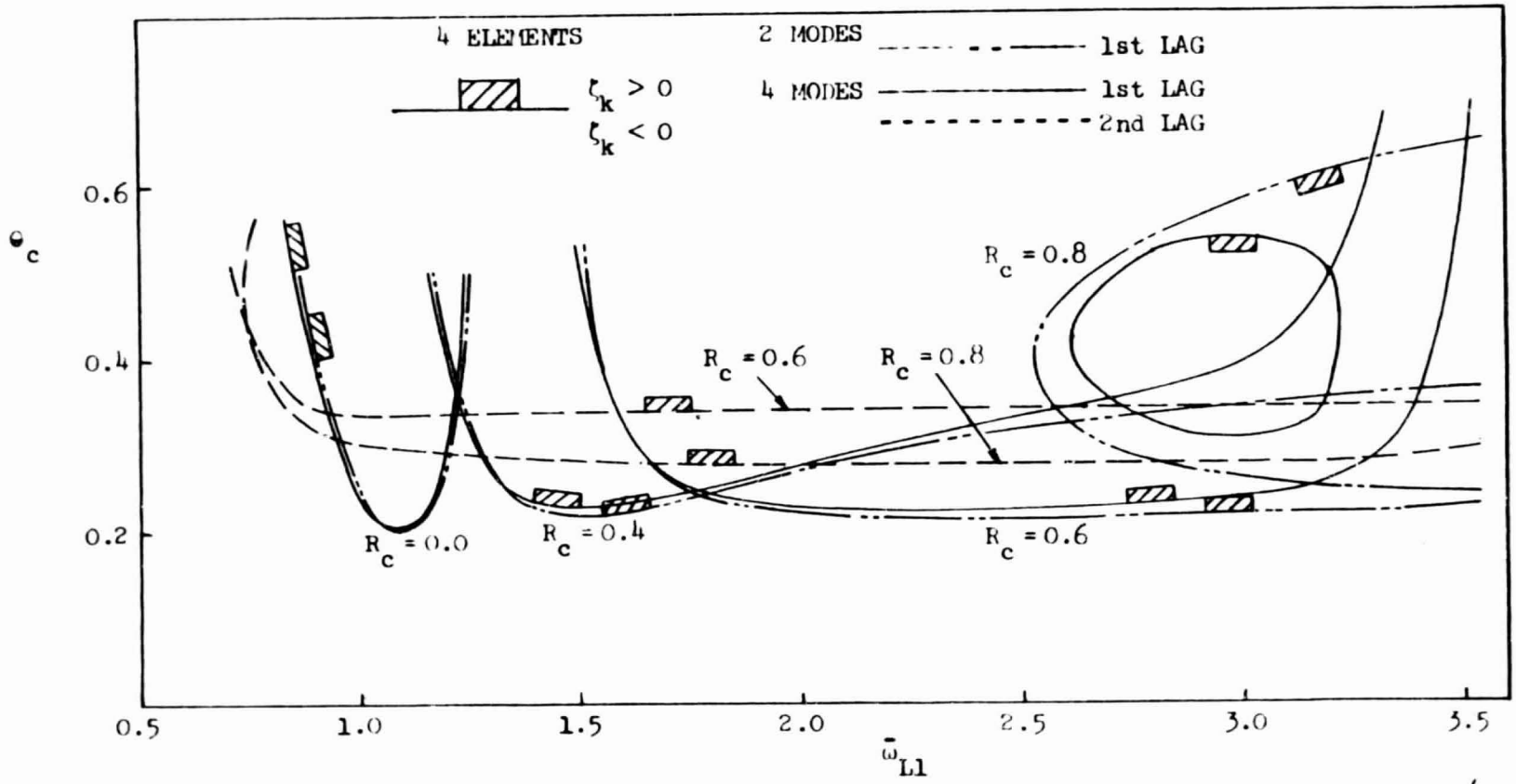

FIGURE 15: Convergence of Flap-Lag Stability Boundaries When the Number of Modes is Changed[†] ($\sigma = 0.10$; $\gamma = 5.0$; $\bar{\omega}_{F1} = 1.15$)

[†]Curves represent points at which real part of eigenvalues associated with predominantly lag modes are zero.

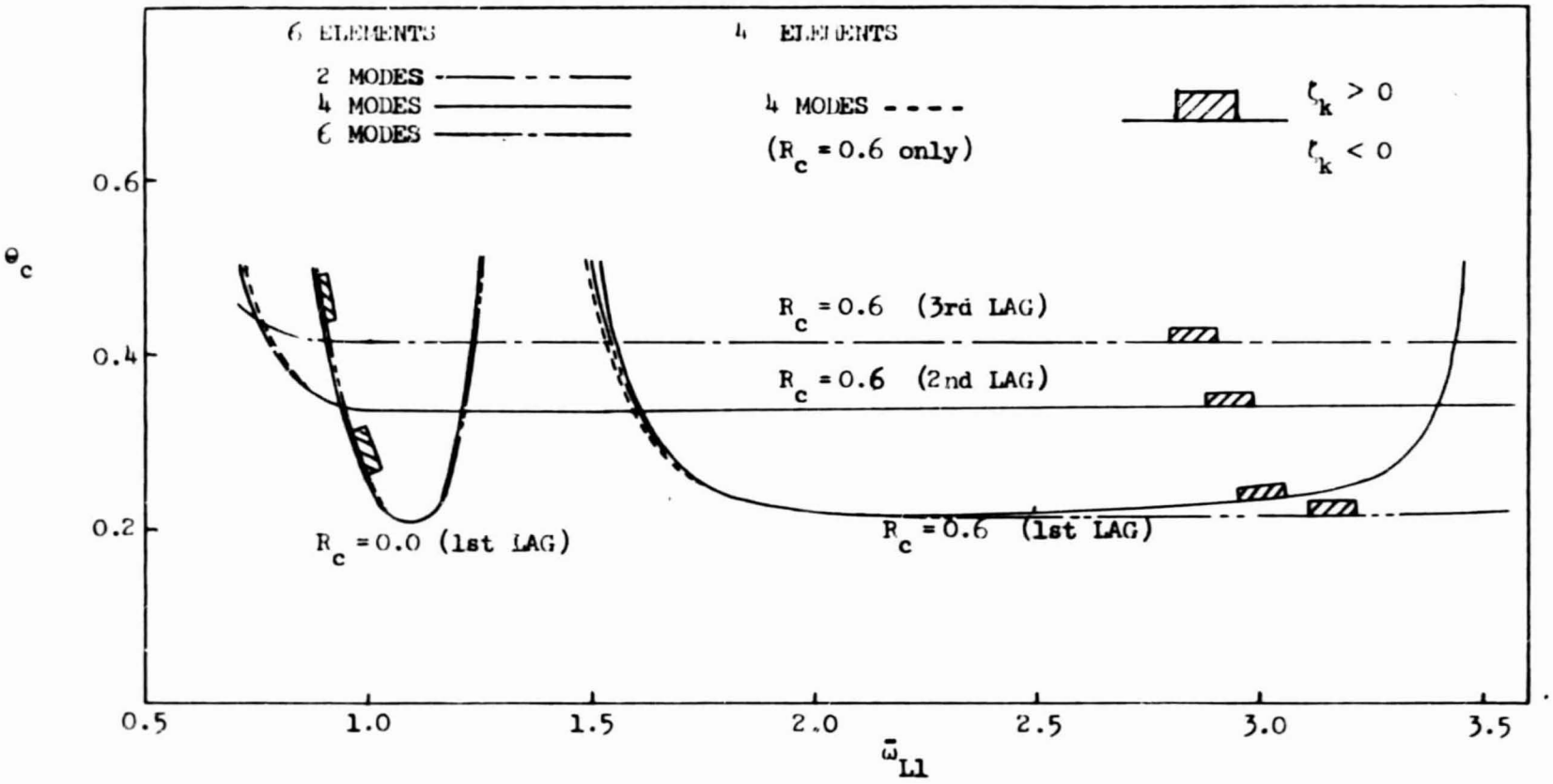

FIGURE 16: Convergence of Flap-Lag Stability Boundaries When the Number of Modes and Elements is Changed[7]

(σ = 0.10; γ = 5.0; $\bar{\omega}_{F1}$ = 1.15)

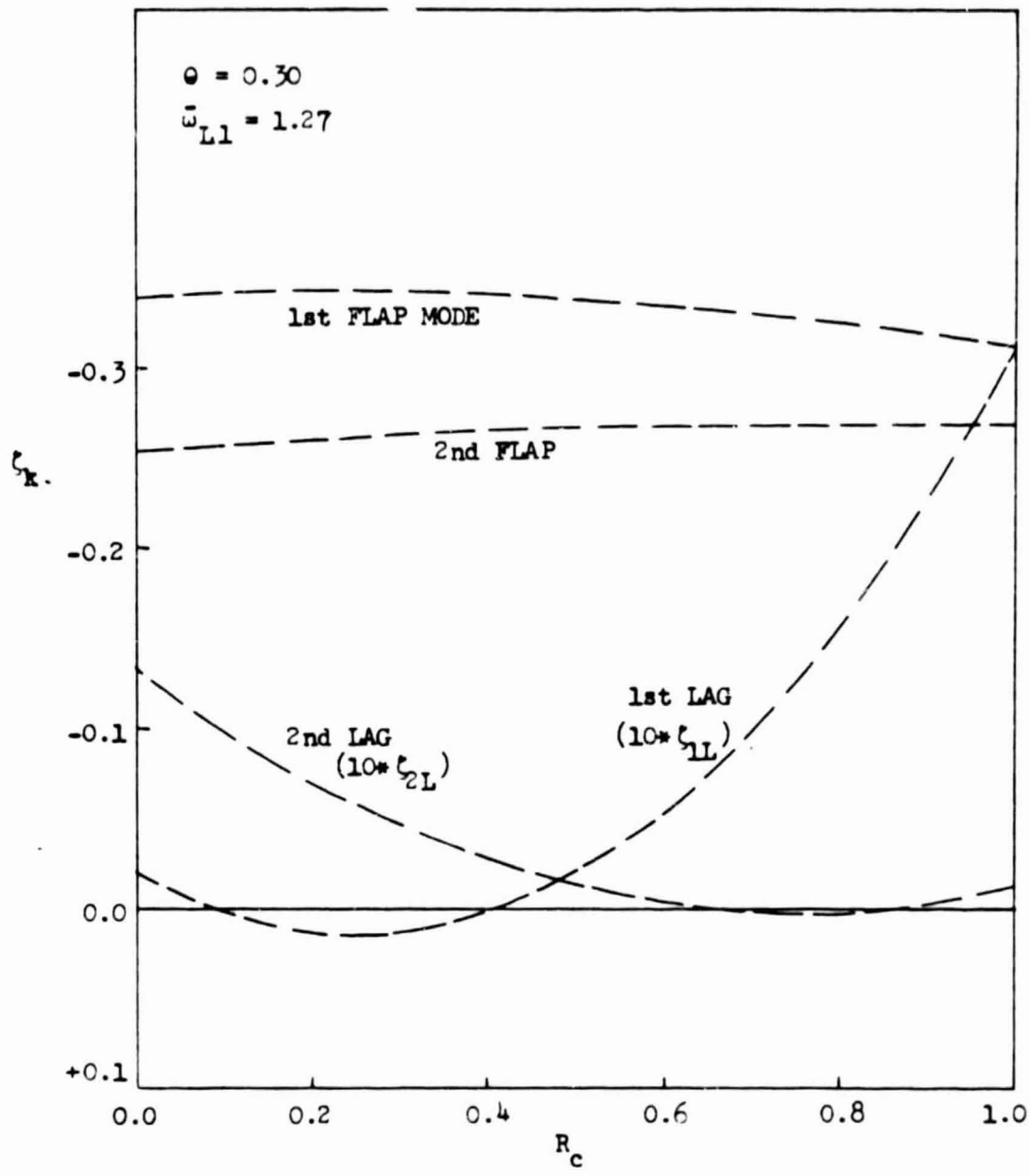

FIGURE 17: Real Part of Eigenvalues (Eq. 3.23) as a Function of Elastic Coupling

(E = 4, M = 4, σ = 0.10, γ = 5.0, $\bar{\omega}_{F1}$ = 1.15)

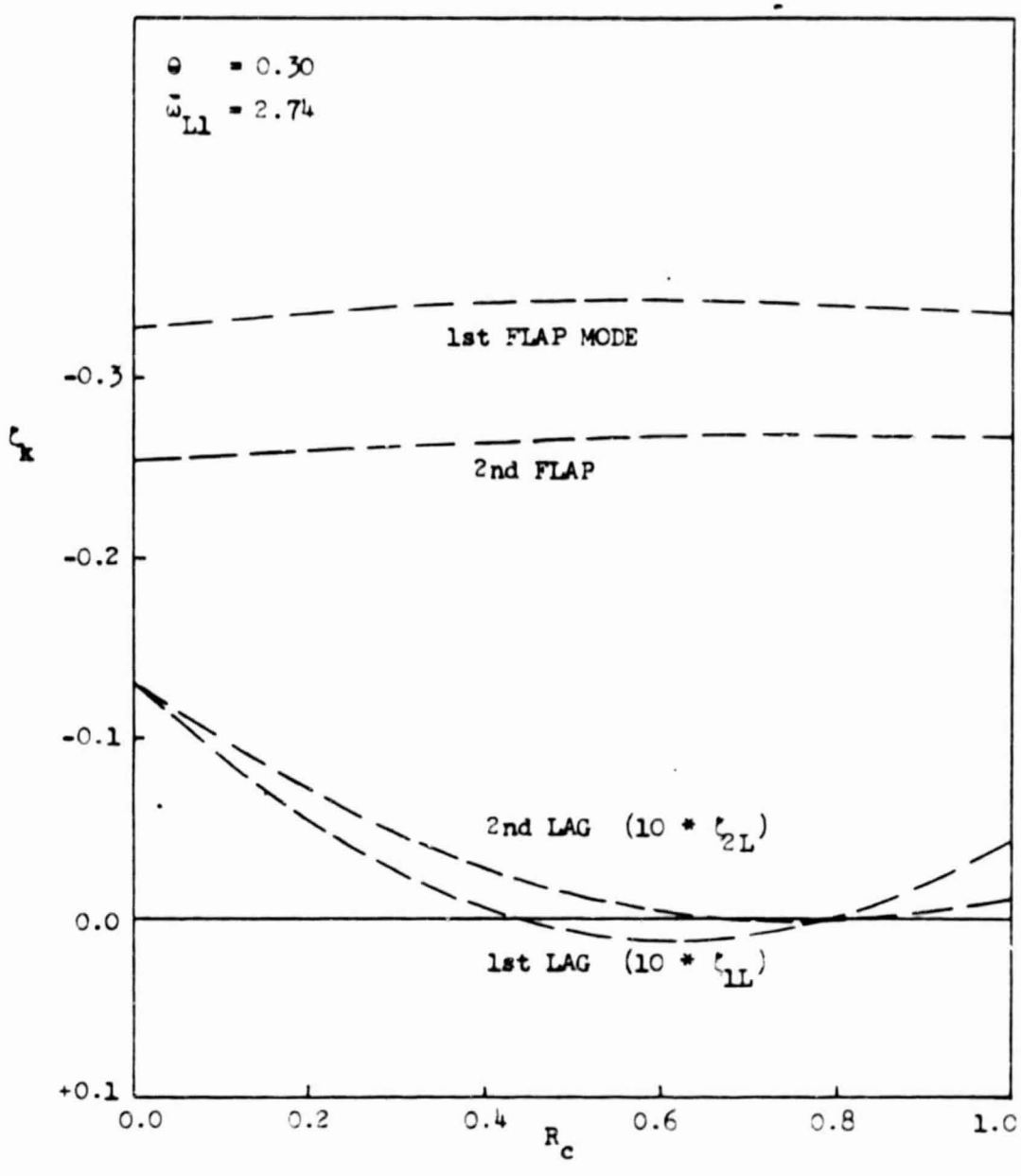

FIGURE 18: Real Part of Eigenvalues (Eq. 3.23) as a Function of Elastic Coupling

(E = 4; M = 4: σ = 0.10: γ = 5.0: $\bar{\omega}_{F1}$ = 1.15)

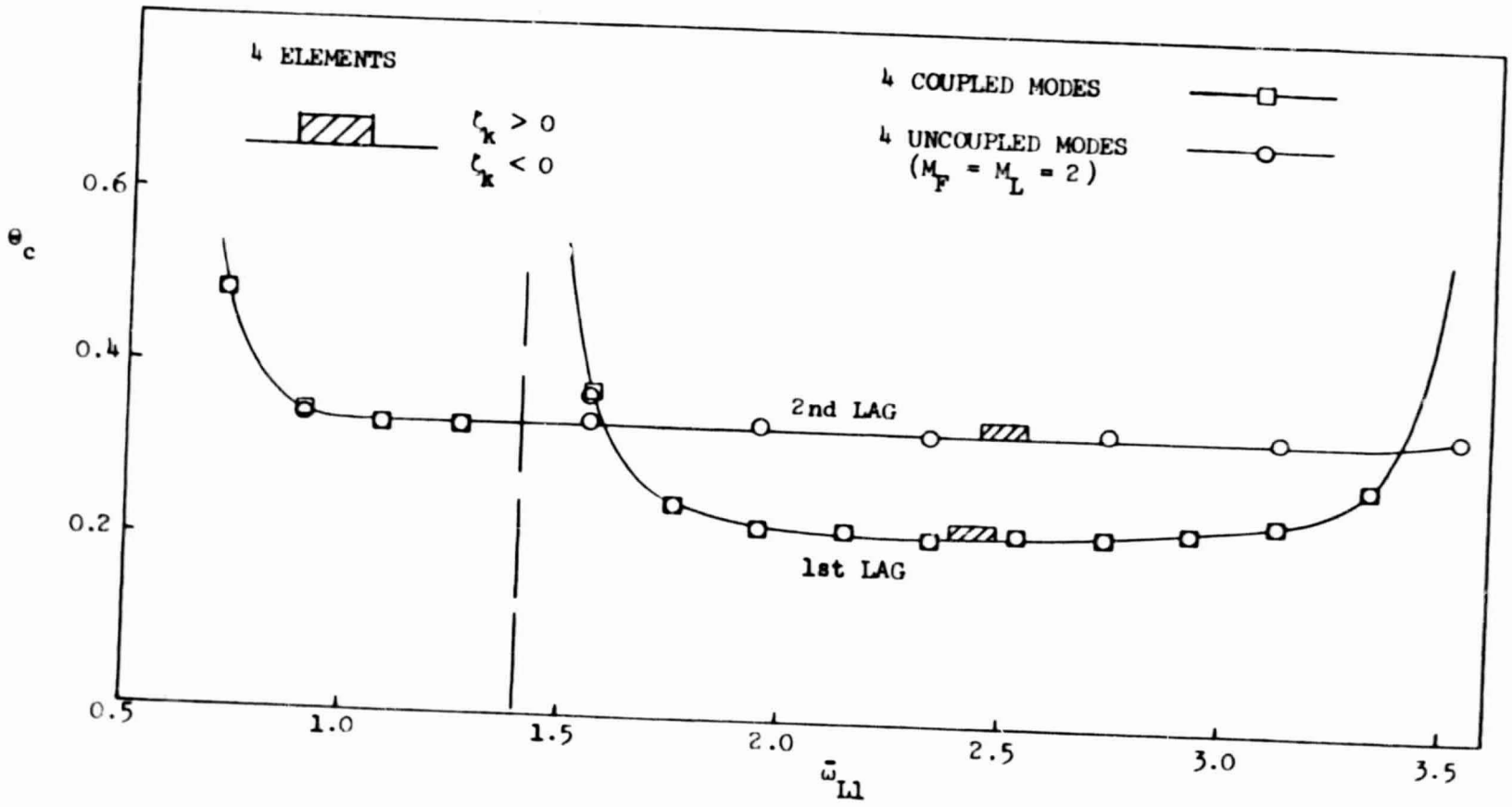

FIGURE 19: Comparison of Flap-Lag Stability Boundaries Using Uncoupled Versus Coupled Modes* ($R_c = 0.6$; $\sigma = 0.10$; $\gamma = 5.0$; $\bar{\omega}_{F1} = 1.15$)

*For $\bar{\omega}_{L1} > 1.4$ the third flap mode is used in place of the second lag mode in the coupled mode analysis.

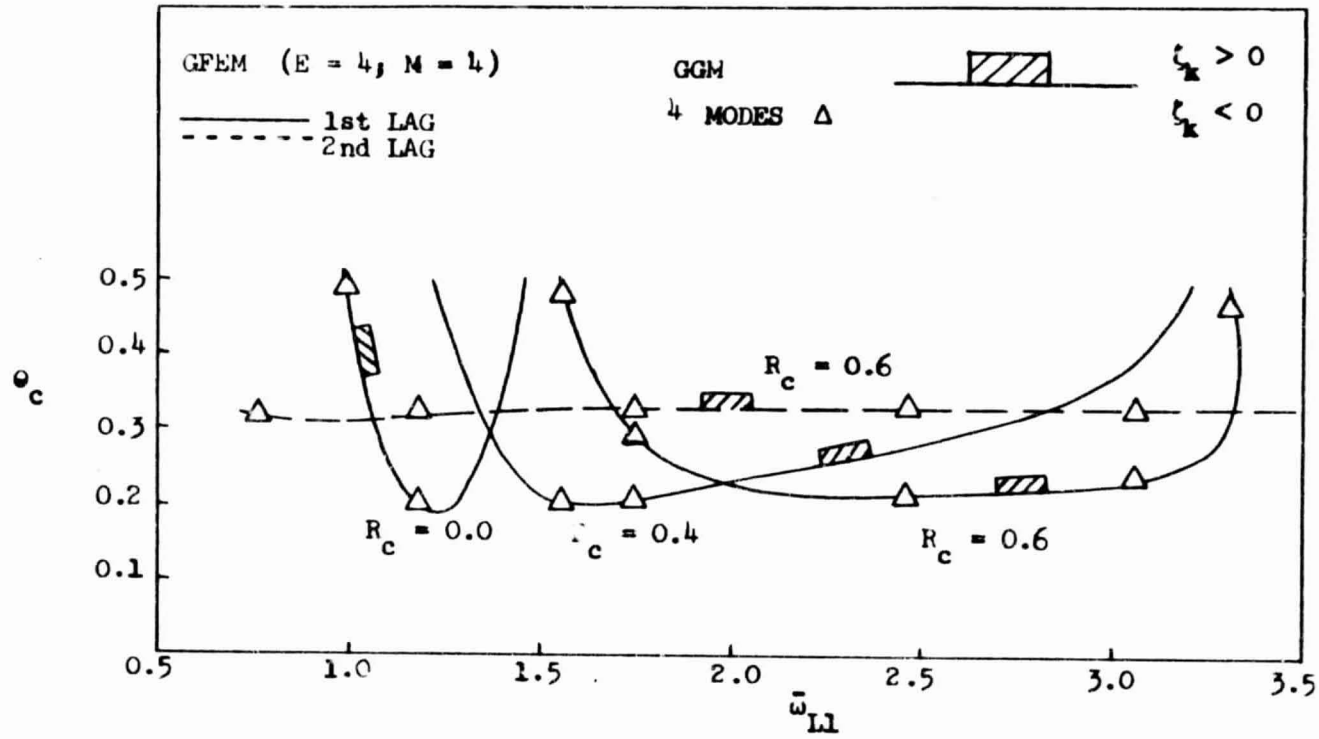

FIGURE 20: Comparison of Flap-Lag Stability Boundaries When Using GFEM Versus Global Galerkin Method (GGM)[#]

($\sigma = 0.10$, $\gamma = 5.0$, $\bar{\omega}_{Fl} = 1.15$)

[#]Eqs. of Motion are those from Ref. [57] without torsion.

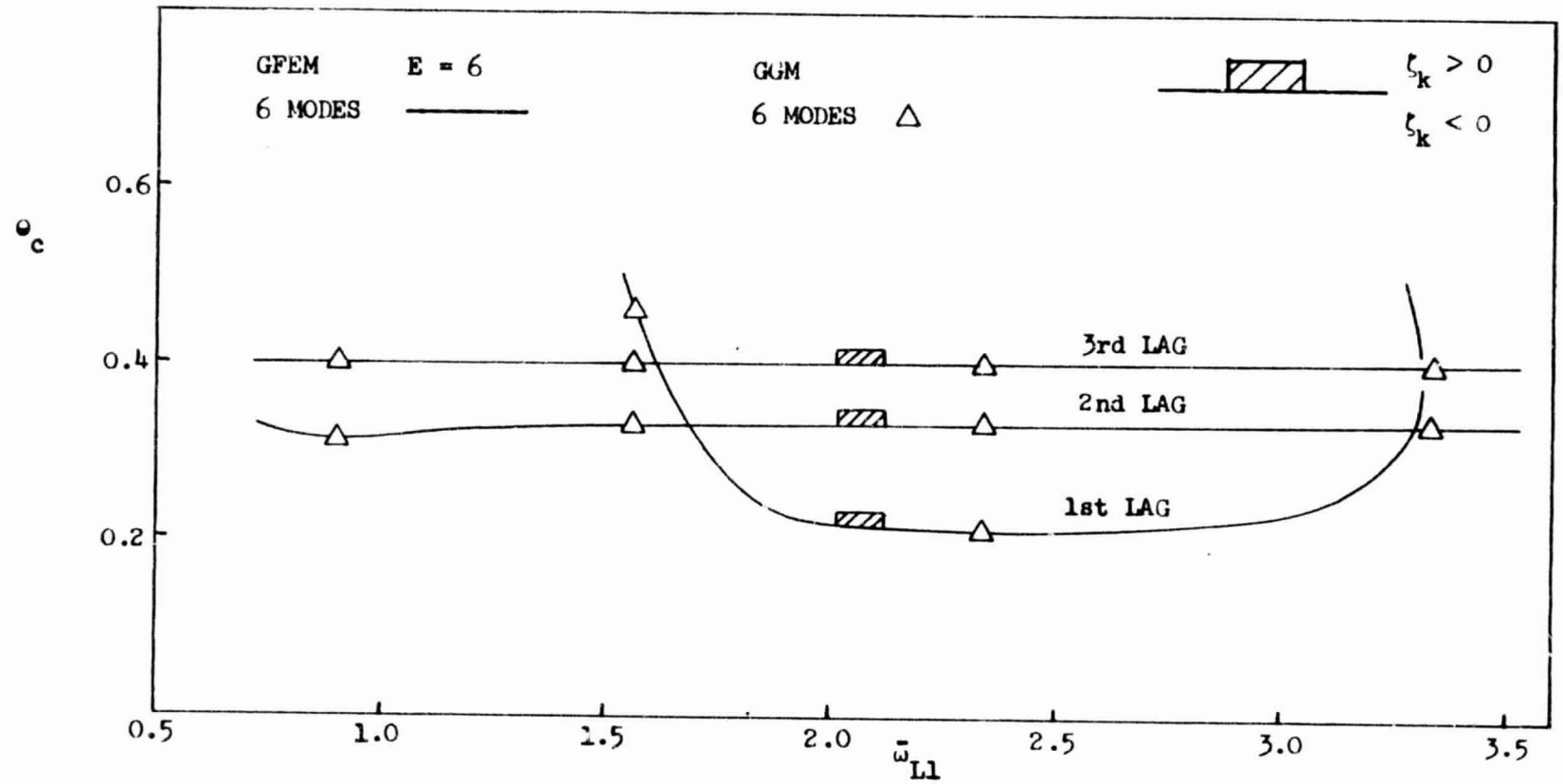

FIGURE 21: Comparison of Flap-Lag Stability Boundaries When Using the GFEM Versus the Global Galerkin Method (GGM)

($R_c = 0.6$, $\sigma = 0.10$; $\gamma = 5.0$; $\bar{\omega}_{F1} = 1.15$)

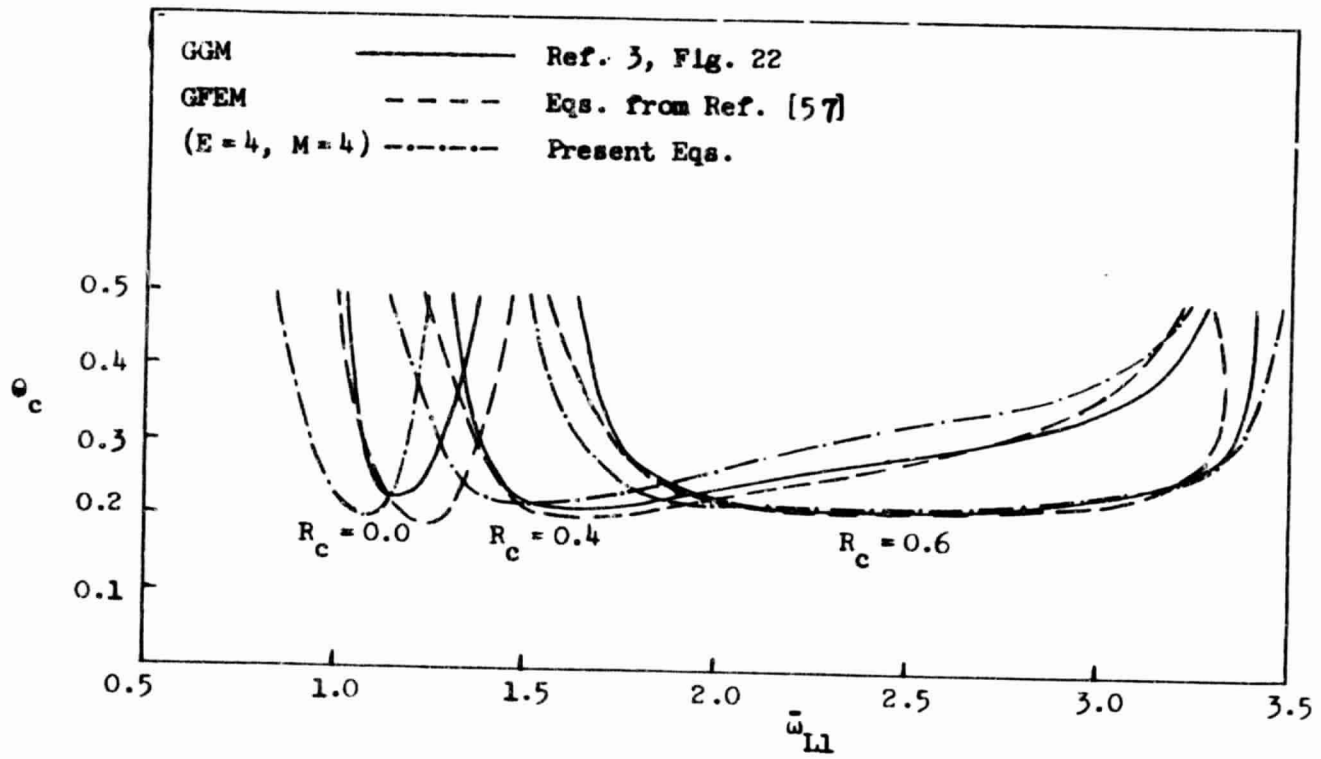

FIGURE 22: Comparison of Results from Different Sets of Nonlinear Equations of Motion (σ = 0.10, γ = 5.0, $\bar{\omega}_{F1}$ = 1.15)

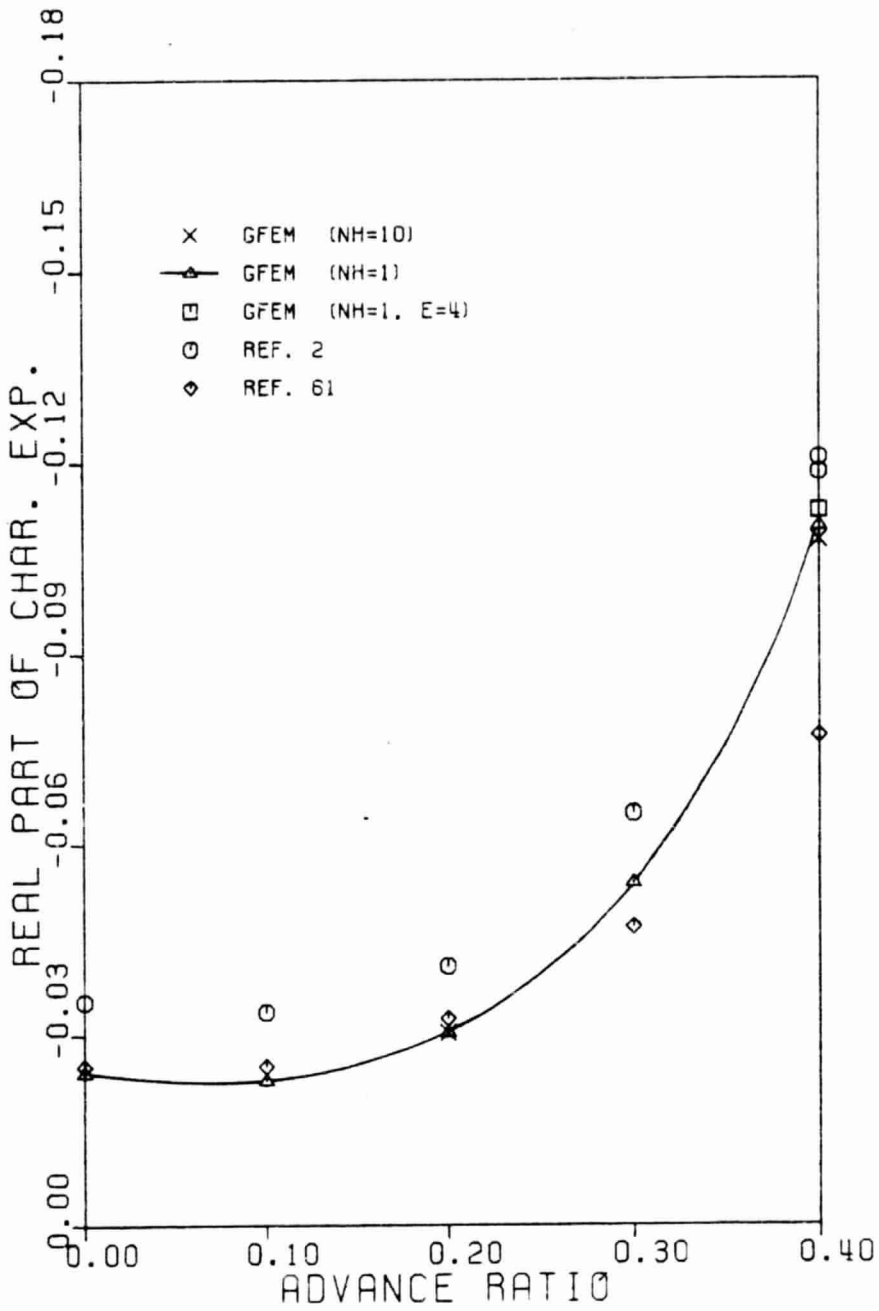

FIGURE 23a: Comparison of Lag Stability When Using the GFEM Versus the Global Galerkin Method

($N_{psi} = N_{rki} = 120$; K = 1; $N_{rev} = 3$; all other data from Table 5.2)

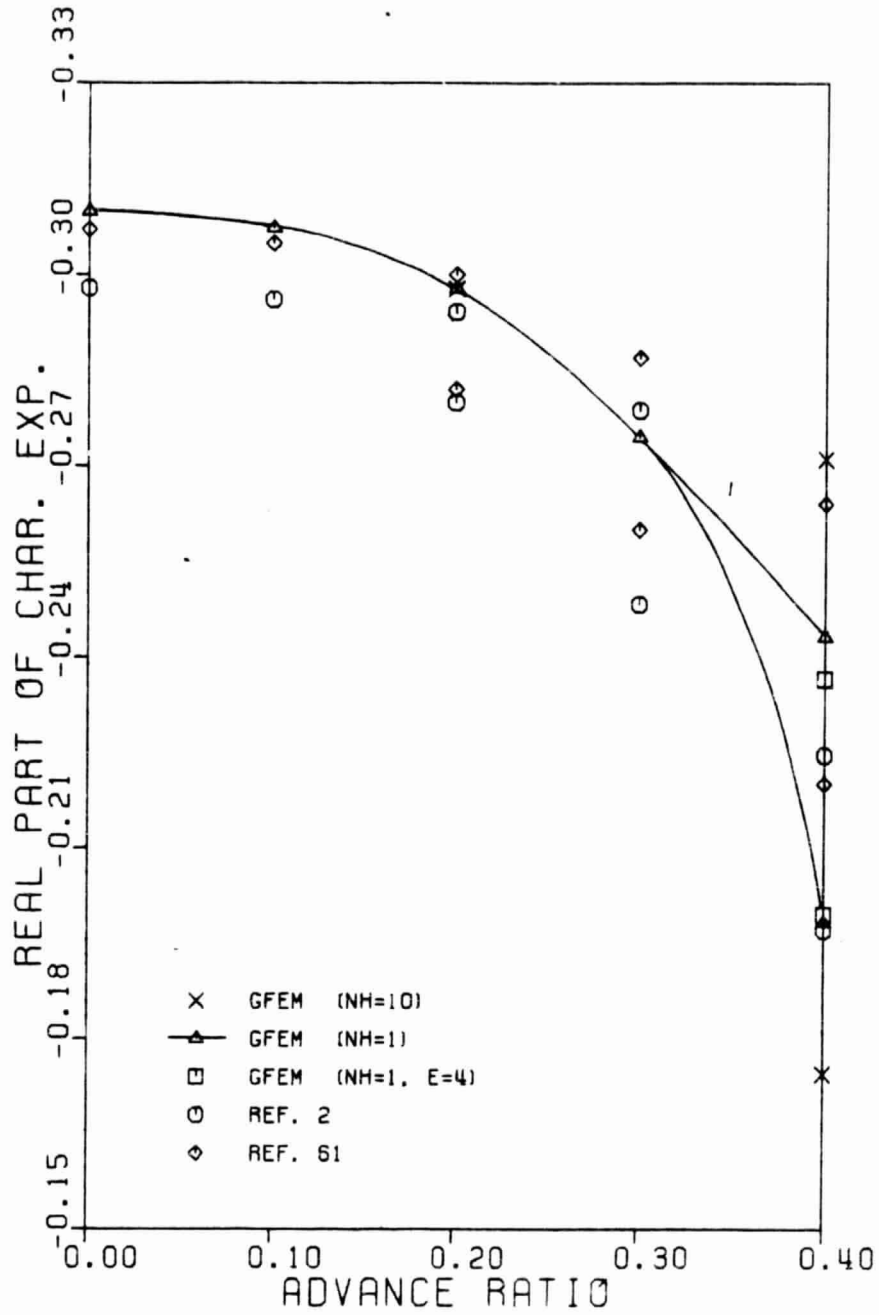

FIGURE 23b: Comparison of Flap Stability When Using the GFEM Versus the Global Galerkin Method

($N_{psi} = N_{rki} = 120$; K = 1; $N_{rev} = 3$; all other data from Table 5.2)

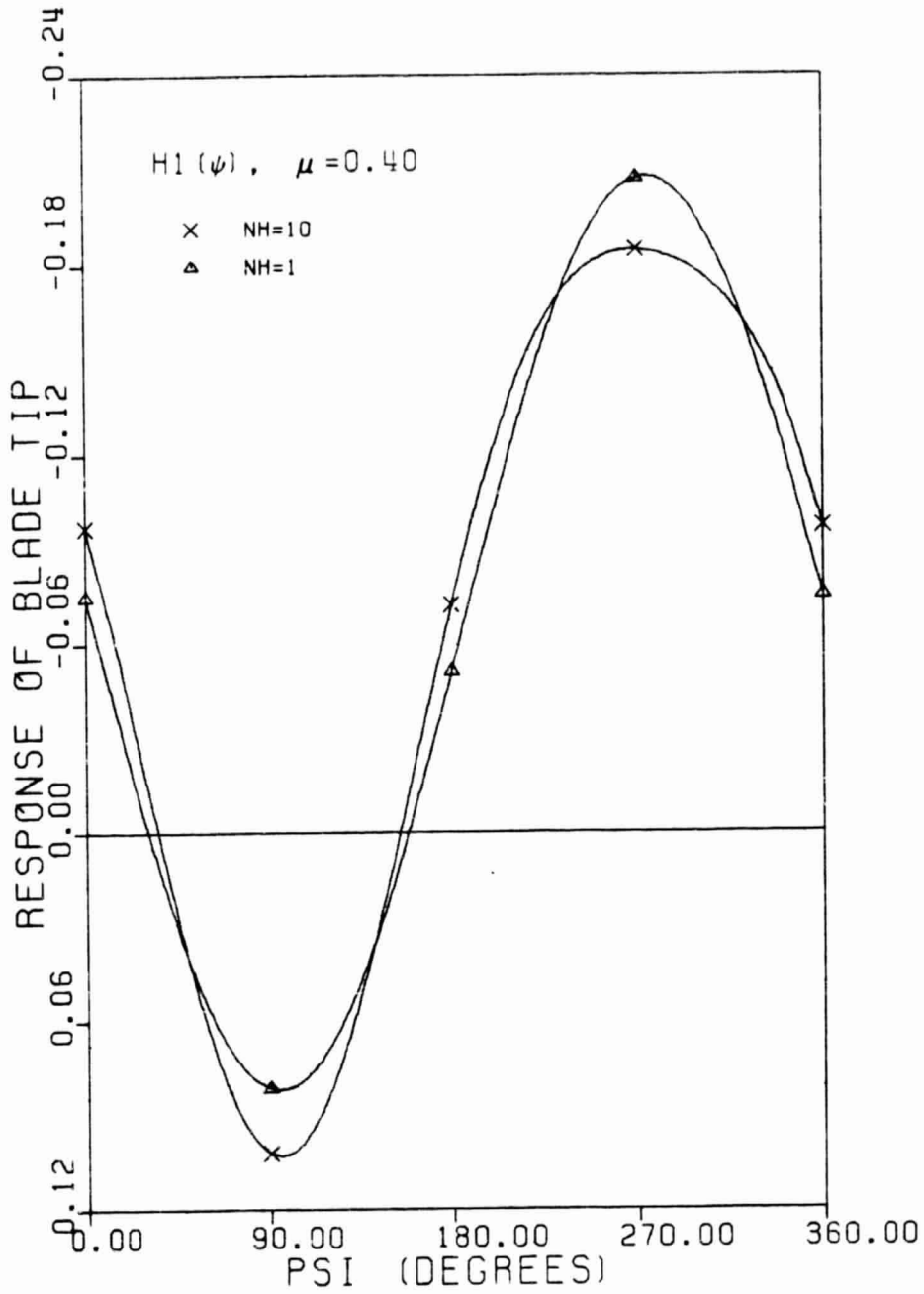

FIGURE 24a: Contribution of Higher Harmonics to the Lag Steady-State Response*

($N_{psi} = N_{rki} = 120$; K = 1; $N_{rev} = 3$; all other data from Table 5.2)

*In all plots the response is normalized w.r.t. length of elastic portion of the blade.

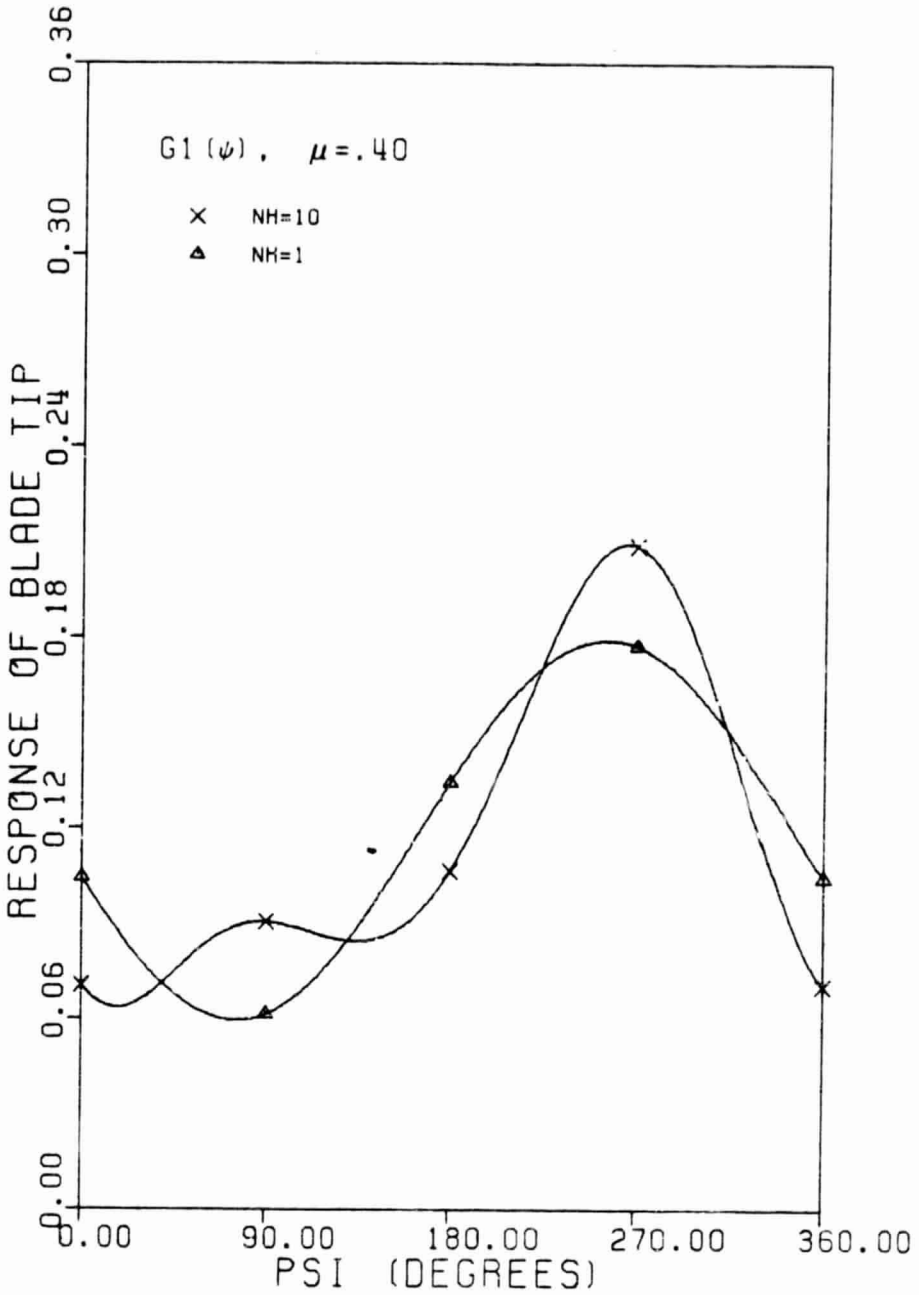

FIGURE 24b: Contribution of Higher Harmonics to the Flap Steady-State Response

($N_{psi} = N_{rki} = 120$; K = 1; $N_{rev} = 3$; all other data from Table 5.2)

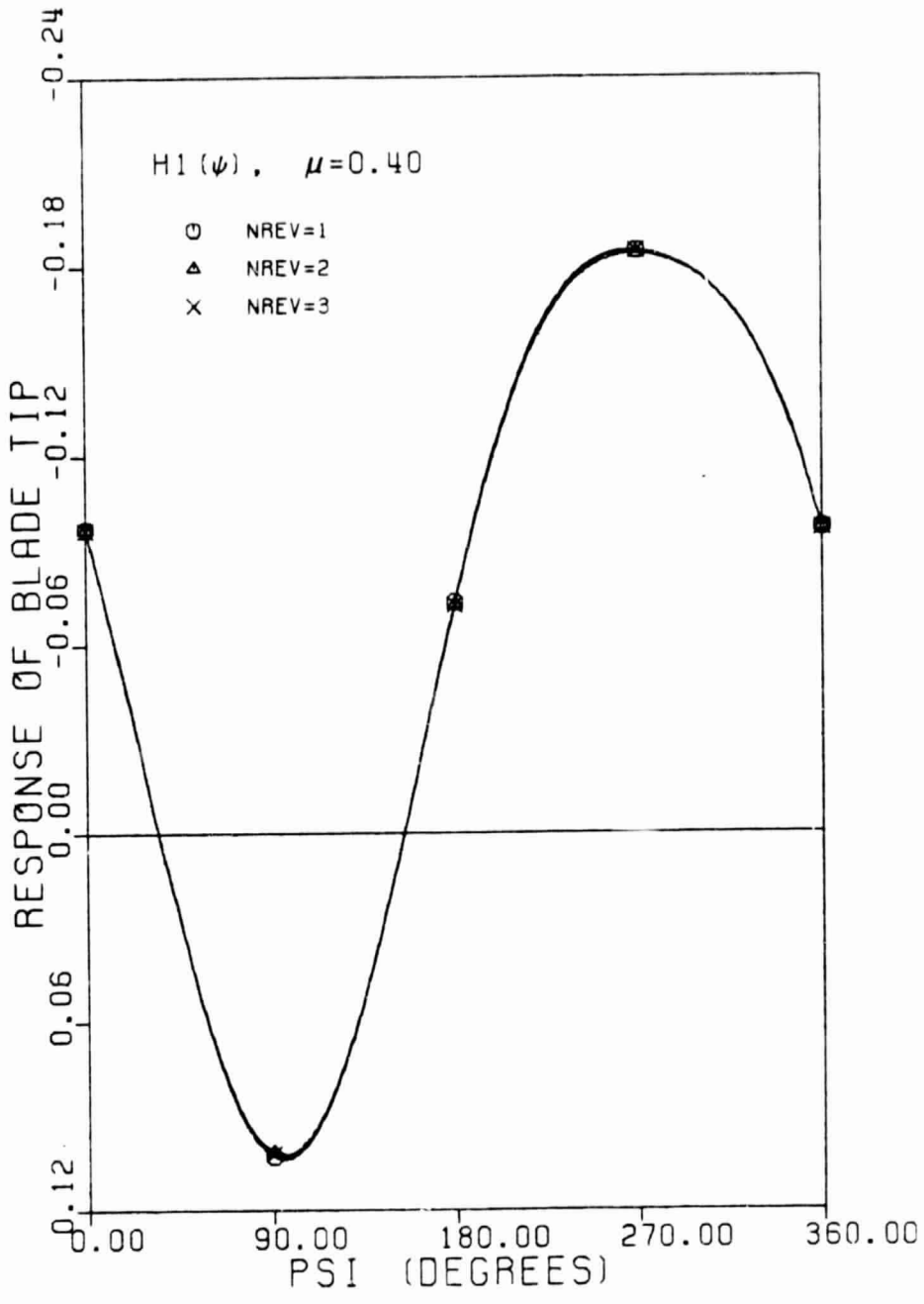

FIGURE 25a: Periodicity of Lag Steady-State Response for Three Consecutive Rotor Revolutions

($N_{psi} = N_{rki} = 120$; K = 2; all other data from Table 5.2)

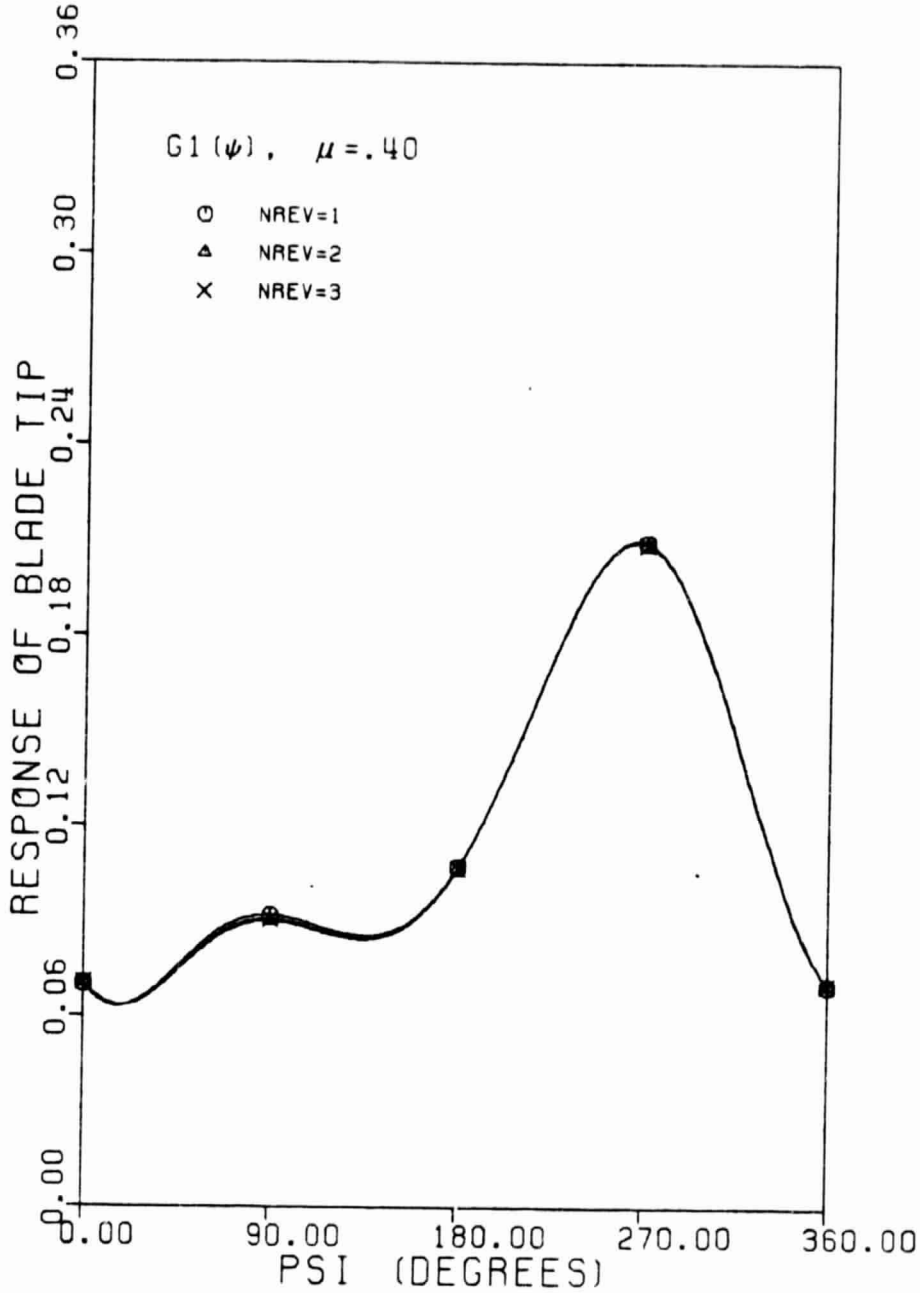

FIGURE 25b: Periodicity of Flap Steady-State Response for Three Consecutive Rotor Revolutions

($N_{psi} = N_{rki}$ = 120; K = 2; all other data from Table 5.2)

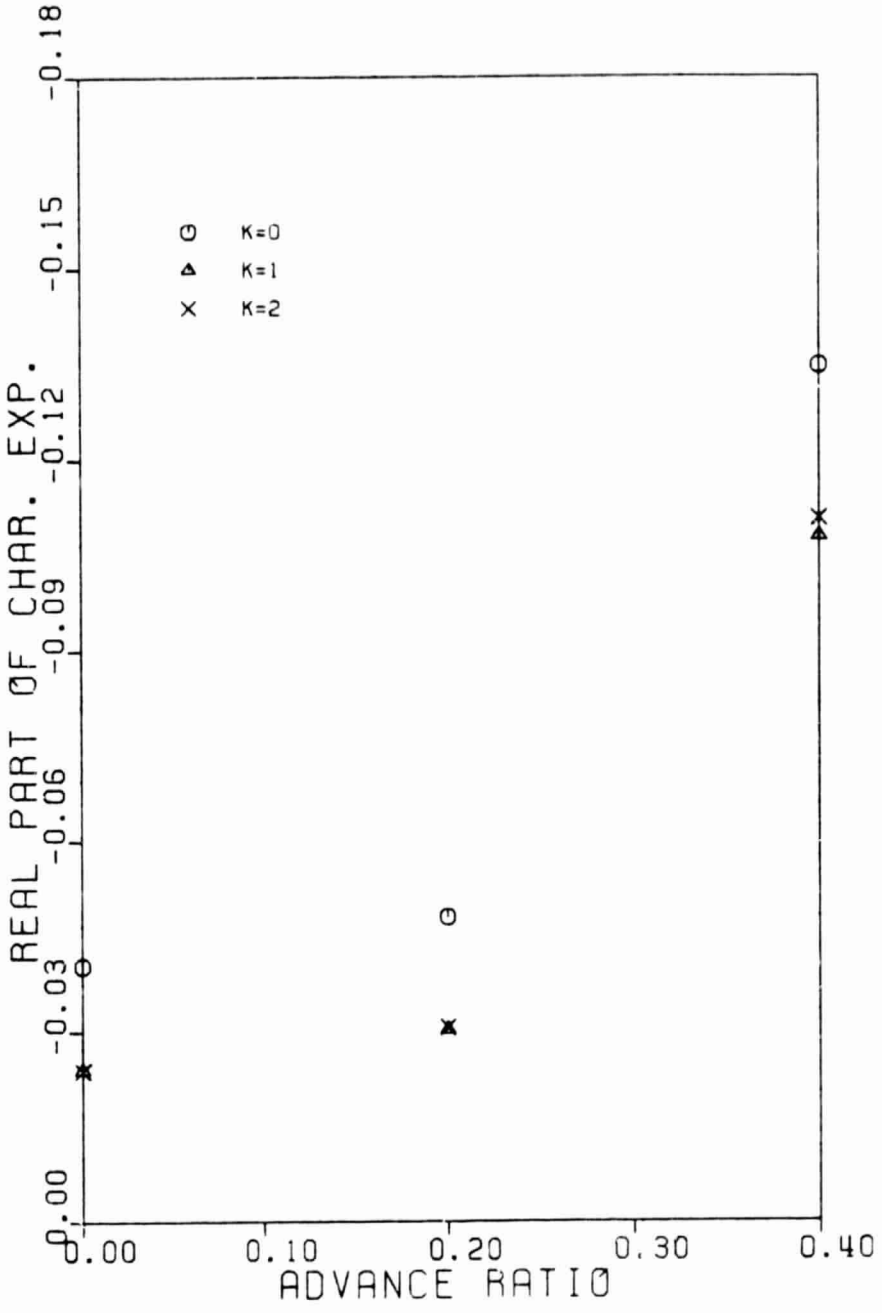

FIGURE 26a: Effect of Nonlinear Terms on Lag Stability

($N_{psi} = N_{rki} = 120$; $N_{rev} = 3$; all other data from Table 5.2)

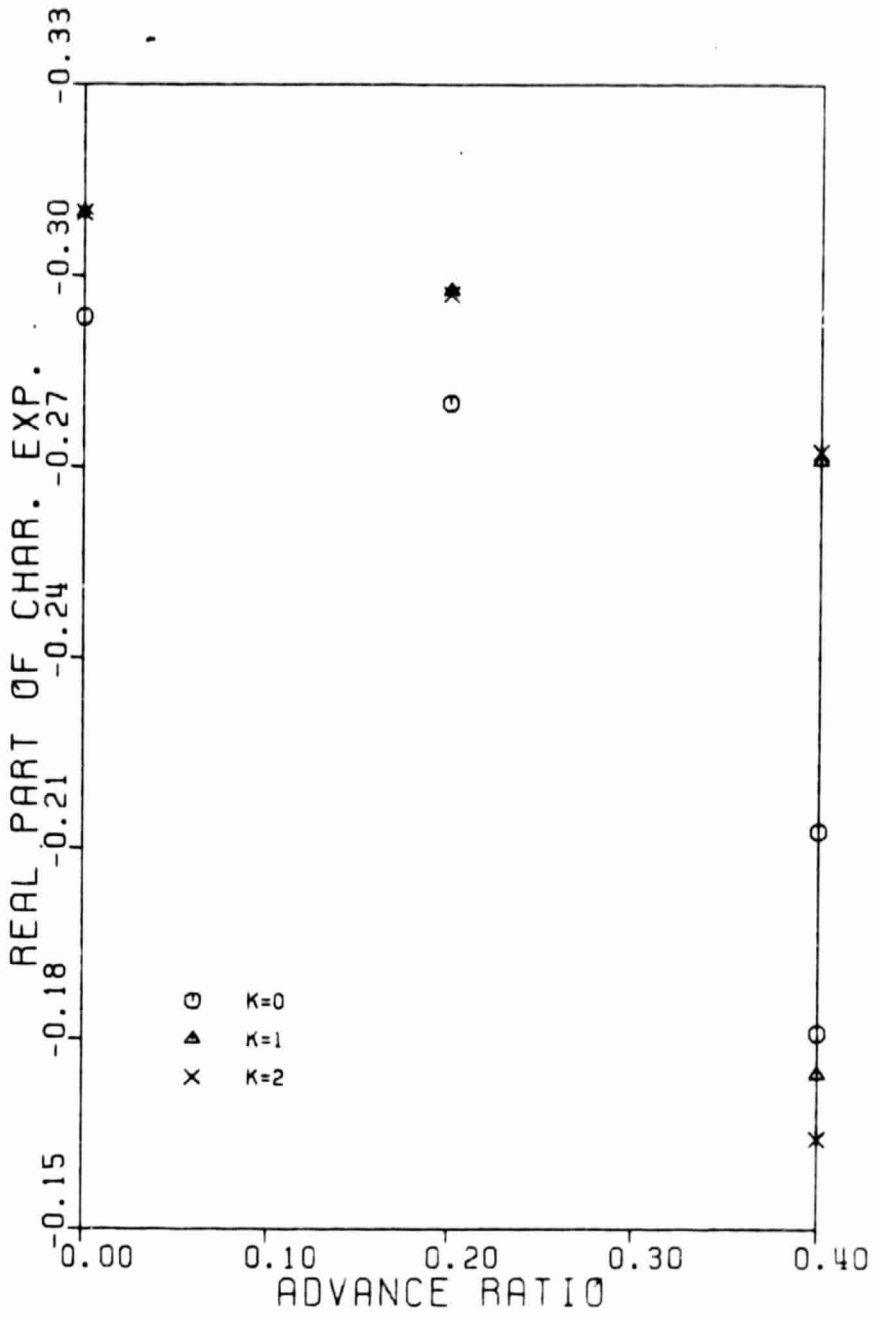

FIGURE 26b: Effect of Nonlinear Terms on Flap Stability

($N_{psi} = N_{rki} = 120$; $N_{rev} = 3$; all other data from Table 5.2)

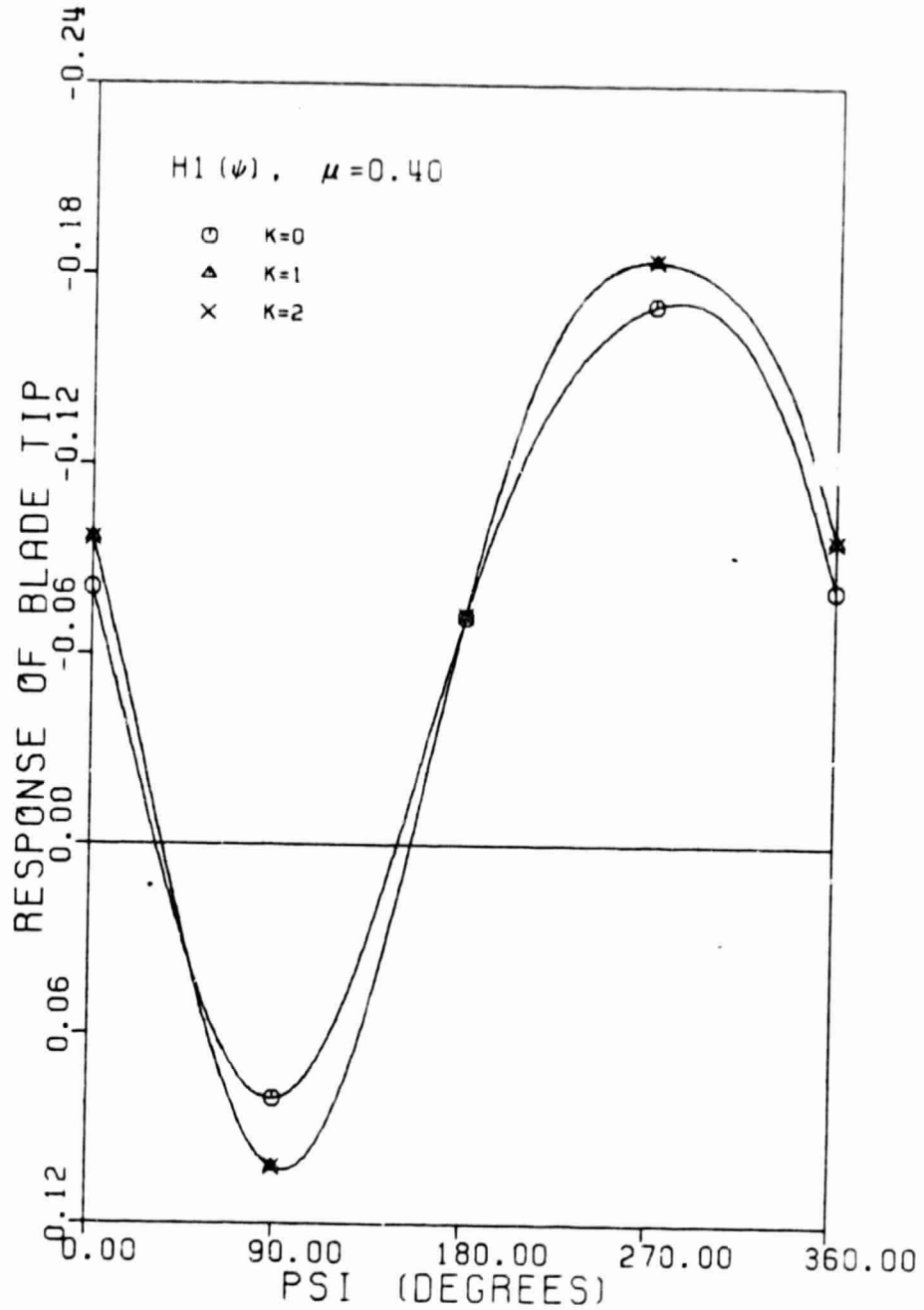

FIGURE 27a: Effect of Nonlinear Terms on Lag Steady-State Response

($N_{psi} = N_{rki} = 120$; $N_{rev} = 3$; all other data from Table 5.2)

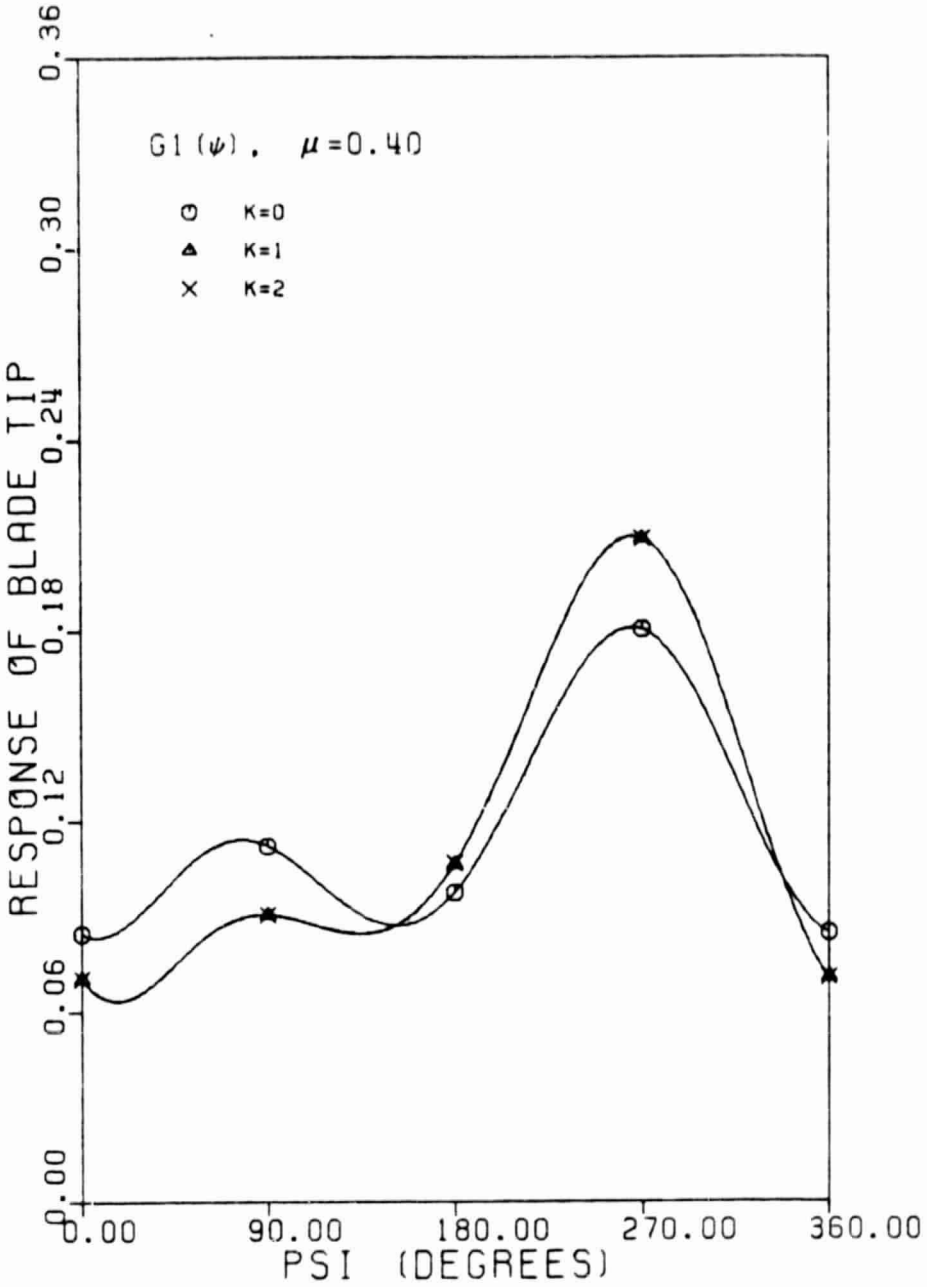

FIGURE 27b: Effect of Nonlinear Terms on Flap Steady-State Response

($N_{psi} = N_{rki} = 120$; $N_{rev} = 3$; all other data from Table 5.2)

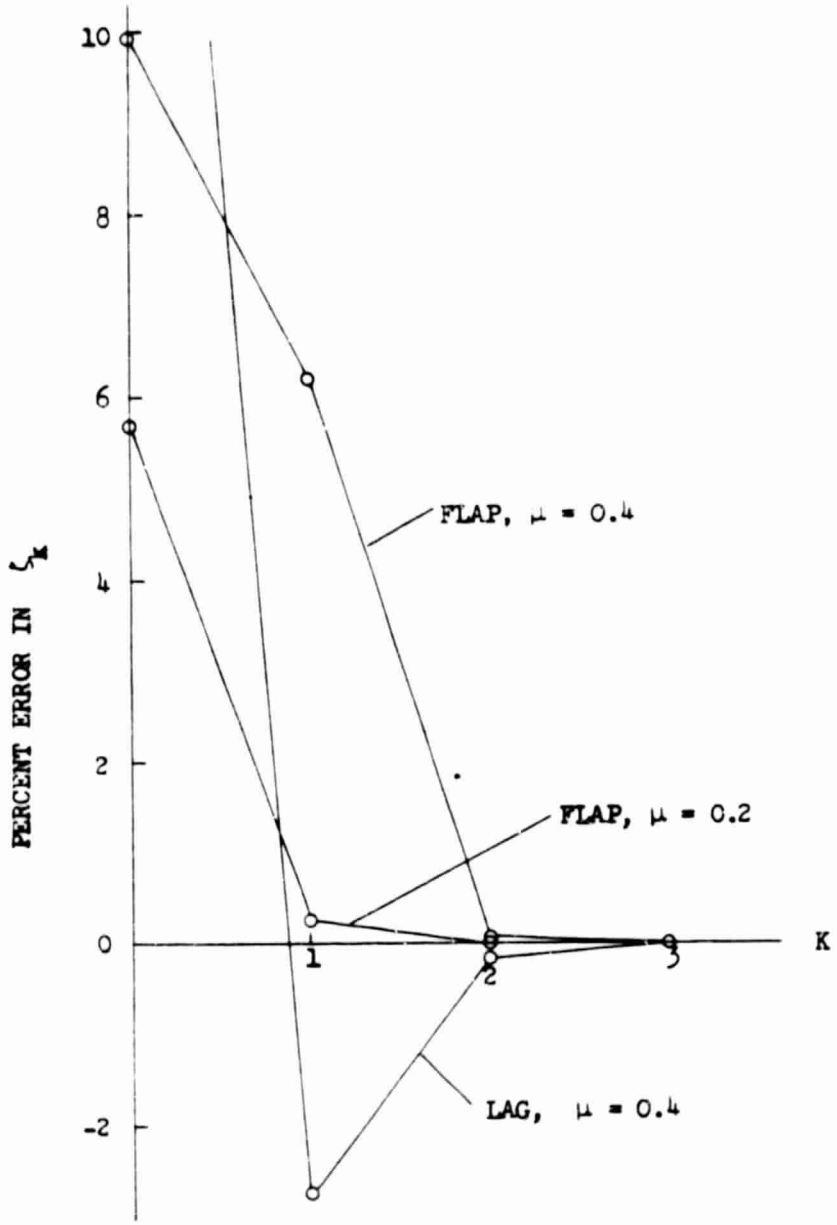

FIGURE 28: Convergence of Real Parts of Characteristic Exponents as a Function of the Number of Quasilinearization Steps ($N_{psi} = N_{rki} = 120$; $N_{rev} = 2$; all other data from Table 5.2)

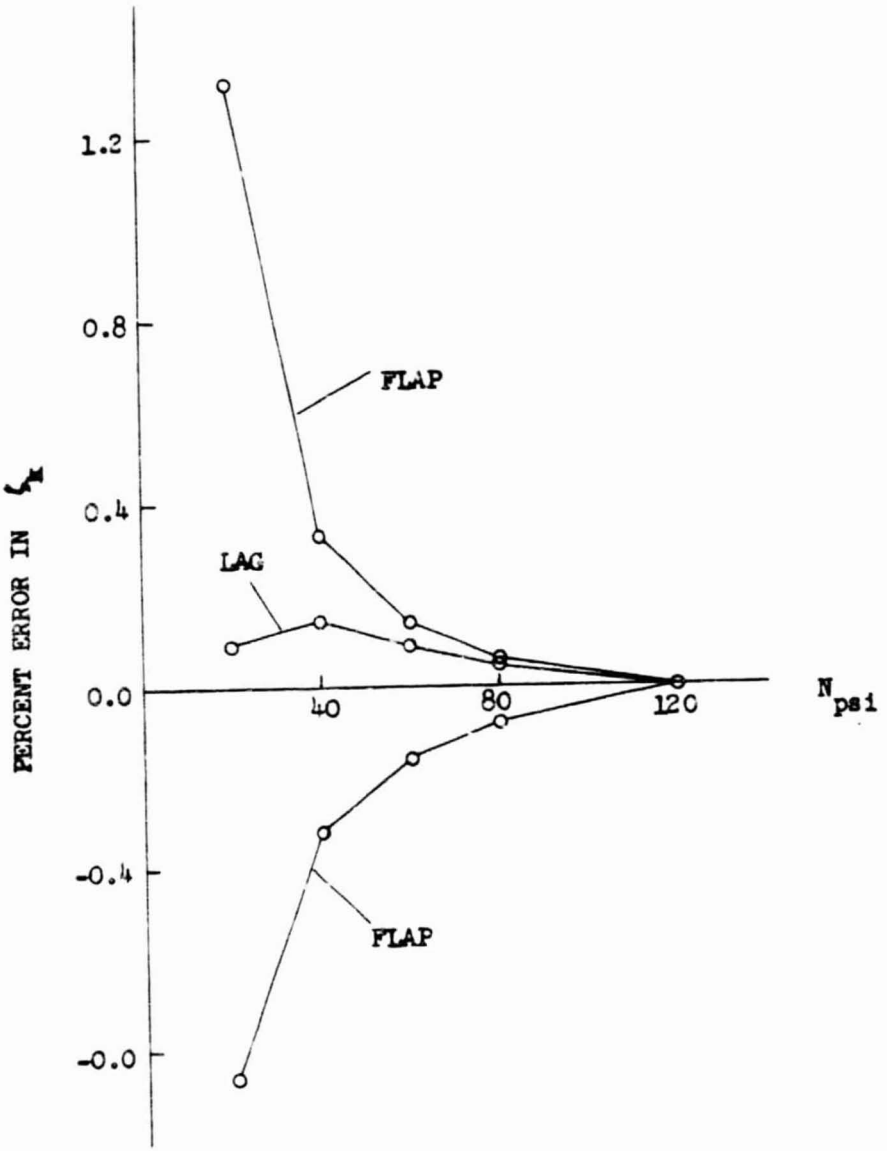

FIGURE 29: Convergence of Real Parts of Characteristic Exponents as a Function of the Number of Azimuthal Steps ($N_{psi} = N_{rki}$; K = 3; N_{rev} = 3; μ = 0.4; all other data from Table 5.2)

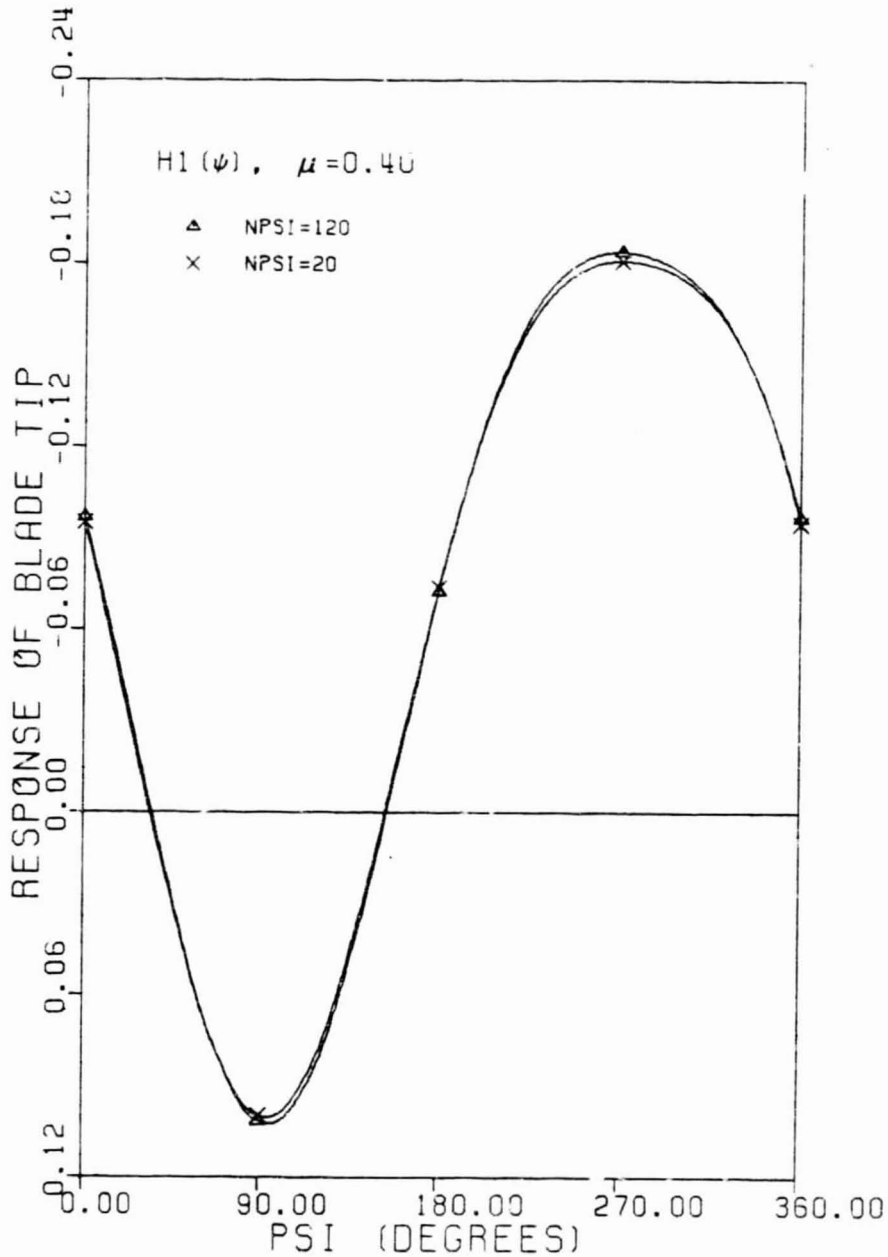

FIGURE 30a: Effect of the Number of Azimuthal Steps on Lag Steady-State Response

($N_{psi} = N_{rki}$; K = 3; N_{rev} = 3; all other data from Table 5.2)

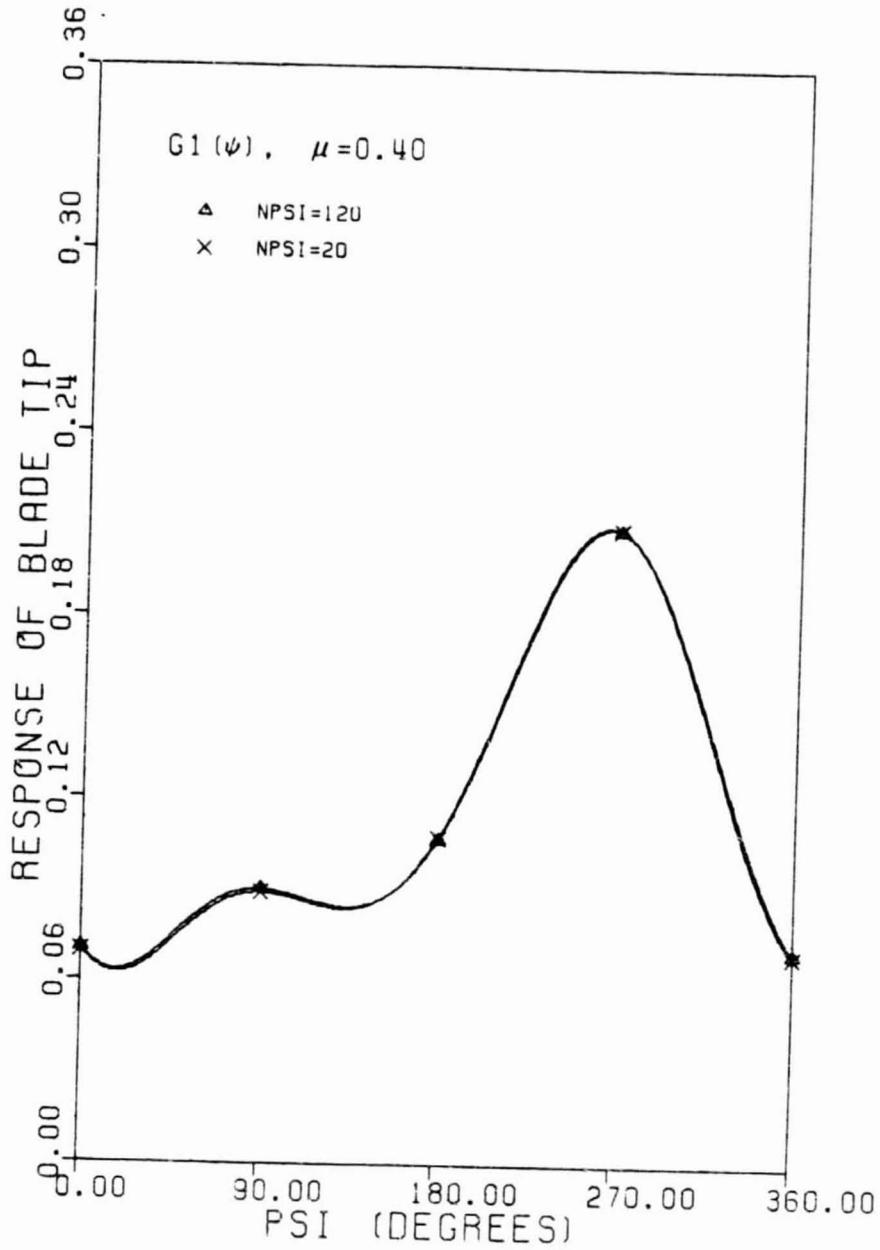

FIGURE 30b: Effect of the Number of Azimuthal Steps on Flap Steady-State Response

($N_{psi} = N_{rki}$; K = 3; N_{rev} = 3; all other data from Table 5.2)

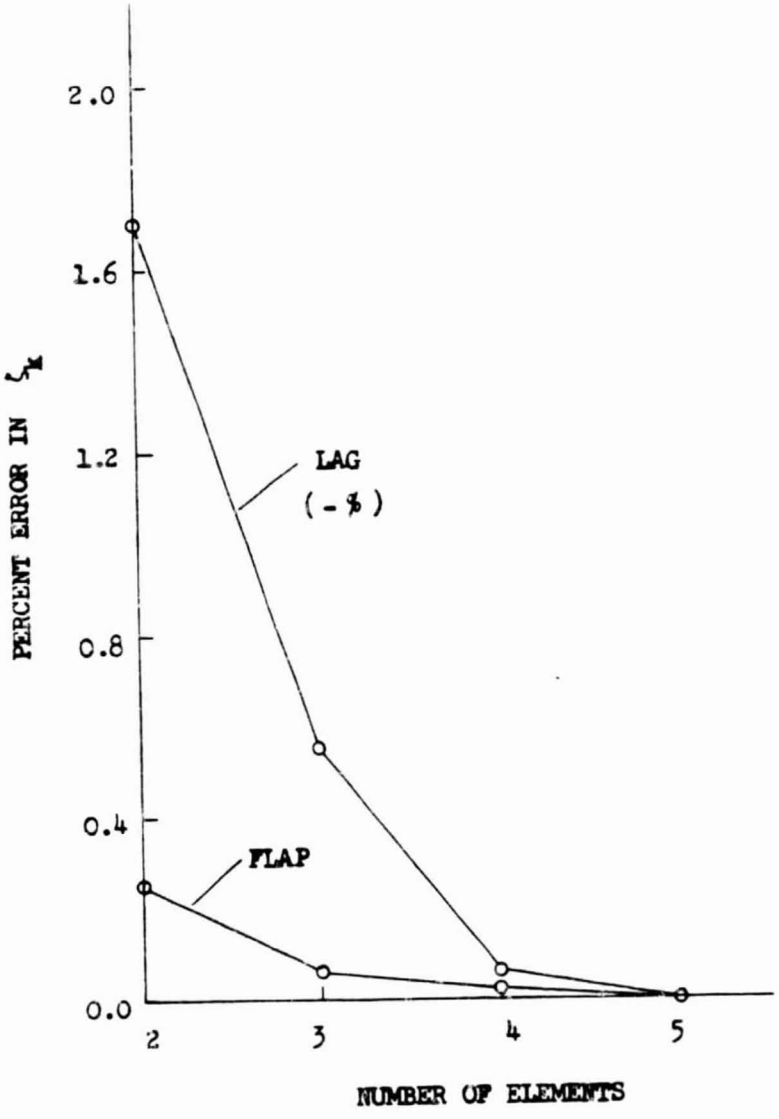

FIGURE 31: Convergence of Flap-Lag Stability When the Number of Elements is Changed (M = 2; $\bar{\omega}_{L1}$ = 0.732; R_c = 0.6; μ = 0.4; propulsive trim; C_W = 0.005; all other data from Table 5.3)

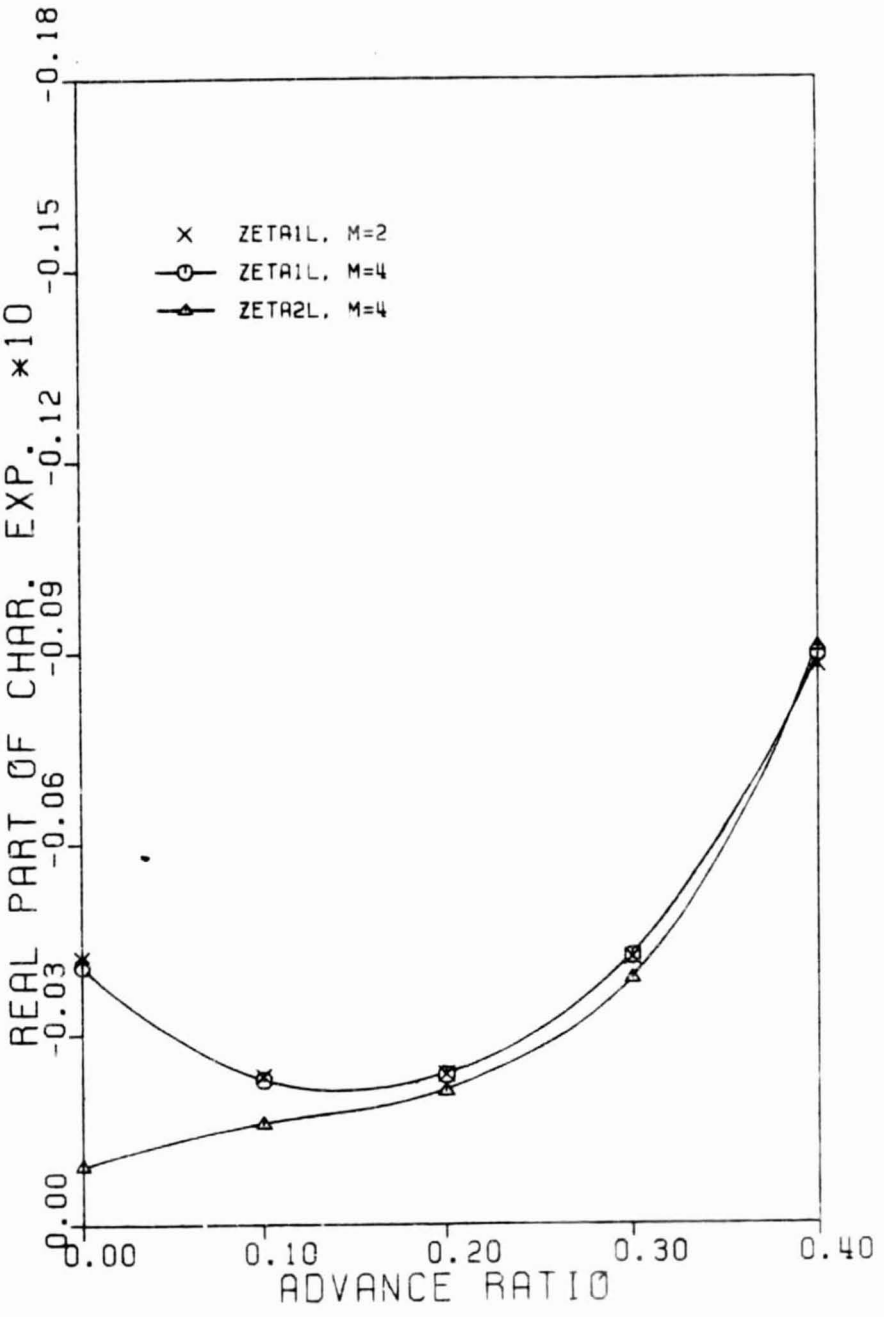

FIGURE 32a: Lag Stability When the Number of Modes is Changed

(E = 4; $\bar{\omega}_{L1}$ = 0.732; R_c = 0.6; propulsive trim; C_w = 0.005; all other data from Table 5.3)

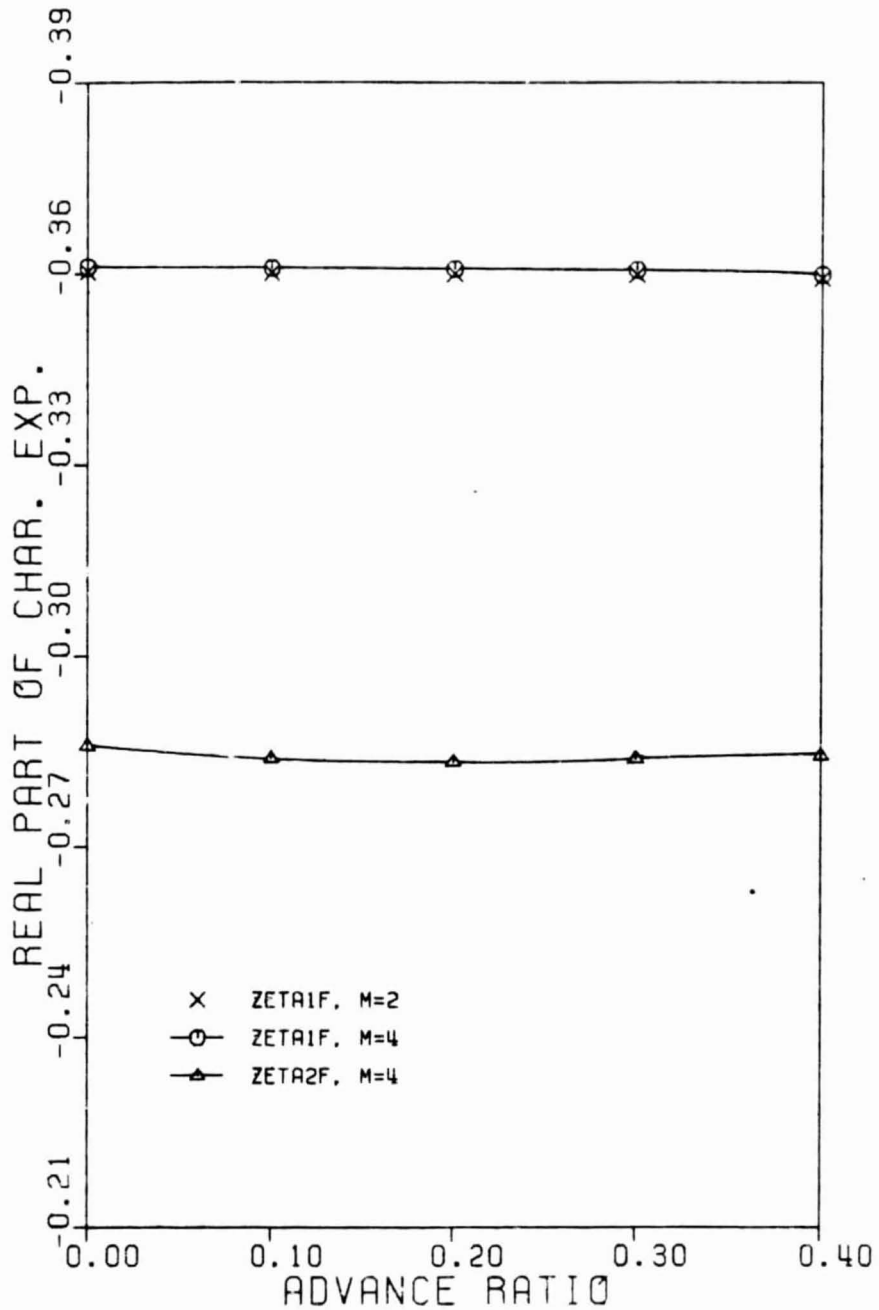

FIGURE 32b: Flap Stability When the Number of Modes is Changed

($E = 4$; $\bar{\omega}_{L1} = 0.732$; $R_c = 0.6$; propulsive trim; $C_w = 0.005$; all other data from Table 5.3)

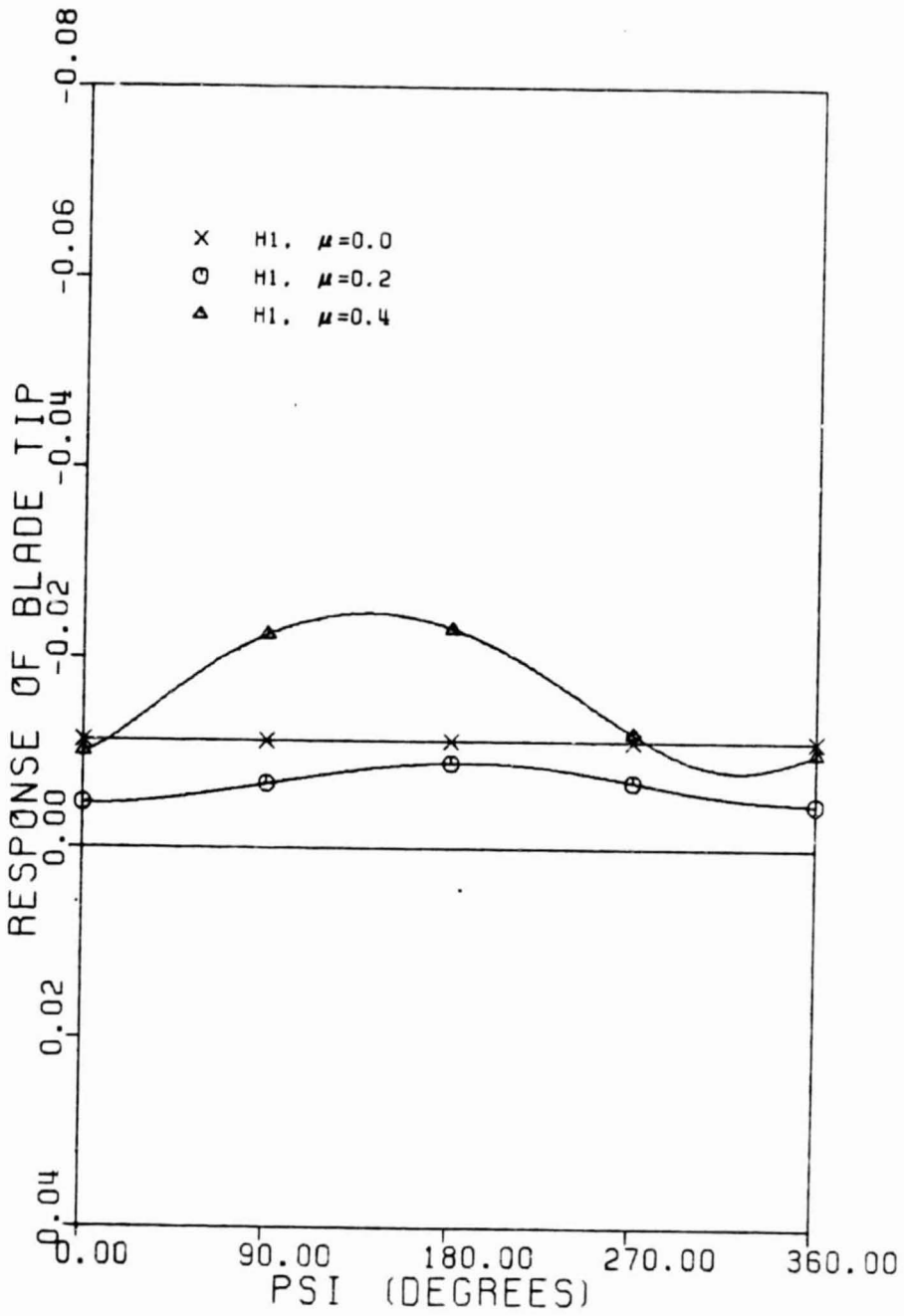

FIGURE 33a: Lag Steady-State Response as a Function of Advance Ratio

($E = 4$; $M = 2$; $\bar{\omega}_{L1} = 0.732$; $R_c = 0.6$; propulsive trim; $C_w = 0.005$; all other data from Table 5.3)

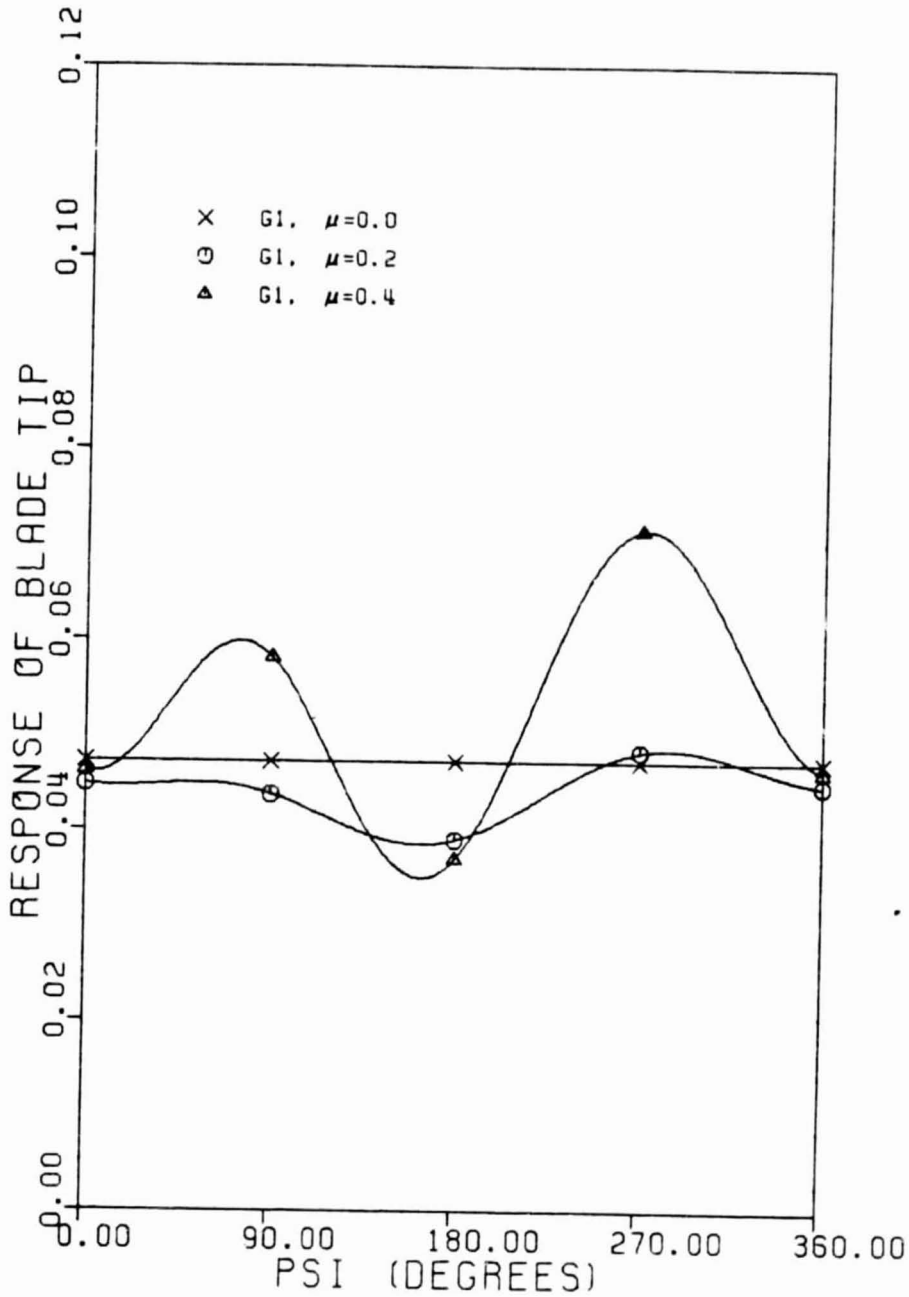

FIGURE 33b: Flap Steady-State Response as a Function of Advance Ratio

(E = 4; M = 2; $\bar{\omega}_{L1}$ = 0.0732; R_c = 0.6; propulsive trim; C_w = 0.005; all other data from Table 5.3)

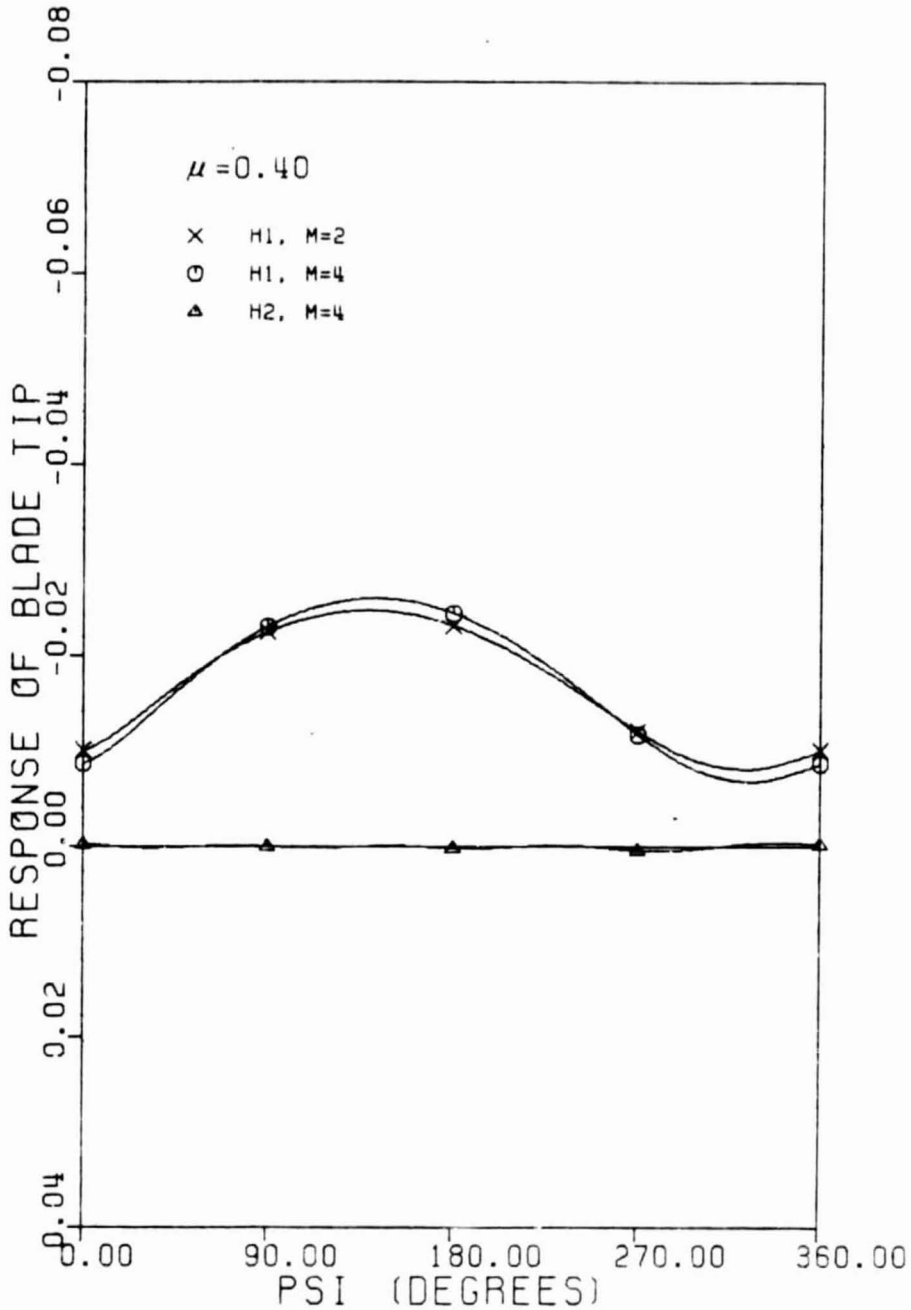

FIGURE 34a: Lag Steady-State Response When the Number of Modes is Changed

($E = 4$; $\bar{\omega}_{L1} = 0.732$; $R_c = 0.6$; propulsive trim; $C_w = 0.005$; all other data from Table 5.3)

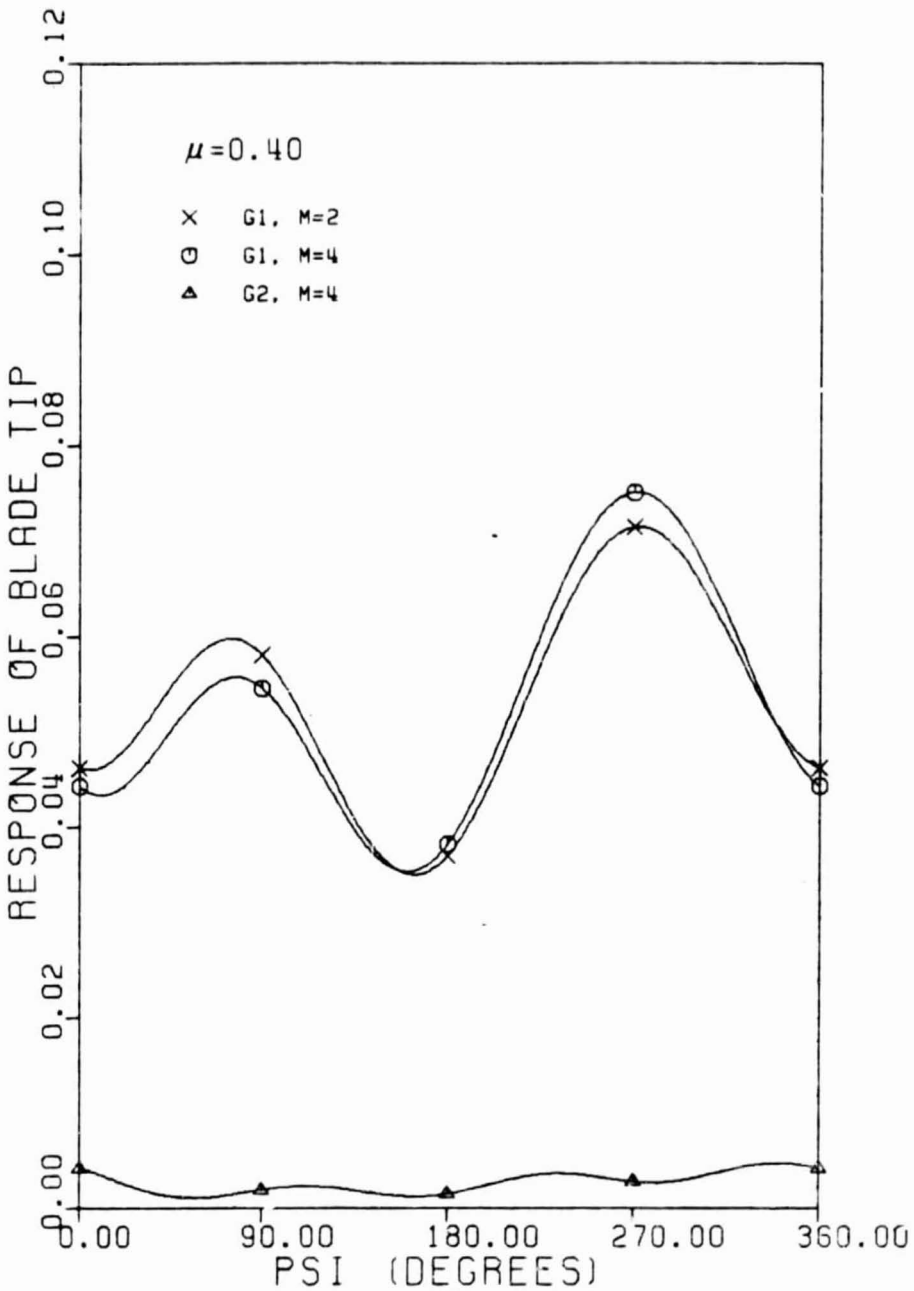

FIGURE 34b: Flap Steady-State Response When the Number of Modes is Changed

($E = 4$; $\bar{\omega}_{L1} = 0.732$; $R_c = 0.6$; propulsive trim; $C_w = 0.005$; all other data from Table 5.3)

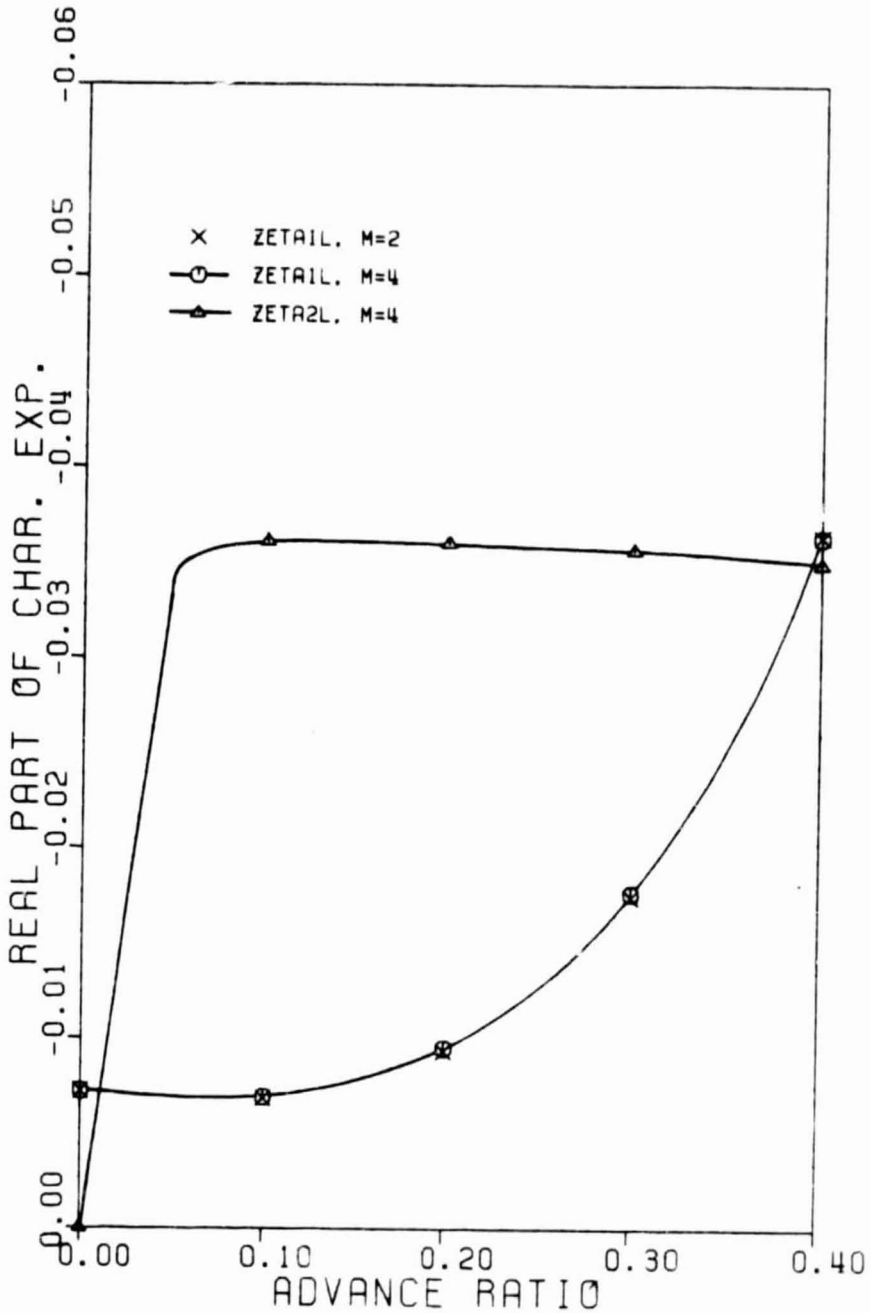

FIGURE 35a: Lag Stability When the Number of Modes is Changed, Stiff Inplane Blade

($E = 4$; $\bar{\omega}_{L1} = 1.417$; $R_c = 0.8$; propulsive trim; $C_w = 0.01$; all other data from Table 5.3)

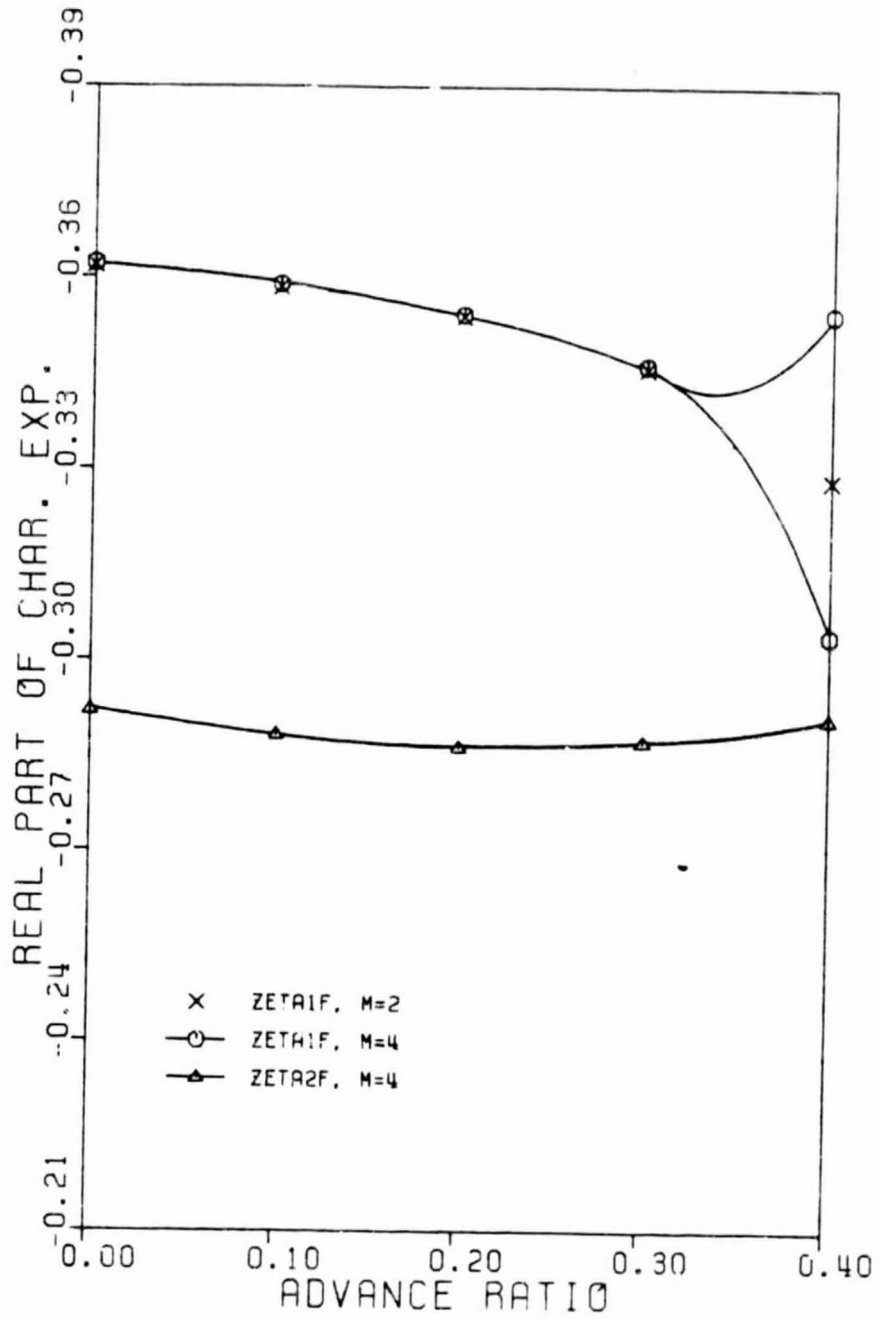

FIGURE 35b: Flap Stability When the Number of Modes is Changed, Stiff Inplane Blade

($E = 4$; $\bar{\omega}_{\zeta 1} = 1.417$; $R_c = 0.8$; propulsive trim; $C_w = 0.01$; all other data from Table 5.3)

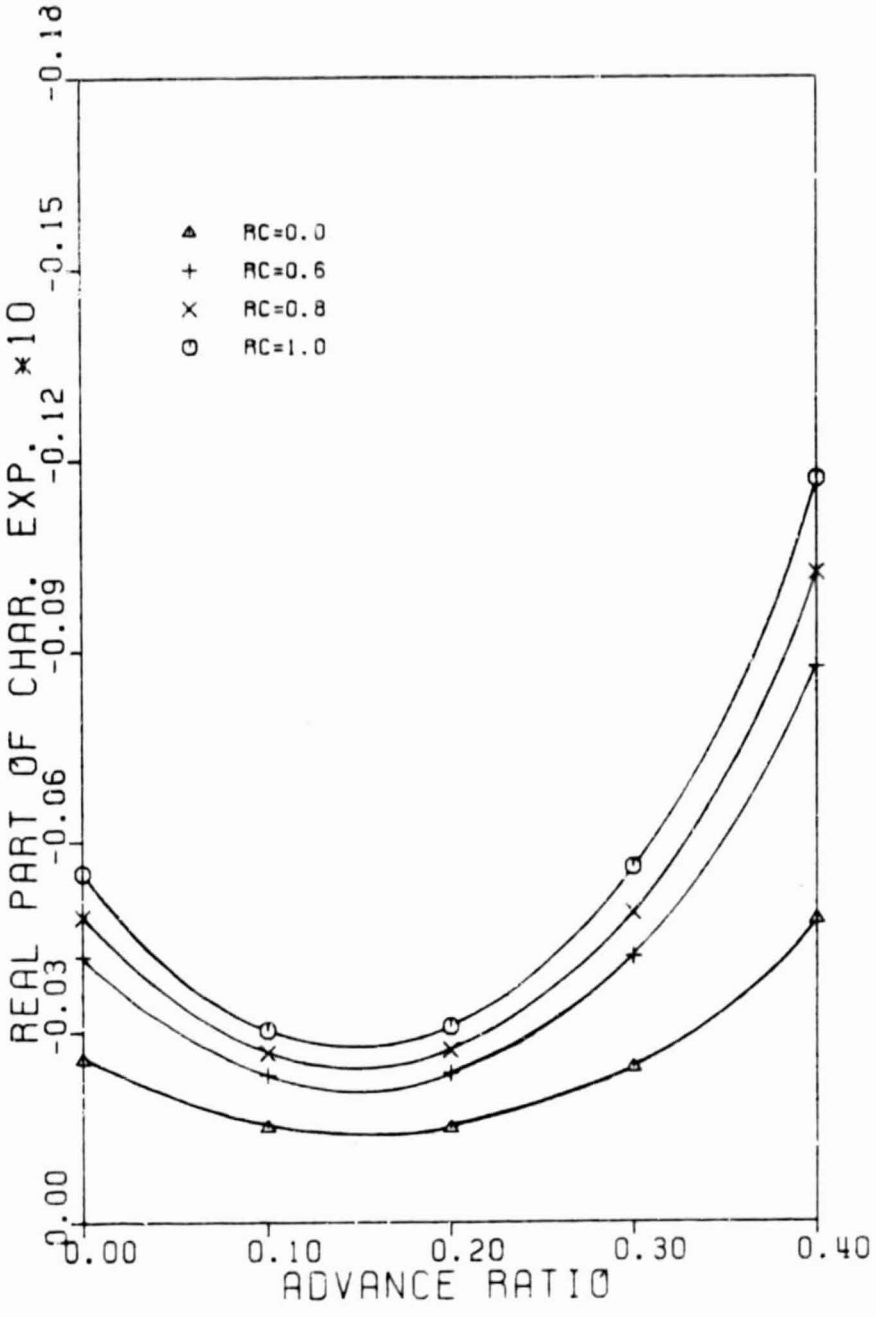

FIGURE 36: Effect of Elastic Coupling on the Stability of the First Lag Mode Plotted Versus Advance Ratio

($E = 3$; $M =$; $\bar{\omega}_{L1} = 0.732$; propulsive trim; $C_w = 0.005$; all other data from Table 5.3)

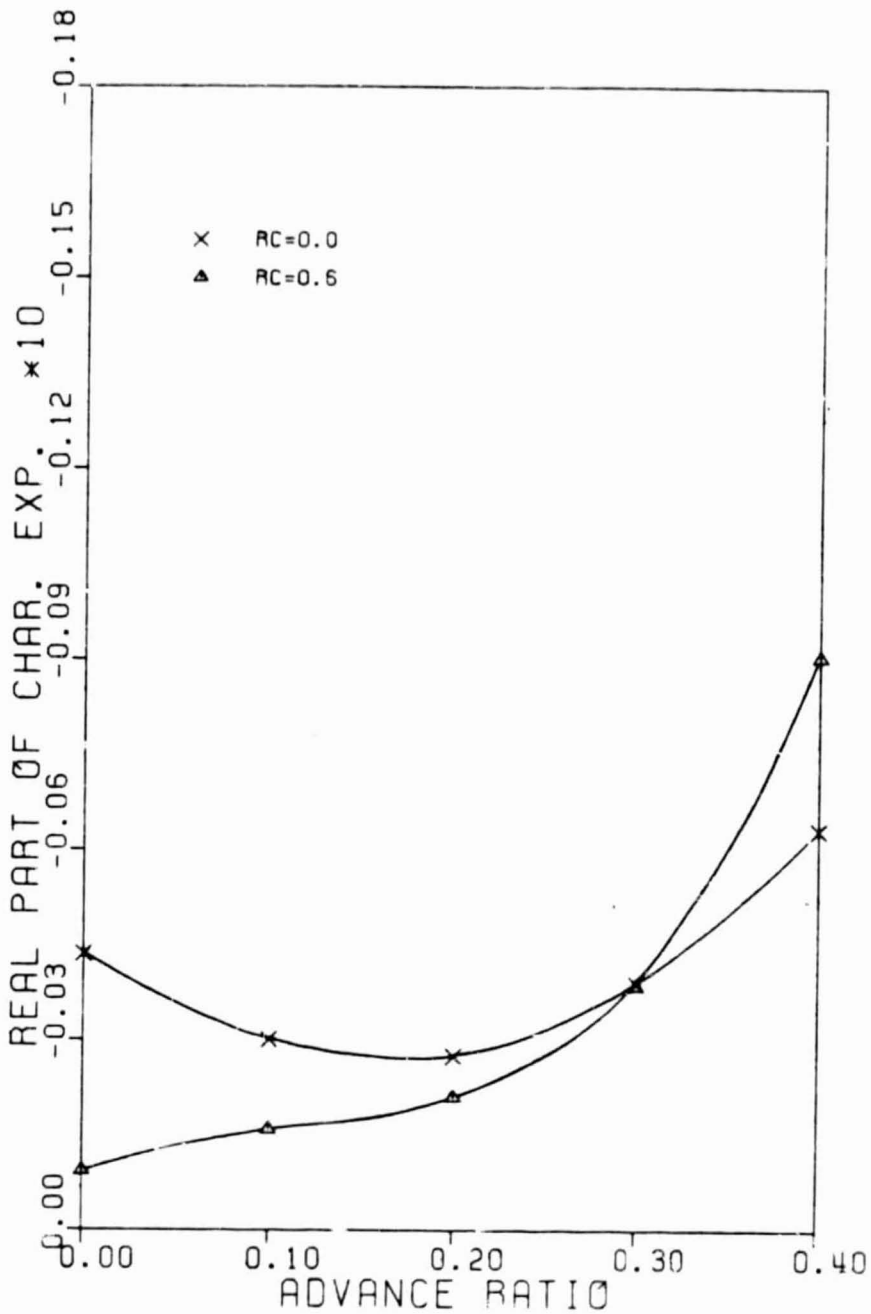

FIGURE 37: Effect of Elastic Coupling on the Stability of the Second Lag Mode Plotted Versus Advance Ratio

(E = 4; M = 4; $\bar{\omega}_{L1}$ = 0.732; propulsive trim; C_w = 0.005; all other data from Table 5.3)

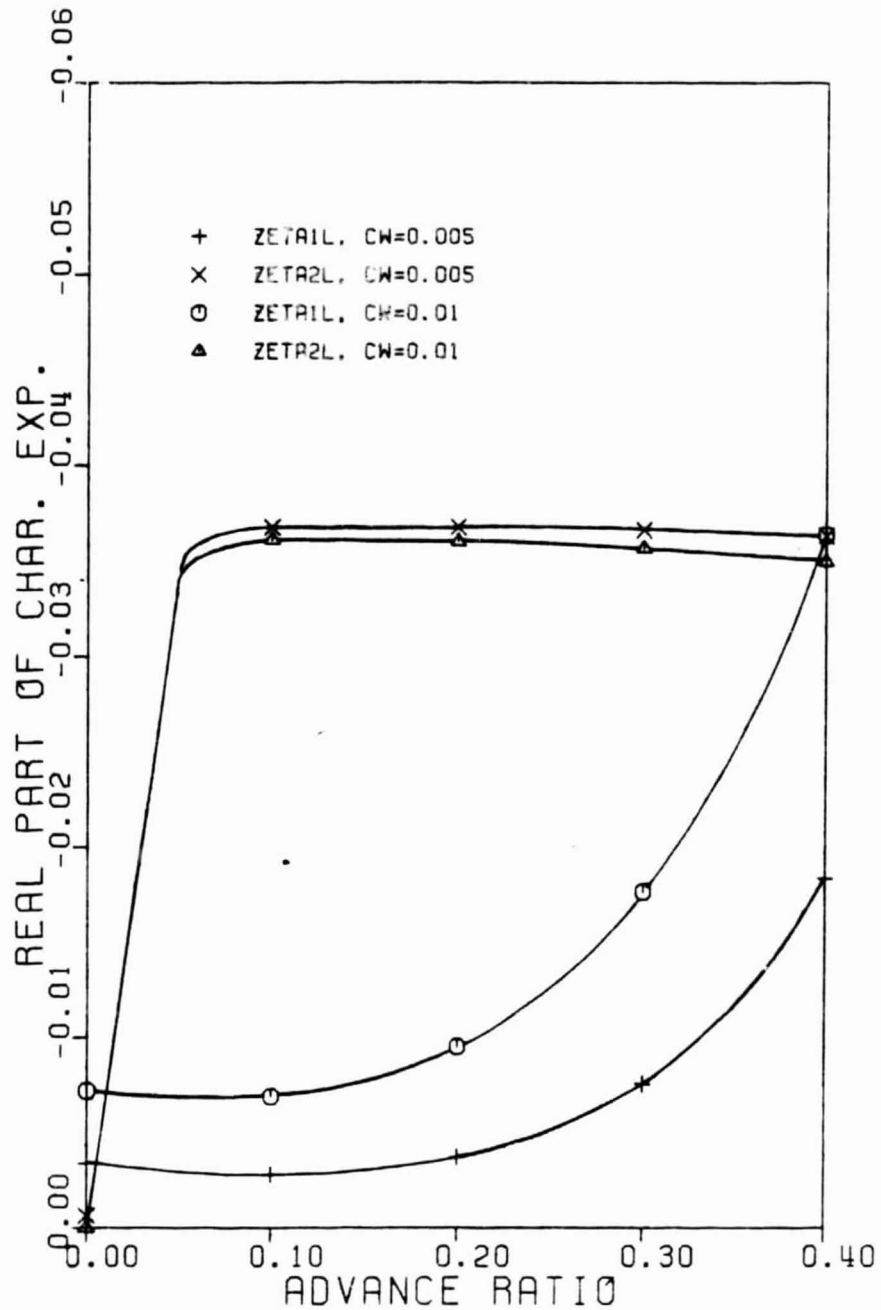

FIGURE 38a: Lag Stability for Two Different Weight Coefficients Versus Advance Ratio

(E = 4; M = 4; $\bar{\omega}_{L1}$ = 1.417; R_c = 0.8; propulsive trim; all other data from Table 5.3)

C-3

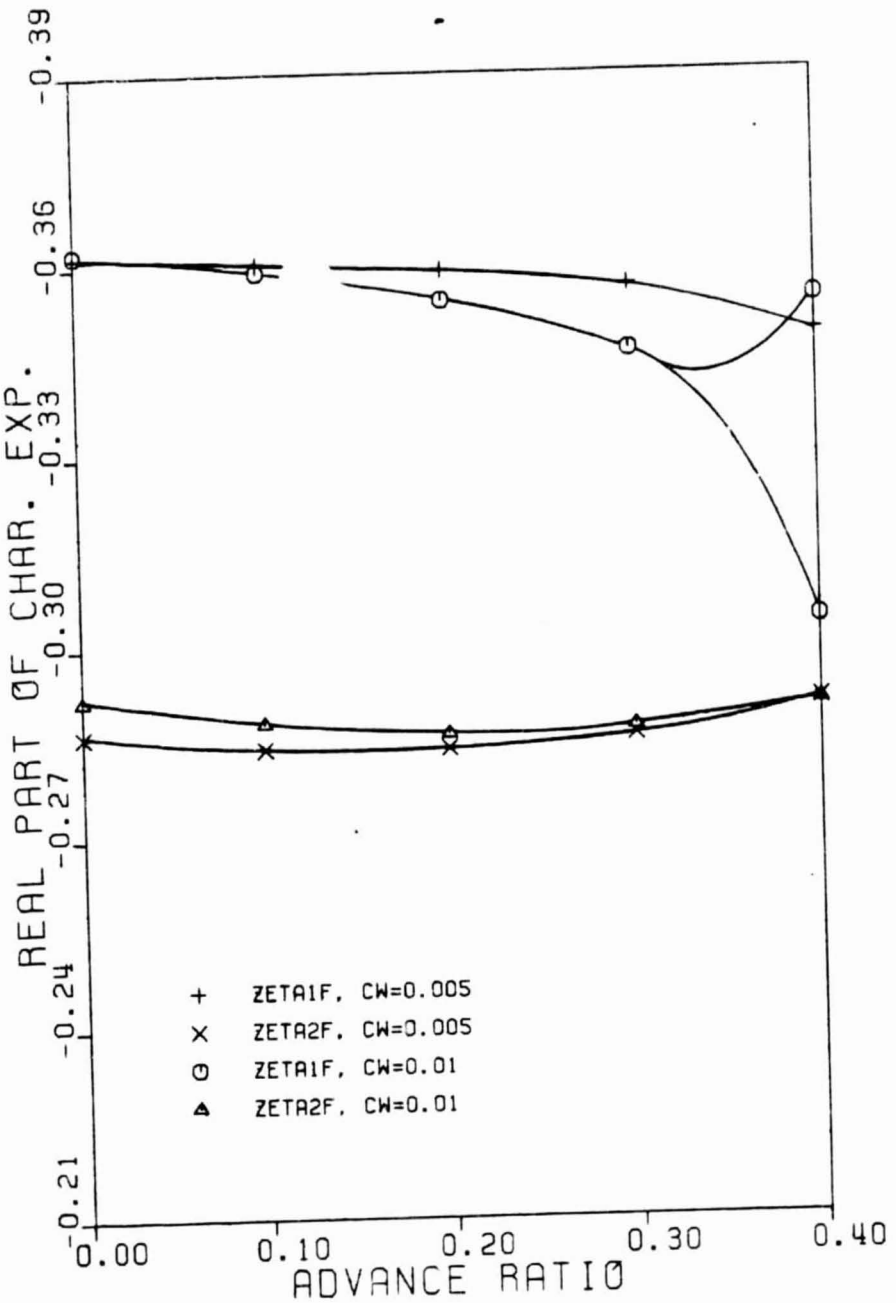

FIGURE 38b: Flap Stability for Two Different Weight Coefficients Versus Advance Ratio

($E = 4$; $M = 4$; $\bar{\omega}_{L1} = 1.417$; $R_c = 0.8$; propulsive trim; all other data from Table 5.3)

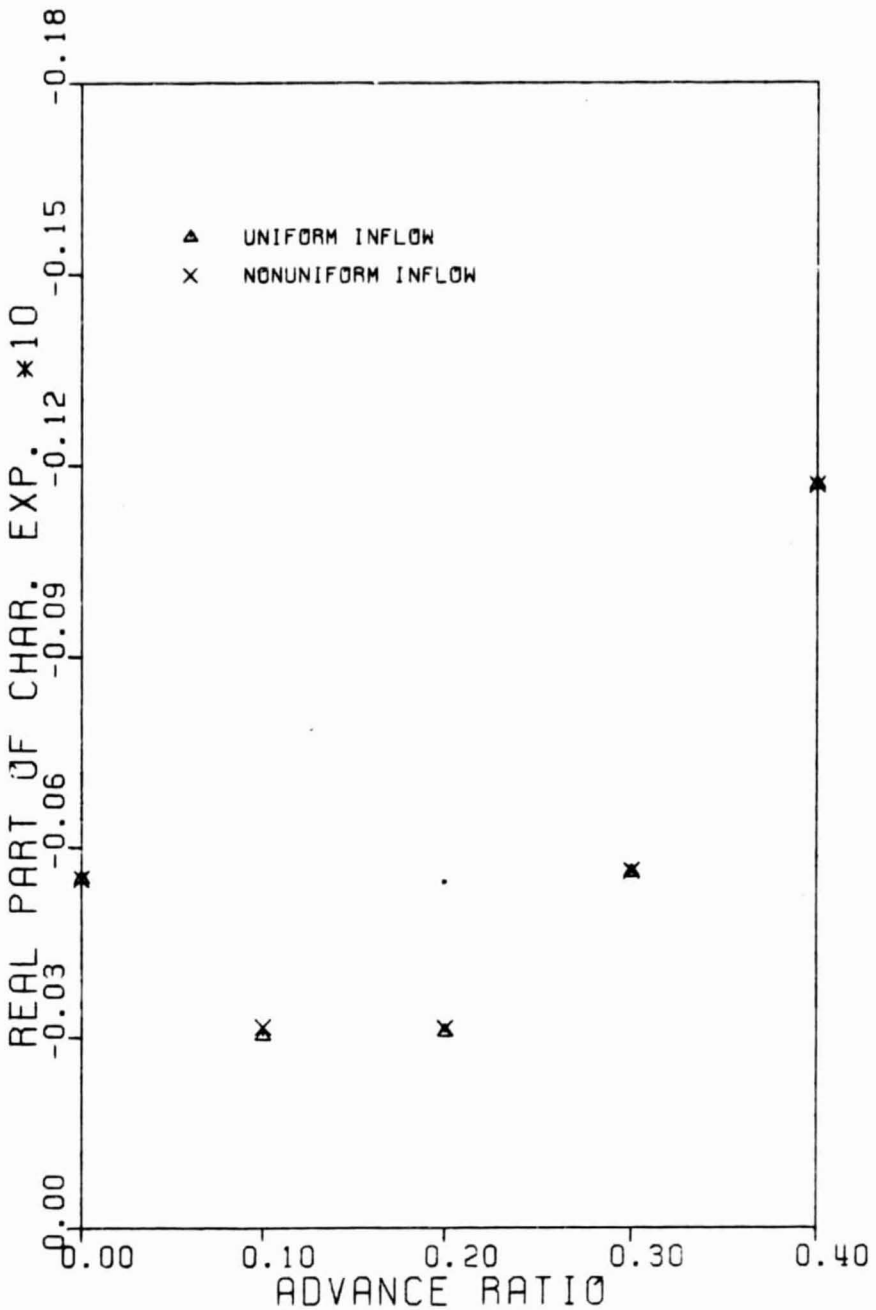

FIGURE 39: Influence of Nonuniform Inflow on Lag Stability

($E = 3$, $M = L$, $\bar{\omega}_{L1} = 0.732$; $R_c = 1.0$; propulsive trim; $C_w = 0.005$; all other data from Table 5.3)

TABLE 1

COMPARISON OF GLOBAL GALERKIN AND FINITE ELEMENT GALERKIN METHODS

$\sigma = 0.05$; $\gamma = 5.0$; $\bar{\omega}_{F1NR} = 0.4$; $\bar{\omega}_{L1NR} = 1.1$; $R_c = 1.0$

Finite element results based on three elements and one mode per degree of freedom; Global Galerkin results based on one mode per degree of freedom.

	Global Galerkin $\theta = 0.20$	GFEM $\theta = 0.20$	Global Galerkin $\theta = 0.45$	GFEM $\theta = 0.45$
$\bar{\omega}_{L1}$ $(\theta = 0)$	1.179967	1.18026	1.179967	1.18026
$\bar{\omega}_{F1}$ $(\theta = 0)$	1.140290	1.14150	1.140290	1.14150
h_1^0	0.016719	0.016484 (-1.4%)	0.087953	0.086768 (-1.3%)
g_1^0	0.070289	0.066521 (-5.4%)	0.187816	0.177959 (-5.2%)
ζ_{1L}	-0.026198	-0.026168 (-.11%)	-0.066079	-0.065838 (-.36%)
ζ_{1F}	-0.307892	-0.308048 (.05%)	-0.281260	-0.281628 (.13%)

$$\Delta\% = \frac{\text{GFEM - Global Galerkin}}{\text{Global Galerkin}} \cdot 100$$

TABLE 2

PROPULSIVE TRIM VALUES*

μ	λ_0	α_R	θ_0	θ_{1s}	θ_{1c}
0.0	.07071	.0000	.2970	-.0000	.0000
0.1	.04577	.0031	.2652	-.0605	.0038
0.2	.02850	.0187	.2559	-.1178	.0072
0.3	.02880	.0406	.2874	-.1878	.0113
0.4	.03939	.0672	.3577	-.2853	.0166

*Based on $C_W = 0.01$; taken from results of Ref. [2]. Used for configurations where data in Table 5.2 was employed.

TABLE 3

PROPULSIVE TRIM VALUES*

μ	λ_0	α_R	θ_0	θ_{1s}	θ_{1c}
0.0	.05000	.0000	.1432	-.0003	.0002
0.1	.02518	.0094	.1084	-.0247	.0078
0.2	.02057	.0406	.1086	-.0487	.0151
0.3	.03463	.0875	.1454	-.0867	.0248
0.4	.05653	.1250	.2110	-.1501	.0382

*Based on data in Table 5.3; $C_W = 0.005$, uniform inflow. Calculated with trim program from Ref. [63].

TABLE 4: FOURIER COEFFICIENTS OF STEADY-STATE RESPONSE WHEN USING ONE AND TEN HARMONICS

(Results pertain to response plotted in Figs. 24)

	NH = 1	
	h_1	g_1
	CONSTANT TERMS	
1	-0.63047E-01	0.11936E+00
	SINE TERMS	
1	0.14433E+00	-0.57833E-01
	COSINE TERMS	
1	-0.11865E-01	-0.15027E-01

	NH = 10	
	h_1	g_1
	CONSTANT TERMS	
1	-0.62985E-01	0.11936E+00
	SINE TERMS	
1	0.14417E+00	-0.57849E-01
2	-0.49644E-02	0.36560E-02
3	0.88004E-03	0.12577E-02
4	0.23353E-03	-0.39137E-03
5	0.18575E-04	-0.57260E-04
6	-0.12173E-04	-0.19869E-04
7	-0.15282E-04	-0.10889E-04
8	-0.13324E-04	-0.96163E-05
9	-0.12404E-04	-0.80081E-05
10	-0.10909E-04	-0.71937E-05
	COSINE TERMS	
1	-0.11636E-01	-0.15032E-01
2	-0.21675E-01	-0.30516E-01
3	-0.73437E-03	-0.28532E-02
4	-0.22548E-04	-0.22230E-03
5	0.50308E-04	-0.53274E-04
6	0.39837E-04	-0.33600E-04
7	0.41726E-04	-0.30667E-04
8	0.40969E-04	-0.29284E-04
9	0.41057E-04	-0.29574E-04
10	0.39808E-04	-0.28595E-04

TABLE 5

STEADY-STATE RESPONSE AT FIRST THREE COMPLETE BLADE REVOLUTIONS*

ψ	$\dot{h}_1(\psi)$	$\dot{g}_1(\psi)$	$h_1(\psi)$	$g_1(\psi)$
0	.13852	-.04481	-.09814	.07095
2π	.13830	-.04874	-.09685	.07137
4π	.13822	-.04821	-.09740	.07072
6π	.13849	-.04858	-.09724	.07102

*First-order state variable vector at $\psi = n \cdot 2\pi$, $n = 0,1,\ldots,3$. Results pertain to response plotted in Figs. 25.

APPENDIX A

COORDINATE TRANSFORMATIONS

The transformations between the various coordinate systems are given below. Note that for rotations of order $O(\varepsilon_D)$ the small angle assumption is used.

$$\begin{Bmatrix} \underset{\sim}{i} \\ \underset{\sim}{j} \\ \underset{\sim}{k} \end{Bmatrix} = \begin{bmatrix} \cos\Psi & \sin\Psi & 0 \\ -\sin\Psi & \cos\Psi & 0 \\ 0 & 0 & 1 \end{bmatrix} \begin{Bmatrix} \hat{X} \\ \hat{Y} \\ \hat{Z} \end{Bmatrix}$$

$$\begin{Bmatrix} \hat{e}_x \\ \hat{e}_y \\ \hat{e}_z \end{Bmatrix} = \begin{bmatrix} 1 & 0 & \beta_p \\ 0 & 1 & \\ -\beta_p & 0 & 1 \end{bmatrix} \begin{Bmatrix} \underset{\sim}{i} \\ \underset{\sim}{j} \\ \underset{\sim}{k} \end{Bmatrix}$$

$$\begin{Bmatrix} \hat{e}'_x \\ \hat{e}'_y \\ \hat{e}'_z \end{Bmatrix} = \begin{bmatrix} 1 & \bar{v}_{,x} & \bar{w}_{,x} \\ -(\bar{v}_{,x} + \phi\bar{w}_{,x}) & 1 & \phi \\ -(\bar{w}_{,x} - \phi v_{,x}) & -(\phi + \bar{v}_{,x}\,\bar{w}_{,x}) & 1 \end{bmatrix} \begin{Bmatrix} \hat{e}_x \\ \hat{e}_y \\ \hat{e}_z \end{Bmatrix}$$

APPENDIX B

INTEGRALS AND COEFFICIENTS

$$y_O = \eta \cos \Theta_G - \zeta \sin \Theta_G$$

$$z_O = \eta \sin \Theta_G + \zeta \cos \Theta_G$$

$$\iint \eta^2 \, dA = I_2$$

$$\iint \zeta^2 \, dA = I_3$$

$$\iint \rho \, dA = m$$

$$\iint \rho \, y_O \, dA = m \, x_I \cos \Theta_G$$

$$\iint \rho \, z_O \, dA = m \, x_I \sin \Theta_G$$

$$\iint \rho \, \eta^2 \, dA = I_{m2}$$

$$\iint \rho \, \zeta^2 \, dA = I_{m3}$$

$$\iint \rho \, \eta \, \zeta \, dA = 0$$

$$\int_0^{\ell} m \, x_O^2 \, dx_O = I_b$$

$$\bar{T} = -\int \bar{m}(\bar{e}_1 + \bar{x}_0 + 2\dot{\bar{v}})d\bar{x}_0$$

$$T_1(\bar{x}_0) = \int_{\bar{x}_0}^{1} \bar{m}(\bar{e}_1 + \bar{x}_0)d\bar{x}_0$$

$$\bar{u}(\bar{x}_0) = -\frac{1}{2}\int_0^{\bar{x}_0} (\bar{v}_{,x}^2 + \bar{w}_{,x}^2)d\bar{x}_0$$

$$\sigma = \frac{2n_b b_e R}{\pi R^2} \qquad \text{and} \qquad \gamma = \frac{2a \rho_A b_e R^4}{I_b}$$

where b_e = equivalent constant value of semichord b

$$\Gamma = \gamma \frac{I_b \cdot l}{2m_0 R^4}$$

$$B_{22} = \bar{E}\bar{I}_2 \cos^2 R_c \Theta_G + \bar{E}\bar{I}_3 \sin^2 R_c \Theta_G$$

$$= \bar{E}\bar{I}_2 - (\bar{E}\bar{I}_2 - \bar{E}\bar{I}_3) \sin^2 R_c \Theta_G$$

$$B_{23} = \frac{1}{2}(\bar{E}\bar{I}_2 - \bar{E}\bar{I}_3) \sin 2R_c \Theta_G$$

$$B_{33} = \bar{E}\bar{I}_2 \sin^2 R_c \Theta_G + \bar{E}\bar{I}_3 \cos^2 R_c \Theta_G$$

$$= \bar{E}\bar{I}_3 + (\bar{E}\bar{I}_2 - \bar{E}\bar{I}_3) \sin^2 R_c \Theta_G$$

$$B_4 = \frac{1}{2}(\bar{E}\bar{I}_2 - \bar{E}\bar{I}_3) \cos 2R_c \Theta_G$$

$$B_{m22} = 2(\bar{I}_{m2} \cos^2 \Theta_G + \bar{I}_{m3} \sin^2 \Theta_G)$$

$$B_{m23} = (\bar{I}_{m2} - \bar{I}_{m3}) \sin 2\Theta_G$$

$$B_{m33} = 2(\bar{I}_{m2} \sin^2 \Theta_G + \bar{I}_{m3} \cos^2 \Theta_G)$$

$$B_{m4} = (\bar{I}_{m2} - \bar{I}_{m3}) \cos 2\Theta_G$$

$$B_{m0} = (\bar{I}_{m2} + \bar{I}_{m3})$$

$$x_{IS} = \bar{m}\, \bar{x}_I \sin \Theta_G$$

$$x_{IC} = \bar{m}\, \bar{x}_I \cos \Theta_G$$

For uniform blade:

$$\Gamma = \gamma \frac{\ell^4}{6R^4}$$

$$\bar{\omega}^2_{L1NR} = \frac{EI_2}{m_0 \Omega^2 \ell^4} (\beta_1 \ell)^4$$

$$\bar{\omega}^2_{F1NR} = \frac{EI_3}{m_0 \Omega^2 \ell^4} (\beta_1 \ell)^4$$

$$\bar{\omega}^2_{T1NR} = \frac{GJ}{\Omega^2 \ell^2 (I_{m2} + I_{m3})} \cdot \frac{\pi^2}{4}$$

APPENDIX C

ELEMENT INTERPOLATION

$$\underset{\sim}{\gamma} = \underset{\sim}{\eta} = \begin{Bmatrix} 1 - 3\dfrac{\bar{x}_e^2}{l_e^2} + 2\dfrac{\bar{x}_e^3}{l_e^3} \\ \bar{x}_e\left(1 - 2\dfrac{\bar{x}_e}{l_e} + \dfrac{\bar{x}_e^2}{l_e^2}\right) \\ 3\dfrac{\bar{x}_e^2}{l_e^2} - 2\dfrac{\bar{x}_e^3}{l_e^3} \\ \bar{x}_e\left(-\dfrac{\bar{x}_e}{l_e} + \dfrac{\bar{x}_e^2}{l_e^2}\right) \end{Bmatrix}$$

$$\underset{\sim}{\phi} = \begin{Bmatrix} 1 - 3\bar{x}_e + 2\bar{x}_e^2 \\ 4\bar{x}_e - 4\bar{x}_e^2 \\ -\bar{x}_e + 2\bar{x}_e^2 \end{Bmatrix}$$

APPENDIX D

MATRICES FOR HOVER

The various matrix operators and element matrices required for the treatment of the flap-lag problem in hover are presented below.

$$\bar{x}_0 = \bar{x}_e + \bar{r}_e$$

$$[A_1] = \Gamma \begin{bmatrix} -2\frac{R}{\ell}\lambda\beta_p + \theta\bar{x}_0\beta_p & 0 \\ \bar{x}_0\beta_p & 0 \end{bmatrix}$$

$$[A_2] = \Gamma \begin{bmatrix} (\theta\bar{x}_0 - 2\frac{R}{\ell}\lambda)\bar{w}_{,x} + \lambda\frac{R}{\ell}\bar{x}_0\bar{w}_{,x}D_x & 0 \\ \bar{x}_0\bar{w}_{,x} - \bar{x}_0^2\bar{w}_{,x}D_x & 0 \end{bmatrix}$$

$$[A_1^e] = \Gamma \int_0^{\ell_e} \begin{bmatrix} \underset{\sim}{\gamma}\underset{\sim}{\gamma}^T(-2\frac{R}{\ell}\lambda\beta_p + \theta\beta_p\bar{x}_0) & \underset{\sim}{0} \\ \underset{\sim}{\eta}\underset{\sim}{\gamma}^T\bar{x}_0\beta_p & \underset{\sim}{0} \end{bmatrix} d\bar{x}_e$$

$$[A_2^e] = \Gamma \int_0^{\ell_e} \begin{bmatrix} \underset{\sim}{\gamma}\underset{\sim}{\gamma}^T(\theta\bar{x}_0 - 2\frac{R}{\ell}\lambda)\underset{\sim}{\eta}_{,x}^T g^{e0} + \underset{\sim}{\gamma}\underset{\sim}{\gamma}_{,x}^T\frac{R}{\ell}\bar{x}_0\,\underset{\sim}{\eta}_{,x}^T g^{e0} & \underset{\sim}{0} \\ \underset{\sim}{\eta}\underset{\sim}{\gamma}^T\bar{x}_0\,\underset{\sim}{\eta}_{,x}^T g^{e0} - \underset{\sim}{\eta}\underset{\sim}{\gamma}_{,x}^T\bar{x}_0^2\,\underset{\sim}{\eta}_{,x}^T g^{e0} & \underset{\sim}{0} \end{bmatrix} d\bar{x}_e$$

$$[\bar{A}_2^e] = \Gamma \int_0^{\ell_e} \left[\begin{array}{c|c} \underset{\sim}{\gamma}\underset{\sim}{\gamma}^T(\theta\bar{x}_0 - 2\,\frac{R}{\ell}\,\lambda)\underset{\sim}{\eta}^T_{,x}\,\underset{\sim}{g}^{e0} + \underset{\sim}{\gamma}\underset{\sim}{\gamma}^T_{,x}\,\frac{R}{\ell}\,\lambda\bar{x}_0\,\underset{\sim}{\eta}^T_{,x}\,\underset{\sim}{g}^{e0} & \underset{\sim}{\gamma}\underset{\sim}{\eta}^T_{,x}(\theta\bar{x}_0 - 2\frac{R}{\ell}\lambda)\,\underset{\sim}{\gamma}^T\underset{\sim}{h}^{e0} + \underset{\sim}{\gamma}\underset{\sim}{\eta}^T_{,x}\,\frac{R}{\ell}\,\bar{x}_0\,\lambda\,\underset{\sim}{\eta}^T_{,x}\,\underset{\sim}{h}^{e0} \\ \hline \underset{\sim}{\eta}\underset{\sim}{\gamma}^T\bar{x}_0\,\underset{\sim}{\eta}^T_{,x}\,\underset{\sim}{g}^{e0} - \underset{\sim}{\eta}\underset{\sim}{\gamma}^T_{,x}\bar{x}_0^2\,\underset{\sim}{\eta}^T_{,x}\,\underset{\sim}{g}^{e0} & \underset{\sim}{\eta}\underset{\sim}{\eta}^T_{,x}(\bar{x}_0\,\underset{\sim}{\gamma}^T\,\underset{\sim}{h}^{e0} + \bar{x}_0^2\,\underset{\sim}{\gamma}^T_{,x}\,\underset{\sim}{h}^{e0}) \end{array}\right] d\bar{x}_e$$

$$[B] = \left[\begin{array}{cc} B_{22} & B_{23} \\ B_{23} & B_{33} \end{array}\right]$$

$$[B^e] = \int_0^{\ell_e} \left[\begin{array}{cc} \underset{\sim}{\gamma}_{,xx}\,\underset{\sim}{\gamma}^T_{,xx}\,B_{22} & \underset{\sim}{\gamma}_{,xx}\,\underset{\sim}{\eta}^T_{,xx}\,B_{23} \\ \underset{\sim}{\eta}_{,xx}\,\underset{\sim}{\gamma}^T_{,xx}\,B_{23} & \underset{\sim}{\eta}_{,xx}\,\underset{\sim}{\eta}^T_{,xx}\,B_{33} \end{array}\right] d\bar{x}_e$$

$$[C_{Ax}] = \left[\begin{array}{cc} 2\int_0^{\bar{x}_0}(\bar{v}_{,x}\,D_x) & 2\int_0^{\bar{x}_0}(\bar{w}_{,x}\,D_x) \\ 0 & 0 \end{array}\right] d\bar{x}_0$$

$$[C^{e}_{Ax}] = \int_0^{\ell_e} \left[\begin{array}{c|c} \gamma 2(h^{e0})^T \int_0^{\bar{x}_e} \underset{\sim}{\gamma}_{,x}\, \underset{\sim}{\gamma}^T_{,x}\, d\bar{x}_e & \gamma 2(g^{e0})^T \int_0^{\bar{x}_e} \underset{\sim}{\eta}_{,x}\, \underset{\sim}{\eta}^T_{,x}\, d\bar{x}_e \\ \hline \underset{\sim}{0} & \underset{\sim}{0} \end{array}\right] d\bar{x}_e$$

$$[C^{ei}_{Ax}] = \left[\begin{array}{c|c} \int_0^{\ell_e} \underset{\sim}{\gamma}\, d\bar{x}_e\, 2(\underset{\sim}{h}^{i0})^T \int_0^{\ell_i} \underset{\sim}{\gamma}_{,x}\, \underset{\sim}{\gamma}^T_{,x}\, d\bar{x}_i & \\ \hline \underset{\sim}{0} & \end{array}\right.$$

$$\left.\begin{array}{|c} \int_0^{\ell_e} \underset{\sim}{\gamma}\, d\bar{x}_e\, 2(\underset{\sim}{g}^{i0})^T \int_0^{\ell_i} \underset{\sim}{\eta}_{,x}\, \underset{\sim}{\eta}^T_{,x}\, d\bar{x}_i \\ \hline \underset{\sim}{0} \end{array}\right]$$

$$[C_{T2}] = \left[\begin{array}{cc} 2D_x(\bar{v}_{,x} \int_{\bar{x}_0}^{1}) & 0 \\ 2D_x(\bar{w}_{,x} \int_{\bar{x}_0}^{1}) & 0 \end{array}\right] d\bar{x}_0$$

$$\{c\} = [\Lambda]^T \{F\}^S$$

$$[D_1] = \Gamma \left[\begin{array}{cc} \theta \frac{R}{\ell} \lambda + 2 \frac{C_{d0}}{a} \bar{x}_0 & \theta(\bar{x}_0 + e_1) - 2 \frac{R}{\ell} \lambda \\ \frac{R}{\ell} \lambda - 2\theta \bar{x}_0 & \bar{x}_0 + \bar{e}_1 \end{array}\right]$$

$$[D_2] = \Gamma \begin{bmatrix} \theta\dot{\bar{w}} & -2\beta_p \bar{v} - \dot{\bar{w}} \\ 0 & \dot{\bar{v}} \end{bmatrix}$$

$$[D_3] = \Gamma \begin{bmatrix} 0 & -2\bar{v}\bar{w}_{,x} + \bar{x}_0 \bar{v}_{,x}\bar{w}_{,x} \\ 0 & 0 \end{bmatrix}$$

$$[D_1^e] = \int_0^{\ell_e} ([\Psi]^T [D_1] [\Psi]) d\bar{x}_e$$

$$[D_2^e] = \Gamma \int_0^{\ell_e} \begin{bmatrix} \underset{\sim}{0} & \underset{\sim\sim}{\gamma}\underset{\sim}{\eta}^T 2\beta_p \underset{\sim}{\gamma}^T \underset{\sim}{h}^{e0} \\ \underset{\sim}{0} & \underset{\sim}{0} \end{bmatrix} d\bar{x}_e$$

$$[D_3^e] = \Gamma \int_0^{\ell_e} \begin{bmatrix} \underset{\sim}{0} & (\underset{\sim}{g}^{e0})^T \underset{\sim}{\eta}_{,x} \underset{\sim\sim}{\gamma}\underset{\sim}{\eta}^T (\bar{x}_0 \underset{\sim}{\gamma}_{,x}^T \underset{\sim}{h}^{e0} - 2\underset{\sim}{\gamma}^T \underset{\sim}{h}^{e0}) \\ \underset{\sim}{0} & \underset{\sim}{0} \end{bmatrix} d\bar{x}_e$$

$$[d] = [\Lambda]^T([G]^S + [D_1]^S + [D_2]^S + [D_3]^S + [T_2]^S + [T_2^i]^S - [C_{Ax}]^S - [C_{Ax}^i]^S)[\Lambda]$$

$$\{F\} = -\begin{Bmatrix} 0 \\ \\ \beta_p(\bar{x}_0 + \bar{e}_1) \end{Bmatrix}$$

$$+ \Gamma \begin{Bmatrix} -\Theta(\bar{x}_0 + \bar{e}_1)\frac{R}{\ell}\lambda + \left(\frac{R}{\ell}\right)^2\lambda^2 - \frac{C_{d0}}{a}\bar{x}_0(\bar{x}_0 + 2\bar{e}_1) \\ \\ \Theta\bar{x}_0(\bar{x}_0 + 2\bar{e}_1) - (\bar{x}_0 + \bar{e}_1)\frac{R}{\ell}\lambda \end{Bmatrix}$$

$$\{F^e\} = \int_0^{\ell_e} [\Psi]^T \{F\} d\bar{x}_e$$

$$[G] = \begin{bmatrix} 0 & -2\beta_p \\ \\ 2\beta_p & 0 \end{bmatrix}$$

$$[G^e] = \int_0^{\ell_e} ([\Psi]^T [G][\Psi]) d\bar{x}_e$$

$$[I_1] = \begin{bmatrix} 1 & 0 \\ \\ 0 & 1 \end{bmatrix}$$

$$[I_1^e] = \int_0^{\ell_e} ([\Psi]^T [I][\Psi]) d\bar{x}_e$$

$$[K_1] = \begin{bmatrix} 1 & 0 \\ \\ 0 & 0 \end{bmatrix}$$

$$[K^e] = \int_0^{\ell_e} ([\Psi]^T [K_1][\Psi]) d\bar{x}_e$$

$$[k] = [\Lambda]^T ([B]^S + [T_1]^S - [K_1]^S + [A_1]^S + [\bar{A}_2]^S)[\Lambda]$$

$$[m] = [\Lambda]^T [I_1]^S [\Lambda]$$

$$[S_B] = \begin{bmatrix} B_{22} D_x^4 & B_{23} D_x^4 \\ B_{23} D_x^4 & B_{33} D_x^4 \end{bmatrix}$$

$$[S_{T1}] = \begin{bmatrix} D_x(T_1 D_x) & 0 \\ 0 & D_x(T_1 D_x) \end{bmatrix}$$

$$T_1 = \frac{1}{2} [(1 + 2\bar{e}_1) - \bar{x}_0(\bar{x}_0 + 2\bar{e}_1)]$$

$$[s_L] = [\Lambda]^T ([B]^S + [T_1]^S - [K_1]^S + [A_1]^S)[\Lambda]$$

$$[s_{NL}] = [\Lambda]^T [A_2]^S [\Lambda]$$

$$[T_1] = \begin{bmatrix} T_1 D_x & 0 \\ 0 & T_1 D_x \end{bmatrix}$$

$$[T_2] = \begin{bmatrix} 2\bar{v}_{,x} \int_{\bar{x}_0}^{\bar{l}} (\ ) & 0 \\ 2\bar{w}_{,x} \int_{\bar{x}_0}^{\bar{l}} (\ ) & 0 \end{bmatrix} d\bar{x}_0$$

$$[T_1^e] = \int_0^{\ell_e} \begin{bmatrix} \underset{\sim}{\gamma}_{,x} \underset{\sim}{\gamma}_{,x}^T T_1 & \underset{\sim}{0} \\ \underset{\sim}{0} & \underset{\sim}{\eta}_{,x} \underset{\sim}{\eta}_{,x}^T T_1 \end{bmatrix} d\bar{x}_e$$

$$[T_2^e] = \int_0^{\ell_e} \begin{bmatrix} \underset{\sim}{\gamma}_{,x} \underset{\sim}{\gamma}_{,x}^T \underset{\sim}{h}^{e0} 2 \int_{\bar{x}_e}^{\ell_e} \underset{\sim}{\gamma}^T d\bar{x}_e & \underset{\sim}{0} \\ \underset{\sim}{\eta}_{,x} \underset{\sim}{\eta}_{,x}^T \underset{\sim}{g}^{e0} 2 \int_{\bar{x}_e}^{\ell_e} \underset{\sim}{\gamma}^T d\bar{x}_e & \underset{\sim}{0} \end{bmatrix} d\bar{x}_e$$

$$[T_2^{ei}] = \begin{bmatrix} \int_0^{\ell_e} \underset{\sim}{\gamma}_{,x} \underset{\sim}{\gamma}_{,x}^T d\bar{x}_e \underset{\sim}{h}^{e0} 2 \int_0^{\ell_i} \underset{\sim}{\gamma}^T d\bar{x}_i & \underset{\sim}{0} \\ \int_0^{\ell_e} \underset{\sim}{\eta}_{,x} \underset{\sim}{\eta}_{,x}^T d\bar{x}_e \underset{\sim}{g}^{e0} 2 \int_0^{\ell_i} \underset{\sim}{\gamma}^T d\bar{x}_i & \underset{\sim}{0} \end{bmatrix}$$

APPENDIX E

SOLUTION OF THE NONLINEAR EQUILIBRIUM EQUATIONS IN HOVER

The final nonlinear static equilibrium position equations are given as

$$\{f\} = [s_L]\{q^O\} + [s_{NL}(q^O)]\{q^O\} - \{c\} = 0 \quad , \tag{E.1}$$

see Eq. (3.18). The solution to this system is obtained by applying the iterative Newton-Raphson technique [47]. The solution increment during iteration step n can be expressed as

$$\{\delta q^O\}_n = \{q^O\}_n - \{q^O\}_{n-1} = -[J]^{-1}_{n-1}\{f\}_{n-1} \tag{E.2}$$

where the Jacobian matrix [J] is given by

$$[J] = \frac{\partial f_i}{\partial q^O_j} = [s_L] + \frac{\partial}{\partial q^O_j}([s_{NL}(q^O)]\{q^O\}) \quad . \tag{E.3}$$

In order to illustrate the evaluation of the nonlinear term and its derivative, it is helpful to use indicial notation [33]. In the following lower/upper case subscripts will be used for the element/system nodal parameters, while Greek subscripts will be used for the generalized modal coordinates.

On the element level the nonlinear term is, see Eq. (3.14),

$$[A_2^e]\{a^{e0}\} \tag{E.4}$$

or, in indicial notation,

$$(A_2^e)_{ijk} \cdot a_j^{e0} \cdot a_k^{e0} \quad . \tag{E.5}$$

Using Eq. (3.16) to express a_k^{e0} in terms of its modal representation, (E.5) becomes

$$(A_2^e)_{ijk} \cdot a_j^{e0} \cdot \Lambda_{k\alpha}\, q_\alpha^0 \tag{E.6}$$

or

$$(A_2^e\ \Lambda)_{ij\alpha} \cdot a_j^{e0} \cdot q_\alpha^0 \quad . \tag{E.7}$$

Here, $(A_2^e\ \Lambda)$ is a new third-order tensor. This tensor is now assembled to yield an expression for the system, namely,

$$(A_2\ \Lambda)_{IJ\alpha} \cdot a_J^0 \cdot q_\alpha^0 \quad . \tag{E.8}$$

Now, the modal reduction is completed as indicated by Eq. (3.20), i.e.,

$$\Lambda_{\gamma I} \quad (A_2 \Lambda)_{IJ\alpha} \quad \Lambda_{J\beta} \quad q^0_\beta \quad q^0_\alpha \tag{E.9}$$

or

$$(s_{NL})_{\gamma\beta\alpha} \cdot q^0_\beta \cdot q^0_\alpha \ . \tag{E.10}$$

Note that expression (E.10) can be written in matrix form which will yield the final expression for the nonlinear term as it is presented in Eq. (E.1).

The derivative of $(s_{NL})_{\gamma\beta\alpha}$ is simply taken according to the chain rule

$$\frac{\partial}{\partial q^0_j} (s_{NL})_{i\ell k} q^0_\ell q^0_k = (s_{NL})_{i\ell k} \left(\frac{\partial q^0_\ell}{\partial q^0_j} q^0_k + q^0_\ell \frac{\partial q^0_k}{\partial q^0_j} \right)$$

$$= (s_{NL})_{ijk} q^0_k + (s_{NL})_{i\ell j} q^0_\ell \ . \tag{E.11}$$

APPENDIX F

ELEMENT MATRICES FOR FORWARD FLIGHT

The element matrices for the coupled flap-lag-torsion problem in forward flight, see Equation (4.20), are defined below. Each coupled element matrix can be written in a partitioned form, e.g.:

$$[A_1^e] = \left[\begin{array}{c|c|c} [A^e_{1LL}] & [A^e_{1LF}] & [A^e_{1LT}] \\ \hline [A^e_{1FL}] & [A^e_{1FF}] & [A^e_{1FT}] \\ \hline [A^e_{1TL}] & [A^e_{1TF}] & [A^e_{1TT}] \end{array}\right] \qquad (F.1)$$

Since some of the element matrices are rather lengthy expressions, they will be defined in terms of the sub-matrices. Sub-matrices which are not listed below are identically zero.

$$[A_1^e] = \Gamma \int_0^{\ell_e} \left[\begin{array}{c|c|c} \underset{\sim}{\gamma}\underset{\sim}{\gamma}^T \rho_p (Q_G F_1 - 2F_2) & \underset{\sim}{\gamma}\underset{\sim}{\eta}^T_{,x} (Q_G F_1 - 2F_2 & \underset{\sim}{\gamma}\underset{\sim}{\phi}^T F_1 F_2 \\ + \underset{\sim}{\gamma}\underset{\sim}{\gamma}^T_{,x} (Q_G F_2 + 2 \frac{C_{dO}}{a} F_1) F_3 & + \dot{Q}_G F_4) F_3 & \\ \hline \underset{\sim}{\eta}\underset{\sim}{\gamma}^T \rho_p F_1 & \underset{\sim}{\eta}\underset{\sim}{\eta}^T_{,x} F_1 F_3 & -\underset{\sim}{\eta}\underset{\sim}{\phi}^T F_1^2 \\ + \underset{\sim}{\eta}\underset{\sim}{\gamma}^T_{,x} (F_2 - 2Q_G F_1) F_3 & & \\ \hline \bar{b} \frac{R}{\ell} \bar{x}_A (\underset{\sim}{\phi}\underset{\sim}{\gamma}^T \rho_p F_1 & \underset{\sim}{\phi}\underset{\sim}{\eta}^T_{,x} \bar{b} \frac{R}{\ell} \bar{x}_A F_1 F_3 & -\underset{\sim}{\phi}\underset{\sim}{\phi}^T \bar{b} \frac{R}{\ell} \bar{x}_A F_1^2 \\ + \underset{\sim}{\phi}\underset{\sim}{\gamma}^T_{,x} (F_2 - 2Q_G F_1) F_3) & & \end{array}\right] d\bar{x}_e$$

$$[A_2^e] = \Gamma \int_0^{\ell_e} \left[\begin{array}{c|c|c} (\underset{\sim}{\chi\chi}^T(\Theta_G F_1 - 2F_2 - 2\beta_p F_3) + \underset{\sim}{\chi\chi}'^T_{,x}(\Theta_G F_3^2 + F_1 F_2))\bar{w}^e_{,x} & -\underset{\sim}{\chi\eta}^T_{,x} F_3^2 \bar{w}^e_{,x} & \underset{\sim}{\chi\phi}^T(\beta_p F_1 \bar{v}^e + F_2 F_3 \bar{v}^e_{,x} + F_1 F_3 \bar{w}^e_{,x}) \\ \hline (\underset{\sim}{\eta\chi}^T F_1 + \underset{\sim}{\eta\chi}'^T_{,x}(F_3^2 - F_1^2))\bar{w}^e_{,x} & \underset{\sim}{0} & -\underset{\sim}{\eta\phi}^T 2F_1 F_3 \bar{v}^e_{,x} \\ \hline \bar{b}\frac{R}{\ell}\bar{x}_A(\underset{\sim}{\phi\chi}^T F_1 + \underset{\sim}{\phi\chi}'^T_{,x}(F_3^2 - F_1^2))\bar{w}^e_{,x} & \underset{\sim}{0} & -\underset{\sim}{\phi\phi}^T \bar{b}\frac{R}{\ell}\bar{x}_A 2F_1 F_3 \bar{v}^e_{,x} \end{array}\right] d\bar{x}_e$$

$$[A_3^e] = \Gamma \int_0^{\ell_e} \left[\begin{array}{c|c|c} \underset{\sim}{0} & \underset{\sim}{\gamma}\underset{\sim}{\eta}^T_{,x}(-2F_3\bar{v}^e + F_1F_3\bar{v}^e_{,x})\bar{w}^e_{,x} & \underset{\sim}{\gamma}\underset{\sim}{\phi}^T(F_1\bar{v}^e + F_3^2\bar{v}^e_{,v})\bar{w}^e_{,x} \\ \hline \underset{\sim}{0} & \underset{\sim}{0} & \underset{\sim}{0} \\ \hline \underset{\sim}{0} & \underset{\sim}{0} & \underset{\sim}{0} \end{array}\right] d\bar{x}_e$$

$$[B_1^e] = \int_0^{\ell_e} \left[\begin{array}{c|c|c} \underset{\sim}{\gamma}_{,xx}\underset{\sim}{\gamma}^T_{,xx} B_{22} & \underset{\sim}{\gamma}_{,xx}\underset{\sim}{\eta}^T_{,xx} B_{23} & \underset{\sim}{0} \\ \hline \underset{\sim}{\eta}_{,xx}\underset{\sim}{\gamma}^T_{,xx} B_{23} & \underset{\sim}{\eta}_{,xx}\underset{\sim}{\eta}^T_{,xx} P_{33} & \underset{\sim}{0} \\ \hline \underset{\sim}{0} & \underset{\sim}{0} & \underset{\sim}{\phi}_{,x}\underset{\sim}{\phi}^T_{,x}\bar{G}\bar{J} \end{array}\right] d\bar{x}_e$$

$$[B^1_{cTT}] = \begin{bmatrix} \bar{K}_\phi & 0 & 0 \\ 0 & 0 & 0 \\ 0 & 0 & 0 \end{bmatrix}$$

$$[B_2^e] = \int_0^{\ell_e} \left[\begin{array}{c|c|c} -\underset{\sim}{\gamma}_{,xx}\underset{\sim}{\gamma}^T_{,xx}\, 2B_{23}\, \phi^e & \underset{\sim}{\gamma}_{,xx}\underset{\sim}{\eta}^T_{,xx}(2B_4\, \phi^e - \bar{G}\bar{J}\, \phi^e_{,x}) & \underset{\sim}{0} \\ \hline \underset{\sim}{\eta}_{,xx}\underset{\sim}{\gamma}^T_{,xx}(2B_4\, \phi^e + \bar{G}\bar{J}\, \phi^e_{,x}) & \underset{\sim}{\eta}_{,xx}\underset{\sim}{\eta}^T_{,xx}\, 2B_{23}\, \phi^e & \underset{\sim}{0} \\ \hline \phi\underset{\sim}{\gamma}^T_{,xx}(-B_{23}\, \bar{v}^e_{,xx} + 2B_4\, \bar{w}^e_{,xx}) & \phi\underset{\sim}{\eta}^T_{,xx}\, B_{23}\, \bar{w}^e_{,xx} + \phi_{,x}\underset{\sim}{\eta}^T_{,x}\, \bar{G}\bar{J}\, \bar{v}^e_{,xx} & \underset{\sim}{0} \end{array}\right] d\bar{x}_e$$

$$[C_1^e] = \int_0^{\ell_e} \begin{bmatrix} \underset{\sim}{0} & -\underset{\sim}{\gamma}\underset{\sim}{\eta}^T \bar{m}\, 2\beta_p & \underset{\sim}{0} \\ \underset{\sim}{\eta}\underset{\sim}{\gamma}^T \bar{m}\, 2\beta_p & \underset{\sim}{0} & \underset{\sim}{0} \\ \underset{\sim}{\phi}\underset{\sim}{\gamma}^T x_{IC}\, 2\beta_p + \underset{\sim}{\phi}\underset{\sim}{\gamma}_{,x}^T B_{m23} & \underset{\sim}{\phi}\underset{\sim}{\eta}_{,x}^T B_{m33} & \underset{\sim}{0} \end{bmatrix} d\bar{x}_e$$

$$[C_{2TL}^e] = \int_0^{\ell_e} [\underset{\sim}{\phi}\underset{\sim}{\gamma}^T x_{IC}\, 2\underset{\sim}{\eta}_{,x}^T \underset{\sim}{g}^e + \underset{\sim}{\phi}\underset{\sim}{\gamma}_{,x}^T 2B_{m4}\, \underset{\sim}{\phi}^T \underset{\sim}{f}^e] d\bar{x}_e$$

$$[C_{21TF}^e] = \int_0^{\ell_e} [\underset{\sim}{\phi}\underset{\sim}{\eta}_{,x}^T B_{m33}\, \underset{\sim}{\gamma}_{,x}^T \hat{n}^e] d\bar{x}_e$$

$$[C_{AxLL}^e] = \int_0^{\ell_e} \left[2\bar{m}\, \underset{\sim}{\gamma} \int_0^{\bar{x}_e} ((\underset{\sim}{h}^e)^T \underset{\sim}{\gamma}_{,x}) \underset{\sim}{\gamma}_{,x}^T d\bar{x}_e \right] d\bar{x}_e$$

$$[C_{AxLF}^e] = \int_0^{\ell_e} \left[2\bar{m}\, \underset{\sim}{\gamma} \int_0^{\bar{x}_e} ((\underset{\sim}{g}^e)^T \underset{\sim}{\eta}_{,x}) \underset{\sim}{\eta}_{,x}^T d\bar{x}_e \right] d\bar{x}_e$$

$$[C_{AxLL}^{ei}] = \left[\int_0^{\ell_e} 2\bar{m}\, \underset{\sim}{\gamma}\, d\bar{x}_e \int_0^{\ell_i} ((\underset{\sim}{h}^i)^T \underset{\sim}{\gamma}_{,x}) \underset{\sim}{\gamma}_{,x}^T d\bar{x}_i \right]$$

$$[C_{AxLF}^{ei}] = \left[\int_0^{\ell_e} 2\bar{m}\, \underset{\sim}{\gamma}\, d\bar{x}_e \int_0^{\ell_i} ((\underset{\sim}{g}^i)^T \underset{\sim}{\eta}_{,x}) \underset{\sim}{\eta}_{,x}^T d\bar{x}_i \right]$$

$$[D_S^e] = \int_0^{\ell_e} \left[\begin{array}{c|c|c} \underset{\sim}{\gamma\gamma}^T \bar{g}_{SL} & \underset{\sim}{0} & \underset{\sim}{0} \\ \underset{\sim}{0} & \underset{\sim}{\eta\eta}^T \bar{g}_{SF} & \underset{\sim}{0} \\ \underset{\sim}{0} & \underset{\sim}{0} & \underset{\sim}{\phi\phi}^T \bar{g}_{ST} \end{array}\right] d\bar{x}_e$$

$$[D_1^e] = \Gamma \int_0^{\ell_e} \left[\begin{array}{c|c|c} \underset{\sim}{\gamma\gamma}^T(\Theta_G F_2 + 2\,\frac{C_{d\Theta}}{a}\,F_1) & \underset{\sim}{\gamma\eta}^T(\Theta_G F_1 - 2F_2 + \dot{\delta}_G F_4) & \underset{\sim}{\gamma\phi}^T F_2 F_4 \\ \underset{\sim}{\eta\gamma}^T(F_2 - 2\Theta_G F_1) & \underset{\sim}{\eta\eta}^T F_1 & -\underset{\sim}{\eta\phi}^T F_1 F_4 \\ \underset{\sim}{\phi\gamma}^T \bar{b}\,\frac{R}{\ell}\,\bar{x}_A(F_2 - 2\Theta_G F_1) & \underset{\sim}{\phi\eta}^T \bar{b}\,\frac{R}{\ell}\,\bar{x}_A F_1 & \underset{\sim}{\phi\phi}^T F_1 F_5 \end{array}\right] d\bar{x}_e$$

$$[D_2^e] = \Gamma \int_0^{\ell_e} \left[\begin{array}{c|c|c} \underset{\sim}{\gamma\gamma}^T(\Theta_G F_3\, \bar{w}^e_{,x} + F_2\, \phi^e) & \underset{\sim}{\gamma\eta}^T(\Theta_G\, F_3\, \bar{v}^e_{,x} - 2\beta_p\, \bar{v}^e - 2F_3\, \bar{w}^e_{,x} + F_1\, \phi^e) & \underset{\sim}{\gamma\phi}^T\, F_3 F_4\, \bar{w}^e_{,x} \\ \hline \underset{\sim}{\eta\gamma}^T(F_3\, \bar{w}^e_{,x} - 2F_1\, \phi^e) & \underset{\sim}{\eta\eta}^T\, F_3\, \bar{v}^e_{,x} & \underset{\sim}{0} \\ \hline \underset{\sim}{\phi\gamma}^T(F_3\, \bar{w}^e_{,x} - 2F_1\, \phi^e)\bar{b}\, \frac{R}{\ell}\, \bar{x}_A & \underset{\sim}{\phi\eta}^T\, \frac{R}{\ell}\, \bar{x}_A\, F_3\, \bar{v}^e_{,x}\, \bar{b} & \underset{\sim}{0} \end{array}\right] d\bar{x}_e$$

$$[D_3^e] = \Gamma \int_0^{\ell_e} \left[\begin{array}{c|c|c} \underset{\sim}{\gamma\gamma}^T\, F_3\, \phi^e\, \bar{w}^e_{,x} & \underset{\sim}{\gamma\eta}^T(-2\bar{v}^e\, \bar{w}^e_{,x} + F_1\, \bar{v}^e_{,x}\, \bar{w}^e_{,x} + F_3\, \phi^e\, \bar{v}^e_{,x}) & \underset{\sim}{0} \\ \hline \underset{\sim}{0} & \underset{\sim}{0} & \underset{\sim}{0} \\ \hline \underset{\sim}{0} & \underset{\sim}{0} & \underset{\sim}{0} \end{array}\right] d\bar{x}_e$$

$$[D_{22}^e] = \Gamma \int_0^{\ell_e} \begin{bmatrix} \underset{\sim}{\gamma\gamma}^T \Theta_G \dot{\bar{w}}^e & -\underset{\sim}{\gamma\eta}^T \dot{\bar{w}}^e & \underset{\sim}{\gamma\phi}^T F_4 \dot{\bar{w}}^e \\ \underset{\sim}{0} & \underset{\sim}{\eta\eta}^T \dot{\bar{v}}^e & \underset{\sim}{0} \\ \underset{\sim}{0} & \underset{\sim}{\phi\eta}^T \bar{b} \frac{R}{\ell} \bar{x}_A \dot{\bar{v}}^e & \underset{\sim}{0} \end{bmatrix} d\bar{x}_e$$

$$[D_{32LL}^e] = \Gamma \int_0^{\ell_e} \left[\underset{\sim}{\gamma\gamma}^T \phi^e \dot{\bar{w}}^e \right] d\bar{x}_e$$

$$[F_I^e] = \int_0^{\ell_e} \left\{ \begin{array}{l} -\underset{\sim}{\gamma}(x_{IC} + x_{IS} \ddot{\Theta}_G) + \underset{\sim}{\gamma}_{,x}(x_{IC}(\bar{e}_1 + \bar{x}_0) - B_{m23} \dot{\Theta}_G) \\ \underset{\sim}{\eta}(\bar{m} \beta_p(\bar{e}_1 + \bar{x}_0) + x_{IC} \ddot{\Theta}_G) + \underset{\sim}{\eta}_{,x}(x_{IS}(\bar{e}_1 + \bar{x}_0) - B_{m33} \dot{\Theta}_G) \\ \underset{\sim}{\phi}(x_{IC} \beta_p(\bar{e}_1 + \bar{x}_0) + \frac{1}{2} B_{m23} + B_{m0} \ddot{\Theta}_G) \end{array} \right\} d\bar{x}_e$$

$$[F_A^e] = \Gamma \int_0^{\ell_e} \left\{ \begin{array}{l} \underset{\sim}{\gamma}(\Theta_G F_1 - F_2 + \dot{\Theta}_G F_4) F_2 + \frac{C_{d0}}{a} F_1^2 \\ \underset{\sim}{\eta}(-\Theta_G F_1 + F_2 - \dot{\Theta}_G F_4) F_1 \\ \underset{\sim}{\phi}(\bar{b} \frac{R}{\ell} \bar{x}_A (F_2 - \Theta_G F_1) F_1 + \dot{\Theta}_G F_1 F_5) \end{array} \right\} d\bar{x}_e$$

$$[I_1^e] = \int_0^{\ell_e} \begin{bmatrix} \underset{\sim}{\gamma\gamma}^T \bar{m} & \underset{\sim}{0} & \underset{\sim}{0} \\ \underset{\sim}{0} & \underset{\sim}{\eta\eta}^T \bar{m} & \underset{\sim}{0} \\ -\underset{\sim}{\phi\gamma}^T x_{IS} & \underset{\sim}{\phi\eta}^T x_{IC} & \underset{\sim}{\phi\phi}^T B_{m0} \end{bmatrix} d\bar{x}_e$$

$$[L^e_{2TL}] = \int_0^{\ell_e} [-\underset{\sim}{\phi}\underset{\sim}{\gamma}^T x_{IC}\, \underset{\sim}{\phi}^T \underset{\sim}{f}^e + \underset{\sim}{\phi}_{,x}^T B_{m0}\, \underset{\sim}{\eta}_{,x}^T \underset{\sim}{g}^e]d\bar{x}_e$$

$$[K^e_{1LL}] = \int_0^{\ell_e} [-\underset{\sim}{\gamma}\underset{\sim}{\gamma}^T \bar{m}]d\bar{x}_e$$

$$[K^e_{1TL}] = \int_0^{\ell_e} [\underset{\sim}{\phi}\underset{\sim}{\gamma}^T x_{IS} - \underset{\sim}{\phi}\underset{\sim}{\gamma}_{,x}^T(x_{IS}(\bar{e}_1 + \bar{x}_0) + B_{m4}\, \beta_p)]d\bar{x}_e$$

$$[K^e_{1TF}] = \int_0^{\ell_e} [\underset{\sim}{\phi}\underset{\sim}{\eta}_{,x}^T x_{IC}(\bar{e}_1 + \bar{x}_0)]d\bar{x}_e$$

$$[K^e_{1TT}] = \int_0^{\ell_e} [\underset{\sim}{\phi}\underset{\sim}{\phi}^T B_{m4}]d\bar{x}_e$$

$$[K^e_{2TT}] = \int_0^{\ell_e} [\underset{\sim}{\phi}\underset{\sim}{\phi} x_{IC}(\underset{\sim}{\gamma}^T \underset{\sim}{h}^e - \underset{\sim}{\gamma}_{,x}^T \underset{\sim}{h}^e(\bar{e}_1 + \bar{x}_0))]d\bar{x}_e$$

$$[T^e_1] = \int_0^{\ell_e} \begin{bmatrix} \underset{\sim}{\gamma}_{,x}\underset{\sim}{\gamma}_{,x}^T T_1 & \underset{\sim}{0} & \underset{\sim}{0} \\ \underset{\sim}{0} & \underset{\sim}{\eta}_{,x}\underset{\sim}{\eta}_{,x}^T T_1 & \underset{\sim}{0} \\ \underset{\sim}{0} & \underset{\sim}{0} & \underset{\sim}{0} \end{bmatrix} d\bar{x}_e$$

$$[T^{e}_{2LL}] = \int_0^{\ell_e} \left[2\underset{\sim}{\gamma}_{,x} \int_{\bar{x}_e}^{\ell_e} \bar{m}\, \underset{\sim}{\gamma}^T d\bar{x}_e (\underset{\sim}{\gamma}^T_{,x}\, \underset{\sim}{h}^e) \right] d\bar{x}_e$$

$$[T^{e}_{2FL}] = \int_0^{\ell_e} \left[2\underset{\sim}{\eta}_{,x} \int_{\bar{x}_e}^{\ell_e} \bar{m}\, \underset{\sim}{\gamma}^T d\bar{x}_e (\underset{\sim}{\eta}^T_{,x}\, \underset{\sim}{h}^e) \right] d\bar{x}_e$$

$$[T^{ei}_{2LL}] = \left[2 \int_0^{\ell_e} \underset{\sim}{\gamma}_{,x} (\underset{\sim}{\gamma}^T_{,x}\, \underset{\sim}{h}^e) d\bar{x}_e \int_0^{\ell_i} \bar{m}\, \underset{\sim}{\gamma}^T d\bar{x}_i \right]$$

$$[T^{ei}_{2FL}] = \left[2 \int_0^{\ell_e} \underset{\sim}{\eta}_{,x} (\underset{\sim}{\eta}^T_{,x}\, \underset{\sim}{g}^e) d\bar{x}_e \int_0^{\ell_i} \bar{m}\, \underset{\sim}{\gamma}^T d\bar{x}_i \right]$$

APPENDIX G

LINEARIZATION OF FORWARD FLIGHT EQUATIONS

The nonlinear flap-lag-torsion equations of motion, Equation (4.22),

$$\underset{\sim}{G} = [m(\underset{\sim}{q})]\{\ddot{q}\} + [d(\underset{\sim}{q}, \dot{\underset{\sim}{q}})]\{\dot{q}\} + [k(\underset{\sim}{q})]\{q\} + \{f\} = 0 \quad (G.1)$$

are linearized using a Taylor series expansion. The nonlinear mass, damping, and stiffness matrices and the forcing vector are defined below in indicial notation. The range of the indices is 1 through M, where M is the total number of modes used in the analysis.

$$[m(\underset{\sim}{q})] = m_{1ij} + m_{2ijk} \cdot q_k \quad (G.2)$$

$$\begin{aligned}[d(\underset{\sim}{q}, \dot{\underset{\sim}{q}})] = {} & c_{1ij} + d_{Sij} + d_{1ij} \\ & + (c_{2ijk} + t_{2ijk} - c_{Axijk} + d_{2ijk} + d_{3ijk\ell} \cdot q_\ell) q_k \\ & + (c_{2ijk} + d_{22ijk} + d_{32ijk\ell} \cdot q_\ell) \dot{q}_k \end{aligned} \quad (G.3)$$

$$\begin{aligned}[k(\underset{\sim}{q})] = {} & b_{1ij} + t_{1ij} + k_{1ij} + a_{1ij} \\ & + (b_{2ijk} + k_{2ijk} + a_{2ijk} + a_{3ijk\ell} \cdot q_\ell) q_k \end{aligned} \quad (G.4)$$

$$\{f\} = f_{Ii} + f_{Ai} \quad (G.5)$$

where

$$m_{1ij} = [\Lambda]^T [I_1]^S [\Lambda]$$

$$m_{2ijk}\, q_k = [\Lambda]^T [I_2]^S [\Lambda]$$

$$t_{2ijk}\, q_k = [\Lambda]^T ([T_2]^S + [T_2^i]^S)[\Lambda]$$

$$c_{A\_ijk}\, q_k = [\Lambda]^T([C_{Ax}]^S + [C_{Ax}^i]^S)[\Lambda]$$

$$b_{1ij} = [\Lambda]^T([B_1]^S + [B_c]^S)[\Lambda]$$

$$f_{Ii} = [\Lambda]^T \{F_I\}^S$$

$$f_{Ai} = [\Lambda]^T \{F_A\}^S \quad .$$

All other quantities in Equations (G.2) - (G.5) are obtained directly from the corresponding (upper case) system matrices, i.e.,

$$c_{1ij} = [\Lambda]^T [C_1]^S [\Lambda] \quad ,$$

etc.

The derivatives of $\underset{\sim}{G}$, Equation (4.24) and Equation (4.34), are then defined as follows:

$$\frac{\partial G_i}{\partial q_n} = b_{1in} + t_{1in} + k_{1in} + a_{1in}$$

$$+ (b_{2ink} + k_{2ink} + a_{2ink} + a_{3ink\ell}\, q_\ell) q_k$$

$$+ (b_{2ijn} + k_{2ijn} + a_{2ijn} + a_{3ijn\ell}\, q_\ell) q_j$$

$$+ a_{3ijkn}\, q_k\, q_j$$

$$+ (c_{2ijn} + t_{2ijn} - c_{Axijn} + d_{2ijn} + d_{3ijn\ell}\, q_\ell$$

$$+ d_{3ijkn}\, q_k + d_{32ijkn}\, \dot{q}_k) \dot{q}_j$$

$$+ m_{2ijn}\, \ddot{q}_j \quad , \qquad (G.6)$$

$$\frac{\partial G_i}{\partial \dot{q}_n} = c_{1in} + d_{Sin} + d_{1in}$$

$$+ (c_{2ink} + t_{2ink} - c_{Axink} + d_{2ink} + d_{3ink\ell}\, q_\ell) q_k$$

$$+ (c_{21ink} + d_{22ink} + d_{32ink\ell}\, q_\ell) \dot{q}_k$$

$$+ (c_{21ijn} + d_{22ijn} + d_{32ijn\ell}\, q_\ell) \dot{q}_j \quad , \qquad (G.7)$$

$$\frac{\partial G_i}{\partial \ddot{q}_n} = m_{1in} + m_{2ink}\, q_k \quad . \qquad (G.8)$$